Institut für Wasser und Gewässerentwicklung
Universität Karlsruhe (TH)

Spatial Time Domain Reflectometry
for Monitoring Transient Soil Moisture Profiles

Rolf Becker

Heft 228

2004

Spatial Time Domain Reflectometry
for Monitoring Transient Soil Moisture Profiles

Zur Erlangung des akademischen Grades eines

DOKTOR-INGENIEURS

von der Fakultät für

Bauingenieur-, Geo- und Umweltwissenschaften
der Universität Fridericiana zu Karlsruhe (TH)

vorgelegte

DISSERTATION

von

Dipl.-Phys. Rolf Becker
aus Wesel

Hauptreferent:	Prof. Dr.-Ing. Erich Plate
Korreferent:	Prof. Dr.-Ing. Franz Nestmann
Korreferent:	Prof. Dr.-Ing. Werner Wiesbeck

Karlsruhe 2004

To my friends

Zusammenfassung

Time Domain Reflektometrie (TDR) ist ein verlässliches Verfahren zur Bestimmung der Bodenfeuchte, das sich in unzähligen hydrologischen Untersuchungen bewährt hat. Ein großer Nachteil herkömmlicher TDR-Verfahren ist, dass diese nur Punktmessungen oder mittlere Wassergehalte entlang der eingesetzten Bodenfeuchtesonden liefern.

Spatial TDR ist ein erweitertes Verfahren, mit dem komplette Bodenfeuchteprofile entlang einzelner Sonden in hoher räumlicher und zeitlicher Auflösung bestimmt werden können. Kombiniert man viele solcher Profilmessungen in einem begrenzten Areal (*TDR-Cluster*)ergibt sich ein verlässliches Bild der vertikalen Feuchteverteilung im Untergrund und der lateralen Unterschiede aufgrund der kleinskaligen Variabilität des Bodens.

Die vorliegende Dissertation leistet einen grundlegenden Beitrag zum Aufbau eines fernabfragbaren, autarken Messsytems zur kontinuierlichen Beobachtung räumlich verteilter, vertikaler Bodenfeuchteprofile mit Spatial TDR. Dieses Verfahren beruht auf einem Rekonstruktionsalgorithmus zur inversen Schätzung der Wassergehaltsverteilung, der für den genannten Anwendungsfall erweitert werden musste.

Empirische Kalibrationsverfahren wurden entwickelt, um die elektrischen Eigenschaften einer neuartigen Dreistabsonde mit beschichteten Stäben zu bestimmen. Um die neue Messmethode optimal auf den gewählten Boden anzupassen wurden weitere Labormessungen durchgeführt.

Das gesamte Verfahren zur Bestimmung von Wassergehaltsprofilen wurde anhand eines Beregnungsversuchs im Labor getestet. Dazu wurden vier Dreistabsonden in einem Lysimeter installiert, das mit schwach schluffigem Sand gefüllt war. Die Ergebnisse zeigen fortschreitende Infiltrationsfronten in hoher räumlicher und zeitlicher Auflösung. Lokale Effekte wie Verdichtungshorizonte und laterale Umverteilung des Wassers im Bodenkörper konnten mit dem Messsytem beobachtet werden.

Parallel zu den Laborexperimenten wurde ein zweites Messsystem mit solarer Stromversorgung und Funkmodem ausgestattet und in einem Feldversuch über mehrere Monate getestet. Die 47 Bodenfeuchtesonden des TDR-Clusters waren in einer Senke installiert, die zeitweise von einem Wasserlauf durchflossen wurde. Die sich ändernde Ausdehnung des gesättigten Flächenanteils konnte mit Spatial TDR sowohl in der Fläche als auch in vertikalen Querschnitten beobachtet werden.

Darüber hinaus wurde Spatial TDR auf ein Infiltrationsmodell angewandt, das auf der analytischen Lösung der Richards-Gleichung unter konstanten Flussrandbedingungen beruht. Für das gewählte Modell konnte trotz des großen Informationsgehalts der rekonstruierten Bodenfeuchteprofile keine Verbesserung bei der Schätzung bodenhydraulischer Parameter erzielt werden, weil unterschiedliche Lagerungsdichten des Bodens, laterale Flusskomponenten und inhomogene Anfangswassergehalte durch das Modell nicht abgebildet werden konnten.

Schließlich wurde ein neuartiges TDR-Gerät entworfen, gebaut und getestet, um eine kostengünstige Alternative zu kommerziellen Produkten aufzuzeigen. Die Abtastschaltung des neuen TDR-Instruments beruht auf Deltamodulation. Dieser Regelkreis unterscheidet sich wesentlich von den sonst üblichen Abtast-Halte-Gliedern. Der Prototyp zeigt bereits eine gute Übereinstimmung des abgetasteten Signals mit den Ergebnissen konventioneller Instrumente und könnte deshalb bald für Spatial TDR einsetzbar sein.

Abstract

Time Domain Reflectometry (TDR) is a reliable method for soil moisture determination, which has proven to be a success in innumerable hydrological investigations. However, a major disadvantage of conventional TDR methods is, that they are only yielding point measurements or average water content along the applied soil moisture probes.

Spatial TDR is an extended method, which allows the retrieval of complete soil moisture profiles along individual probes in high spatial and temporal resolution. The combination of many profile measurements in a limited area gives a reliable picture of the vertical moisture distribution in subsoil and of the lateral differences caused by small scale variability of soil.

The current dissertation offers fundamental contributions to the realization of a remotely accessible, self-contained measuring system for continuous monitoring of spatially distributed vertical soil moisture profiles with Spatial TDR. This method is based on a reconstruction algorithm for inverse estimation of water content profiles, which had to be extended for the actual application.

Empirical calibration methods have been developed to determine the electrical properties of a novel 3-rod-probe with coated rods. Additional laboratory measurements have been conducted to optimally adapt the new methodology to the soil under test.

The complete method for the water content profile retrieval was tested in the laboratory with a precipitation experiment. Therefore four 3-rod-probes were installed in a lysimeter filled with silty sand. The results show propagating infiltration fronts in high spatial and temporal resolution. Local effects like compaction layers and lateral redistribution of water in the soil body could be observed by the measuring system.

Parallel to the laboratory experiments a second measuring system was equipped with a solar power supply and a wireless modem and tested for several months in a field application. The 47 soil moisture probes of the TDR cluster were installed in a valley, which was temporarily influenced by an ephemeral creek. The variable extent of the saturated area could be observed by Spatial TDR, both, laterally and in vertical cross-sections.

In addition Spatial TDR was applied to an infiltration model based on the analytical solution of Richards' equation under constant flux boundary conditions. Despite the large information content of the reconstructed soil moisture profiles no improvement in estimating the soil hydraulic parameters was reached for this particular model. Lateral flow components and inhomogeneous initial water content, caused by locally different soil compaction, could not be mapped by this insufficient model.

Finally a novel TDR instrument was designed, built, and tested to present a cost-effective alternative to commercial products. The sampling circuit of the new TDR instrument is based on delta modulation. This closed-loop control circuit differs substantially from standard sample-and-hold circuits. The prototype already shows a good accordance of the sampled signal with the results of conventional instruments and could therefore be ready for Spatial TDR application soon.

Contents

Contents

1. Introduction

Importance of Soil Moisture at Different Scales

Water is a vital resource, which we have to protect and which we are to be protected from. We need a better understanding of hydrological processes to address the society's growing needs for freshwater supply and risk mitigation of droughts and floods. The water content in the upper soil layers, which are referred to as *vadose zone*, plays an important role in many hydrological and meteorological processes at different spatial and temporal scales. These scales are not independent from each other but are coupled through the individual processes (e.g. *Blöschl* (1996), p. 71).

At the regional to continental scale soil moisture determines the partitioning of the net radiative forcing into sensible and latent heat flux and thus the transition from potential to actual evaporation at larger time scales (*Dooge*, 1986). The resulting near-surface atmospheric humidity and temperature influence the atmospheric boundary layer and thus the local climate. *Entekhabi et al.* (1999) (s. Fig. 1 therein) state, that regional soil moisture has a huge impact on the numerical forecasting of hydro-climatological anomalies like extreme precipitation and droughts. According to the authors water content is of same importance as sea surface temperature (SST) for global climate models.

At the catchment scale it controls soil hydraulic properties and therefore the infiltration and surface runoff generation at the event time scale (*Grayson et al.*, 1997). For a small catchment *Peschke et al.* (1998) show, that the relative contribution of subcatchments to the total runoff is highly correlated with the extent of saturated areas within the subcatchments, a consequence of the local soil moisture state. Also the occurrence of fast drainage processes, such as preferential and subsurface storm flow, seems to be controlled to a far extent by the moisture state of the subsurface (*McGlynn et al.* (2002); *Zehe and Flühler* (2001)). Actual soil moisture patterns are reflections of the underlying dominating hydrological processes (*Western et al.*, 2001).

At the field scale the actual soil moisture state in the root zone controls the water supply for plants and crops. Furthermore fast percolation of fertilizers or pesticides into deeper soil strata may occur on the event time scale due to macropore flow, the activation of which is also controlled by soil moisture. Chemicals transported beyond the biologically active soil strata experience only a slow or no decomposition and may threaten ground water quality.

These examples illuminate the broad spectrum of todays and future challenges science has to cope with. Hydrological science has already made a valuable contribution to the understanding of environmental dynamics, but today it seems, that further progress is only possible, if we gain more insight into the underlying processes. Observation is the source of knowledge and observation comprises measurement.

1. Introduction

Soil Water Content Measurements at Different Scales

Soil water content and its evolution in space and time carry important information about the state and dynamic of an environmental system. This underlines the exigence for soil water content measurements across a wide range of spatial and temporal scales. There is no best way of measuring soil moisture. The selected method has to fit the spatial and temporal scale of the dynamic process of interest.

The following examples are not a comprehensive review of the state of the art technologies but are meant for demonstrating typical space and time scales of different measuring instruments.

Remote sensing with active and passive microwave instruments is the most promising technique for measuring soil water content variations on a large spatial scale. The European ERS-2 satellite is equipped with a variety of remote sensing instruments for different purposes. *Walker et al.* (2004) have used an active sensor (C-band vertically polarized synthetic aperture radar) of ERS-2 to determine near-surface moisture with a lateral (azimuthal) resolution of 8–30 m. The satellite has a 35-day repeat cycle.

A new promising instrument for global survey will be the HYDROS satellite, specially designed for global soil moisture, freeze, and thaw measurement (*Entekhabi*, 2003). It is a combination of active microwave radar and passive radiometer. After its launch in 2009 it will provide global water content data for the upper 2–5 cm of soil at a footprint size of 10×10 km^2 and 3-day-revisits. The accuracy of the water content measurements is stated to be ± 4 %vol, when the water content of the vegetation cover does not exceed 5 kg/m^3 (*NASA*, 2004).

The next smaller spatial scale is the regional scale, which is also covered by remote sensing but with air-borne instruments. The ESTAR synthetic aperture microwave radiometer (*Le Vine et al.*, 1994) is an example of a spacecraft based instrument for soil moisture measurements. The so-called *brightness temperature* yielded by the microwave radiometer has to be related to soil moisture by empirical relationships. The footprint size of the airborne instrument ESTAR is dependent on the spacecraft's altitude and the beam width. For the Southern Great Plains 1997 (SGP97) hydrology experiment (*Jackson et al.*, 1999) an area of 10000 km^2 was scanned with a areal resolution of approximately 0.8×0.8 km^2.

Active microwave radars are also used as airborne remote sensing instruments for soil moisture detection. As with the spacecraft based instruments airborne active radar instruments reveal a better spatial resolution than passive instruments.

Microwave remote sensing of soil moisture is influenced by vegetation cover and surface roughness, which complicates the extraction of the soil moisture induced signal portion from the total signal.

A noninvasive instrument applicable at the field scale is the *ground penetrating radar* (GPR, *Huisman et al.* (2003a)). This active sensor is quite similar to the microwave remote sensing instruments. The radar comprises a transmitter and a receiver which are separated by the baseline. GPR can be used with a single antenna separation or a variable baseline length. The so-called *ground wave* propagates directly from the radar transmitter to the receiver right beneath the soil surface. The ground wave allows to derive near-surface moisture (*Huisman et al.*, 2003b).

2

If the soil reveals a subsurface layer sufficiently reflecting the electromagnetic waves emitted by the radar it is possible to use tomography techniques to reconstruct subsurface structures in two- or even three dimensions from GPR data. It is still important to know the depth of this reflector in order to transform the time dependent reflection signal to space correctly. This relationship also influences the accuracy of the local water content determination.

On the small scale soil moisture can be determined by means of a variety of physical principles. Most of these methods require in situ measurements. Some of the techniques observing different physical variables that change with water content are: weight of soil before and after oven drying, neutron scattering, gamma ray attenuation, direct measurement of soil electric conductivity, electrical resistance of soil water adsorbed by gypsum blocks, dimensionally varying elements, soil water suction measurement by tensiometers, and methods utilizing the dielectric properties of water.

The dielectric permittivity of water expresses its ability to interact with electric fields. A *time domain reflectometer* (TDR)[1] measures the travel-time of an electromagnetic pulse along a waveguide buried in soil. The higher the soil water content the slower the pulse due to the dielectric permittivity of water. In principle TDR is similar to GPR as it emits pulses and records the echo. The difference is, that TDR utilizes guided waves for what it is referred to as *cable radar*, too. The term *sampling TDR* is sometimes used throughout the thesis to distinguish this class of instruments from other devices also named TDR, which are not able to record the total TDR signal trace, but measure the pulse travel-time only.

A *capacitance probe* is another instrument based on soil dielectric properties changing with water content. Misleadingly, this method is sometimes referred to as *frequency domain reflectometry* (FDR), which suggests this method to be the counterpart of TDR in the frequency domain, but it is not, because the information content of a capacitance measurement is much poorer than with a sampling TDR. A *vector network analyzer* (VNA) is another instrument working in the frequency domain, which does yield the same or more information than TDR. Therefore the VNA is the instrument, that deserves the name FDR.

The above list of methods and instruments is far from being comprehensive. A large amount of information about measurement principles and instruments is available in scientific journals and from different Internet sites. For a discussion about the different principles, available instruments, and a comparison of methods see for example *Schmugge et al.* (1980), *Charlesworth* (2000), *Topp and Ferre* (2002), *Robinson et al.* (2003a), *Topp* (2003), *Walker et al.* (2004), *Microirrigation Forum* (2004), *SOWACS* (2004).

Determination of Lateral and Vertical Water Content Distribution

Gravitation imposes a principal axis to many natural systems. In first approximation the earth's crust is transversal to the gravitational force. The soil is often layered due to its genesis by sedimentation, and the atmosphere also reveals stratification. Of course, this symmetry is broken by forces imposed by solar radiation, earth rotation, or processes of

---

[1]Throughout the text, the abbreviation *TDR* will be used for both, the principle (time-domain reflectometry) and the instrument (time-domain reflectometer).

the inner earth but many systems and processes may still be separated into lateral and vertical components, often with different spatial and temporal scales.

Most measuring instruments cannot gain information of a variable's lateral and vertical distribution simultaneously. Remote sensing is ideal to determine the lateral water content distribution within a near-surface layer at larger spatial scales, but it cannot look deep into the soil. Hydrological models may be used to extend the surface information to the vertical space dimension. These models are regularly updated by means of different data assimilation schemes (e.g. *Walker et al.* (2001)).

Like remote sensing GPR is capable of gaining near-surface water content distribution on a larger scale. Depending on the particular soil conditions GPR may be used to derive two-dimensional soil moisture distribution along a transect, but this requires a subsurface layer, which strongly reflects the electromagnetic waves emitted by the radar. Furthermore it is important to know the depth of the reflector in order to transform the time dependent reflection signal to space.

In-situ methods have in common, that they basically provide point measurements of the water content at a particular location in soil or average soil moisture across a certain spatial interval. To yield vertical water content profiles, point measurement devices may be combined and buried in different depths. Some measurement principles allow application of vertically installed access tubes, too, through which the sensor can be lowered to different soil depths. Another method of profile retrieval exists for measurement techniques, which are capable of measuring the average water content along sensors of different lengths. Such probes may be installed vertically in the soil in a nested scheme, so that the spatial measuring interval of a longer probe encompasses that of a shorter probe. By balancing the different average water contents a soil moisture profile can be determined. The results are sometimes of poor accuracy due to the small scale variability of the soil.

It is not possible to derive lateral soil moisture distribution directly from point measurements. Geostatistical methods like *kriging* (*Kitanidis*, 1997) are often used to spatially interpolate point measurements. *Lehmann* (1995) investigated several kriging algorithms to perform an up-scaling of approximately 60 distributed soil moisture measurements to the field scale in a small catchment of 6 km^2. However, the methods capable of incorporating additional prior information like land use or topographic index (*Beven and Kirkby*, 1979) showed, that the soft prior estimate will prevail over the hard measurements, if the sampling locations are too far apart to be statistically correlated. Under the unfavorable condition of a too sparse sampling grid, kriging mainly yields the prior information fed into the algorithm, an unsatisfying result for hydrological process studies.[2] Interpolation cannot generate information but can only help to interpret measurements.

Problem Identification

Infiltration and surface runoff generation are two examples of important hydrological processes at the field scale. Those processes are responsible for groundwater recharge and generation of high floods, respectively. The soil moisture state at the onset of precipitation decides, which of both processes will dominate throughout a storm event. The

---

[2]The effect of spatial correlation structure on kriging results is discussed in App. C.

4

complex mechanisms of runoff generation at the process scale are only partly understood. To better understand a system its state variables have to be observed. A state change is caused by fluxes, e.g. a changing soil moisture in a control volume may be the result of evaporation at the soil surface, transpiration by plants, lateral subsurface flow, or vertically percolating water into deeper soil zones. Soil moisture measurements are very useful to gain insight into the very nature of the underlying processes, but they have to be planned carefully. The monitoring scheme has to fit the typical scales of the interesting processes both in space and time. If this requirement is not met a scale gap will occur.

Merz and Plate (1997) have demonstrated by hydrological modeling, that the spatial distribution of soil moisture has a vast impact on the runoff generation under moderate moisture conditions. They tried to improve the calibration of their hydrological event model by means of soil moisture data derived with a coarse spatially distributed TDR network (*Lehmann*, 1995; *Bárdossy and Lehmann*, 1998). However, the contribution of overland flow for the observed events was so small, that a doubling of the runoff coefficient[3] had nearly no impact on the amount of infiltrated water and thus on soil moisture. Furthermore the temporal resolution of the measurements was in the range of a week and thus far too coarse to assess hydrological processes like infiltration on the event scale. In this particular case the information gained by the actual water content measurement scheme was too poor to lead to an improved model calibration.

Western et al. (2001) have used spatially distributed measurements of water content in the topsoil on a regular, dense grid to assess dominant hydrological processes by means of the areal moisture pattern. However, such a measurement scheme yields data at a temporal resolution in the order of one day, which is still far too coarse for observing fast infiltration and drainage processes due to preferential flow. Moreover, these measurements do not give information about the vertical moisture distribution.

The problem of the spatial and temporal scale gap between process and measurement can be illuminated with the example of runoff generating processes: For flood risk assessment in small catchments the soil moisture state just before a storm event is a valuable information whereas the moisture state a week ago is unimportant; a single moisture measurement location is not enough to reliably assess the moisture state of a larger area due to the small scale variability of soil; even diligent observation of the spatial moisture distribution in one area may be of limited use only for the assessment of another area, if the dominating runoff generating processes are different; a measurement of the average water content in the upper decimeters of the soil is insufficient to detect locally saturated soil layers which may lead to an incorrect assessment of the remaining soil water storage capacity.

These examples clearly show an exigence for frequent, spatially distributed water content profile measurements on the event time scale (hours to one day) and the typical spatial process scale, which is also referred to as *representative elementary volume* (REV; *Bear* (1972)). Besides these environmental conditions additional constraints are imposed by practical and also monetary considerations. Accuracy of measurement, soil disturbance,

---

[3]Fraction of precipitation that runs off directly on the surface.

installation, reliability, maintenance, extensibility, automated measurements, power consumption, remote access, man-machine-interface, data handling, and last but not least cost are some practical issues of concern.

The question arises, which measurement techniques are available to realize an operational, unattended system for monitoring soil moisture profiles with high temporal and spatial resolution near the REV.

Remote sensing data are operational, but have a low areal resolution and are unable to resolve important subsurface features. Furthermore, their recurrence period is in the order of days or weeks and thus far away from the event time scale.

GPR is not operational, because its antennas have to be moved to gain spatial information about the subsoil. Additionally a well-known reflecting layer in the ground is necessary, which limits the applicability.

Some of the in-situ measurements are operational. Techniques utilizing access tubes containing longitudinally movable moisture sensors could be automated, but installation is laborious and invasive. To make things worse a whole bundle of access tubes should be installed to get a representative picture of the vertical water content distribution within a limited area.

A common approach to assess soil moisture profiles is to install moisture probes yielding point measurements at different depths of vertical soil profiles. Again, not one soil moisture profile is needed but many. This makes the approach also laborious, invasive, and expensive.

An extension of common TDR technology is deemed the most promising base technology for the intended measurement system. A recorded TDR signal not only contains information about the average water content but also about the moisture distribution along the probe buried in soil. It would be a vast achievement if it were possible to extract a water content profile from the information hidden in a TDR signal.

Requirements

A measuring system focusing on the observation of soil moisture on the process scale has to meet the following requirements:

1. monitoring of moisture profiles in the upper decimeters of soil;

2. high temporal and spatial resolution of water content profiles;

3. water content profiles in real-time with respect to the infiltration process;

4. many distributed probes to consider small-scale variability of soil properties;

5. probe installation must be simple and as little invasive as possible;

6. simple, robust and cost-effective probe design;

7. remotely controllable, cost-effective data loggers extensible and configurable to the evolving needs during the research project;

8. presentation of the results in an understandable form and accessible to the public.

The Spatial TDR Approach

To address the above listed requirements an advanced TDR technology referred to as *Spatial TDR* is used and adapted to the special application. This method allows the determination of soil moisture profiles along individual probes at high spatial and temporal resolution, because the recorded full TDR signal is evaluated instead of pulse travel-time only. Spatial TDR comprises three components:

1. a sampling TDR,

2. a soil moisture reconstruction algorithm, and

3. an appropriate waveguide as moisture probe.

The instrument must be a sampling TDR to get the detailed, continuous signal trace over time. The moisture probe (waveguide) has to fulfill certain requirements imposed by the measurement principle as well as by practical considerations.

The most important component of Spatial TDR is an algorithm for the inverse parameter estimation referred to as reconstruction algorithm. This algorithm is necessary, because it is impossible to derive the moisture profile directly from the recorded TDR waveform. The water content along the moisture probe influences the dielectric properties of the system *probe/soil*, which in their turn determine the signal propagation of the emitted TDR pulse. The dielectric profile has to be estimated indirectly by inverse modeling. Therefore the signal propagation along the waveguide embedded in soil is simulated numerically by an appropriate model. This problem is referred to as the *direct problem*. The numerical model is fed with a supposed distribution of the dielectric properties along the waveguide. The solution of this direct problem yields a simulated TDR measurement, which is compared to the actual TDR measurement. Now the supposed dielectric profile must be modified, until the simulated TDR waveform matches the real measurement. The corresponding distribution of dielectric properties is the best estimate for the real situation and used to calculate the water content profile along the waveguide.

Several soil moisture reconstruction algorithms have already been developed (*dos Santos*, 1997; *Feng et al.*, 1999; *Oswald*, 2000; *Todoroff and Luk*, 2001; *Heimovaara et al.*, 2004). For this thesis the method suggested by *Schlaeger* (2002) (s. also *Schlaeger*, 2005) has been chosen to retrieve soil moisture profiles. The reasons for this particular choice are:

- The direct problem is expressed by the so-called *telegraph equation*. This partial differential equation describes the propagation of a voltage wave along a nonuniform transmission line. Under simplifying assumptions this wave equation can be derived from Maxwell's equations, the fundamental electromagnetic laws. Therefore it is near to the physics of wave propagation.

- Explicit formulation of wave splitting is not necessary. Multiple reflections, which are stated to be a problem by some authors using wave splitting algorithms (without Green's function), are automatically contained in the approach.

- Signal attenuation caused by ionic conductance of soil is considered, whereas some other algorithms neglect this essential problem.

- Due to its sophisticated optimization algorithm it is much faster than comparable products, so that it allows to derive moisture profiles in real-time[4].

- Know-how and support has been provided by the author of this algorithm.

Several TDR probes may be connected to a single sampling TDR by means of multiplexers (*Heimovaara and Bouten*, 1990). Hence, by deriving moisture profiles for all probes of the cluster a quasi three-dimensional image of soil moisture dynamic can be gained every few minutes.

Spatial TDR has been developed and extensively used by the *Soil Moisture Group* (SMG), an interdisciplinary research team at the University of Karlsruhe, aiming at development and practical application of new innovative measuring principles and evaluation methods. Currently the emphasis is put on environmental survey and construction monitoring (*Scheuermann et al.*, 2001; *Becker et al.*, 2002; *Scheuermann et al.*, 2002; *Schlaeger*, 2002; *Schuhmann*, 2002; *Hübner et al.*, 2004; *Soil Moisture Group*, 2004).

Scientific Focus and Structure of the Thesis

The current thesis lays the technological foundation for a novel measurement system for continuous monitoring of soil moisture profiles along many probes distributed in field. For the first time the Spatial TDR approach is used for a soil moisture measurement system performing observations at the spatial and temporal scale of infiltration and runoff generating processes.

The reconstruction algorithm of *Schlaeger* (2002) has already proven to be a success in many applications of the SMG, where it was mostly used in conjunction with a special ribbon cable connected from both sides yielding two independent TDR measurements. The advantage of two measurements is the improved quality of the reconstructed moisture profile, but this method is only applicable with special probes which can be connected from two sides. Installation of such a ribbon cable means digging or drilling, which is laborious and invasive. The soil hydraulic properties would be vastly disturbed. Therefore rod-probes are suggested, which can be plugged into the soil from the surface, but they allow measurements from only one side.

In the scope of the thesis the method of soil moisture profile retrieval has been adapted to a coated 3-rod-probe. Such a probe is easy to install, robust, and insensitive to direct current (DC) conductivity of saline soils because of its coating. Therefore it meets the requirements for many practical field applications. An important part of the thesis is the calibration of this probe for the application with Spatial TDR.

The high costs of sampling TDR instruments are of major concern for many hydrological research projects, even if the devices are driving several moisture probes. Therefore a novel TDR dedicated to Spatial TDR application has been designed and built within the scope of this thesis. The working prototype named *OBSERVER* is based on technologies completely different from methods implemented in commonly available TDR instruments. It is a study to present alternatives to commercial equipment.

---

[4]Real-time means faster than the typical time scale of the underlying hydrological process.

The thesis is organized in three chapters. Theoretical foundations of Spatial TDR as well as the detailed calibration procedures necessary for the application of this novel method in conjunction with 3-rod-probes is given in chapter 2.

Chapter 3 comprises introductory information about signal recording with TDR and technical details about the novel TDR instrument *OBSERVER*. Performance measurements are presented and the discussed.

Chapter 4 is the essence of the thesis, for it focuses on application of Spatial TDR. First the extension of the Spatial TDR method to the application of 3-rod-probes is tested in a lysimeter experiment on the laboratory scale. It demonstrates the ability of Spatial TDR to monitor event-driven infiltration with unprecedented spatial and temporal resolution.

Then the accuracy of Spatial TDR is assessed in two ways. First it is compared to an alternative moisture measuring method. Second, the theoretical accuracy of Spatial TDR is investigated by electrodynamic modeling based on the full wave solution of Maxwell's equations.

The third section of the chapter focuses on the comparison between the OBSERVER and a commercial TDR instrument.

The fourth application investigates, whether the enormous gain of information yielded by Spatial TDR can improve the estimation of soil hydraulic parameters by inverse modeling. The infiltration model used is based on the analytical solution of Richards' equation under constant flux boundary condition.

Finally the remote controllable TDR probe cluster is introduced, many components of which have been developed within this thesis. The cluster is mainly designed for a flood warning system based on distributed soil water profile measurements in real-time but its core has already been adapted to monitor infiltration in dikes, too.

2. Spatial Time Domain Reflectometry

The recently developed method called *Spatial Time Domain Reflectometry* allows to derive moisture profiles along single probes with high spatial and temporal resolution. It is a combination of three different components: 1. a sampling time domain reflectometer, 2. an algorithm to reconstruct the moisture distribution from the sampled TDR signal by inverse modeling, and 3. a waveguide (probe) suited for this particular application.

The current chapter gives an overview about the different aspects of Spatial TDR. After a short introduction of the physical principles of water content determination utilizing electromagnetic interaction, fundamentals of conventional time domain reflectometry are elucidated. It will be explained what Sampling TDR instruments do and why their sampling feature is important for the novel Spatial TDR methodology.

This is followed a discussion about the extended principles of Spatial TDR: the reconstruction algorithm to derive water content profiles along single probes together with its theoretical foundation.

The third component of Spatial TDR is an appropriate probe. In order to use rod probes with the reconstruction algorithm it was necessary to extend the algorithm by a certain relationship between electrical parameters of the probe/soil system. Furthermore a new calibration procedure for coated rod probes was established to derive parameters necessary to run the reconstruction. But first an introduction about water content measurements with conventional TDR is given.

2.1. Determination of Soil Moisture with Electromagnetic Methods

Electromagnetic measuring methods are indirect methods to determine moisture of matter. The measuring process is based on the determination of the material's dielectric properties, which are affecting electromagnetic fields in many ways.

Dielectrics comprise polar components which are aligned in an electric field. This polarization influences the external field. Water molecules (H_2O) reveal a remarkably large dipole moment. Due to its strong electro-negativity the oxygen atom attracts the electrons in the charge clouds of the covalent bonds more than the hydrogen atoms which leads to a mean displacement of the electrons toward the oxygen. The angular structure of the molecule leads to an observable separation of the charge density. From outside the molecule looks like two opposite charges separated by a certain distance: a dipole. An electric field interacts with these charges and applies a torque at the molecule. This makes water easy to polarize and the molecules want to align with the electric field vector. This material characteristic has a strong influence on electromagnetic fields.

The polarization of molecules reduces for example the velocity of an electromagnetic wave propagating in the material. A dielectric also increases the capacitance of a capacitor (charge storing device) when it is put into its electromagnetic field. The first effect is exploited by TDR to measure water content, the second by capacitance probes.

The strength of the interaction between electric field and charge is expressed by the so-called *relative dielectric permittivity* ϵ. Its meaning can be best understood by looking at Coulomb's law expressing the force $\vec{F}$ on a test charge q due to a static electric field $\vec{E}$ generated by a point charge Q:

$$\vec{F} = q\vec{E} = \frac{1}{4\pi\epsilon\epsilon_0} \frac{Qq}{r^2} \vec{e}_r \, , \tag{2.1}$$

with $\vec{r} = r\vec{e}_r$ being the separation vector between the two point charges. In vacuum the absolute dielectric permittivity is ϵ_0. Therefore the relative dielectric permittivity of vacuum is $\epsilon = 1$. If the charges were embedded in a material with relative dielectric permittivity of $\epsilon = 10$, the mutual electric force between the charges would be reduced to $1/10$ of the force in vacuum. The relative dielectric permittivity defined by interaction with static electric fields is also referred to as *static relative dielectric permittivity* ϵ_s. Some typical values of the static relative dielectric permittivity for pure materials are given in App. A.2, Tab. A.1.

Debye Relaxation

In dynamic electric fields several media reveal a dielectric permittivity which is not static but dependents on the frequency of the field. The following explanations concentrate on the dielectric water because of its importance in soil science. The polarization of water molecules follows the changing electric field direction. If the change is too fast, the rotation of the dipoles will lag behind the field. It decreases the effective polarization of the material and leads to a reduction of its dielectric permittivity with increasing frequency. This effect is called *Debye Relaxation* (e.g. *Kaatze*, 1996). The frequency dependent relative dielectric permittivity of water becomes a complex function and reads

$$\epsilon(\omega) = \epsilon_\infty + \frac{\epsilon_s - \epsilon_\infty}{1 + i\omega/\omega_r} \, , \tag{2.2}$$

with ω the angular frequency of the electric field and ω_r the angular relaxation frequency of water. The coefficients ϵ_s and ϵ_∞ are the permittivity limits for low and very high frequencies: $\epsilon(\omega \to 0) = \epsilon_s$ (static permittivity), $\epsilon(\omega \to \infty) = \epsilon_\infty$. The relaxation frequency of unfrozen water at 0°C is $f_r = 2\pi\omega_r = 9$ GHz (*Kaatze*, 1996). Ionic conductance leads to losses expressed by an additional imaginary component. The extended Debye formula (e.g. *Ulaby et al.*, 1986) reads

$$\epsilon(\omega) = \epsilon_\infty + \frac{\epsilon_s - \epsilon_\infty}{1 + i\omega/\omega_r} - i\frac{\sigma}{\omega\epsilon_0} \, , \tag{2.3}$$

with σ the ionic conductivity. Separation of real and imaginary component of the Debye equation yields:

$$\epsilon(\omega) = \underbrace{\left[\epsilon_\infty + \frac{\epsilon_s - \epsilon_\infty}{1 + (\omega/\omega_r)^2}\right]}_{\epsilon' \,,\, \text{polarizability}} - i \underbrace{\left[\frac{(\epsilon_s - \epsilon_\infty)(\omega/\omega_r)}{1 + (\omega/\omega_r)^2} + \underbrace{\frac{\sigma}{\omega\epsilon_0}}_{\text{conduction}}\right]}_{\epsilon'' \,,\, \text{relaxation}} = \epsilon' - i(\epsilon'' + \frac{\sigma}{\omega\epsilon_0}) \,. \quad (2.4)$$

The minus sign in front of the imaginary part is a convention often used in literature. The ratio of imaginary to real component of the complex dielectric permittivity defines the slope of the loss tangent:

$$\tan\delta(\omega) = \frac{\epsilon''(\omega) + \sigma/(\omega\epsilon_0)}{\epsilon'(\omega)} \,. \quad (2.5)$$

The loss tangent is a convenient form to express the relative importance of dielectric losses and ionic conductance with respect to the dielectric polarization. $\tan(\delta) = 0$ in lossless cases.

It was a simplified assumption to relate dielectric permittivity to the molecular level only. In reality water molecules form clusters or hydrate covers around dissolved ions. These formations modify the polarizability of participating water dipoles depending on the ion concentration. A measure for the concentration is salinity S which is the ratio of salt mass to total mass of the solution. Salinity not only influences ionic conductivity σ, but also static permittivity ϵ_s and even relaxation frequency ω_r of water. All the above listed variables depending on salinity are dependent on temperature T, too. Only ϵ_∞ is a constant.

A detailed listing of empirical relationships describing $\epsilon_s(S, T)$, $\sigma(S, T)$, and $\omega_r(S, T)$ for saline water is given by *Ulaby et al.* (1986), *App. E-2*. A clearly arranged summary of all necessary formulas and calibration relationships covering many practical cases is presented by *Hübner* (1999). For more details about dielectric properties of water see *Hasted* (1973), *Kaatze* (1996), and references therein.

Mixing Rules and Soil Calibration

Soil water content is of major concern for this thesis but water is only one soil constituent. The material *soil* is a mixture of at least three phases: rock, air, and water, with different dielectric properties. Thus if dielectric permittivity is measured it will be an effective dielectric permittivity of the mixture. A large number of mixing rules have been formulated to express the resulting effective permittivity by the permittivities of individual components, somehow weighted by their volume fraction. An example for such a rule is the general power law of *Greffe and Grosse* (1992):

$$\epsilon_m^\alpha = \sum_{i=1}^{N}(V_i/V)\epsilon_i^\alpha \,, \text{ with } \sum_{i=1}^{N}(V_i/V) = 1 \,. \quad (2.6)$$

It describes the effective permittivity ϵ_m of a mixture of N components, each of which with relative dielectric permittivity ϵ_i and volume fraction (V_i/V) on the total volume

V. The exponent α is a geometric anisotropy factor. If the medium is perfectly layered, then $\alpha = -1$, in case the electrical field vector $\vec{E}$ is perpendicular to the layers (series of capacitors), and $\alpha = 1$, if $\vec{E}$ is parallel to the layers (parallel circuit of capacitors). However no general mixing rule has been found so far, which could cover the broad spectrum of different soils. For practical purposes often calibration functions are determined relating the effective dielectric permittivity ϵ_m of the specific mixture directly to the volumetric water content θ. The most famous example for such an empirical calibration is that of *Topp et al.* (1980):

$$\epsilon_m = 3.03 + 9.3\,\theta + 146\,\theta^2 - 76.7\,\theta^3 \; . \tag{2.7}$$

The main reason for not having found a general theoretical model describing the relationship between soil moisture and effective dielectric permittivity of the bulk material is found in the existence of complicated physical interactions between the soil constituents.

Interaction of Constituents

At list of main effects is given by *Hilhorst* (1998): Intermolecular forces between water and soil lead to a modification of the dielectric properties of molecules next to the particle surface (monolayer); clay consists of microscopic layers between which water can be bound leading to a modification of permittivity; colloids like clay particles form a hydrate cover which is polarized in an electric field, an effect referred to as colloidal dielectric dispersion or counterion diffusion polarization.

Besides these surface phenomena another important effect is the Maxwell-Wagner effect. At low frequencies the relaxation of water can be neglected but if the soil water permittivity reveals an imaginary part due to ionic conductivity (s. Eq. 2.4), the imaginary part mixes into the real part of the compound material's effective permittivity (e.g. *Schlaeger*, 2002). This effect looks like a relaxation at low frequencies. For a detailed discussion of these effects see *Hilhorst* (1998) and references therein.

Apparent Dielectric Permittivity

A TDR measures the travel-time of a pulse running along a probe of known length. Pulse velocity can be determined from travel-time and probe length. The dielectric permittivity of the soil the probe is installed in leads to a reduction of propagation velocity v. The velocity derived from TDR measurements is

$$v = c_0/\sqrt{\epsilon_a} \; , \tag{2.8}$$

where the constant c_0 is the speed of light and ϵ_a the *apparent relative dielectric permittivity*. The latter is labeled 'apparent' because it is indirectly determined by a TDR measurement and may differ from the real component of the complex dielectric permittivity.

A TDR pulse comprises a wide band of frequency components depending on the pulse rise-time. It can be seen as a superposition of many sine-waves of different frequency, amplitude, and phase. Eq. 2.4 shows that the dielectric permittivity is generally frequency dependent and so is the phase velocity of individual frequency components (sine-waves), an effect called dispersion. In dispersive soils high frequency components travel faster

than low frequency components. It can be shown that dispersion leads to a reduction of pulse rise-time which aggravates the determination of pulse travel-time. It is even difficult to define *the one* dielectric permittivity, because of the frequency dependence. *Topp et al.* (1980) gave a relationship between apparent dielectric permittivity ϵ_a and real component ϵ' of the actual dielectric permittivity:

$$\epsilon_a = \frac{\epsilon'(\omega)}{2}(1 + \sqrt{1 + \tan^2 \delta(\omega)}) \ . \tag{2.9}$$

TDR measurements do not only show the pulse propagation velocity, but also contain information about ionic conductance leading to signal attenuation. *Topp et al.* (2000) found a way to extract the loss tangent from TDR measurements and additional conventional conductivity measurements so they were able to solve 2.9 for ϵ'.

Choice of Soil and Other Experimental Conditions
It is not the objective of the thesis to investigate the complex behavior of certain substances in varying electromagnetic fields but to develop and test new methods and instruments. Therefore a loamy sand has been chosen for the laboratory experiments, with moderate properties both electric and hydraulic. A closer description of the chosen loamy sand is given in App. A.1.
The soil solution shows only a weak ionic conductance so that the effect on the experiment is expected to be small. Colloidal interaction is omitted since the material comprises only a negligible clay fraction.
Frequencies contained in the emitted TDR step pulse were limited due to low-pass filtering effects of the long probe connecting coaxial cables of several meters. The reduced signal bandwidth is far away from the relaxation frequency of water so that dielectric relaxation is of no concern. Therefore it can be assumed that the apparent relative dielectric permittivity measured with TDR is indeed very similar to the relative dielectric permittivity of soil. Finally the experiments were performed under room temperature and the temperature variations during the series of experiments had been small.
The basis for all ongoing investigations is the pulse travel-time analysis by TDR. How a TDR actually works and how the travel-time is determined from the measurements is subject to the next section.

2.2. Introduction to Conventional Time Domain Reflectometry

Dielectric materials reduce the propagation velocity of an electromagnetic wave. Therefore velocity measurements of electromagnetic waves can be utilized to assess the dielectric permittivity of the medium under test. A time-domain reflectometer is an instrument which allows to measure the time necessary for an electromagnetic pulse to travel a known distance. From this information the average velocity can be derived.
A TDR instrument basically consists of a voltage step generator and a signal sampler, which allows to continuously record a time varying signal. The sampler is an electronic

component indispensable for the new Spatial TDR method. Some instruments also named TDR by their producers are not capable of tracking the signal continuously over time. Therefore the term *sampling TDR* is sometimes used throughout the text to underline the importance of this technical feature.

The TDR step generator launches repetitive square pulses with steep edges into the system under test (SUT). In case of soil moisture measurement with TDR the SUT is an unshielded waveguide (or transmission line) buried in soil, also referred to as *moisture probe*. This probe is connected to the TDR with a shielded coaxial cable, hereinafter referred to as *connecting cable* or *feeding cable*. The connecting cable transmits the electromagnetic signal to the beginning of the probe with a certain unavoidable attenuation. Since the moisture probe is an unshielded transmission line, it allows the propagating electromagnetic wave to interact with the surrounding medium.

Each transmission line has an *impedance* determined by its geometry and its material. The impedance plays an important role in signal transmission. If the impedance of a transmission line changes with distance, the incident pulse will be partly reflected and partly transmitted at the disturbances. The reflections travel back towards the TDR where they superpose the incident pulse. The superposition of incident and reflected wave is recorded by the sampler.

The resulting signal is referred to as *TDR signal* and the recording is called *reflectogram.* This signal is characteristic for the SUT and carries important information about the internal structure of the system, e.g. the moisture along the probe.

In many experimental configurations the first main reflection occurs at the junction of coaxial cable and probe head due to the impedance discontinuity. The signal is partly reflected at the probe head and partly transmitted into the SUT. The system's reaction to this excitation can be studied by means of the reflected wave.
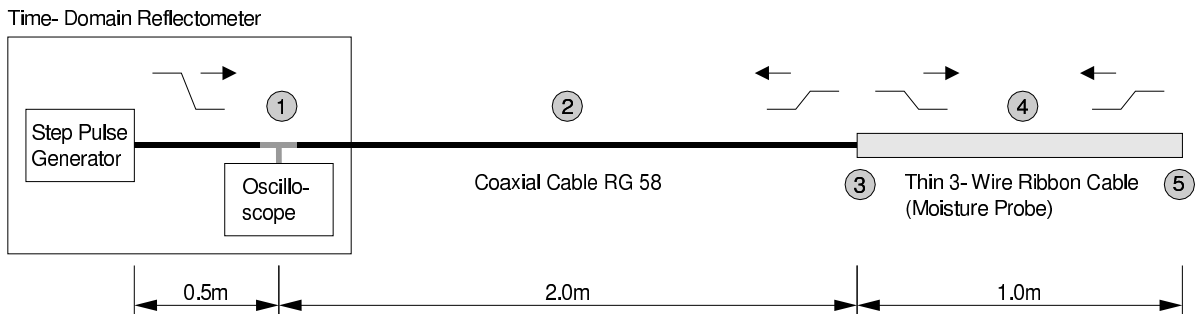
Figure 2.1.: Simple Time-Domain Reflectometer experiment to demonstrate typical signal features. The labels 1–5 correspond to the signal features displayed in Fig. 2.2

The features of a typical TDR signal in soil moisture retrieval can be demonstrated by a simple experiment with a step generator and an oscilloscope as sampler (Fig. 2.1). The sampler is a Hewlett-Packard HP54602B Digital Sampling Oscilloscope with 150 MHz bandwidth, which has been used for many investigations throughout the thesis. The step generator is the signal source of the newly developed TDR (Chap. 3). The common coaxial cable *RG 58* is used in this experiment (see App. B.1).

The step generator is connected with a RG 58 of 0.5 m to a T-connector directly mounted on the oscilloscope. The moisture probe is connected with a second coaxial cable of 2.0 m to the other side of the T-connector. The probe is a 1 m piece of a special 3-wire ribbon cable with an impedance differing from the 50Ω of the coaxial cable (see App. B.1). For this experiment the moisture probe is held in air. The step generator launches fast rising square pulses with a frequency $f_{\text{step}} = 4.0$ MHz into the transmission line.


```
HP54602B
```

```
CH1: -
CH2: TDR signal, vpos=-3V, 0.47m+T+2m+R1m+OE RG58, f=4.0001MHz
CH3: -
CH4: -
```
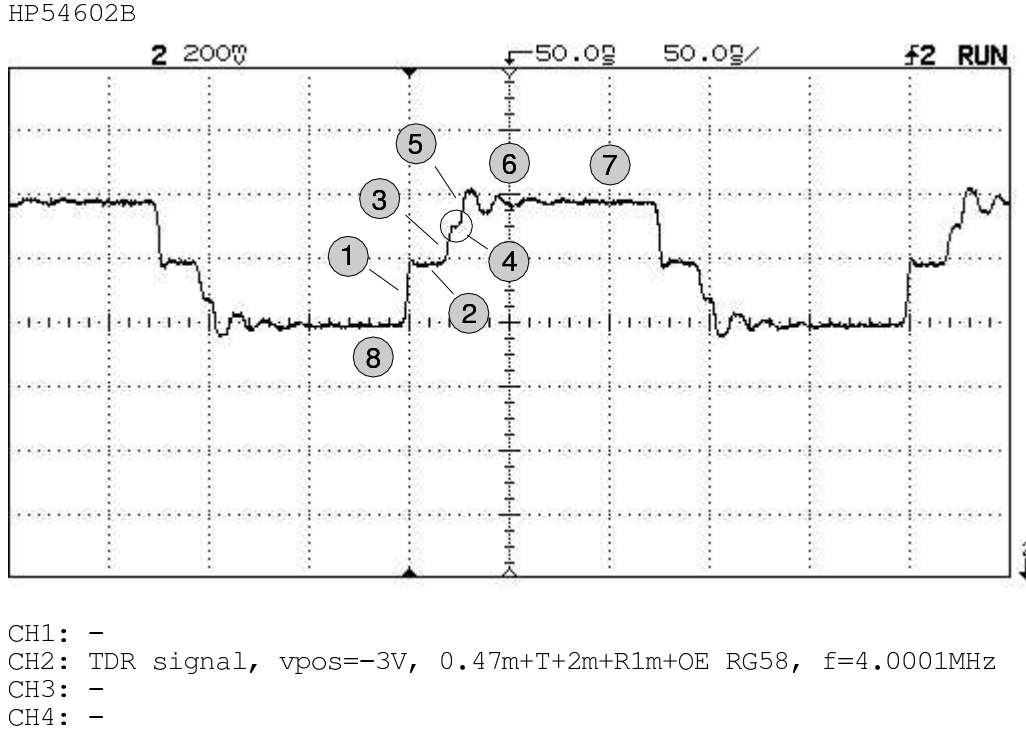
Figure 2.2.: Features of a TDR signal. 1: rising edge of emitted excitation pulse (V_{in}); 2: plateau, pulse traveling along coax; 3: reflection at the junction coax/probe; 4: response of moisture probe; 5: reflection at the probe's end; 6: multiple reflections, ringing; 7: final signal amplitude ($2 V_{\text{in}}$). Excitation pulse repetition rate $f_{\text{step}} = 4$ MHz.

Fig. 2.2 shows the resulting TDR signal from the experiment sampled with the oscilloscope. The oscilloscope's resolution is 50 ns/division horizontally, and 200 mV/division vertically. The sample shows all typical features of TDR. The staircase shape of the signal is due to the superposition of many forth and back propagating square pulses of different amplitude and phase. The period T of the periodic TDR signal equals the period of the excitation pulses:

$$T_{\text{step}} = 1/f_{\text{step}} \approx 250 \text{ ns} .\tag{2.10}$$

The steep rising edge of the excitation pulse travelling through a coaxial cable reaches the oscilloscope first (Fig. 2.2, 1). The height of the step is the voltage of the incident

pulse, here $V_{in} \approx 200$mV. The pulse travels along the coaxial cable with negligible disturbance. Thus the plateau (Fig. 2.2, 2) is formed by the incident pulse only. At the end of the coaxial cable the pulse hits the junction to the moisture probe, where it is partly reflected due to the impedance mismatch. The reflected wave propagates backwards and superposes the plateau of the incident pulse yielding a second step in the TDR signal (Fig. 2.2, 3). The reflection reaches the TDR after time

$$ t = \frac{2l_{coax}}{v_{coax}} = \frac{4 \text{ m}}{0.2 \text{ m/ns}} = 20 \text{ ns} , \tag{2.11} $$

with l_{coax} and v_{coax} being the length of the second RG 58 cable, and the phase velocity of an electromagnetic wave in this cable, respectively. The factor of 2 is because of the signal has to travel forth and back the distance l_{coax}, until the reflection occurs at the sampler.

Part of the energy is not reflected but transmitted into the moisture probe. During the propagation in the probe wave and surrounding medium are interacting. The probe in the experiment is chosen to have an open end which leads to a total reflection (Fig. 2.2, 5). The pulse travels back and is separated again at the junction between coaxial cable and moisture probe. The segment of the TDR signal corresponding to the propagation in the probe (Fig. 2.2, 4) carries the whole information about the soil moisture. A TDR helps to zoom into the signal by stretching the time axis and amplifying the signal amplitude. In nearly all cases the analysis is limited to the time interval between the first reflections at the beginning and the end of the moisture probe but since part of the energy remains in the probe after each signal separation more reflections occur with exponentially decaying amplitude (Fig. 2.2, 6), an effect called *ringing*. This signal portion can be used for further analysis, e.g. to assess ionic conductivity in soil with buried uncoated waveguides (*Topp et al.* (1988), *Zegelin et al.* (1989)). After a while the multiple reflections die out and the signal will reach a constant level of 2 V_{in} (Fig. 2.2, 7), if the signal propagation is lossless.

The falling edge of the incident pulse leads to a disturbance equivalent to the rising edge but in opposite direction. Disturbances caused by the falling signal edge have to disappear, before the next pulse can be launched (Fig. 2.2, 8). Otherwise system responses of consecutive pulses overlap and complicate the analysis.

2.2.1. Determination of Propagation Velocity

The quality of soil moisture measurement with TDR is strongly dependent on the accuracy of travel-time determination. Like conventional methods retrieving average soil moisture the profile reconstruction algorithm of *Schlaeger* (2002) utilizes the travel-time analysis, too, to determine the mean dielectric properties along the moisture probe.

Fig. 2.3 shows a measured TDR reflectogram of a vertically installed 3-rod-probe partially immersed in water. The first slope with inflection point at t_{i0} is due to the reflection at the probe head, the second falling slope with inflection point at t_{ix} is caused by the impedance discontinuity at the air/water interface, the third slope with inflection point t_{i1} belongs the the reflection at the rods' end.

A first difficulty may be the identification of signal slopes and their corresponding reflections, e.g. not the last slope reaching highest in Fig. 2.3 is representative for the reflection at the probe end but the one before.

Also the choice of a reference point representing the absolute time of the reflection can be intricate. In most applications the measurement of time differences between two reflections is of major concern, not so much their absolute instants, which makes the analysis much easier.

Several methods have been proposed to determine the reflection instants from TDR reflectograms. The tangent line method is the most widely used in water content determination with TDR. It defines the crossing of a line fitted to the slope with an appropriate base line to be the reference time (*Heimovaara and Bouten*, 1990). The fitted line can be a real tangent line touching the curve in one point or — useful in case of noisy data — a local linear regression in a chosen environment.
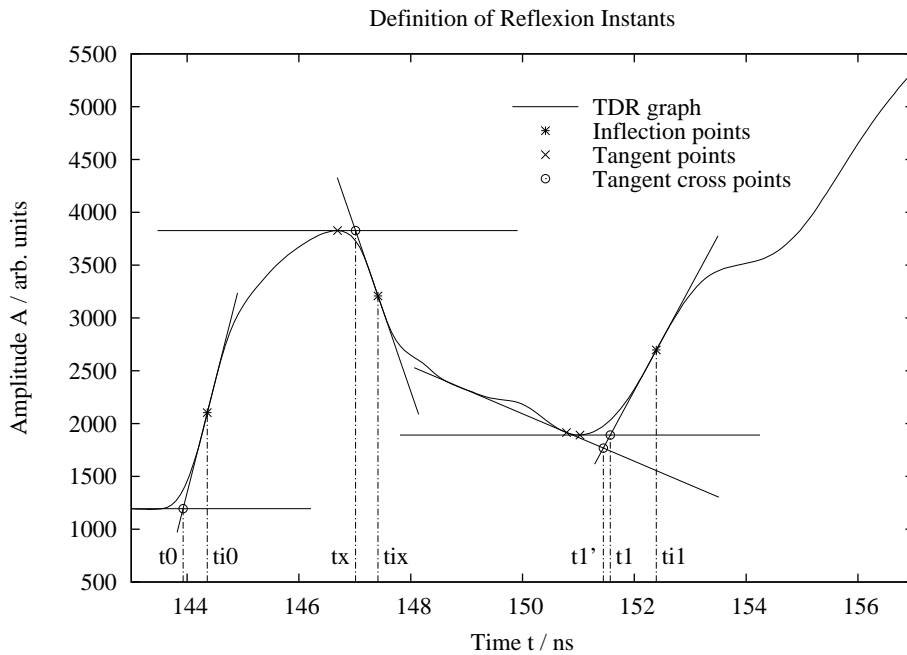
Figure 2.3.: Definition of reflection instants. t_0, t_x, and t_1 are by definition instants of reflections at probe head, air/water interface, and probe end, respectively. They are defined by tangent line crossings. t_{i0}, t_{ix}, and t_{i1} are occurrences of the corresponding inflection points of the slopes. Physical rod length $l = 60\,\mathrm{cm}$, probe head bottom at $x = 42.5\,\mathrm{cm}$ above air/water interface, total connecting cable length $l_{\mathrm{coax}} \approx 14.4\,\mathrm{m}$.

Imprecisions occur due to the choice of the point where the tangent line touches the slope and the broad range of possible reference lines, be it a line parallel to the abscissa, be it a line fitted to a part of the curve preceding the reflection (c.t. Fig. 2.3, t_1 and t_1'). The tangent line methods leave room for interpretation which is often unsatisfying, especially when the signal edges are not sufficiently pronounced due to dispersion or

dissipation.

A tangent line method applicable to a wide variety of curves shapes is fairly difficult to implement. The analysis can only be automated with an acceptable effort if the variety of possible curve shapes is reduced. Generally the automated travel time detection has to be customized for each use case.

The identified reflection instants often have to be corrected, e.g. the reflection at the junction between coaxial cable and probe head is not the instant when the signal enters the rods, and the reflection at the probe's end does not occur precisely at the physical end of the rods.

The observed instances of the reflections at the probe's beginning and end are named t_0 and t_1, respectively (Fig. 2.3). The travel-time t_m is defined to be the round-trip time of the signal forth and back the rods embedded in the material. The index m stands for 'influenced by the material'. The time t_m generally differs from the apparent total travel-time $t_t = t_1 - t_0$, since part of the time t_t is due to the propagation time t_h in the probe head:

$$t_m = t_1 - (t_0 + t_h) = t_t - t_h \ . \tag{2.12}$$

Another uncertainty is the effective probe length which may be different from the physical length, since the electromagnetic field does not stop abruptly at the rods' ends but reaches a little further into the soil. The effect at the probe's end can be taken into account either as an additional travel-time correction or as an effective electrical probe length l' exceeding the physical probe length l (c.t. Fig. 2.11). The latter alternative has been chosen for the current analysis. With l' being the electrical probe length, the wave velocity determined experimentally by TDR is

$$v = 2l'/t_m \ . \tag{2.13}$$

Equation 2.13 expresses the experimental determination of the pulse velocity within the rods. Both correcting factors t_h and l' are difficult to grasp, since they are presumably dependent on the length of the connecting cable with its low-pass filter effect shaping the spectrum of the incident pulse, and dielectric properties of surrounding media. Depending on the construction of the probe head, which is in most cases unshielded, the signal propagation is influenced by the medium embedding the head, too, e.g. when the probe is buried completely in soil or ponded. The reach of the electromagnetic field beyond the physical rod length is also a function of the medium. Thus the values given for the correcting variables t_h and l' must be seen as rather rough and simplified estimates for difficult effects.

2.3. Nonuniform Transmission Line

By means of common travel-time analysis the average water content along a moisture probe can be determined, but much more valuable information is contained in the recorded TDR reflectogram which cannot be exploited by conventional methods. The signal recording carries the complete information about the spatial distribution of

moisture along the waveguide. The core algorithm of Spatial TDR (*Schlaeger*, 2002) is used to derive the water content profile from the TDR reflectogram by inverse modeling. This method models the system probe/soil as a nonuniform transmission line (*Lundstedt*, 1995). To understand the principle of the reconstruction algorithm it is necessary to dive a little deeper into the physics of electromagnetic wave propagation.

From a signal-theoretical point of view soil and buried waveguide may be modeled as a linear time-invariant (LTI) system. The most general approach to evaluating the time domain response of any electromagnetic system is to solve *Maxwell's equations* in the time domain. This set of governing equations form the backbone of electrodynamics and thus of wave propagation. A general formulation of the problem by Maxwell's equations a procedure could take into account all the effects of the system geometry and electric properties. In the case of soil moisture measurement the SUT is the waveguide buried in soil. Soil and waveguide together form a nonuniform transmission line. A traveling wave in this system reacts to changing properties along the transmission line, which are mainly influenced by soil moisture. Thus the temporal evolution of the wave propagation carries information about the soil moisture distribution along the waveguide.

However, the solution of Maxwell's equations for general systems would be rather involved. For practical reason it is important to design a well-behaving waveguide of appropriate geometry which restricts the electromagnetic field to a simple form. The preferred form or mode of travelling waves along transmission lines is the *transverse electromagnetic (TEM) mode*. In TEM mode electric and magnetic field vector are perpendicular and also perpendicular to the direction of wave propagation.

Generally, other modes are also excited in real systems at perturbations like connectors, junctions between connecting cable and probe, or any other major changes in transmission line properties. But if the system is well designed, all higher modes but the TEM mode will disappear after a short distance (*Leviatan and Adams*, 1982). This condition is called *quasi TEM mode.*

If the quasi TEM assumption holds, Maxwell's equations will be drastically simplified. But these equations and their field solutions are still inconvenient for many practical cases, since not electric and magnetic field vectors are measured but voltage and current. If the TEM mode is the dominant mode of wave propagation and some other prerequisites are fulfilled, an equivalent electronic circuit model may be used for transmission line. The equivalent circuit describes the transmission line as a sequence of infinitesimally small circuit blocks consisting of lumped elements like resistors, capacitors, and inductors (s. Fig. 2.4). Application of Kirchhoff's laws to the equivalent-circuit yields a partial differential equation named 'Telegraph Equation' describing the propagation of voltage or current waves along the transmission line. Usually the voltage formulation is used since in many existing problems voltage is easier to measure than current, e.g. a TDR is sampling voltage over time.

It must be emphasized that the equivalent-circuit is nothing but a model for a transmission line to describe certain aspects of such a system. Of course, the transmission line is not a circuit with lumped electronic parts. Generally the propagation of electromagnetic waves in macroscopic domains is described by the Maxwell equations but if the SUT is well-behaving, the equivalent-circuit is valid and main phenomena of wave propagation

like reflection and attenuation can be intuitively studied with this simplified model.

2.3.1. Equivalent-Circuit and Transmission Line Equations

An equivalent-circuit is a simplified model for a transmission line based on lumped electronic parts. Fig. 2.4 shows one infinitesimally small segment of a transmission line modeled as an electronic circuit. The presented circuit is only one particular realization especially suited for the soil moisture reconstruction algorithm. Other equivalent circuits may have to be developed depending on the application and the effects to cover.
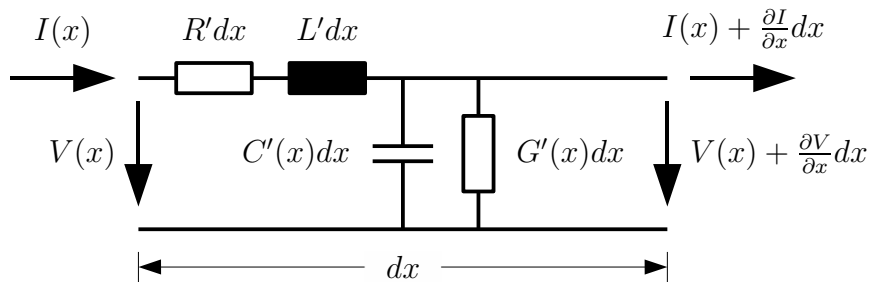
Figure 2.4.: Infinitesimally small segment of the equivalent-circuit model for a transmission line. x is the space coordinate in longitudinal direction.

In this model the properties of a transmission line are described by four parameters given per unit length. The parameters and their units are: series resistance R' (Ω/m), series inductance L' (H/m), shunt capacitance $C'(x)$ (F/m) and effective shunt conductance $G'(x)$ (mS/m). Typical values for different transmission line types are listed in Tab. B.1. A transmission line for soil moisture measurement is an unshielded waveguide (probe) buried in soil. L' and R' are constants of the probe, $C'(x)$ and $G'(x)$ are influenced by the dielectric permittivity of soil and therefore by soil water distribution along the longitudinal probe coordinate x. The parameter G' is called *effective* conductance to emphasize that in most cases coated probes are used so that no DC current between the wires can occur. Nevertheless ionic conductivity in saline soils leads to a signal degradation even without direct current. The parameter G' is needed to model signal attenuation.

If the transmission line is excited, voltage and current waves will propagate along the line. Thus voltage V and current I along the transmission line are generally dependent on space and time:

$$V = V(x,t), \ I = I(x,t). \tag{2.14}$$

The distribution of these variables is described by Kirchhoff's laws. They reveal a unique relationship between current, voltage, and resistance. The voltage law applied to Fig. 2.4

yields:

$$V = R'dxI + L'dx\frac{\partial I}{\partial t} + (V + \frac{\partial V}{\partial x}dx) \Leftrightarrow \frac{\partial V}{\partial x} = -\left(R' + L'\frac{\partial}{\partial t}\right)I \qquad (2.15)$$

The last term on the right side stands for the voltage induced by current flowing through the inductor L'.

Kirchhoff's current law yields:

$$I = G'dx\,V + C'dx\,\frac{\partial V}{\partial t} + (I + \frac{\partial I}{\partial x}dx) \Leftrightarrow \frac{\partial I}{\partial x} = -\left(G' + C'\frac{\partial}{\partial t}\right)V \qquad (2.16)$$

The last term on the right side expresses how the temporal change of voltage across a capacitor C' is linked to a current.

These partial differential equations (PDE) are coupled and must be decoupled to yield an equation in V or I only. Derivation of Eq. 2.15 in space and of Eq. 2.16 in time yields:

$$\frac{\partial^2 V}{\partial x^2} = -\left(\frac{\partial R'}{\partial x} + R'\frac{\partial}{\partial x} + \frac{\partial L'}{\partial x}\frac{\partial}{\partial t} + L'\frac{\partial^2}{\partial t \partial x}\right)I\,, \qquad (2.17)$$

$$\frac{\partial^2 I}{\partial t \partial x} = -\left(G'\frac{\partial}{\partial t} + C'\frac{\partial^2}{\partial t^2}\right)V\,. \qquad (2.18)$$

The last term on the right side of Eq. 2.17 is to be substituted by Eq. 2.18, the third by Eq. 2.15 solved for $\partial I/\partial t$, and the second term by Eq. 2.16. For the current use case it is furthermore assumed that resistive losses along the probe may be neglected: $R' \equiv 0$. Especially for high frequency signals this is not strictly true, because the skin effect forces the electric current to flow in a thin layer just beneath the conductor surface and the limited cross-sectional area increases the resistance (*Jackson*, 1975).

The result of the substitutions together with the simplifying assumption is a homogeneous second order PDE in voltage V:

$$\left(\frac{\partial^2}{\partial t^2} + \frac{G'}{C'}\frac{\partial}{\partial t} + \frac{\frac{\partial}{\partial x}L'}{L'^2C'}\frac{\partial}{\partial x} - \frac{1}{L'C'}\frac{\partial^2}{\partial x^2}\right)V(x,t) = 0 \qquad (2.19)$$

This PDE is a wave equation describing the propagation of a voltage wave along the transmission line. In literature it is sometimes referred to as *telegraph equation*. It is one of the two main columns of the reconstruction algorithm of *Schlaeger* (2002).

There is no rigorous rule stating when the transmission line equation is valid. However, a rule of thumb is often applied demanding that the distance a of the transmission line conductors should be small with respect to the smallest wavelength $\lambda_{\min}$ contained in the signal propagating along the transmission line:

$$a < \lambda_{\min}/2 = v/(2f_{\max})\,, \qquad (2.20)$$

where $f_{\max}$ is the highest frequency component of the signal propagating with velocity v. For the transmission line equation (Eq. 2.19) to be applicable some conditions should be fulfilled as much as possible:

- Wave propagation in TEM mode. The rod distance must be small with respect to typical wave lengths of propagating waves along the probe, otherwise higher modes are favored.

- Surrounding medium changes only in longitudinal direction. Isotropy in every transverse plane is presupposed.

Some aspects the current equivalent-circuit model does not consider:

- Frequency dependent parameters,

- increased rod resistance due to skin effect,

- radiation.

Nevertheless the transmission line model given in Eq. 2.19 is capable of simulating wave propagation along TDR probes in many practical applications very well. Fig. 2.7 shows a comparison between a TDR recording and number of simulated TDR reflectograms for different capacitance distributions along the moisture probe. Capacitance profile C'_8 leads to a simulation which is hardly distinguishable from the measurement.

2.4. Soil Moisture Reconstruction Algorithm

The goal of the reconstruction algorithm is to transform the sampled voltage $V(t)$ from the TDR, which is a function of time, into the soil moisture profile $\theta(x)$, which is a function of space along the buried probe. This *inverse problem* is solved by inverse parameter estimation.

Therefore the voltage pulse propagation is simulated by means of a numerical model with assumed electrical parameter distributions along the waveguide. The mathematical formulation of signal propagation is the *forward problem*. The most general formulation of the wave propagation is by means of Maxwell's equations with their numerical full wave solution which could take into account more effects like radiation and dielectric losses. The analysis could also be moved from time- to frequency-domain to consider frequency-dependent parameters. But both alternative methods would require much more computing time than the proposed method, thus they are currently not feasible for operational infiltration monitoring in real-time.

Schlaeger (2002) uses a special form of the telegraph equation (Eq. 2.19) for describing the propagation of a voltage pulse $V(x, t)$ along the moisture probe. Capacitance $C'(x)$ and effective conductance $G'(x)$ are influenced by the soil water content distribution $\theta(x)$ along the buried waveguide. Inductance L' is a function of the transmission line only and piecewise constant for coaxial cable and moisture probe. The spatial derivative $\partial L / \partial x$ in Eq. 2.19 stands for the change of inductance between coaxial cable and probe. Resistance R' along the waveguide due to skin effect has been neglected. All parameters are given per unit length.

The linear time-invariant system described by the wave equation is excited by the emitted TDR step pulse. To determine the input signal entering the probe a reflection

Input and Output Signal
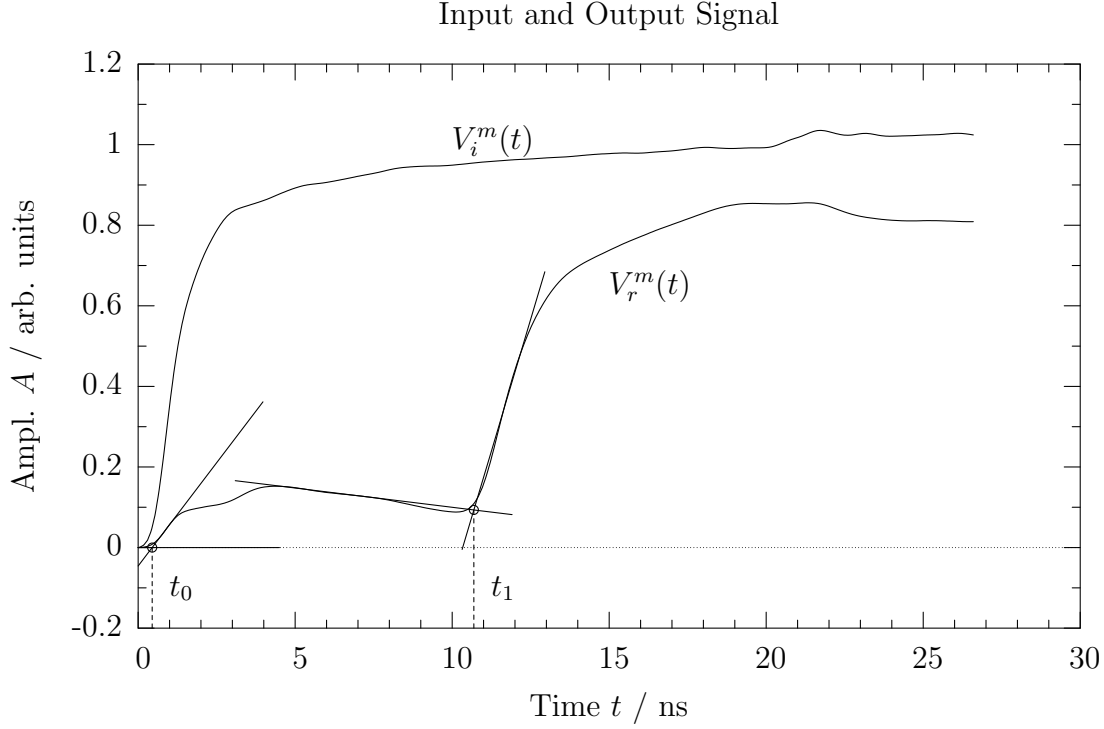
Figure 2.5.: Measured reflectograms of incident voltage step V_i^m and response V_r^m from the probe/soil system.

measurement is performed with a coaxial cable similar to the probe feeding cable. At the end of the open cable a total reflection occurs. The back propagating wave component denoted by V_i^m (Fig. 2.5) is separated from the forward traveling wave. Its shape is similar to the leading edge of the forward traveling pulse just before it hits the probe head.

Eq. 2.19 is solved numerically with appropriate initial and boundary conditions to simulate a TDR measurement for given capacitance and effective conductance profiles along the probe (*Schlaeger*, 2002; *Schlaeger*, 2005). The spatial coordinate of the one-dimensional transmission line has to be discretized for numerical calculation. A typical order of magnitude for the number K of spatial grid points is 100 to 1000. The resulting discrete parameter distribution are listed for the spatial grid points, i.e. $C'(x) = (C'(x_1), \ldots, C'(x_K))$ and $G'(x) = (G'(x_1), \ldots, G'(x_K))$.

The simultaneous determination of both parameter distributions is only possible, if two independent TDR measurements can be performed (*He et al.*, 1994), e.g. using special probes connected from both sides. If ordinary probes with connecting cable at one side only are applied, an empirical relationship $G'(C')$ (Eq. 2.68) is to be considered, which is best to be determined in laboratory for each particular combination of soil and probe. This relationship reduces the number of unknowns from $2K$ to K due to the avoidance of an independent $G'(x)$.

The objective of the reconstruction is to find the parameter distribution C'^* which

minimizes the squared difference between *simulated reflectogram* $V_r^s(t|C')$ and *measured reflectogram* $V_r^m(t)$:

$$J(C') = \int_{t_0'}^{t_1'} \left(V_r^s(t|C') - V_r^m(t) \right)^2 dt \rightarrow \min . \tag{2.21}$$

The travel-time analysis by tangent line method yields the reflection instants t_0 and t_1. The timing interval $[t_0', t_1']$ is slightly shifted with respect to the window $[t_0, t_1]$ to encompass the onset of the signal edges which indicate the beginning of the reflection (s. Fig. 2.7). The error functional is evaluated within the shifted timing window.

The discrete parameter distribution $\vec{C'}(x) = (C'(x_1), \ldots, C'(x_K))$ consisting of K single elements can be seen as a point in a K-dimensional parameter space. For the sake of clearance the vector notation is used throughout the following explanations of the algorithm. The task is to find the optimum $\vec{C'}^*$ within the parameter space, which minimizes Eq. 2.21. This can be achieved e.g. by employing a genetic algorithm as suggested by *Oswald* (2000) or inversion of the $K \times K$ Hessian matrix. However both techniques are extremely time-consuming.
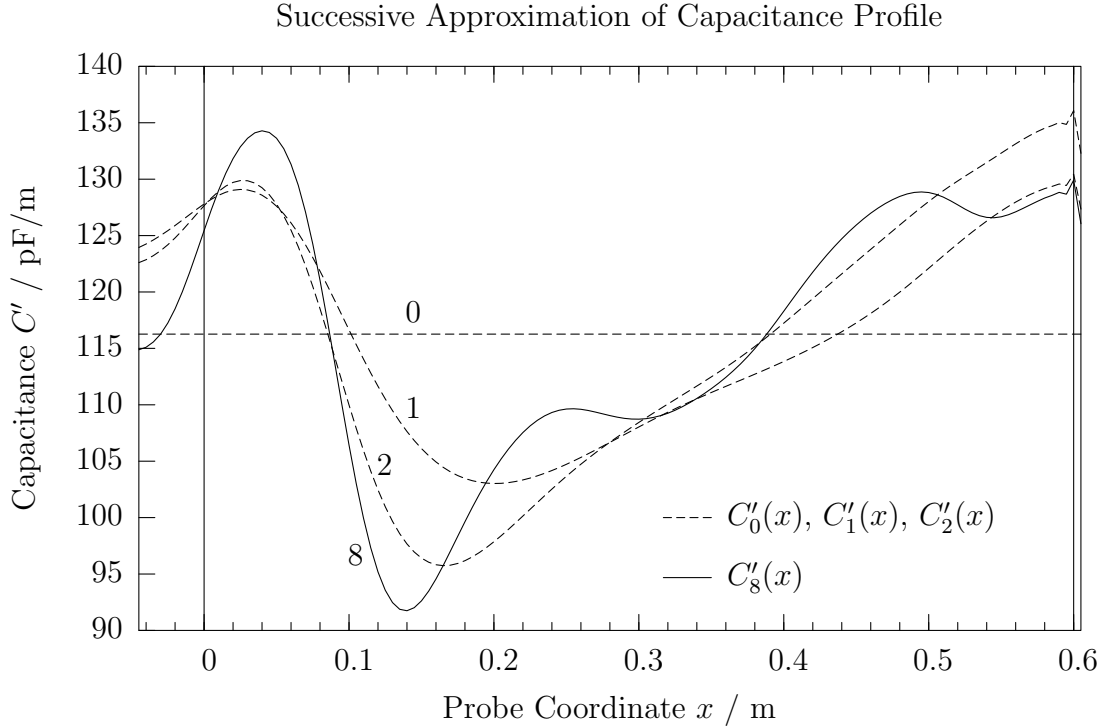
Figure 2.6.: Estimated capacitance profiles of four optimization steps along the 3-rod-probe. The abscissa limits reach from the transition between feeding cable and rod mounts (-0.045 m) to the electric rod length (l'=0.605 m). Vertical lines indicate the physical extent of the probe rods ($0 \leq x \leq l$, $l = 0.6$ m).

Schlaeger (2002) recommends a conjugate-gradient-algorithm for the optimization. He developed a way to efficiently calculate the necessary gradient $\vec{\nabla} J$ of the error functional

precisely by solving the adjoint problem of Eq. 2.19. The vector $\vec{\nabla}J(\vec{C}')$ points from a given point $\vec{C}'$ to the direction of the locally best improvement (steepest descent) of the error functional $J(\vec{C}')$. The gradients from the current and previous optimization steps are merged to yield the search direction $\vec{P}$ to find the minimum of $J(\vec{C}')$ (*Fletcher and Reeves* (1964)). The search is performed by means of an interval search algorithm in the one-dimensional case and a simplex algorithm in the two-dimensional case, if two parameter distributions C' and G' have to be optimized simultaneously. Starting from an initial guess $\vec{C}'_0$ (Fig. 2.6) the TDR pulse propagation is simulated yielding the simulated reflectogram $V_r^s(C'_0)$ (Fig. 2.7). Then gradient of the error functional $\vec{\nabla}J(\vec{C}'_0)$ (Fig. 2.8) is calculated and search direction $\vec{P}_0$ derived. A search along the line going through $\vec{C}'_0$ and pointing in direction $\vec{P}_0$ yields a new point $\vec{C}'_1$ (Fig. 2.6), which leads to the currently best minimum of error functional J.

With this new best solution the procedure is repeated until no further improvement in the minimization of the error functional can be reached. The resulting electric parameter distribution $\vec{C}'^*$ is the optimum in the sense of Eq. 2.21 and therefore the best estimate for the real capacitance profile along the waveguide. It is left to transform the resulting capacitance profile C' into water content profile by means of dielectric permittivity ϵ. This is done in Sec. 4.1.4.
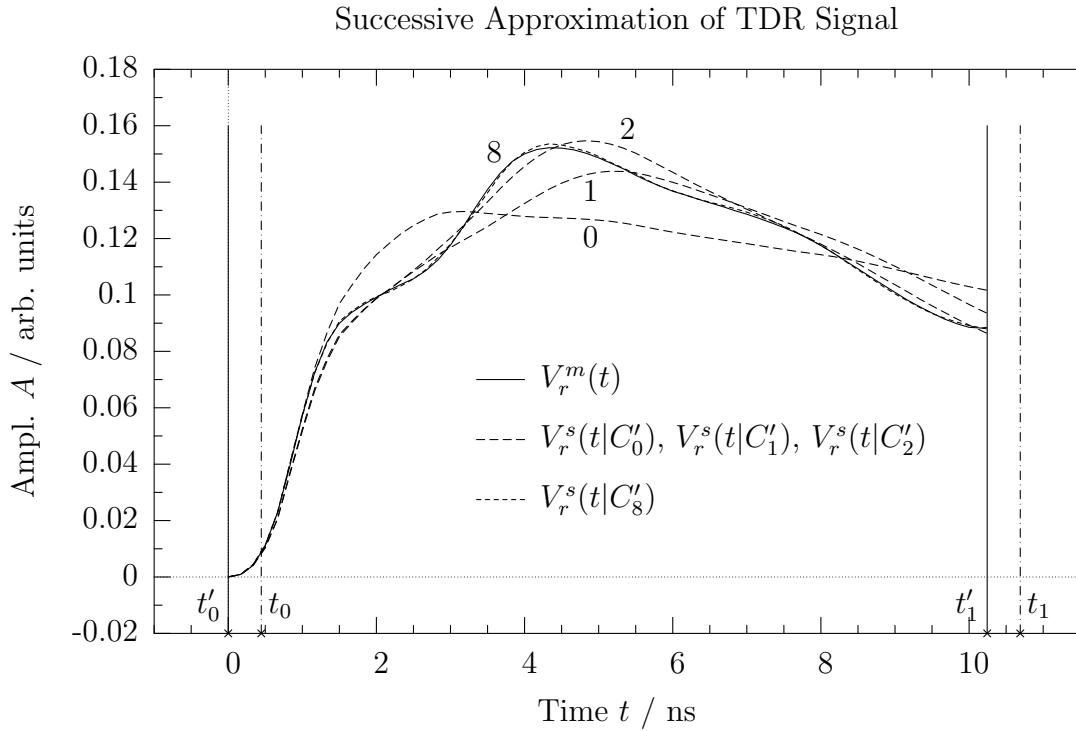
Figure 2.7.: Simulated TDR reflectograms based on capacitance estimates of Fig. 2.6. V_r^m: reflected wave portion from measurement; V_r^s: reflected wave portion from simulation; t_0, t_1: timing window limited by the reflection instants; t'_0, t'_1: shifted timing window within which the error functional is evaluated.

Gradient of Error Functional
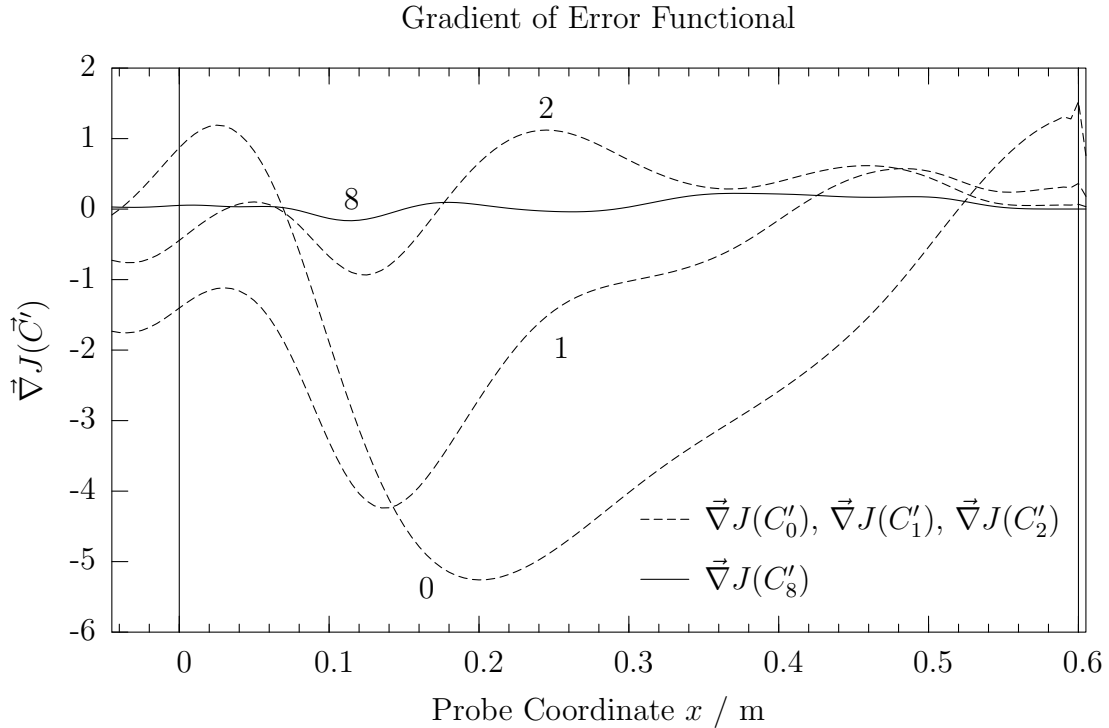
Figure 2.8.: Gradient of error functional based on the current TDR reflectogram estimate of Fig. 2.7. Vertical lines indicate the physical extent of the probe rods. Negative x coordinates lie within the probe head.

2.5. Coated 3-Rod-Probe

To measure soil moisture by means of TDR an unshielded waveguide buried in soil is used as moisture probe. Different TDR applications require different probe designs adjusted to the particular needs. If a probe is designed for calibration in the laboratory to derive a very accurate soil moisture it will not necessarily satisfy the requirements of an on-site measurement device (*Topp et al.*, 1980).

Flexible 3-wire flat-band-cables (ribbon cables) have been used to measure the water content of snow (*Stacheder et al.*, 2004) and soil (*Hübner et al.*, 2004) along distances of many meters, but their application in soil science is limited, because their installation is strongly invasive since it often requires digging of ditches or drilling of fairly large holes.

The most common TDR-probes are composed of two or more small-diameter, continuous parallel metal rods with or without coating. Two-wire probes, e.g. used by *Topp et al.* (1982), have the advantage of little soil disturbance, but they need a balun (transformer) to balance voltage and current between both rods. The balun is a virtual ground which reduces noise and signal loss occurring in unbalanced probes (*White and Zeglin*, 1995). Many probe configurations have been used: balanced parallel wires without a balun (*Malicki and Skierucha*, 1989) balanced parallel wires with a balun (*Topp et al.*, 1982); (*Baker and Lascano*, 1989), unbalanced coaxial pipes (e.g. *Topp et al.* (1980); *Zegelin*

et al. (1989)) and unbalanced multi-wire probes (*Zegelin et al.* (1989); *Heimovaara and Bouten* (1990); *Nissen et al.* (2003)). Simple design, robustness, and little invasive insertion techniques from the soil surface are the main advantages of these rod probes. A new TDR-probe named *SUSU03* with three coated rods and without balun has been built by the SMG (*Schädel*, 2005) for Spatial TDR application. It is designed for monitoring water content profiles in the upper decimeters of soil needed for an improved flood warning system (s. Sec. 4.5).

In principle it is similar to the parallel three-wire transmission lines presented by *Zegelin et al.* (1989) or *Heimovaara and Bouten* (1990) but the rods are additionally coated to reduce signal attenuation due to direct ion conductivity. Highly conductive soils can make the signal reflection from the probe end disappear which means a complete failure of measurement. *Hook et al.* (1992) propose a PIN diode mounted between the ends of uncoated rods to improve the signal detection. By adding a constant voltage (DCV) offset to the TDR pulse the diode becomes conductive and shortens the rod ends. With this configuration the propagating pulse is also reflected but with opposite amplitude. Subtracting this reference signal from the standard TDR measurement reveals the point, where the diode is mounted and the reflection is generated. This method can lead to an improved identification of the reflection instant with lossy signals. However, the diode between the rods is a physical obstacle complicating probe installation. Furthermore *Nichol et al.* (2002) observed that the tangent line method in combination with coated rod probes may be superior to the diode short circuit method with uncoated rods depending on the diode type, especially when the material under test is highly conductive. These arguments led to the decision to use coated rods for the new probe design.

3-rod-probes do not require a balun necessary to balance parallel two-wire probe. The avoidance of a balun is positive for the application with Spatial TDR, because additional parasitic effects and frequency dependence of balun properties are expected to aggravate the accurate determination of signal amplitude over time.

Moreover the field symmetry of the 3-rod-arrangement is advantageous since it resembles the radial field symmetry of the coaxial cable better than a field of two parallel rods. At each transition from one field symmetry to another higher order modes of the EM field are excited which superpose the basic TEM mode. In the strict sense the simple transmission line model with bulk electronic parts displayed in Fig. 2.4 is only valid for pure TEM waves. Higher order modes and radiation cannot be mapped by the model. Thus it is important to design probes with least possible higher order modes.

The probe head consists of a PVC block with three 8 mm screws containing 5 mm internal thread arranged in a line in which the rods can be screwed in. The centers of two adjacent rods are 30 mm apart (s. Fig. 2.9). The feeding cable is a coaxial of type RG213. Its electrical properties are similar to that of the common RG58, but it reveals less attenuation.

The maximum rod length is limited due to the mechanical stress during insertion into the soil and the attenuation of the supplied TDR-signal, which cannot be totally avoided. The rods are 0.6 m long with a solid steel core of 6 mm diameter. The coating is made of a PVC pipe with 6mm inner diameter and 1mm wall thickness. The upper end of the metal core is equipped with a thread (M5) to be screwed into the probe head. The
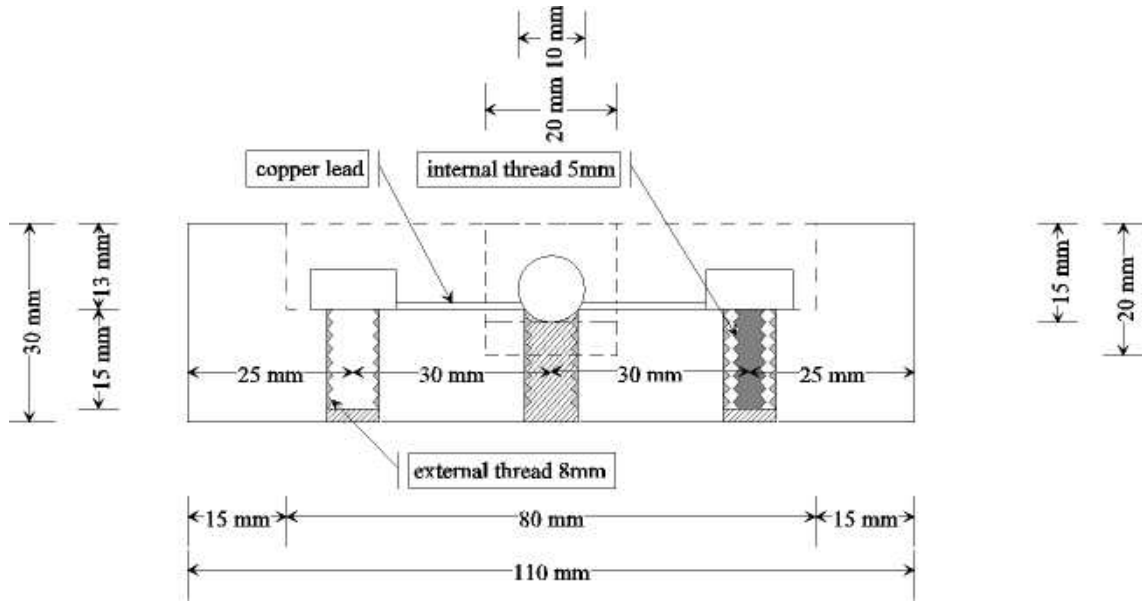
Figure 2.9.: Head of 3-rod-moisture-probe SUSU03. Diagram by courtesy of W. Schädel (*Schädel*, 2005).

lower end of each rod is capped with a PVC tip.

The spacing a of the rods is limited since too large a distance would favor higher order modes of wave propagation violating the TEM condition for the transmission line equation (Eq. 2.19. The geometric constraint is a function of signal wavelength as expressed in Eq. 2.20. This rule of thumb states that the rod spacing a should be smaller than half the minimum wavelength of all frequency components contained in the TDR pulse. In the following will be tested if the probe dimensions fulfill the geometric constraint.

The shortest existing wavelength of all wave components within the TDR pulse limits the maximum geometric extension. Short wavelength means high frequency. *Heimovaara* (1994) showed that after 1 m RG174 coaxial cable the maximum frequency component contained in a TDR pulse emitted by a Tektronix 1502B TDR is about $f_{max} = 1.5$ GHz. This frequency is taken as a reasonable estimate for typical TDR signal bandwidth. Given a fixed frequency the wavelength is still dependent on the pulse propagation velocity v. The lower the velocity the shorter the wavelength. The slowest velocity is reached, when the probe rods are totally immersed in water. The pulse propagation velocity along the probe in water is $v_w \approx 0.26 \, c_0$, where c_0 is the speed of light (s. Tab. 2.1). Substituting v and f_{max} into Eq. 2.20 the limit for the rod spacing yields:

$$a < 0.052 \text{ m} . \tag{2.22}$$

The spacing of two adjacent rods of the 3-rod-probe is 0.03 m and thus fulfills the geometric condition. Nevertheless higher order modes are still excited at major transmission line discontinuities like the transition from feeding cable to rods, but the smaller the rod spacing the shorter the distance within which higher order modes can survive.

30

2.5.1. Probe Calibration

The aim of the following investigation is to determine all electrical parameters of the probe, necessary to apply the reconstruction algorithm and subsequent calibration functions to derive soil moisture profiles.

In case of coated rods calibration parameters of capacitance have to be determined needed to translate the capacitance profile $C'(x)$ resulting from the reconstruction algorithm into the profile $\epsilon(x)$ of the material's permittivity. The function $C'(\epsilon)$ is dependent on the properties of the particular probe (*Hübner* (1999)). In case of the current 3-rod-probe the function contains two parameters: the capacitance C_1' determined by the rod geometry, i.e. their mutual distance, and the capacitance C_2' of the rods' coating. Additionally the rods' inductance L' has to be known to solve the fundamental wave equation (Eq. 2.19) of the reconstruction algorithm.

Two more variables are important to improve the determination of the pulse velocity. These are the travel-time t_h within the probe head (Eq. 2.12) and the electrical rod length l', which is a simplified expression for the fact that the electromagnetic wave interaction with the surrounding medium does not stop abruptly at the rods' end (c.t. Eq. 2.13).

All these parameters can be derived from a single experiment with rods partially immersed into a water basin with variable water level.

Theory

The calibration parameters are determined experimentally through a combination of travel-time and impedance measurements. An often applied equation for the propagation velocity of a wave in medium with relative dielectric permittivity ϵ and relative magnetic susceptibility μ is:

$$v(\epsilon) = \frac{1}{\sqrt{\epsilon\epsilon_0 \cdot \mu\mu_0}} = \frac{c_0}{\sqrt{\epsilon \cdot \mu}} \tag{2.23}$$

In many cases the influence of magnetism on the wave propagation may be neglected and μ is equal to 1. This simple formula can be used to calculate the material's permittivity only in TDR experiments with uncoated rods. Otherwise the wave traveling along the rods experiences an effective dielectric permittivity which is a mixing of the dielectric properties of the rod coating and the permittivity of surrounding medium. In this case the wave velocity can be best expressed in terms of inductance and capacitance per length unit:

$$v(\epsilon) = \frac{1}{\sqrt{L'C'(\epsilon)}} \ , \tag{2.24}$$

with C' being the effective capacitance of the total system probe/material dependent on the material's permittivity ϵ. The inductance L' of the system probe/material may be assumed constant for different materials under test.

According to figure 2.10 the function $C'(\epsilon)$ of the probe rods embedded in the material with relative dielectric permittivity ϵ can be modeled with an equivalent circuit consisting of a series of two capacitors, one describing the constant capacitance of the rod
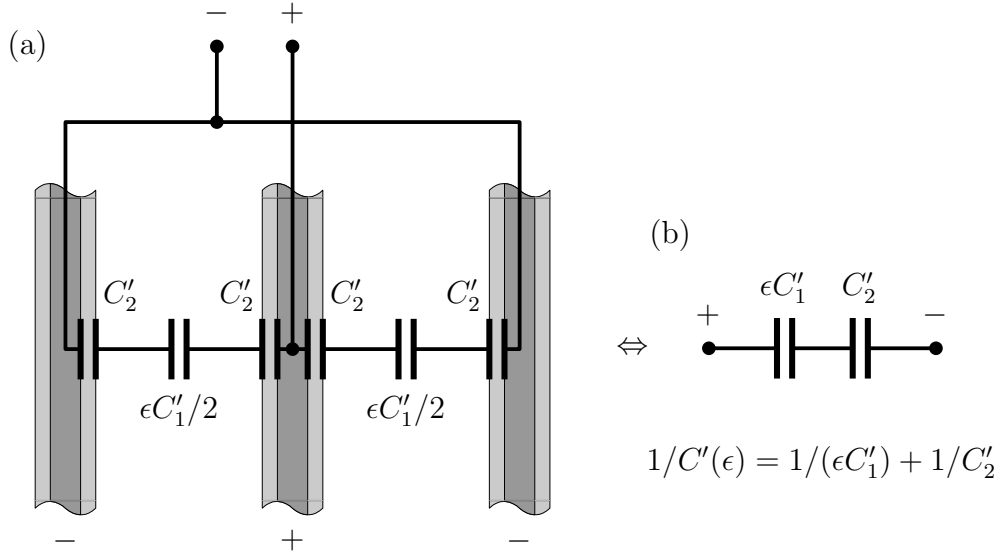
Figure 2.10.: Capacitance of the system probe/material. a: short segment of three parallel rods, metal core in dark, coating in light gray; C_2': capacitance of coating; $\epsilon C_1'/2$: capacitance between rods surrounded by material of relative dielectric permittivity ϵ. b: equivalent circuit and resulting formula for total capacitance as function of the material's variable permittivity ϵ and the constants C_1' and C_2'.

coating, one representing the capacitor between the rods filled with the material and thus depending on ϵ. The total capacitance of a series of two capacitors is

$$\frac{1}{C'(\epsilon)} = \frac{1}{\epsilon C_1'} + \frac{1}{C_2'} \tag{2.25}$$

$$\Leftrightarrow C'(\epsilon) = \frac{(\epsilon C_1') \cdot C_2'}{(\epsilon C_1') + C_2'} \tag{2.26}$$

with C_1' the capacitance of probe determined by the distance of the rods, and C_2' the capacitance of the rods' coating. Both parameters have to be determined by calibration measurements.

The rods' inductance L' may be derived from their impedance Z_2, which acts like a complex resistance on the wave propagation. The complex impedance of a uniform transmission line can be generally expressed as

$$Z = \sqrt{\frac{R' + i\omega L'}{G' + i\omega C'}} . \tag{2.27}$$

In the current case of a probe with coated rods held in air, the resistance R' of the metallic rods and the electrical conductance G' between the rods can be neglected. Since the

probe is coated, the capacitance is the effective capacitance of Eq. 2.26. The impedance of the rods embedded in an medium with permittivity ϵ is:

$$Z(\epsilon) = \sqrt{\frac{L'}{C'(\epsilon)}} \ . \tag{2.28}$$

Whenever the impedance along the signal propagation changes the wave is partially reflected and partially transmitted at this location. An example is the wave splitting caused by the transition from coaxial cable to probe rods with impedance Z_0 and Z, respectively. The reflection coefficient ρ is defined to be the amplitude ratio of reflected $(A_{\rm r})$ over incident $(A_{\rm i})$ wave. The reflection coefficient is linking the amplitude ratio to the change in impedance:

$$\rho = \frac{A_{\rm r}}{A_{\rm i}} = \frac{Z - Z_0}{Z + Z_0} \ . \tag{2.29}$$

Solving for the unknown impedance Z yields:

$$Z = \frac{1 + \rho}{1 - \rho} Z_0 \ . \tag{2.30}$$

Eq. 2.30 is used to determine the rod impedance Z experimentally from TDR reflectograms, with Z_0 the known impedance of the coaxial cable connecting the probe. Let ϵ_a and ϵ_w be the permittivity of air and water, respectively. For the sake of simplicity the corresponding signal propagation velocities along the probe surrounded by air or water will be denoted by v_a and v_w:

$$v_a := v(\epsilon_a) \ , \quad v_w := v(\epsilon_w) \ . \tag{2.31}$$

The unknown L' can now be determined by a combination of Eqs. 2.28 and 2.24 for measurements with rods in air:

$$L' = Z(\epsilon_a)/v_a \ . \tag{2.32}$$

Substitution of Z in the above equation with Eq. 2.30 leads to an expression showing how to determine L' experimentally:

$$L' = \left(\frac{1 + \rho(\epsilon_a)}{1 - \rho(\epsilon_a)} \right) \frac{Z_0}{v_a} \ . \tag{2.33}$$

The reflection coefficient ρ at the transition from coaxial cable with impedance Z_0 to the rods can be determined experimentally by the amplitude ratio of incident to reflected wave. The velocity v_a in air may be derived from one single measurement with the probe held in air or from a more reliable procedure described in the experimental part below. To find the remaining parameters C_1' and C_2' Eq. 2.24 has to be applied with two different permittivities. It is convenient to use the materials air and water with their corresponding permittivities ϵ_a and ϵ_w giving total capacitances $C'(\epsilon_a)$ and $C'(\epsilon_w)$, respectively. Using Eq. 2.25 twice and solving for C_1' yields:

$$C_1' = \frac{\epsilon_w - \epsilon_a}{\epsilon_w \epsilon_a} \cdot \frac{C'(\epsilon_w)C'(\epsilon_a)}{C'(\epsilon_w) - C'(\epsilon_a)} \ . \tag{2.34}$$

$v(\epsilon_a)$ and $v(\epsilon_w)$ are the corresponding wave velocities along the rods surrounded by the two media. The velocities are to be determined experimentally. From Eq. 2.24 follows:

$$C'(\epsilon_a) = \frac{1}{v_a^2 L'} \ , \quad C'(\epsilon_w) = \frac{1}{v_w^2 L'} \tag{2.35}$$

Inserting these equations into the above expression for C_1' yields

$$C_1' = \frac{\epsilon_w - \epsilon_a}{\epsilon_w \epsilon_a (v_a^2 - v_w^2) L'} \tag{2.36}$$

The same procedure for C_2' leads to:

$$C_2' = \frac{\epsilon_w - \epsilon_a}{(\epsilon_w v_w^2 - \epsilon_a v_a^2) L'} \tag{2.37}$$

The velocities v_a and v_w are determined experimentally by an immersion experiment.

Immersion Experiment

One method to determine the necessary calibration parameters v_a and v_w (wave velocity in air and water, respectively) is to perform an experiment in which a vertically installed rod probe is partially immersed into water (Fig. 2.11). The total pulse travel-time (t_t) along the probe is the sum of the individual travel-times in probe head (t_h), air (t_a), and water (t_w). The total travel-time changes with immersion depth, for the wave velocities in the two layers are different. The variable x is the spacing between probe head bottom and water surface. The electric rod length l' is larger than the physical length l, because the electromagnetic field is reaching beyond the rod ends. t_0, t_1, and t_x denote the instants of reflections coming from probe beginning, probe end, and air/water interface, respectively. The time elapsed between t_0 and t_x comprises the pulse travel-time t_a in air and a short portion t_h within the probe head. The following relationships hold:

$$
\begin{aligned}
t_t(x) &= t_1 - t_0 = t_h + t_a(x) + t_w(x) \ , & (2.38)\\
t_a'(x) &= t_x - t_0 = t_a(x) + t_h \ , & (2.39)\\
t_a(x) &= 2x/v_a \ , & (2.40)\\
t_w(x) &= t_1 - t_x = 2(l' - x)/v_w = -2x/v_w + 2l'/v_w \ . & (2.41)
\end{aligned}
$$

According to (*Schaap et al.*, 2003) travel-time analysis in media consisting of many thin layers of different dielectric permittivity may be intricate, if the effective dielectric permittivity is to be determined. The current experiment uses only two layers, so that the above listed relationships are valid.

Several TDR measurements are taken with a stepwise increase of immersion depth and the pulse travel-times in the different media are evaluated using the tangent method.
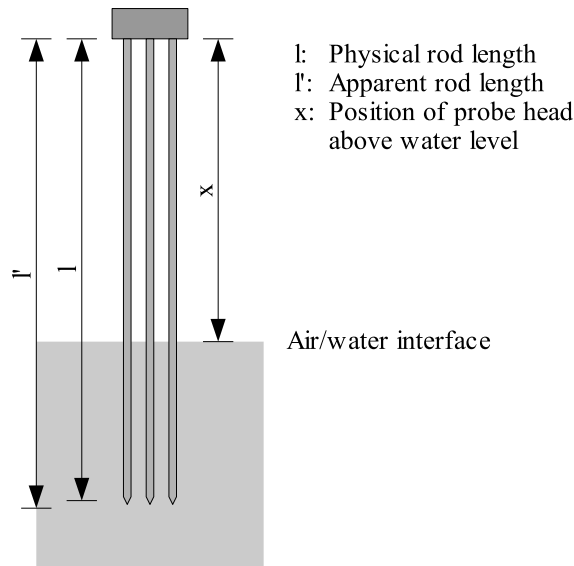
Figure 2.11.: Definition of rod length and water level. The electrical rod length l' is a little longer than the physical length l. The distance x denotes the height of the probe head bottom above the air/water interface (water level).

Linear regression of the resulting travel-times vs. distance yields the intended parameters. A calibration experiment similar to the current has been proposed by *Robinson et al.* (2003b), but the main advantage of the present method is the robustness of wave velocity estimates for air and water due to the large number of measurements entering the linear regression.

Experimental Setup

The water is held in a cylindrical tank which consists of a vertically standing PVC pipe segment of 1.2 m length and 0.6 m diameter. Its bottom is closed with a PVC plate glued to the pipe. A valve is mounted sidewise to the cylinder close to the base. It can be used as inlet or outlet. The probe head is held by a special probe clamp which allows to fix the probe at different heights with respect to the water level. The length of the connecting coaxial cable of 14.4 m is the same as in the main hydrological investigation which follows in Chap. 4.1. Throughout the following analysis the TDR Tektronix 1502C is used.

Wave Velocity along the 3-Rod-Probe in Water and Air

Since the wave velocity in water is less than in air due to the higher permittivity the total travel-time increases with the portion the signal has to travel through water. Fig. 2.12 shows the family of TDR reflectograms resulting from the experiment. The first rising slope is caused by the signal reflection at the transition from coaxial cable to probe head. The curve parameter x denotes the distance in cm from the beginning of the rods to the water level, where a reflection with negative signal slope (transition from higher to lower impedance) occurs. The last reflection is due to the rods' end. The smaller x, the larger the way the wave is influenced by water, and the longer the total travel-time. Values x
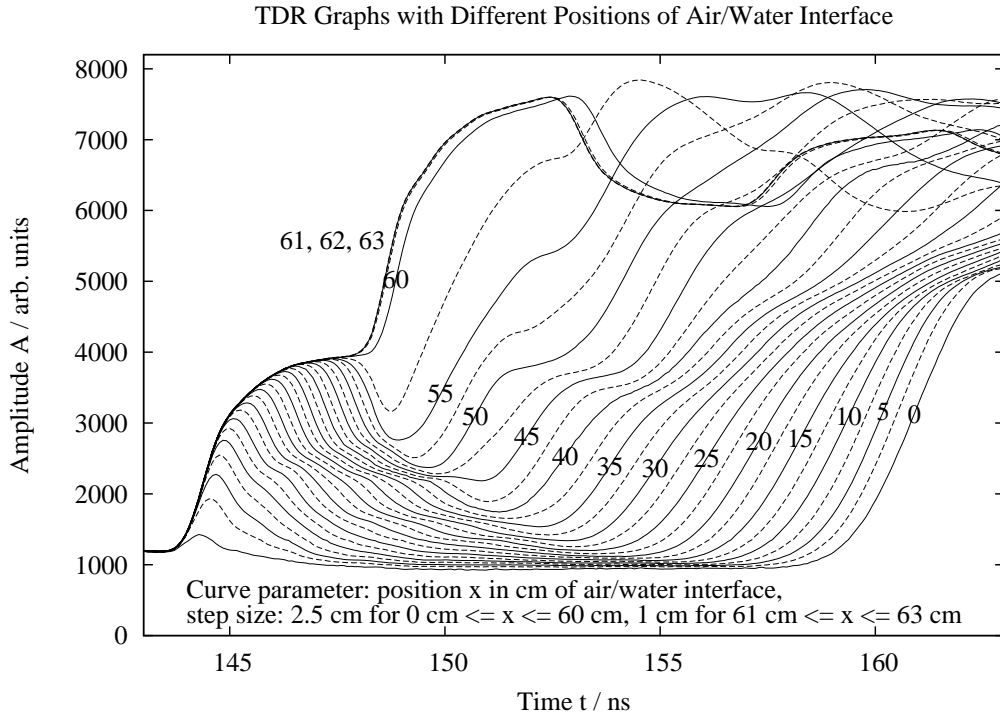
Figure 2.12.: Family of TDR reflectograms of a rod probe partially immersed in water. Curve parameter x is the distance between probe head bottom and the air/water interface. Physical rod length $l = 60$cm, total connecting cable length $l_c \approx 14.4$m.

larger than the rod length l mean that the metal cores of the rods are above the water surface. The curves for $x = 61$ cm, 62 cm, and 63 cm are almost equal but different from the signal with $x = l = 60$ cm, indicating that the interaction between wave and medium reaches beyond the rods' end. Reflectograms recorded with Tektronix 1502C.

Since the wave velocities in air and water are constant, the travel-times are expected to be linear functions of the distances. Figure 2.13 shows experimentally determined travel-times deviating slightly from the ideal linear behavior. This deviation mainly occurs in cases where the water level is within 10 cm below the probe head or near the rods' end. Thus for the linear regression only points have been taken into account where x is between 10 cm and 57.5 cm. The linear regressions yield:

$$
\begin{aligned}
t_a'(x) &= 0.065\,\text{ns/cm} \cdot x + 0.345\,\text{ns} & (2.42) \\
t_w(x) &= -0.252\,\text{ns/cm} \cdot x + 15.216\,\text{ns} & (2.43) \\
t_t(x) &= -0.187\,\text{ns/cm} \cdot x + 15.561\,\text{ns} & (2.44)
\end{aligned}
$$

The signal velocities in air and water can be determined from the slopes of t_a and t_w, respectively. The electrical rod length l' follows from searching x with $t_w(x = l') = 0$ ns. The travel-time t_h within the probe head is defined by $t_h = t_a(x = 0)$.

36

Pulse Travel Time as Function of Water Level
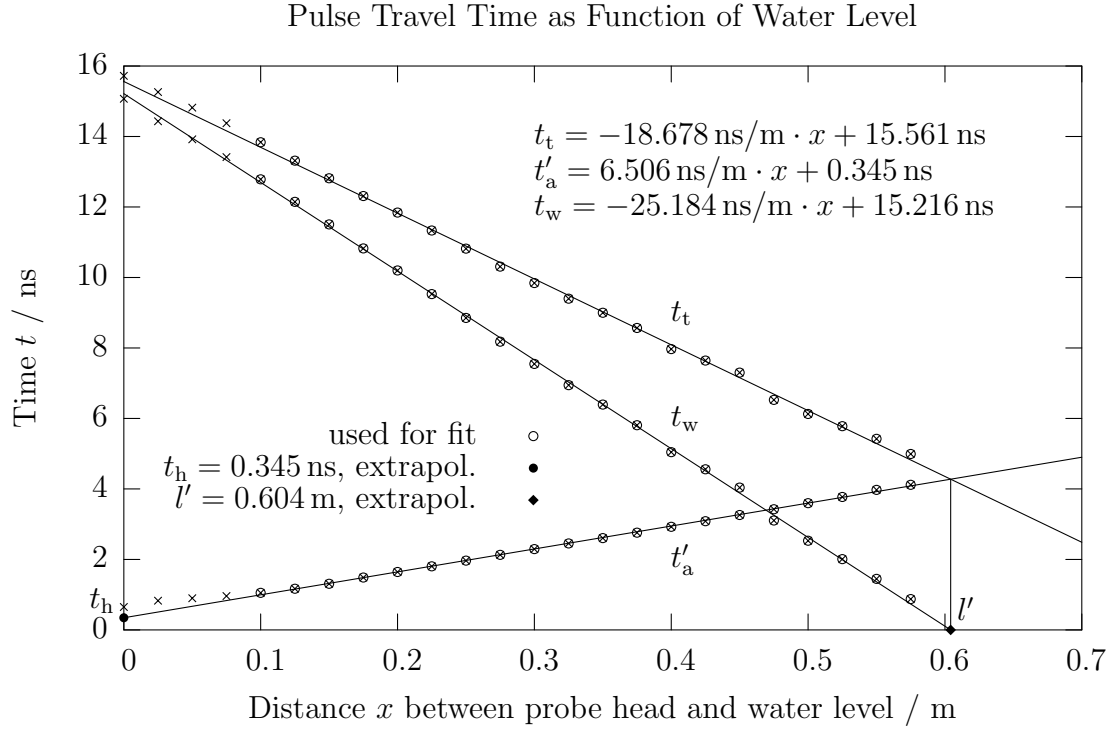
Figure 2.13.: travel-time dependent on plunging depth. x: distance between bottom of probe head and water level, t_t: total travel-time along the rods including probe head, t'_a: travel-time in air including probe head, t_w: travel-time in water only without probe head, t_h: travel-time in probe head, l': electric probe length.

The preliminary results from the current experiment are:

$$
\begin{aligned}
v_a^* &= 3.077 \cdot 10^8\,\text{m/s} \approx 1.026\,c_0 \quad (!) & (2.45)\\
v_w^* &= 0.794 \cdot 10^8\,\text{m/s} \approx 0.265\,c_0 & (2.46)\\
l'^* &= 60.4\,\text{cm} & (2.47)\\
t_h^* &= 0.345\,\text{ns} & (2.48)
\end{aligned}
$$

The experimental determination of v_a yields a value 3% larger than the speed of light (Eq. 2.45) indicating a systematic error of the TDR time base underestimating the travel-time.

Check of TDR Timebase

The TDR time-base is realized by internal delay generators which are cascaded. One delay generator is responsible for the position of the sampling window, one determines the window width. Such delay generators generate a linearly rising voltage ramp by integrating a programmable constant voltage. The integrator is started by an initial input pulse. If the rising voltage ramp exceeds a programmable voltage threshold a

trigger will be fired and an output pulse emitted. Thus threshold and slope of voltage ramp determine the time between input and output pulse. It looks as if the input pulse were delayed. The integrator itself, its external circuitry, and the variable voltage reference are susceptible for nonlinearities and systematic errors. Strictly spoken the calibration or test measurement generally has to be performed for all possible settings of the TDR time-base.

The current time-base test has been conducted with the same sampling window width as in the water tank experiment presented above.[1] The window position is not important, since it is fixed for one set of measurements. Errors in this larger time-base cancel when calculating time differences. One way to test the TDR time-base is to measure travel-times in a well-defined waveguide with variable length. U-shaped hollow waveguides extensible in length like a trombone were used for the experiment. Their length can be controlled precisely with a resolution of 1/10 mm by means of a gear and a nonius. Two of them were connected in series and joined to the TDR. The last connection of the trombones was left open.

Reflectograms for Different Waveguide Lengths
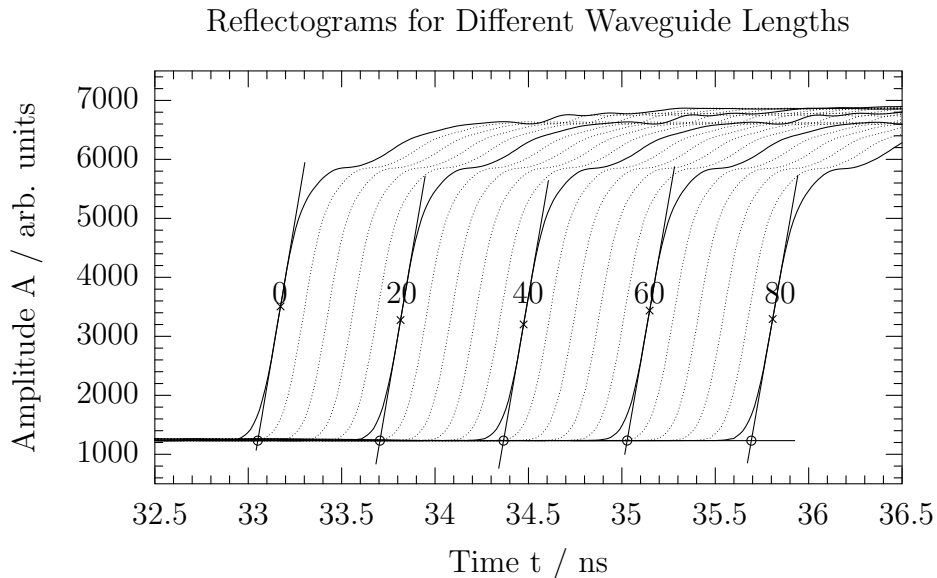
Figure 2.14.: Time-base test of the Tektronix 1502C for one particular setting. Curve parameter of the reflectograms is the length increment Δx of the hollow waveguides in cm.

Fig. 2.14 shows the family of TDR reflectograms sampled for different waveguide lengths together with some of the fitted lines defining the reflection instants. The resulting reflection instants vs. differential waveguide length are displayed in Fig. 2.15.

---

[1]The sampling window width of the Tektronix 1502B/C is controlled by the parameters *dist/div* and *vpp*.

Travel Time for Different Waveguide Lengths
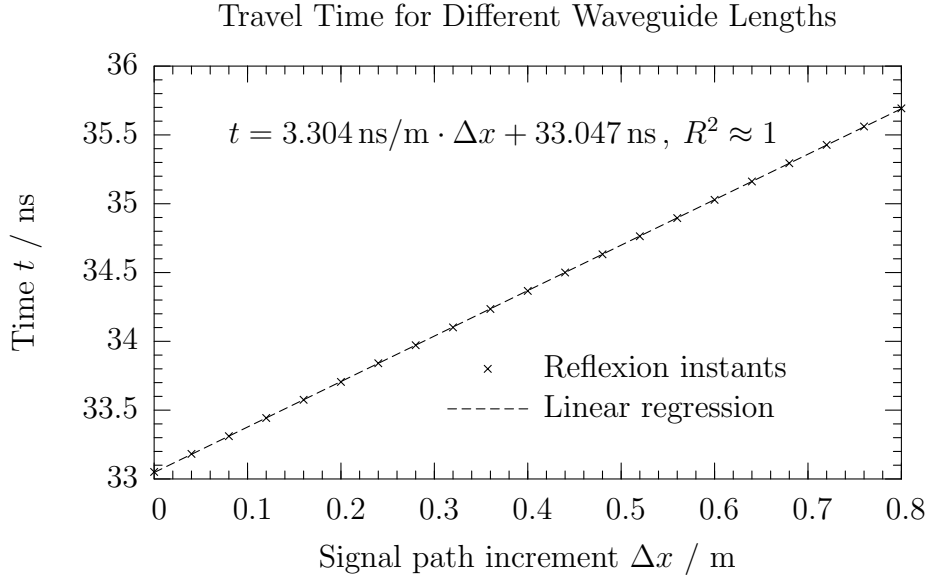
Figure 2.15.: Increase of pulse travel-time as function of signal path increment of the hollow waveguides. Travel-time was derived from reflectograms in Fig. 2.14.

The linear regression formula in Fig. 2.15 yields

$$ t = \frac{1}{v}\Delta x + t_0 = 3.304 \text{ ns/m } \Delta x + 33.047 \text{ ns} , \tag{2.49} $$

where v is the phase velocity of the EM pulse propagating in the hollow waveguides. The nominal velocity of a EM wave in an empty hollow waveguide is the speed of light c_0. The test indeed reveals a phase velocity v approximately 3% larger than c_0.

Correction of Probe Parameters

Due to the evidence of a faulty time-base of the particular TDR instrument the measurements of the water tank experiment are to be corrected. Each time has to be prolonged by the factor $v/c_0 = 1.026$, thus the corrected parameter set finally reads:

$$
\begin{align}
v_a &= 1/1.026 \cdot v_a^* = 3 \cdot 10^8 \text{ m/s} = c_0 \ (+0\%, -1\%) \tag{2.50}\\
v_w &= 1/1.026 \cdot v_w^* = 0.774 \cdot 10^8 \text{ m/s} \approx 0.258 \cdot c_0 \ (\pm 3\%) \tag{2.51}\\
l' &= l'^* = 60.4 \text{ cm} \ (\pm 0.6 \text{ cm}) \tag{2.52}\\
t_h &= 1.026 \cdot t_h^* = 0.354 \text{ ns} \ (\pm 3\%) \tag{2.53}
\end{align}
$$

The errors for the corrected values which are influenced by the time-base are assumptions based on the specification of the Tektronix 1502C (*Tektronix* (1999)). An error of 3% is a reasonable estimate for such kind of measuring devices. The error in v_a has been lowered to 1% because it is assumed from experience in other experiments that the wave velocity along the coated rods in air is negligibly smaller than the speed of light, since

the isolating material has a low permittivity (around 4) and its volume is very small compared to the field extension.

The error in length l' is assumed to consist of a random and a systematic portion. The random error is due to the measurement process of l', the systematic error is caused by the arbitrary but fixed longitudinal extension of the electromagnetic field at the rods' end depending on the particular environment. It can be stated that the field extension is largest in air and the TDR reflectograms do not show any change if the rods are situated more than 1 cm above the water table. Thus the electrical rod length must be $l' < 61\text{cm}$, which is in good accordance with the error given above.

Reflection Coefficient by Amplitude Scaling

The constant rod inductance L' occurring in the wave equation (Eq. 2.19) can be determined by means of the reflection coefficient (c.t. Eq. 2.33). The necessary velocity v_a has been determined earlier in the water tank experiment with partially immersed probe. The remaining unknown reflection coefficient ρ can be derived experimentally in several ways. The easiest and probably most reliable is the graphical scaling of a measured incident pulse amplitude until it matches that of the reflected wave (Fig. 2.16).
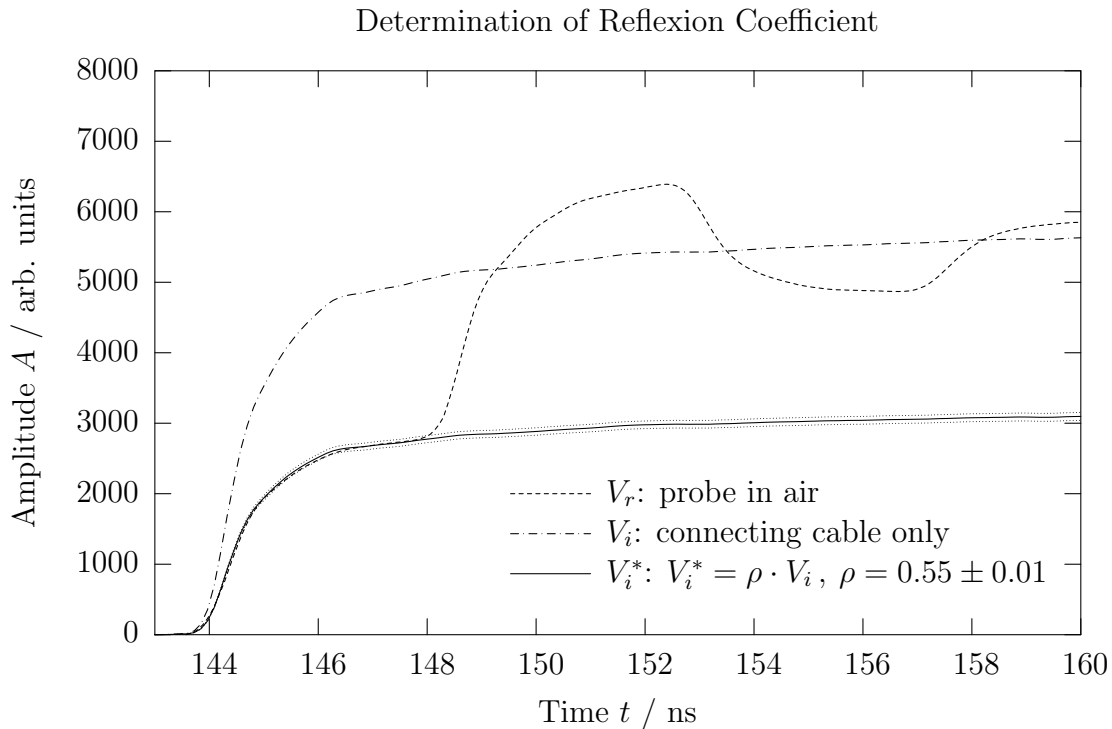
Figure 2.16.: Determination of the reflection coefficient by scaling down the incident wave to the level of the reflected wave. f_1: TDR reflectogram of 3-rod-probe in air, f_2: incident wave, f_3: incident wave scaled down to the level of the first reflection from the probe. Probe connected with 14.4 m RG213 coaxial cable.

To measure the incident wave a coaxial cable with an open end and the length of the probe cable (14.4 m) is connected to the TDR. Since the TDR pulse is fully reflected at the cable's end its amplitude A_i shown in the reflectogram V_i is that of the incident wave at the probe's beginning. The first plateau of the reflectogram V_r with the 3-rod-probe held in air is the amplitude A_r of the reflected pulse due to the impedance mismatch from coaxial cable to rods in air. The curve V_i^* is the result of scaling the initial wave down to the level of the first plateau of V_r. According to Eq. 2.29 the following relationship is valid: $A_r = \rho \cdot A_i$. The scaling factor ρ is the reflection coefficient emerging at the probe's beginning. The graphical method of down scaling the incident amplitude yields a reflection coefficient

$$\rho = 0.55 \pm 0.01 \ . \tag{2.54}$$

Reflection Coefficient by Amplitude Ratio

Another method to determine the reflection coefficient is the direct calculation of the amplitude ratio. The reflection coefficient can be read from the TDR measurement of Fig. 2.17 showing the full initial step pulse and the reflection at the probe head. The jump from amplitude level A_0 to A_1 is the incident pulse. The transition from A_1 to A_2 is the wave portion reflected at the probe head. The variable reflection between A_2 and A_3 are due to different resistor values Z_3 set for termination which are used in the matched impedance method.
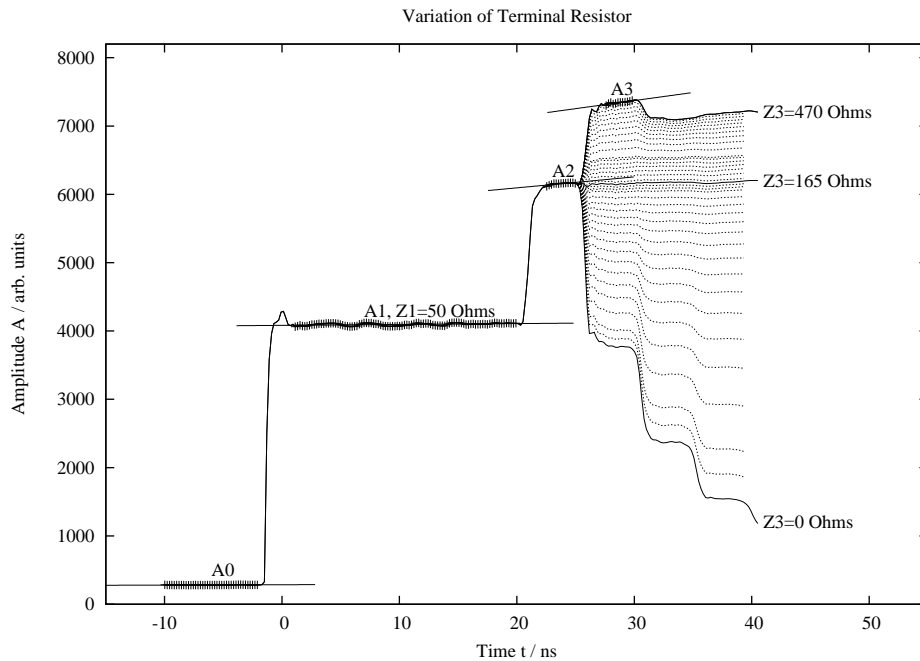
Figure 2.17.: Changing reflection due to variable termination resistor.

It is difficult to reliably determine the amplitude representative for the different signal plateaus, since some of them are not perfectly horizontal. The incline is due to dispersion of the step pulse. The longer the connecting cable, the stronger the deviation from the

ideal horizontal. For larger times the amplitude should converge toward a constant value but in case of short probes the reflection at the end of the rods will occur long before the constant amplitude level is reached.

Since there is no better way up to now, the arithmetic mean of selected points within a plateau (symbolized as crosses in Fig. 2.17) have been chosen to be the reference amplitude for that plateau. The reflection coefficient is

$$\rho = \frac{A_\mathrm{r}}{A_\mathrm{i}} = \frac{A_2 - A_1}{A_1 - A_0} = \frac{6155 - 4096}{4096 - 282} = 0.54 \pm 0.01 \ . \tag{2.55}$$

The error has been estimated by substituting A_2 by the smallest and the largest amplitude of the selected points in the plateau. This value for ρ is slightly less than the scaling method result of Fig. 2.16.

The biggest disadvantage of this procedure is the comparison of amplitudes belonging to signals of very different traveling times. The first step $A_1 - A_0$ is due to the initial voltage step generated in the TDR and recorded directly at its source. The second step $A_2 - A_1$ occurs because of the impedance mismatch where the signal enters the probe. Thus when recorded this reflected wave portion has travelled forth and back the coaxial cable having been influenced by unavoidable dispersion during its propagation. Signal amplitudes of very different history are compared. It is generally not correct to assume the initial step reaching the probe without distortion. The incident wave form seen by the probe head is different from the one sent out by the TDR.

Reflection Coefficient by Matched Impedance

A third method to gain the information necessary to calculate L' does not use the formulation with reflection coefficient (Eq. 2.32) but the equivalent expression with rod impedance Z (Eq. 2.33). The rod impedance can be measured by means of variable termination. Therefore the dips have to be removed from the rods and a a variable resistor $(0 - 470\Omega)$ must be soldered at the bare metallic ends. The idea is to tune the resistor until the reflection at the probe's end vanishes. The resistance is measured with an Ohm-meter. In case of perfect termination the value Z_3 of the resistor is equal to the impedance Z of the rods. The state of perfect termination cannot be identified unambiguously from the TDR recording due to local disturbances at the resistor leads and the signal plateau not being perfectly flat because of the dispersion of the electromagnetic wave. Therefore it is recommended to record a series of TDR reflectograms with different terminations and to display the amplitude differences at the probe's end versus resistance. It is convenient to introduce a relative amplitude difference:

$$d(Z_3) = \frac{A_3(Z_3) - A_2}{A_2} \ . \tag{2.56}$$

The zero crossing of d (Fig. 2.18) indicating the terminal resistance is matching the rod impedance is at

$$Z = Z_3 = 165 \pm 2\Omega \ . \tag{2.57}$$

This impedance has to be transformed into reflection coefficient by means of Eq. 2.29 to be comparable to the above results:

$$\rho = 0.53 \pm 0.014 \ . \tag{2.58}$$
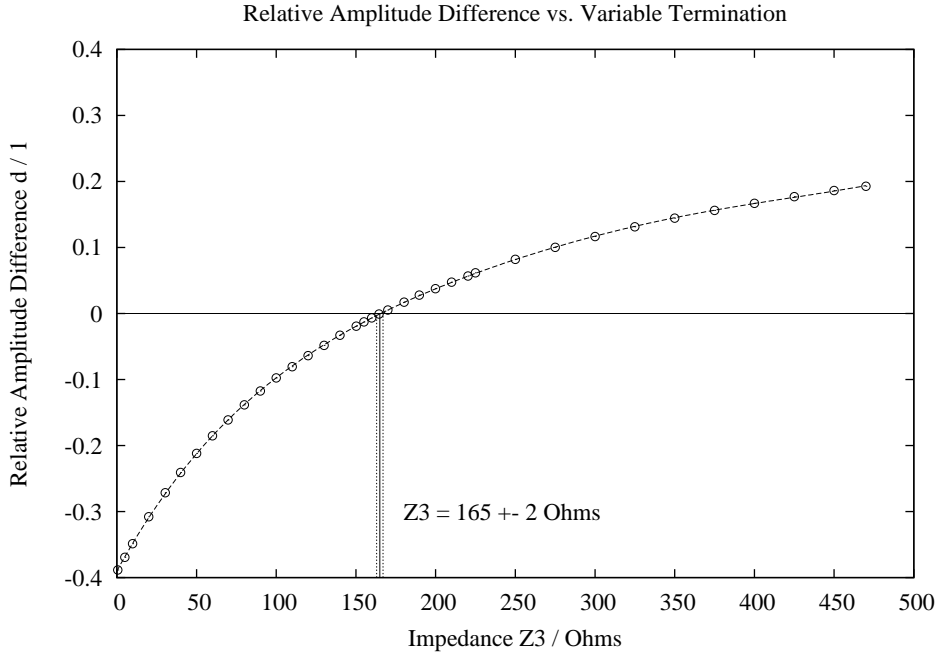
Figure 2.18.: Relative amplitude difference depending on the terminal resistance. Zero crossing at $Z_3 = 165 \pm 2\Omega$.

The error $\Delta\rho$ is derived from Gauss' law of error propagation applied to Eq. /refeqnR12 under the assumption, that the impedance of the coaxial cable is

$$Z_0 = 50 \pm 1\Omega \ . \tag{2.59}$$

Thus

$$
\begin{aligned}
\Delta\rho &= \sqrt{\left(\frac{\partial\rho}{\partial Z_0}\Delta Z_0\right)^2 + \left(\frac{\partial\rho}{\partial Z}\Delta Z\right)^2} \\
&= \sqrt{\left(\frac{-2Z_0}{(Z + Z_0)^2}\Delta Z_0\right)^2 + \left(\frac{2Z}{(Z + Z_0)^2}\Delta Z\right)^2} \\
\Rightarrow \Delta\rho &= \sqrt{(2.16 \cdot 10^{-3} \cdot 1)^2 + (7.14 \cdot 10^{-3} \cdot 2)^2} \approx 0.014 \ . \tag{2.60}
\end{aligned}
$$

The calculated reflection coefficient is a bit too low compared to the value derived from the graphical down-scaling but the ranges overlap.

Calculation of the Rod Inductance

The graphical down-scaling is the handiest method and yields the most reliable result for the particular application. It does not suffer from the dispersion which leads to inclined signal plateaus and it compares two signals filtered similarly by the coaxial cable. Therefore the reflection coefficient of Eq. 2.54 is used throughout the following analysis.

Now all parameters are known to calculate the inductance. When the results for velocity $v(\epsilon_a)$ (Eq. 2.51), reflection coefficient ρ (Eq. 2.54), and the assumption about the impedance Z_0 of the coaxial cable (Eq. 2.59) are inserted into Eq. 2.33, the inductance becomes

$$L' = 575 \pm 23 \, \text{nH/m} \, . \tag{2.61}$$

The error is derived from Gauss' law of error propagation:

$$\Delta L' = \sqrt{\left(\frac{-2\rho}{(1-\rho)^2} \frac{Z_1}{v(\epsilon_a)} \Delta\rho\right)^2 + \left(-L'\frac{\Delta Z_1}{Z_1}\right)^2 + \left(L'\frac{\Delta v(\epsilon_a)}{v(\epsilon_a)}\right)^2}$$

$$\Rightarrow \Delta L' = \sqrt{(906 \cdot 0.01)^2 + (575 \cdot 0.02)^2 + (575 \cdot 0.03)^2} \, \text{nH/m} \tag{2.62}$$

$$\approx 23 \, \text{nH/m} \, . \tag{2.63}$$

Capacitance Coefficients

Now that the rod impedance is known the coefficients C_1' and C_2' of the capacitance model (Eq. 2.26) can be calculated by means of Eqs. 2.36 and 2.37. The velocities $v(\epsilon_a)$ and $v(\epsilon_w)$ in air and water have been determined earlier (Eqs. 2.51 and 2.52). For the permittivity of air and water the following values are taken from literature (*Ulaby et al.* (1986)):

$$\begin{aligned} \epsilon_a &= 1, \quad \text{air similar to vacuum;} \\ \epsilon_w &= 78, \quad \text{water at 25°C.} \end{aligned} \tag{2.64}$$

Further discussions about the permittivity's dependence on frequency, temperature and ion concentration can be found in *Hübner* (1999) and *Schlaeger* (2002).
From Eqs. 2.36 and 2.37 follows:

$$C_1' = 20.5 \pm 0.9 \, \text{pF/m} \, , \qquad C_2' = 356 \pm 30 \, \text{pF/m} \, . \tag{2.65}$$

Errors are calculated with Gauss' law of error propagation under the assumption of negligible errors for the permittivities:

$$\Delta C_1' = C_1' \sqrt{\left(\frac{-2v_a^2}{v_a^2 - v_w^2} \frac{\Delta v_a}{v_a}\right)^2 + \left(\frac{2v_w^2}{v_a^2 - v_w^2} \frac{\Delta v_w}{v_w}\right)^2 + \left(\frac{\Delta L'}{L'}\right)^2}$$

$$= 20.5 \, \text{pF/m} \, \sqrt{(2.12 \cdot 0.01)^2 + (0.14 \cdot 0.03)^2 + (1 \cdot 0.04)^2}$$

$$\approx 20.5 \, \text{pF/m} \cdot 0.045 = 0.92 \, \text{pF/m} \, . \tag{2.66}$$

The particular terms of the error calculation show that C_1' is most sensitive to the error of the velocity in air v_a and second most to the error of the impedance L'. In this case the error of the velocity in water is negligible.

$$\Delta C_2' = C_2' \sqrt{\left(\frac{-2\epsilon_a v_a^2}{\epsilon_a v_a^2 - \epsilon_w v_w^2}\frac{\Delta v_a}{v_a}\right)^2 + \left(\frac{2\epsilon_w v_w^2}{\epsilon_a v_a^2 - \epsilon_w v_w^2}\frac{\Delta v_w}{v_w}\right)^2 + \left(\frac{\Delta L'}{L'}\right)^2}$$

$$= 356 \text{ pF/m } \sqrt{(0.47 \cdot 0.01)^2 + (2.47 \cdot 0.03)^2 + (1 \cdot 0.04)^2)} \text{ pF/m}$$

$$\approx 356 \text{ pF/m} \cdot 0.084 \approx 30 \text{ pF/m} . \tag{2.67}$$

Summary of Probe Parameters and Sensitivity Analysis

Parameter	Value	Abs. Error	Unit	Rel. Error / %	Remark
ϵ_a	1	negl.	—	< 1	definition
ϵ_w	78	negl.	—	< 1	from lit., 25°C
v_a	$3 \cdot 10^8$	$-0.03 \cdot 10^8$	m/s	-1.0	lin. regr.
v_w	$0.774 \cdot 10^8$	$\pm 0.02 \cdot 10^8$	m/s	± 3.0	lin. regr.
t_h	354	± 11	ps	± 3.0	lin. regr.
l'	60.4	± 0.6	cm	± 1.0	lin. regr.
C'_{RG213}	100	—	pF/m	—	cable spec.
L'_{RG213}	250	—	nH/m	—	cable spec.
$Z_0(\text{RG213})$	50	± 1.5	Ω	± 3.0	meas. w/ TDR
$\rho(\epsilon_a)$	0.55	± 0.01	—	± 2.0	scaling method
L'	575	± 23	nH/m	± 4.0	Eq. 2.33
C'_1	20.5	± 0.9	pF/m	± 4.5	Eq. 2.36
C'_2	356	± 30	pF/m	± 8.4	Eq. 2.37

Table 2.1.: Summary of parameters for the 3-rod-probe.

The determination of water content with TDR rod-probes is sensitive to a large number of possible errors in manufacturing, calibration, installation, and data analysis. Some of them can be avoided, others may be neglected, and a few of them have to be accepted. The effects of production tolerances of the rod coating and the influence of imperfect probe installation on the water content determination are of major concern. These variations would lead to a deviation of C'_1 (installation) and C'_2 (coating) from their nominal values, respectively. The question arises, whether the tolerances of the probe parameters are narrow enough to use the calibration results of one probe for all other probes of the same type.

The coating thickness d should be as uniform as possible along the whole length of the rod. The rods consist of a metal core with 6 mm diameter pushed into a PVC tube with

1 mm wall thickness. The procedure of heating the PVC tube and pressing the metal core into it leads to a deformation of the tube. This way of manufacturing leads to a 20% variation of coating thickness. The effect of this error has been simulated with a program to solve 2-D electrostatic problems (Maxwell 2D, Ansoft). The error increases for higher water contents. Other errors like variations in probe length or probe head properties may be neglected because they can be controlled very well. If all rods had the same shape, i.e. mean and variance of the coating were the same, the error could be avoided by using such rods for calibration and determination of the electrical probe parameters.

	Variation/%	5%vol	10%vol	15%vol	20%vol	25%vol	30%vol
d	20	0.05	0.29	0.67	1.20	1.88	2.68
a	8.3	0.49	0.68	0.84	0.98	1.09	1.16
ρ	1.8	0.35	0.53	0.72	0.92	1.14	1.35
v_w	3.0	0.12	0.29	0.51	0.81	1.17	1.59
t_h	3.0	0.06	0.08	0.10	0.12	0.14	0.16
l'	1.0	0.24	0.36	0.50	0.64	0.79	0.93
Z_0	3.0	0.36	0.55	0.75	0.97	1.19	1.41
$Z(\epsilon_a)$	4.1	0.49	0.75	1.02	1.31	1.61	1.92
L'	4.3	0.52	0.79	1.08	1.39	1.71	2.03
C_1'	4.5	0.44	0.61	0.76	0.89	1.00	1.07
C_2'	8.4	0.19	0.39	0.67	1.02	1.44	1.93

Table 2.2.: Absolute error in water content (%vol) at different moisture levels caused by errors from manufacturing (d), installation (a), or calibration (all others).

The probe installation may change its geometry. The nominal distance a of adjacent rods is $a = 3$ cm. If the rods hit an obstacle in the ground they will deviate from the parallel alignment. The longer the rods the more susceptible they are to such kind of error. The rigid steel core of 6 mm diameter prevents a large deviation. Nevertheless a maximum deflection of 10 mm between the outer rods' ends is deemed to be possible. This has nearly the same effect as an increase of the mean distance of 5 mm between the outer rods along their whole length.

The relative errors in the calibration process have been given in the previous section (Tab. 2.1). To investigate the effect of uncertainties ($\pm \Delta P$) of parameter P on the final result a particular water content θ is selected and transformed into relative dielectric permittivity ϵ using the standard calibration function of *Topp et al.* (1980). Then the effective capacitance C' is calculated using $C_1'(P \pm \Delta P)$ and $C_2'(P \pm \Delta P)$. Under the assumption that P is the true parameter value, the capacitance can be transferred to dielectric permittivity with $C_1'(P)$ and $C_2'(P)$, and further into water content using the inverse of the applied calibration functions. Finally the water content resulting

from inaccurately calibration parameters is to be compared to the given water content. Tab. 2.2 shows the absolute errors in water content resulting from the probe parameter variation.

2.5.2. Summary

A new coated 3-rod-probe has been designed and built for applications with Spatial TDR. Probe parameters important for calibration are: capacitance coefficients C'_1 and C'_2 in the probe capacitance model, rod inductance L', electrical rod length l', and pulse travel-time t_h in the probe head. These parameters have been determined by an experiment with a probe partially immersed in water. travel-time analysis and linear regression have led to robust parameter estimates. Additionally it was necessary to determine the reflection coefficient of the probe in air.

To ensure reliable water content measurements, the calibration procedure requires the same feeding cable length than the SUT. Mass production of probes without individual calibration requires precise control of the coating thickness d. Even small variations lead to large measurement errors especially at higher water contents. Another source of error is the installation of the probes into the soil, where stones and roots may bend the rods and change their distance a.

The new probe type has already been used successfully to monitor the temporal progression of infiltration fronts under laboratory conditions. The influence of the probe head on the measurements and the reconstructed water content profiles requires further investigations. Also the robustness for long-term field application still has to be proven and the variation of the rod coating has to be reduced.

2.6. Empirical Relationship between Capacitance and Effective Conductance

The reconstruction algorithm needs two independent TDR measurements to derive the two independent parameter profiles $C'(x)$ and $G'(x)$. According to *Schlaeger* (2002) there are several possibilities to combine two measurements. Most of the methods need a second connection to the probe. In case of the ribbon cable it is no problem to connect the sensor from both sides, but for common rod probes it is currently not feasible but the SMG is working on it (A. Scheuermann, personal note). Another approach to get a 'second measurement' is the evaluation of the TDR reflectogram during the second signal round-trip between T and $2T$, with T being the single round-trip time of the electromagnetic pulse forth and back the probe. The problem here is the low signal amplitude remaining after the first passage and the disturbance due to non-ideal wave splitting at the probe ends.

Up to now the only feasible solution for the application of rod probes with single side connection is the usage of an additional function describing the relationship between capacitance C' and conductance G'. This function is fed into the reconstruction algo-

rithm leaving C' the only unknown. In this way one measurement is enough to apply the reconstruction algorithm.

It is straight forward to assume a dependency of G' on C'. Both are governed by moisture content. Dry soil has little capacitance and no ionic conductance. Wet soil leads to higher capacitance and conductance. Ionic conductance is likely to appear only at moisture contents above a certain threshold leading to linked wet zones. At high moisture contents the conductance reaches its maximum: It saturates. A simple piecewise defined relationship describing G' as function of C' has been proposed by *Hakansson* (1997). It is an exponential saturation function with an onset different from zero:

$$G'(C') = \begin{cases} G'_{\text{sat}} \left(1 - e^{-(C'-C'_0)/C'_d}\right), & \text{if } C' \geq C'_0 \; ; \\ 0, & \text{if } 0 \leq C' < C_0 \; . \end{cases} \tag{2.68}$$

The experimental determination of C'-G'-pairs under different soil moisture conditions is based on the assumption that these parameters do not vary along the probe if the soil will be perfectly mixed, i.e. C' and G' are constant for a particular moisture.

The reconstruction algorithm is used to determine the values. First a constant effective conductance G' is guessed and fed into the program. The reconstruction is interrupted after the first iteration. The result of this first step is the constant capacitance profile C', which leads to the best approximation in the sense of the best similarity of measured and simulated TDR signal. A wrong guess for G' leads to a simulated TDR signal which differs from the measured TDR reflectogram in the slope of the plateau (s. Fig. 2.20). The simulation is repeated with different values for G' until no further improvement can be reached.

2.6.1. Experiment

A PVC box of $20 \, \text{cm} \times 20 \, \text{cm} \times 70 \, \text{cm}$ and wall thickness $8 \, mm$ is used to hold the 3-rod-probe so that its head is outside and the rods inside the cavity (s. Fig. 2.19). The middle rod runs along the box center so that the walls are approximately $10 \, \text{cm}$ away from it. A movable plate positioned near the rods' end forces the rods to be parallel to each other and the side walls.
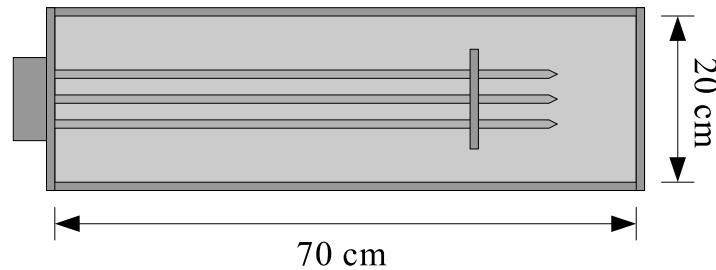
Figure 2.19.: Top view of the box holding the probe. Soil with homogenized water content is filled in the cavity (light gray).

The probe is connected to the TDR via the same electric path as the 3-rod-probes installed in the large lysimeter for infiltration experiments (s. Fig. 4.2). The path consisting of coaxial cables (RG213) and multiplexers (SNAPMUX) has a total length of approximately 14 m.

The soil is homogenized by means of a mobile cement mixer. Stones of several centimeters size are added during mixing to yield a better homogenization. The mixer pot is capped with a plastic foil to reduce dust emission.

The material is packed into the box in layers of a few centimeters thickness. Each layer is compacted by stomping with a heavy metal plate mounted to an iron rod. When the box is half filled, the probe is inserted from the side. In the same way the rest of the volume is filled. After this preparation a TDR sample is taken. The procedure is repeated several times with different water content.

2.6.2. Results

Fig. 2.20 shows the impact of the chosen conductance on the reconstructed (simulated) TDR signal after the first iteration of the algorithm. Two cases with different average soil moisture are shown. The upper curve bundle (1.1–1.4) is related to a drier condi-
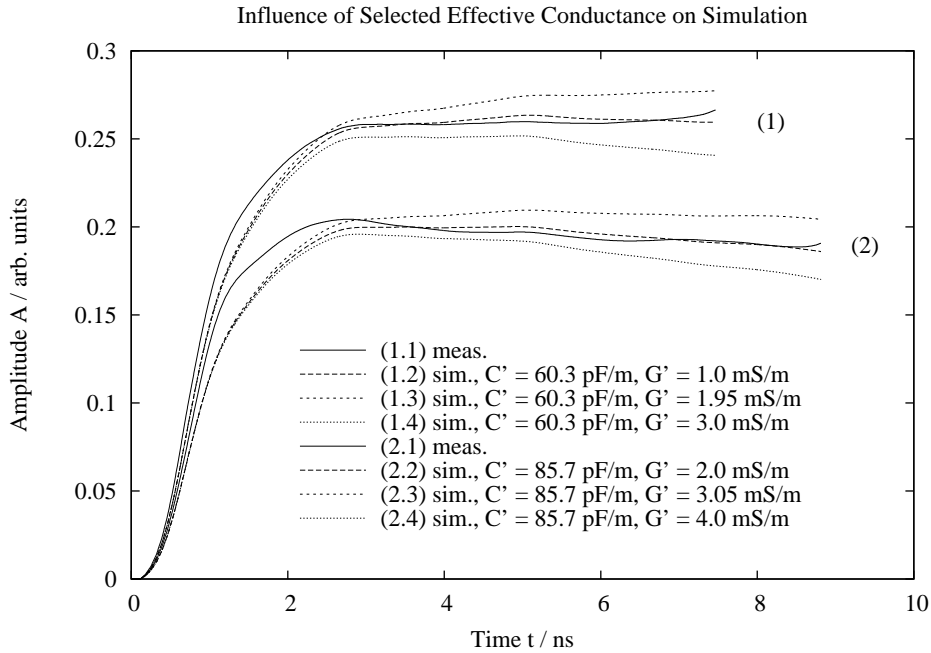
Figure 2.20.: Influence of the selected effective conductance G' on the TDR signal simulation for two different moisture states.

tion leading to a lower capacitance. The simulated TDR curves belonging to the same bundle differ in the chosen effective conductance G'. The value of G' leading to the best approximation to the measured TDR signal is taken. All acquired pairs of C' and G' for

different moisture conditions are displayed in Fig. 2.21. The derived model parameters are listed in Tab. 2.3.

Empirical Relationship between C' and G'
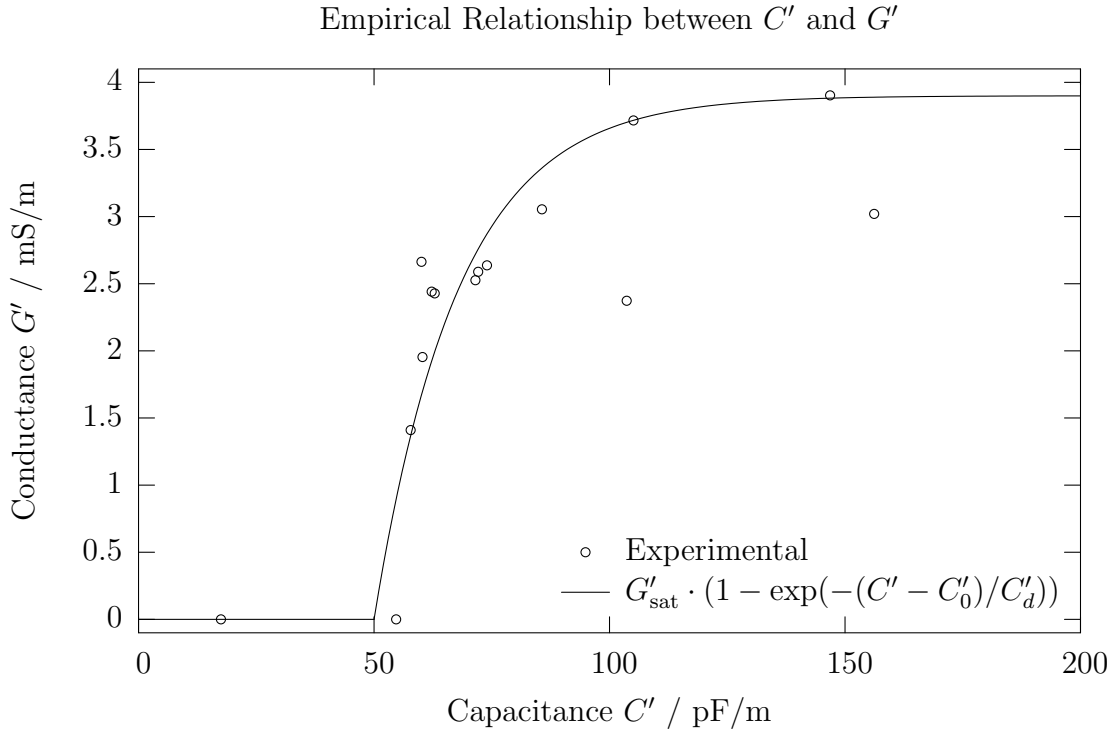
Figure 2.21.: Empirical relationship between capacitance C' and effective conductance G' for different moisture states.

Variable	Value	Unit
C_0'	50	pF/m
C_d'	18	pF/m
G_{sat}'	3.9	mS/m

Table 2.3.: Parameters for the C-G-model.

2.6.3. Discussion

Some difficulties occurred during the soil preparation. Under wet conditions somewhere above 20%vol the mixture showed liquid behavior under compaction. It was impossible to compact the jelly like matter.

Some outliers have been produced (Fig. 2.21), the cause of which is unclear. One possible reason among others could be that under certain moisture conditions fine sand and

small stones in the soil tend to build aggregates. When the material in a very dry dust-like condition was wetted a little bit, aggregates of small stones coated with very fine moist sand emerged from mixing in the cement mixer. Thus the water was not equally distributed but concentrated in these tiny clods. It is plausible that this configuration could lead to a reduced bulk conductance since the probability for large linked conducting structures is reduced. Nevertheless the piecewise defined saturation function proposed by *Hakansson* (1997) approximates the measurement sufficiently well.

Parameter uncertainties for the empirical relationship are hardly assessable. The applied model is plausible but not physically based. More experimental data would be needed to assess the quality of the particular parametric form. Since the rise of the function is very steep it could probably be reduced further by a simple threshold function (Heaviside function).

The disadvantage of the presented approach is the dependency of the C'-G'-relationship on probe and soil. Thus this kind of calibration should be done for each particular use case in order to yield the best results for soil moisture profile reconstruction. Nevertheless the presented empirical relationship is the best that is available up to now.

2.7. Electrical Characteristics of Selected Soil

The calibration function of *Topp et al.* (1980) is widely used to relate dielectric permittivity and volumetric water content (s. Eq. 2.7). The authors used four different soil types from which they derived the empirical relationship. The dielectric permittivity of the soil chosen for the following experiments was determined in laboratory for various water contents to check, if its behavior is conformal with the findings of *Topp et al.* (1980).

Therefore soil samples of the chosen silty sand (c.t. App. A.1) with different moisture content were prepared. The relative dielectric permittivity ϵ of each soil sample was derived by TDR with a well-calibrated uncoated short rod probe and the basic TDR rule which has been already used several times:

$$v = \frac{2l}{t} = \frac{c_0}{\sqrt{\epsilon}} \Rightarrow \epsilon = \left(\frac{c_0 t}{2l}\right)^2 , \tag{2.69}$$

where v is the pulse propagation velocity along a probe of length l and c_0 speed of light. Volumetric water content was determined by the oven drying method. With this method a wet soil sample of known volume V_T is weighted yielding its total mass m_T. Then the soil is dried in an oven at $105°C$ and weighted again. The remaining mass of the dry soil is denoted by m_S. The mass loss $m_W = m_T - m_S$ is that of evaporated water. The gravimetric water content is defined as:

$$w = \frac{m_W}{m_S} . \tag{2.70}$$

In case of non-swelling and non-shrinking soil the total sample volume V_T remains constant after drying and is thus equal to the volume V_S of dry soil: $V_T = V_S$. The bulk

density of the dry material reads:

$$\rho_\mathrm{T} = \frac{m_\mathrm{S}}{V_\mathrm{T}} \Leftrightarrow V_\mathrm{T} = \frac{m_\mathrm{S}}{\rho_\mathrm{T}} \ . \tag{2.71}$$

The volumetric water content θ is the ratio of water volume V_W to the total soil volume. For bulk density ρ_T of dry material and density ρ_W (≈ 1000 kg/m^3) of water are known, θ can now be related to gravimetric water content w:

$$\theta = \frac{V_\mathrm{W}}{V_\mathrm{T}} = \frac{m_\mathrm{W}}{\rho_\mathrm{W}} \cdot \frac{\rho_\mathrm{T}}{m_\mathrm{S}} = w \cdot \frac{\rho_\mathrm{T}}{\rho_\mathrm{W}} \ . \tag{2.72}$$

With the oven drying method a soil sample of volume V_T is taken and the mass m_W of the evaporated water is measured. Thus a simpler form of the above equation more appropriate to this method is:

$$\theta = \frac{V_\mathrm{W}}{V_\mathrm{T}} = \frac{m_\mathrm{W}}{\rho_\mathrm{W}}/V_\mathrm{T} \tag{2.73}$$

For each particular moisture state one TDR measurement with a short probe ($l \approx 10$ cm) was conducted to derive the relative dielectric permittivity ϵ. Four soil samples were taken, their volumetric water content was determined and averaged ($\overline{\theta}$). Additionally the electric conductance σ was measured with a common conductivity meter. Table 2.4 shows the result. S and ρ are relative water saturation and bulk density, respectively. Soil moisture averages and their related dielectric permittivities are displayed in Fig. 2.22

$\overline{\theta}$ / %vol	ϵ / 1	σ / mS/m	S %	ρ / g/cm^3
0	2.9	0	0	—
1.96	3.1	0.7	5.5	1.71
9.47	5.4	14.0	25.2	1.65
18	8.9	27.8	54.2	1.77
26.7	14.4	43.4	74.1	1.73
31.9	17.4	45.0	93.7	1.75

Table 2.4.: Electrical characteristics of the silty sand.

together with the model of *Topp et al.* (1980). Additionally a simple exponential curve was fitted:

$$\theta = -41.1\% + 30.1\% \cdot \epsilon^{0.31} \ . \tag{2.74}$$

For a relative permittivity of $\epsilon = 9$ ($\theta \approx 17$ %vol) both curves deviate by 1.5 %vol. Larger differences are found on the dry branch but they are not relevant because 1. a volumetric water content below 5 %vol is seldom reached in field applications and 2. a difference between 0 %vol and 3 %vol is of no concern anyway for most practical applications. Thus the experimental results are in good accordance with *Topp et al.* (1980). The relationship between volumetric water content and electric conductance is displayed in Fig. 2.23.

Dielectric Permittivity and Volumetric Water Content of Soil
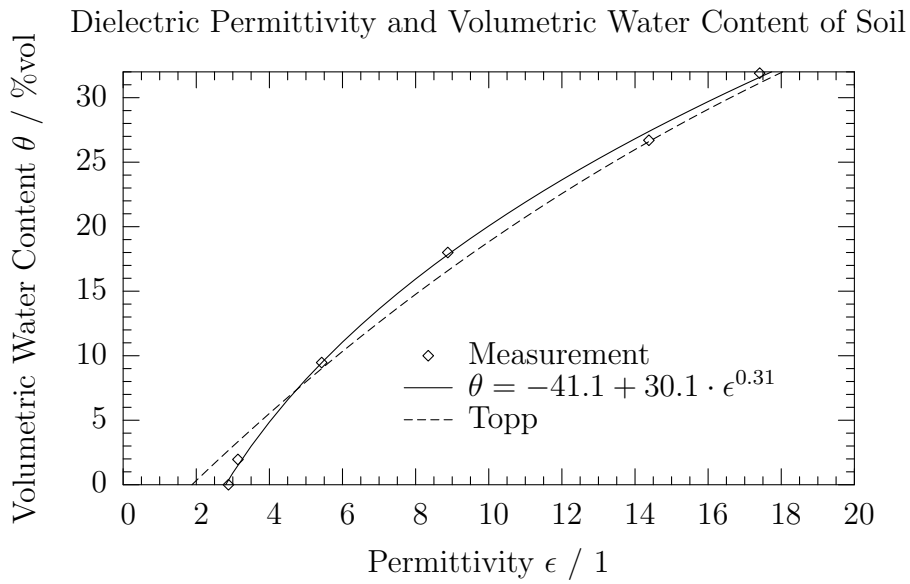
Figure 2.22.: Empirical relationship between volumetric soil water content θ and relative dielectric permittivity ϵ of soil. A power law (Eq. 2.74) fits the data well. The commonly used calibration function of *Topp et al.* (1980) is given for comparison (s. Eq. 2.7).

Electric Conductance and Volumetric Water Content of Soil
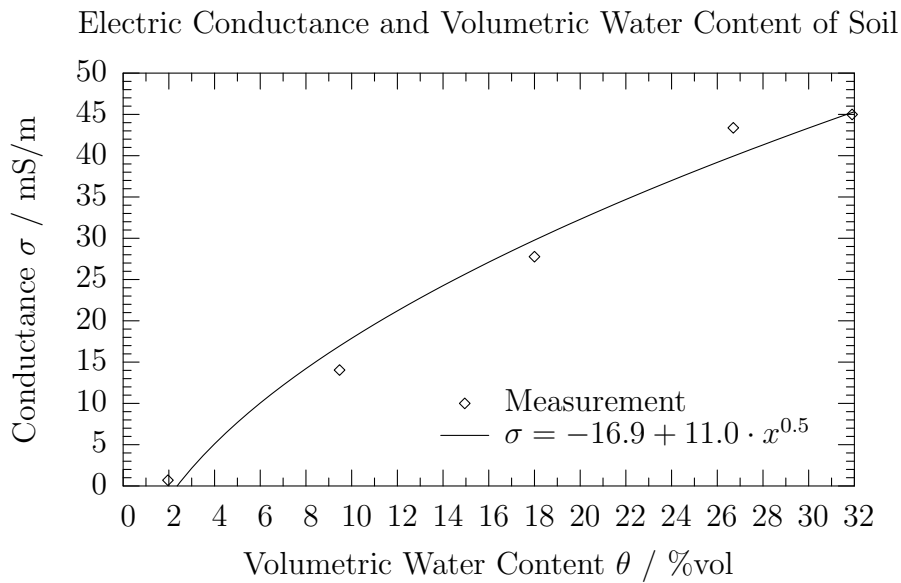
Figure 2.23.: Empirical relationship between volumetric soil water content θ and ionic conductance σ of soil.

3. OBSERVER: A Novel TDR Instrument Based on Delta Modulation

3.1. Motivation

Due to the lack of robust sampling TDR instruments, cost-effective in high volume applications like flood warning or other monitoring systems and especially designed for moisture profile reconstruction, it was one major goal of this thesis to explore new ways of building an innovative TDR instrument based on the vast achievements in high speed digital electronics of the recent years. The outcome of this investigation is a new TDR called *OBSERVER* (Fig. 3.1). This acronym stands for *One Bit Sampling Electromagnetic Reflectometer for Vadose Zone Evolution Recording*. This working prototype of a novel TDR instrument is completely different from common TDR technology. It is built upon one of a last generations of fast digital circuits in combination with the well-known principle of delta modulation, which has not been applied to TDR, yet.

The market of high speed electronics is driven by the need for ever higher bandwidth in digital networks, which leads to rapid progress in this segment. An example of this impressive development is the history of Motorola's ECL product line (*ON Semiconductor*, 1988). ECL stands for *Emitter Coupled Logic*, the fastest logic family up to now, much faster than CMOS or Schottky TTL. *MECL I* was the first of Motorola's ECL families.[1] It was introduced in 1962 and offered toggle rates[2] of 30 MHz and 8 ns propagation delay.[3] In those days the performance was far beyond the state-of-the-art. It took years for other logic families to reach this performance.

Another remarkable family was *MECL III* of 1968 with a 500 MHz flip-flop toggle rate and 1 ns signal rise-time. Because of the fast edge speeds, transmission line design and multi-layer printed circuit boards were recommended above 200 MHz. Nowadays these unavoidable requirements are matter-of-course and fulfilled in every high-speed design but in those years they caused problems and thus found little acceptance.

To satisfy the need for a logic family with less strong requirements the 10K series was introduced in 1971. The circuits had a typical propagation delay of 2 ns and were slew rate limited to 3.5 ns, which made them relatively easy to use. The technological progress

---

[1]Other companies have been producing ECL circuits, too. Motorola was just chosen as an example because of the easily available product descriptions.

[2]Rate of possible consecutive switching between two (digital) states.

[3]Delay between input signal and output response.

led to the famous supercomputer CRAY-1, which was installed first at Los Alamos National Laboratory in 1976. Seymour Cray, the designer of this system, decided to use low-density/high-speed ECL circuits to reach a new world-record in speed: 160 million 16-bit fixed-point arithmetic operations per second! The *star network processor* of this computer was assembled from more than 3000 ECL 10K/100K circuits. These power consuming densely packed parts required liquid freon cooling.

But then the Internet revolution has started and led to an increasing demand for even higher performances. During the last decade of the last century *ECLinPS* was brought to market by ON Semiconductor, the spin-off of the Motorola semiconductor branch. Members of this family can work at frequencies above 4 GHz, offer pulse rise-times less than 200 ps, and provide a propagation delay below 330 ps.

Figure 3.1.: OBSERVER V2, second prototype for a new Time-Domain-Reflectometer based on Delta Modulation and Direct Digital Synthesis.

ON's newest achievement is called *GigaComm.* This latest ECL family operates at bandwidths far beyond 10 GHz. It is especially suited for Gigabit Ethernet, and optical network equipment with data rates greater than 10 Gbit/s.

The other important driving force for the development of highly sophisticated electronic components is the telecommunication market with its ever rising demand on speed and integration needed for small devices accompanied by little power consumption. The *Direct Digital Synthesizer* (DDS) important for the signal generation in the OBSERVER is an offspring of this evolution. During the last two years incredible improvements have been made concerning the signal quality of DDS.[4] This purely digital solution for tunable

---

[4]Compare for example spurious free dynamic range (SFDR) and phase stability of the DDS parts AD9832 and AD9954 (*Analog Devices*, 2004).

signal generation has become an interesting alternative to analog counter-parts like phase locked loops (PLL).

What can be expected in near future? At the end of 2001 Hitachi presented a new transistor prototype[5] with a cutoff frequency of 124 GHz.[6] An ECL circuit based on these transistors obtained a propagation delay of 5.7 ps! So at least one or two orders of magnitude in circuit speed-up with respect to todays common technology is to be expected.

The technological progress in nowadays electronics is opening new applications in high frequency sampling which had been impossible a few years ago. The OBSERVER is a consequent application of these new achievements in combination with traditional sampling principles known for many years. *Monett* (2004) suggested to combine delta modulation with equivalent-time sampling which he refers to as *Binary Sampler*. He recommended to realize the sampler in ECL, for the sake of speed and simple design. Because of the exigence for improved and inexpensive moisture measuring instruments for hydrological research it was decided to use this sampling technology to build a novel TDR instrument. Design improvements finally leading to the OBSERVER were made in cooperation with ADD Automation (*Monett*, 2004).

Within the scope of this thesis demand and specification for the novel TDR instrument have been formulated and two prototypes realized (OBSERVER V1 and V2). Therefore the design of the sampler was improved, a local storage integrated, a parallel port interface realized, and the control software developed.

3.2. Introduction to Digitization

To better understand the principles and dynamic behavior of OBSERVER it is necessary to introduce some basics about digital signal processing. A TDR essentially consists of an excitation pulse generator and a sampler, which is recording the overlay of emitted and reflected signal. Often the only possible way to store and analyze a signal is to translate it into a sequence of numbers which can be processed with a computer. This procedure is called *digitization*. The two pillars of digitization are *sampling* and *quantization* (*Pohlmann*, 2000). Sampling is the discretization of the domain of a signal, e.g. time or space whereas quantization denotes the process of mapping an analog signal range to a set of discrete values (Fig. 3.2). It is also referred to as analog-to-digital conversion (ADC). In TDR application signal domain is time and co-domain or range is voltage.

Quantization and sampling in real applications are often far from ideal. Distortion or errors limit the performance of an instrument, an important issue for the OBSERVER, too. It is necessary to understand the principles and challenges of digitization not only to conceive the sampler but also to figure out, how Direct Digital Synthesis (DDS) works, which is an essential building block for the OBSERVER. It will be explained later how DDS is linked to sampling.

---

[5]SiGeC Heterojunction Bipolar Transistor (HBT)

[6]The highest frequency a transistor can amplify current.
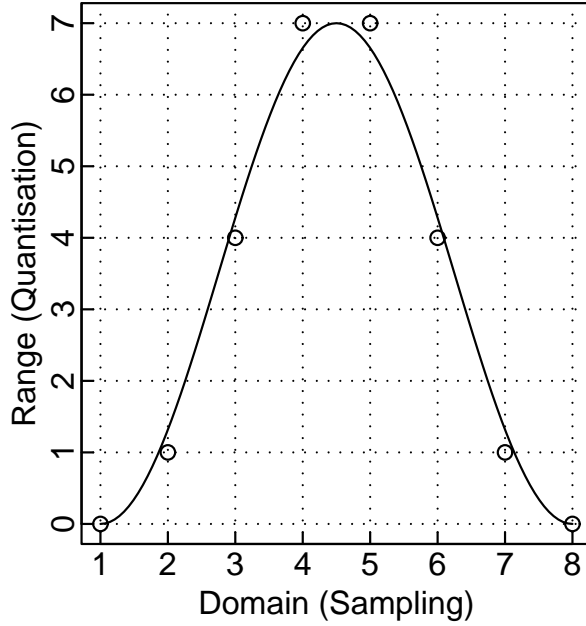
Figure 3.2.: Digitization is sampling and quantization. Only the discrete points of the grid line crossing are available to form a digital representation (points) of the analog signal (line). In the domain 8 samples are taken and the signal is quantized with 3-bit resolution, i.e. with maximum $2^3 = 8$ different quantization levels.

To understand the effects of digitization the spectrum of the signal must be investigated. Each well-behaving time dependent signal $g(t)$ can be composed by superposition of a sometimes infinite number of fundamental functions. A common set of base functions are trigonometric functions like sinusoids, each of which with three parameters: amplitude, frequency, and phase. A more convenient representation of these base functions especially for calculation are the complex functions called phasors:

$$G'(\omega, t) = G(\omega)e^{i\omega t} \ , \ \text{with} \ \omega = 2\pi f \ , \tag{3.1}$$

with complex amplitude $G(\omega)$. Frequency dependent phase $\phi(\omega)$ and real amplitude $A(\omega)$ are implied by $G(\omega)$, which becomes obvious from the Euler-representation of this complex number:

$$G(\omega) = |G(\omega)|e^{i\phi(\omega)} \ , \ \text{with} \ |G(\omega)| = A(\omega) \ . \tag{3.2}$$

Thus

$$G'(\omega, t) = A(\omega) \ e^{i(\omega t + \phi)} \ . \tag{3.3}$$

$G(\omega)$ is referred to as the *complex spectrum* of signal $g(t)$. It can be determined by *Fourier-Transformation*. The Fourier transform of a function $g(t)$ is defined as

$$G(\omega) = \mathcal{F}\{g\}(\omega) = \int_{-\infty}^{+\infty} g(t)e^{-i\omega t}dt \ , \tag{3.4}$$

with its inverse transform

$$g(t) = \mathcal{F}^{-1}\{G\}(t) = \frac{1}{2\pi} \int\limits_{-\infty}^{+\infty} G(\omega)e^{i\omega t}d\omega = \frac{1}{2\pi} \int\limits_{-\infty}^{+\infty} G'(\omega, t)d\omega \; . \tag{3.5}$$

The last equation shows that $g(t)$ is indeed a superposition of functions $G'(\omega, t)$. The factor $1/(2\pi)$ is an integration constant to guarantee that $\mathcal{F}^{-1}\mathcal{F} = 1$. It is arbitrary in which transform (direct, inverse, or distributed in both) it occurs. Transformation and inverse transformation are very similar and have similar transformation properties.

In many applications not the complex spectrum is given but the real valued power spectrum P or power spectral density, i.e.

$$P(\omega) = G^*(\omega)G(\omega) = |G(\omega)|^2 \; , \tag{3.6}$$

with G^* the complex conjugate of G. It can be shown that $P(\omega)$ is the Fourier transform of the autocorrelation function of g. The power spectrum reveals an even symmetry, i.e. $P(\omega) = P(-\omega)$, because the autocorrelation is symmetric and the Fourier transform conserves symmetry.

One of the most important properties of Fourier transformation often applied in theory of signals and systems is that it transfers convolution into multiplication and vice versa. It is expressed by the convolution theorem:

$$\mathcal{F}\{g * h\} \;=\; \mathcal{F}\{g\} \cdot \mathcal{F}\{h\} \; , \tag{3.7}$$
$$\mathcal{F}\{g \cdot h\} \;=\; \mathcal{F}\{g\} * \mathcal{F}\{h\} \; . \tag{3.8}$$

Numerically the Fourier Transform is computed by means of Fast-Fourier-Transform (FFT) algorithms. Since a sampled signal is a discrete, finite sequence of numbers the calculation principle is also referred to as Discrete Fourier Transform (DFT). One property of DFT is that if a signal is sampled at n_t equidistant times the spectrum will be represented at n_t equidistant frequencies.

3.2.1. Sampling and Aliasing

A sample is a simplified representation of the signal, a code, from which the true signal can be reconstructed. An important property of a sampled signal is that it reveals a periodic spectrum the form of which is dependent on the way of sampling. The temporal distance between two samples is called sampling period T_s. Its reciprocal, the sampling frequency $f_s = 1/T_s$, tells how many samples are taken per unit time. It is assumed for now that the signal amplitude is represented correctly so that the effects of quantization errors may be neglected.

In many cases the signal amplitude at a certain instant has to be stored before it can be quantized. Sample & Hold (S&H) circuits are analog storage elements especially designed for this purpose (Fig. 3.2.1). A S&H can be thought of consisting of a capacitor C building a storage for analog voltages connected to the input voltage by means of a
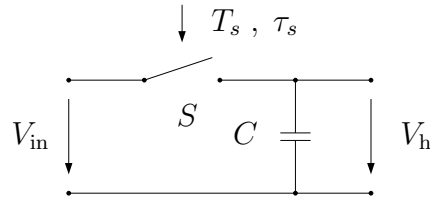
Figure 3.3.: Principle of Sample & Hold. V_{in}: input voltage; V_{h}: hold voltage; C: capacitor, storage element; S: switch with sampling (switching) period T_s and sample time τ_s, which is the time the switch is closed for sampling.

switch S. Every T_s seconds the switch is closed for a short duration τ_s. During this time the input voltage charges the capacitor.

Generally the input signal g is changing during time τ_s. This leads to an averaging of the signal around the sampling instant t_n. The averaged signal g_1 for sampling time t_n yields

$$g_1(t_n) = \int_{t_n-\tau_s/2}^{t_n+\tau_s/2} g(t)dt = \int_{-\infty}^{+\infty} g(t)\text{rect}_{\tau_s}(t-t_n)dt = g * \text{rect}_{\tau_s}(t_n) \, , \qquad (3.9)$$

with the rectangular function being defined as

$$\text{rect}_{\tau_s}(t) = \begin{cases} 1 & : \quad -\tau/2 \le t \le \tau/2 \, , \\ 0 & : \quad \text{elsewhere} \, . \end{cases} \qquad (3.10)$$

According to Eq. 3.9 the effect of S&H can be expressed by a convolution. In reality S&H does not perform ideal switching. The real behavior can be better described by a more general impulse response function h:

$$g_1(t) = g * h(t) \qquad (3.11)$$

This equation describes the filtering of g due to finite sampling time τ_s. It does not consider the discrete distribution of samples in time yet. This discretization has a fundamental impact on the spectrum. The signal representation at discrete times can be expressed conveniently by multiplication with a delta comb (*Bracewell* (2000); *Jähne* (2002)):

$$g_2(t) = g_1(t) \sum_n \delta(t - nT_s) \, . \qquad (3.12)$$

The signal g_2 is identical to zero almost everywhere except for discrete times t_n, which fulfill the condition

$$t_n = nT_s \, . \qquad (3.13)$$

The convolution theorem (Eq. 3.8) states that a multiplication of two functions becomes a convolution in the frequency domain. Therefore the Fourier transform of g_2 (Eq. 3.12) yields

$$
\begin{aligned}
G_2(\omega) &= \mathcal{F}\{g_1\} * \mathcal{F}\left\{\sum_n \delta(t - nT_s)\right\} \\
&= G_1(\omega) * \sum_n \delta(\omega - n\omega_s) = \sum_n G_1(\omega - n\omega_s) \,.
\end{aligned}
\tag{3.14}
$$

The new spectrum G_2 is an infinite repetition of the spectrum G_1 with period

$$
\omega_s = 2\pi f_s = 2\pi/T_s \,.
\tag{3.15}
$$

The delta comb has the property that its Fourier transform is a delta comb, too, a rule which was applied in Eq. 3.14. An elegant proof easy to understand of this non-trivial transform is given by *Bracewell* (2000), pp. 246.
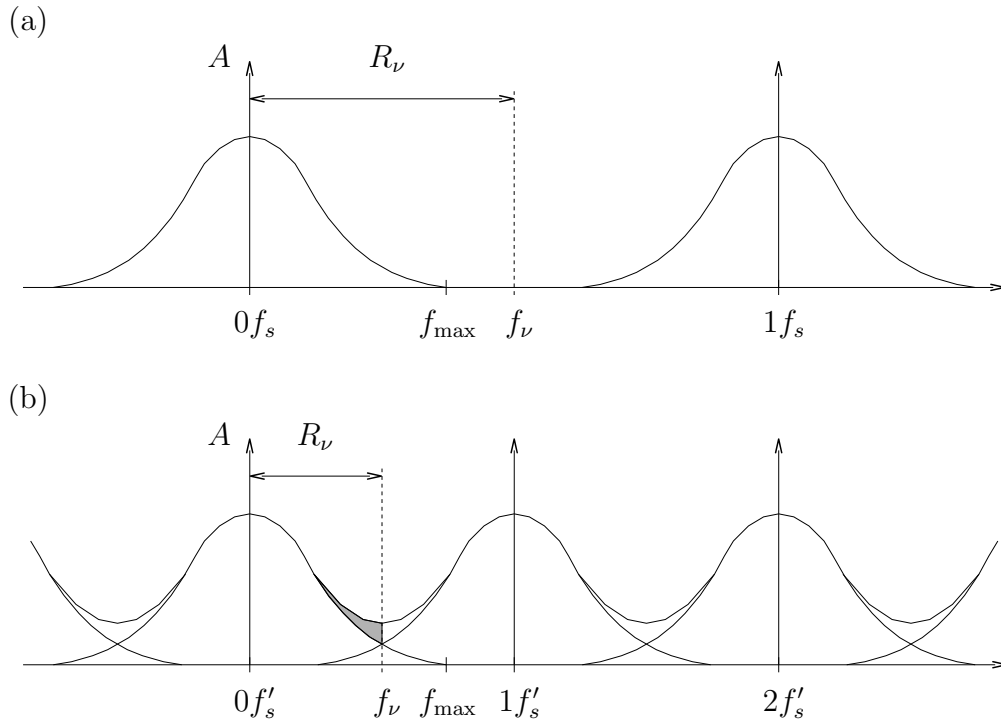
Figure 3.4.: Periodic spectrum for different sampling frequencies. f_s, f_s': sampling frequencies; $f_{\max}$: bandwidth of the signal; f_ν: Nyquist frequency; R_ν: Nyquist range; gray area: aliased frequency components; (a): Nyquist condition fulfilled: single spectra clearly separated; (b): Nyquist condition violated: spectra overlapping.

Depending on the bandwidth of the signal and the sampling frequency the single spectra map overlap. The sampling theorem by Nyquist or Shannon states that if the spectra

do not overlap (Fig. 3.4, a) the complete signal can be reconstructed correctly from its sample without distortion. Therefore the signal must first be band-limited, i.e. its spectrum must have a maximum frequency $f_{\max}$ beyond which the amplitude is zero. Second, the sampling frequency f_s must be at least twice as high as the maximum frequency. The relation

$$f_\nu = 1/2 f_s > f_{\max} \tag{3.16}$$

is called Nyquist condition and f_ν Nyquist-frequency. The Nyquist-range R_ν denotes the frequency interval $[0 \ldots f_\nu]$. If the signal spectrum is not covered completely by the Nyquist-range, the signal has to be low-pass filtered so that the spectral components vanish beyond the Nyquist-frequency. Of course, this leads to another signal deformation. Since sharp edges in the signal require high frequency components these edges are smoothed due to the low-pass filtering.

If the Nyquist-condition is violated (s. Fig. 3.4, b), so-called aliasing occurs: frequency components larger than the Nyquist-frequency are folded into the Nyquist-range (*Analog Devices*, 1999b).

This effect is due to the periodicity and symmetry of the spectrum. Aliased images of spectral components folded into the Nyquist band cannot be distinguished from the true components and thus they cannot be filtered. The spectrum is spoiled making a correct reconstruction of the original signal impossible. Aliasing has to be avoided. The sampling frequency must fit the particular signal and appropriate filtering must be applied before sampling.

3.2.2. Quantization Error and Spurs

Not only aliasing is a source of signal distortion but also amplitude quantization. This kind of distortion is deemed to be the major limitation for DDS performance in the OBSERVER. The quantization leads to a coarse staircase approximation of the actual signal. Fig. 3.6 shows different examples for digitizing a sine-wave

$$A(t) = A_0 \cdot \sin(2\pi f_0 t) \text{ , with } A_0 = 1, f_0 = 1 \text{ MHz} . \tag{3.17}$$

Quantization error is the difference between the nominal signal amplitude and the generally imprecise digital value at a sampling instant (e.g. Fig. 3.6, 2a).

The ideal spectrum of a pure sine-wave consists of a single spectral line but the sharp edges of the staircase imply high frequency components which appear as discrete *spurs* (spectral lines) besides the fundamental f_0 in the spectrum. Often these spurs are harmonics of the fundamental, i.e. occur at $2 f_0$, $3 f_0$, ... in the spectrum. Spurs beyond the Nyquist-frequency are aliased within the Nyquist-range. These isolated but often grouped spectral lines are difficult to handle. Throughout this section only spurs due to quantization are discussed. It must be emphasized that other error sources like phase truncation in DDS and nonlinearities in amplitude quantization may also produce spurs.

The overall strength of quantization distortion can be expressed by the *signal-to-noise ratio* (SNR). The term *signal-power-to-quantization-noise-power ratio* (SQR or SQNR)
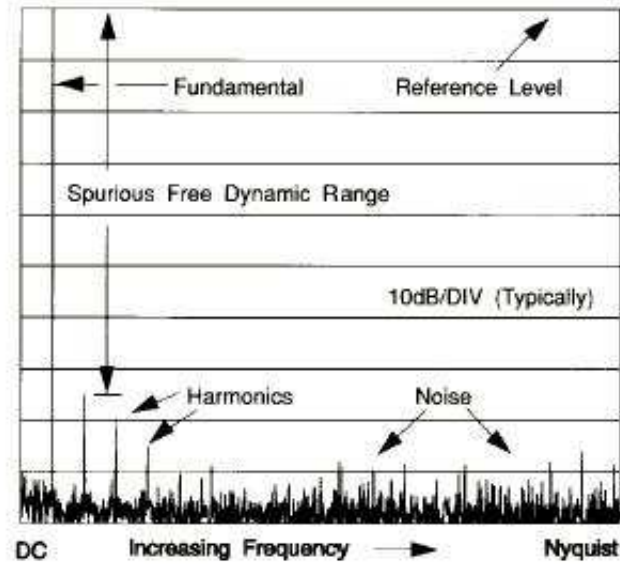
Figure 3.5.: Parameters of a spectrum (from *Analog Devices* (1999b)).

expresses more precisely what this value actually means, but the notation SNR will be used throughout the text anyway, because it is more common. If the full scale amplitude range of the signal is quantized with n_b bit resolution (2^{n_b} different amplitude levels), The SNR yields

$$\mathrm{SNR(dB)} = 1.76 + 6.02\, n_b \ , \tag{3.18}$$

the *6 dB per bit rule.* The derivation of this equation (*Pohlmann*, 2000) implies a uniform distribution of the input signal's amplitude between two adjacent quantization and that the total quantization range is fully exploited. The constant term in Eq. 3.18 is the contribution of the periodic sine-wave used to derive the formula. Other periodic test signals yield different values. Thus the actual quantization noise may be correlated with the input signal.

Strictly speaking an analytically derived SNR is valid only for its particular class of test functions like for example sinusoids or random functions with Gaussian amplitude distribution. Of course, the higher the resolution n_b, the lower the quantization noise, the larger the signal power with respect to the noise power (SNR). It should be emphasized that this general equation only specifies the total noise power due to quantization errors and does not provide any information about distribution and amplitude of the spurs.

Given a fixed amplitude resolution the total quantization noise power is constant. The broader the Nyquist range the more widely the noise is distributed and the lower the noise amplitude, since the product of spectral width and noise amplitude is constant (*Analog Devices* (1999b), p. 18). The SNR can be improved by oversampling. To sample a sine of frequency f_0 without aliasing a minimum sample frequency $2\, f_0$ is necessary. A higher sampling rate leads to a broadening of the Nyquist range, in other words: the higher

the sampling rate, the less the root-mean-square (rms) of the error amplitudes. The reduction of the noise level (increase of SNR) by oversampling is expressed by the term

$$C_{\mathrm{os}}(\mathrm{dB}) = 10 \log_{10} \left(f_s / (2 f_0) \right) , \tag{3.19}$$

with a sampling frequency $f_s > 2\,f_0$. If the signal under test is periodic the effect of oversampling may be enhanced by sampling many signal periods. With n_p the number of periods taken into account it yields

$$C'_{\mathrm{os}}(\mathrm{dB}) = 10 \log_{10} \left(n_p \cdot f_s / (2 f_0) \right) . \tag{3.20}$$

The product $n_t = n_p \cdot f_s$ is the total number of samples, which determines the lowering of the noise floor (*Maxim*, 2001). The final expression of SNR considering oversampling and sampling over multiple periods is

$$\mathrm{SNR}(\mathrm{dB}) = 1.76 + 6.02\,n_b + 10 \log_{10} \left(n_p \cdot f_s / (2 f_0) \right) . \tag{3.21}$$

This simple equation allows to calculate the SNR by means of known parameters but it not valid for all cases. The delta modulator used in the OBSERVER is a closed loop device the quantization noise of which is much more difficult to describe.

SNR is a fuzzy performance measure since it is the ratio between usable signal power and unwanted bulk noise power. In many practical applications it is not necessary to determine the SNR precisely. It can rather be seen as a rough estimate of what is actually going on in the technical system.

But some applications like the signal generation by DDS in the OBSERVER require more precise information about the strength of spurs. The ratio of power stored in the spurs to the power of the fundamental defines the *total harmonic distortion* (THD). If n_h spurs with amplitude $A_{\mathrm{H},i}$ are within the Nyquist range, the THD in dB is:

$$\mathrm{THD}(\mathrm{dB}) = 10 \log_{10} \left(\sum_{i=1}^{n_h} A_{\mathrm{H},i}^2 \Big/ A_0^2 \right) = 20 \log_{10} \left(\sqrt{\sum_{i=1}^{n_h} A_{\mathrm{H},i}^2} \Big/ A_0 \right) . \tag{3.22}$$

Another very useful dynamic performance parameter is the *spurious-free-dynamic-range* (SFDR). It is similar to THD but takes into account only the power stored in the maximum spur. If A_{Hmax} is the maximum spur amplitude the SFDR yields:

$$\mathrm{SFDR}(\mathrm{dB}) = 10 \log_{10} \left(\frac{A_{\mathrm{Hmax}}^2}{A_0^2} \right) = 20 \log_{10} \left(\frac{A_{\mathrm{Hmax}}}{A_0} \right) \tag{3.23}$$

It gives quantitative information about the largest amplitude of all unwanted signal components. The SFDR in sampling follows a 6dB-per-bit-rule fairly well (*Analog Devices*, 1999b) and at least the lower bound of the actual SFDR is sufficiently predictable:

$$\mathrm{SFDR}(\mathrm{dB}) \approx 6.02\,n_b . \tag{3.24}$$

It will be shown later why it is important to reach a SFDR as large as possible for the DDS in the OBSERVER signal generators. The examples given in Fig. 3.6 demonstrate how the SFDR can be reduced in sampling the sine-wave of Eq. 3.17. The different actions step-by-step:

Fig. 3.6, 1a: The signal with fundamental frequency $f_0 = 1$ MHz is sampled with $n_s = 7$ samples per signal period which in this case means a sampling frequency of $f_s = 7$ MHz. The amplitude resolution is $n_b = 3$ bit, leading to 8 (2^{n_b}) possible quantization levels (not all of them are populated in this example).

Fig. 3.6, 1b: The spectrum of 1a. The frequency range displayed is $0 \ldots f_s$ with Nyquist-frequency $f_\nu = f_s/2 = 3.5$ Mhz. The spectrum is symmetric about f_ν. Samples were taken over $n_p = 1000$ periods leading to a total of $n_t = n_s \cdot n_p = 7000$ points entering the DFT. The oversampling rate is $f_s/(2f_0) = 3.5$ (Eq. 3.21). The fundamental $f_0 = 1$ MHz has the maximum amplitude (0 dB). Major harmonic spurs within the Nyquist range occur at $2f_0$ and $3f_0$. SNR and SFDR have been predicted with Eqs. 3.21 and 3.24, respectively. The actual SNR calculated from the spectrum is given in brackets. The amplitude of the largest spur (at $2f_0$) is shortly below the predicted SFDR of approx. 20 dB. The largest spurious component is 20 dB (factor 10) smaller than the fundamental.

Fig. 3.6, 2a: The quantization resolution is the same but the sine is sampled with $n_s = 20$ samples per period. With the larger number of samples the quantization errors emerge more clearly.

Fig. 3.6, 2b: Spectrum of 2a with $n_p = 350$ periods. Thus the total number of samples entering the DFT is the same as in case 1b ($n_t = 7000$). Neither SNR nor SFDR have become larger in relation to case 1b. It is important to recognize, that the distribution of spurs has changed. The spur at $2f_0$ has vanished completely and the major spurs within the Nyquist range ($f_\nu = 10f_0 = 10\,\text{MHz}$) are at 3, 5, 7, and $9f_0$.

Fig. 3.6, 2c: Spectrum of 2a with $n_p = 1400$ periods. The total number n_t of samples is 4 times larger than in 2b ($n_t = 28000$). As expected from Eq. 3.21 the rms noise floor is lowered by 6 dB, but the SFDR has not changed.

Fig. 3.6, 3a: The signal is sampled with $n_s = 20$ samples per period and the quantization resolution is increased to 10 bits leading to 1024 possible amplitude levels. The quantization errors are no longer resolvable.

Fig. 3.6, 3b: Spectrum of 3a with the same number of total samples as in 2c. The SFDR is vastly increased by another 42 dB which is the effect of 7 bits more in the amplitude resolution (Eq. 3.24).

To summarize the observations: It is shown from the above examples that a poor SFDR due to low amplitude quantization resolution cannot be compensated by higher sampling rates or extended sampling over many signal periods. The only effect of these actions is a modification of the spur pattern. To reduce SFDR the only way is to increase the number of bits in the amplitude resolution. Since the power of the spurs is a part of the noise, THD and SNR would be reduced at the same time, too.
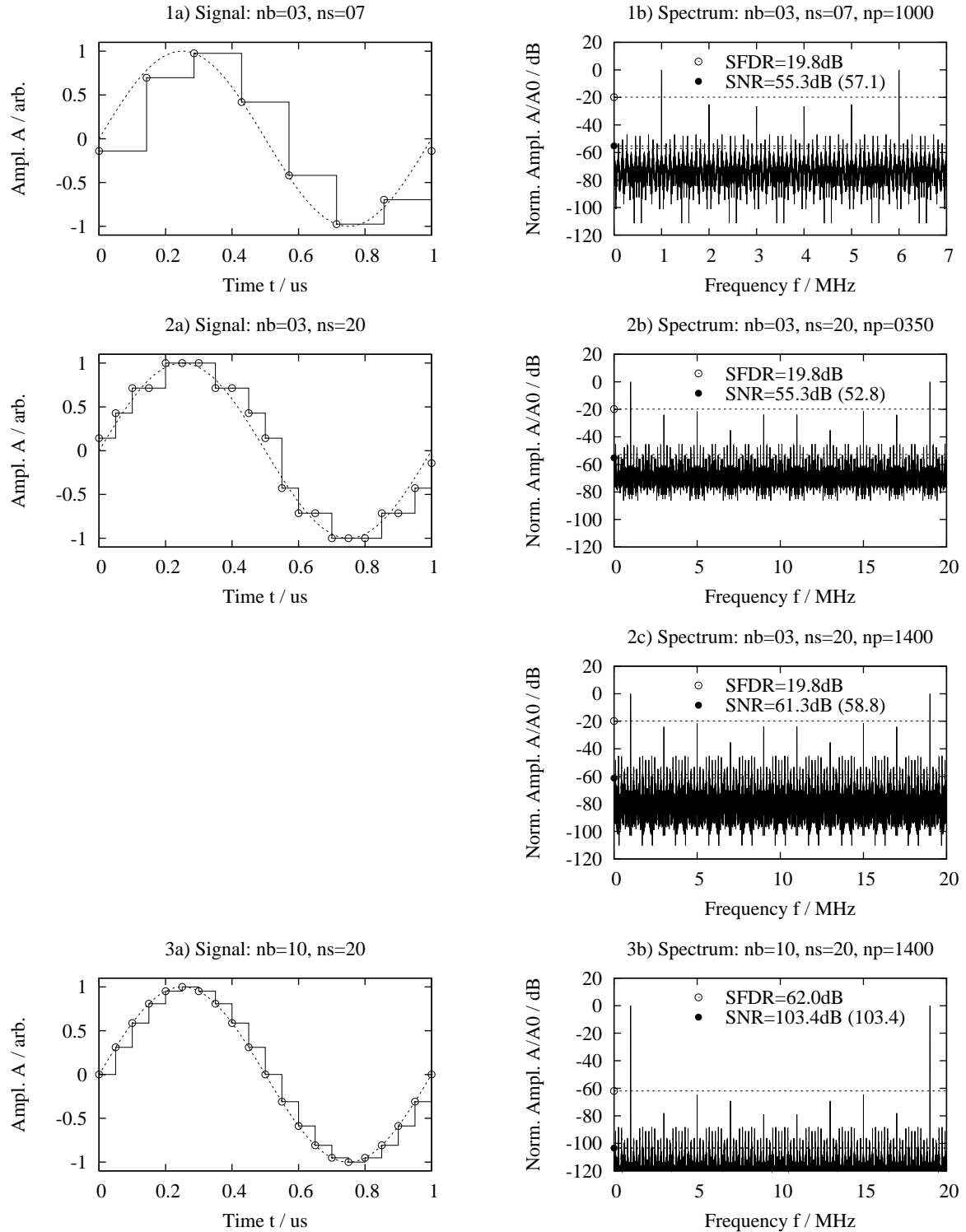
Figure 3.6.: Different quantizations of a sine-wave with 1 MHz fundamental frequency and the corresponding spectra from Discrete Fourier Transform (DFT). nb: number of bits for amplitude quantization. ns: number of samples per period. np: number of periods entering the DFT. SNR: predicted signal-to-noise ratio, actual value in brackets. SFDR: predicted spurious-free dynamic range.

3.2.3. Aperture Jitter and Phase Noise

Every sample has an uncertainty in timing because clock and TDR pulse occur at times which deviate from the ideal. Thus samples can be situated on the time axis only with a certain probability. The uncertainty in the nominal phase difference between emitted excitation pulse (or trigger in sampling oscilloscopes) and sampling strobe is called *timing jitter*, *time jitter*, or *aperture jitter* in literature. According to the Fourier transform theorems a shift in time domain leads to an additional phase angle in frequency domain. Therefore the uncertain timing is also referred to as *phase noise*.

Aperture jitter causes amplitude errors in steep signal portions. In horizontal segments of the waveform it has no effect which distinguishes it from other amplitude noise (*Souders et al.*, 1990).

Jitter is a stochastic process ϵ_J which can have more than one physical cause. It generally differs from sampler to sampler. Even within one sampler different configurations or operation modes can cause different jitter patterns. These uncertainties cause systematic errors in sampling, which may be difficult to compensate depending on the jitter's nature. Aperture jitter manifests itself as an additional noise contribution in the spectrum of the sampled signal. If nT_s is the nominal sampling instant given sampling period T_s, the true sampling instant is expressed by:

$$t_n = nT_s + \epsilon_J \; . \tag{3.25}$$

In the simplest case the jitter follows a Gaussian distribution, i.e. $\epsilon_J \sim \mathcal{N}(0, \sigma_J^2)$. *Kobayashi et al.* (1999) shows that if this assumption holds the phase noise power P_J induced by sampling a sinusoidal input function $A(t) = A_0 \sin(2\pi f_0 t)$ will yield:

$$P_J = A_0^2 \left(1 - e^{-2\pi^2 f_0^2 \sigma_J^2} \right) \; . \tag{3.26}$$

The noise power is independent of the sampling frequency, i.e. higher sampling rates do not diminish the effect of jitter. The phase noise power increases with increasing input signal frequency. This is clear since higher frequencies are associated to steeper signal edges in the time domain. An sampling instant uncertainty with standard deviation σ_J leads to larger errors the steeper the signal edges are. Since the signal power of the sinusoidal input function is is equal to $A_0^2/2$, the signal-to-noise ratio is given by

$$\text{SNR} = A_0^2/(2P_J) \; . \tag{3.27}$$

Kobayashi et al. (1999) extend this investigation to more general signals, exploiting their Fourier-series expansion.

If the jitter is purely random and follows a unique probability distribution it will be possible in some situations to apply a correction to the affected signal. One method derives the jitter probability density function from the signal. With this information a deconvolution may be applied to remove the effect of timing jitter from the true waveform (*Gans*, 1983), (*Verspecht*, 1994). Another procedure determines the median from a large number of samples to smooth the signal (*Souders et al.*, 1990).

Later it will be shown from measurements that OBSERVER suffers from jitter, too. It is a major drawback, that this jitter in some cases is far from being Gaussian. Depending on the instrument settings this stochastic process reveals systematic, periodic portions in addition to purely random components. However these systematic components are still impossible to predict up to now. They are probably due to the way of signal generation by means of DDS and may be explained by spurious frequencies in the DDS output spectrum. The effects of spurs will be discussed later.

3.2.4. Real-Time- and Equivalent-Time-Sampling

In real-time sampling a signal is sampled with high sampling frequency (Fig. 3.7, A). This sampling method has been implicitly presupposed in the former elaboration. Real-time sampling is required if the signal under investigation is transient like a particle scattering event in high energy physics or non-periodic like in speech or movie streams. The higher the bandwidth of the input signal the higher the sampling frequency must be. In TDR applications for soil moisture determination the typical total pulse round-trip time is in the range of nanoseconds. To track the important edges caused by the signal reflections a sampling period deep in the sub-nanosecond range must be achieved. Otherwise the edges will be at least distorted if not completely invisible. Commercial TDR instruments have pulse rise-times around 250 ps. In literature a rule of thumb is found relating the pulse rise-time t_r to the bandwidth f_{max} of the pulse train:

$$t_r \cdot f_{max} = 0.35 \ \ldots \ 1 \ . \tag{3.28}$$

The constant on the right side varies between different literature references. The exact value is not important since in real spectra it is difficult to determine f_{max} without doubt, anyway. This rule tells us that a rise-time of a periodic square wave below 1 ns leads to a bandwidth greater than 1 GHz.

The pulse is filtered due to low-pass filter effects of coaxial probe cable and waveguide buried in soil. This diminishes the bandwidth of the pulse. But to specify the demands on the sampling device it is assumed that $f_{max} = 1$ GHz. Then the sampling frequency must be at least $f_s > 2f_{max} = 2$ GHz because of the sampling theorem. Additionally the analog-to-digital converter (ADC) must be able to quantize the signal amplitude with high resolution (e.g. ≥ 10 bits) to reach low quantization distortion. Fast real-time samplers with high resolution are extremely expensive. Slower ADCs may be combined in an interleaved mode to sample the signal at higher frequency. But still this technique is demanding and costly.

If the signal under investigation is periodic, an elegant and efficient solution to this problem is equivalent-time sampling. With this method the complete sample of a repetitive, stationary signal is composed by interleaved samples taken over many signal periods (s. Fig. 3.7, B). Such samplers take e.g. one sample per period and sweep the sample instant slowly across the signal. Equivalent-time sampling enables the sampler to acquire signals up to the analog bandwidth of the sampling system regardless of the sampling rate. This method leads to cost-effective samplers. The applicability to repet-

itive, stationary signals only is a disadvantage of this technology, but of no concern in soil moisture measurement with TDR.
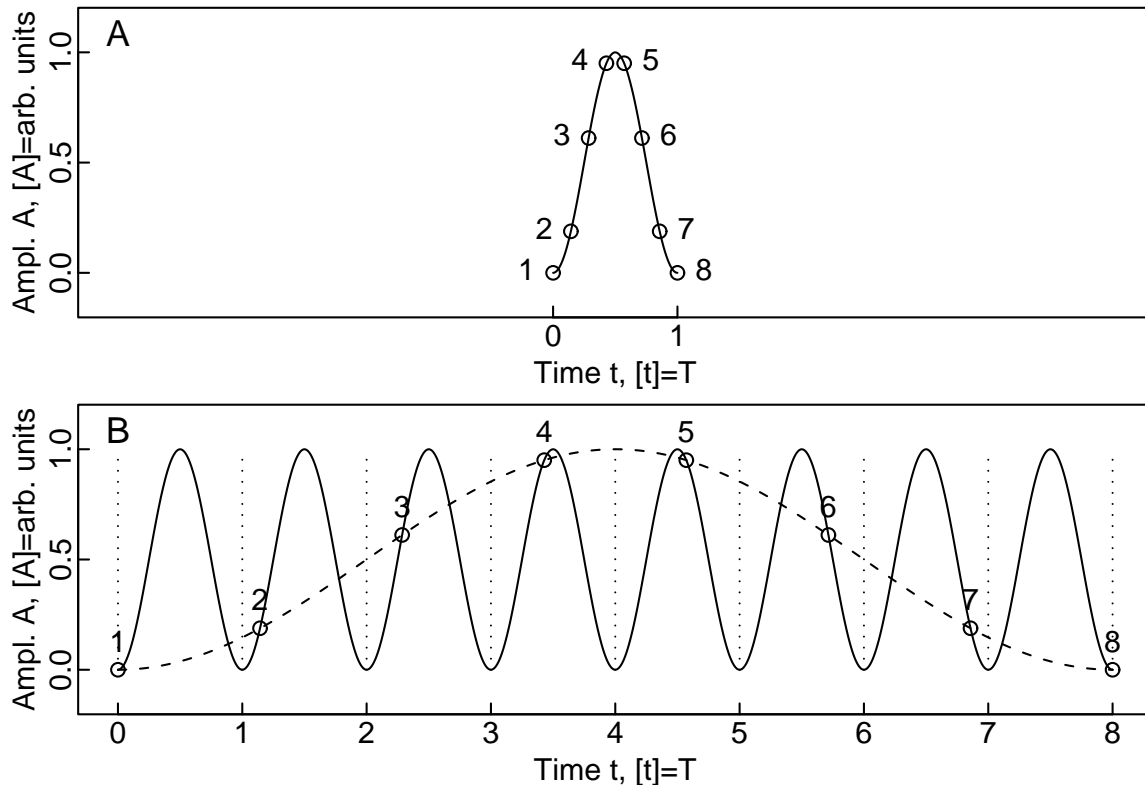
Figure 3.7.: Real-time vs. equivalent-time sampling. A: real-time sampling, all samples taken within one signal occurrence, which may be transient; B: equivalent-time sampling, samples taken at different phases of a repetitive signal. The dashed line is an image of one signal period at a much longer time scale.

3.2.5. Conventional Sampling Gates

Conventional samplers often use a diode bridge acting as a fast switch (*Mulvey*, 1970; *Akers and Vilar*, 1986). The signal to be sampled is connected to the bridge's high frequency input. The diodes are inversely biased and the input signal must not exceed the inverse bias voltage. Short needle pulses of opposite amplitude fed into the switching input of the diode bridge control the opening of this sampling gate. The the gate is closed until the sampling pulses are applied. The amplitude of these pulses exceed the bias, the diodes conduct for a short time and the input signal is gated to the storage capacitor. The capacitor is loaded to the level of the input signal and holds the load when the gate disconnects it from the input signal again. The hold phase allows more time to process the information, e.g. for analog-to-digital conversion.

The generation of the necessary needle pulses is not trivial. They must be extremely short, highly symmetric, stable in amplitude, and precise in time. The width of the

pulses determines the aperture of the sampling gate. The larger the aperture, the lower the bandwidth of the sampler. Step recovery diodes (SRD) (*Aeroflex/Metelics*, 2004) may be used to shape the sharp pulses (*Hewlett-Packard*, 1984). These parts are not easy to handle. They are sensitive to electrostatic discharge (ESD) and need stable current sources. Furthermore the temperature dependence of the minority charge carriers leads to an uncertainty in the precise timing of the pulse (*Kirkby*, 1999).
The sampler of OBSERVER is based on delta modulation, which is a completely different sampling methodology. It does not require a conventional sampling gate. More technical details about OBSERVER are given below.

3.3. Principle of Delta Modulation

Like other TDR instruments OBSERVER is sampling not in real-time but equivalent-time (*Tektronix*, 2003). It differs significantly from conventional TDR instruments because its sampler does not use common sampling bridge or gate circuits (s. Sec. 3.2.5). Instead, it is a special closed-loop control circuit called *Delta Modulator* (DM) (*Steele*, 1975).
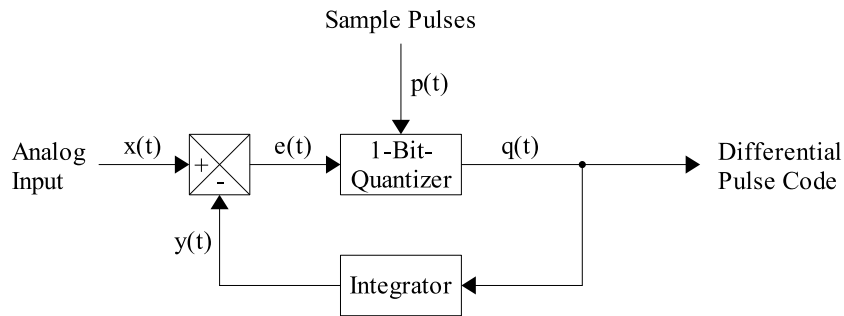
Figure 3.8.: General principle of delta modulation.

A DM (Fig. 3.8) is a codec (encoder/decoder), which encodes the error $e(t)$ between the input signal $x(t)$ and a prediction $y(t)$ with one bit resolution. The encoder tries to minimize the error

$$e(t) = x(t) - y(t) \ . \tag{3.29}$$

by driving the prediction $y(t)$ towards $x(t)$. At each pulse of a periodic sample clock the quantizer checks the sign of the error and codes it by a positive of negative constant voltage $\pm \Delta V_q$ at the quantizer output $q(t)$ such that

$$
\begin{aligned}
e(t) > 0 &\Rightarrow q(t) = +\Delta V_q \ , \\
e(t) < 0 &\Rightarrow q(t) = -\Delta V_q \ .
\end{aligned}
\tag{3.30}
$$

In the case of OBSERVER the output $q(t)$ is held up to the next sample instant. An integrator is used as a first-order predictor yielding $y(t)$. Integration of q(t) between

two sampling instants t_n and t_{n+1}, during which $q(t)$ is constant, leads to a negative or positive voltage step $\pm\gamma$ added to the last level of y. Thus if the last prediction $y(t_n)$ is smaller than the current input $x(t_n)$ at sample instant t_n ($e(t_n) > 0$) the integrator will predict the input signal to be even larger at the next sample instant ($y(t_{n+1}) = y(t_n)+\gamma$) and vice versa. In this way prediction $y(t)$ follows input $x(t)$.

The output $q(t)$ of the 1-bit-quantizer can have two different states only, which may be identified with two logic states 0 and 1. The resulting binary sequence is the differential pulse code for the input signal. It is to be transmitted to a receiver, e.g. a microcontroller or a PC, where it is digitally integrated to reconstruct the sampled signal amplitude.

The binary stream is sequentially analyzed. Starting from an arbitrary initial value an amplitude counter is incremented whenever the current bit of the pulse code is 1 and decremented otherwise. The corresponding time of the actual amplitude value is coded by the current bit position in the stream because the samples were taken at equidistant times.

According to the comprehensive article about history of quantization by *Gray and Neuhoff* (1998), Sec. B, delta modulation belongs to the class of scalar quantization with memory. It performs predictive sampling, since it memorizes the last error between true and quantized signal and predicts (assumes) that this tendency holds on.

DM lead to a highly compressed code since it is free of redundancy. Normally sampled signals are not much changing from sample to sample. If the absolute amplitude were coded with a binary word, only the least significant bits would be changing, whereas most significant bits would be constant and therefore redundant. DM is advantageous in many applications but its performance is difficult to tackle theoretically.

3.3.1. Delta Modulation Circuit with ECL D-Flip-Flop

An elegant technical realization of the DM has been proposed by *Monett* (2004). The DM consists of two main functional blocks: an edge triggered ECL D-Flip-Flop (D-FF), and an integrator, the output of which is coupled back to the input of the D-FF (Fig. 3.9). A D-FF is a simple storage element. At each rising edge of the D-FF clock signal the logic input state is evaluated, shifted to the output, and latched. An input variation does not influence the output, unless a clock pulse is fired. The D-FF samples the input state and its clock acts like a sampling clock.

The ECL family uses differential input and output stages. The differential input of the D-FF consists of the two signals D and $\overline{D}$ (Boolean Algebra: *not D*). The voltage difference

$$\Delta V_D = V_D - V_{\overline{D}} \tag{3.31}$$

between these signals is used to physically represent the logic states:

$$\Delta V_D > 0 \quad \longleftrightarrow \quad \text{logic 1} \ ,$$
$$\Delta V_D < 0 \quad \longleftrightarrow \quad \text{logic 0} \ .$$

The high frequency signal under investigation V_{in} is connected to D, whereas $\overline{D}$ is fed with the output V_{out} of the integrator. The commonly available, cost effective ECL D-FF

acts in principle like a specialized strobed comparator (*Laug et al.*, 1992). It compares the voltage difference

$$\Delta V_{\text{in}} = V_{\text{in}} - V_{\text{out}} \tag{3.32}$$

at each rising edge of a sampling clock pulse. The frequency of the sampling clock is denoted by f_{clk}. Thus the period between to consecutive sampling strobes occurring at t_{n-1} and t_n is

$$T_{\text{clk}} = t_n - t_{n-1} = f_{\text{clk}}^{-1} \ . \tag{3.33}$$

If ΔV_{in} is positive or negative, the voltage difference

$$\Delta V_Q = V_Q - V_{\overline{Q}} \tag{3.34}$$

at the output of the D-FF will become a positive or negative constant value, respectively. It is important, that even a very small input voltage difference leads to a full scale output voltage swing, a typical characteristic of ECL.[7]
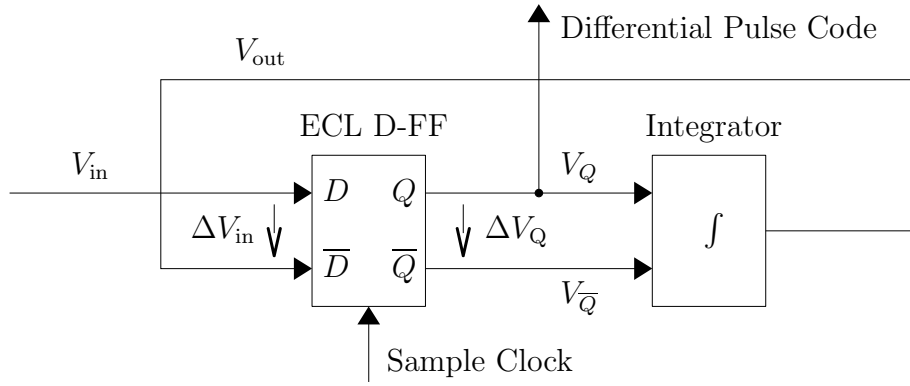
Figure 3.9.: Delta modulator with ECL D-Flip-Flop.

In the next stage of the control system the integrator integrates ΔV_Q, which is a positive or negative value, constant between two consecutive clock pulse edges occurring at time t_{n-1} and t_n. For $t \in [t_{n-1}, t_n[$ the output voltage yields

$$
\begin{aligned}
V_{\text{out}}(t) &= \frac{1}{t_c} \int_{t_{n-1}}^{t} \Delta V_Q(t) dt + V_{\text{out}}(t_{n-1}) \\
&= \frac{1}{t_c} \Delta V_Q(t_{n-1})(t - t_{n-1}) + V_{\text{out}}(t_{n-1}) \\
&= \frac{\pm |\Delta V_Q|}{t_c}(t - t_{n-1}) + V_{\text{out}}(t_{n-1}) \ .
\end{aligned}
\tag{3.35}
$$

---

[7]For a detailed description of ECL gates see *ON Semiconductor* (1988), Chap. 1.

Integration up to the time t adds a linearly rising or falling voltage ramp to the former voltage level $V_{\text{out}}(t_{n-1})$. The slope of the ramp is determined by the integrator's time constant t_c and the constant voltage $|\Delta V_Q|$. The slew rate yields

$$\frac{\partial V_{\text{out}}}{\partial t} = \frac{\pm |\Delta V_Q|}{t_c} \ . \tag{3.36}$$

Thus up to the next sampling instant t_n the output voltage becomes

$$
\begin{aligned}
V_{\text{out}}(t_n) &= \frac{\pm |\Delta V_Q|}{t_c}(t_n - t_{n-1}) + V_{\text{out}}(t_{n-1}) \\
&= \frac{\pm |\Delta V_Q|}{t_c}\frac{1}{f_{\text{clk}}} + V_{\text{out}}(t_{n-1}) = V_{\text{out}}(t_{n-1}) \pm \gamma \ ,
\end{aligned}
\tag{3.37}
$$

with

$$\gamma = \frac{|\Delta V_Q|}{t_c}\frac{1}{f_{\text{clk}}} = \left|\frac{\partial V_{\text{out}}}{\partial t}\right|\frac{1}{f_{\text{clk}}} \ . \tag{3.38}$$

From one sampling pulse to the next the output voltage changes by $\pm\gamma$. This constant determines the granularity of the amplitude quantization.

The resulting voltage V_{out} is fed back to the $\overline{D}$ input of the D-FF. The working principle of this closed loop can be best explained with an example (s. Fig. 3.10): Assume V_{in} to be greater than V_{out} at sampling time t_0: $\Delta V_{\text{in}} = V_{\text{in}} - V_{\text{out}} > 0$. Thus the output ΔV_Q of the D-FF is set positive. This leads to a rising voltage ramp at the output of the integrator, which drives V_{out} towards V_{in}. The output voltage does not change the direction until at some sample strobe the feedback voltage V_{out} exceeds V_{in}, i.e. $\Delta V_{\text{in}} = V_{\text{in}} - V_{\text{out}} < 0$. Then the D-FF changes its output state and ΔV_Q becomes negative, leading to a falling feedback voltage correcting the error between input and feedback. Therefore V_{out} is a piecewise linear approximation of V_{in} consisting of segments with constant positive or negative slope (s. Fig. 3.10).

3.3.2. Slope Overload, Amplitude Range, and Quantization Noise

The precise recording of steep rising edges of incident and reflected waves play the essential role in TDR applications. The sampler of a TDR instrument must be able to follow these fast changes. The same holds for the OBSERVER's delta modulator. If its integrator's time constant t_c is chosen too large, the feedback will not be agile enough to follow the changes of the input signal (s. Fig. 3.11, A). This condition is called *slope overload*.

To investigate the avoidance of slope overload, the input is assumed to be sinusoidal with amplitude A_0 and frequency f_0:

$$V_{\text{in}}(t) = A_0 \sin(2\pi f_0 t) \ . \tag{3.39}$$

Its maximum slew rate is the first derivative around its zero crossings. Slope overload is generally avoided, if the slew rate of the feedback is larger than the maximum slew rate of the input signal:

$$2\pi f_0 A_0 < \frac{|\Delta V_Q|}{t_c} = \frac{\gamma}{T_{\text{clk}}} \ . \tag{3.40}$$

PSpice Simulation of the ECL Delta Modulator
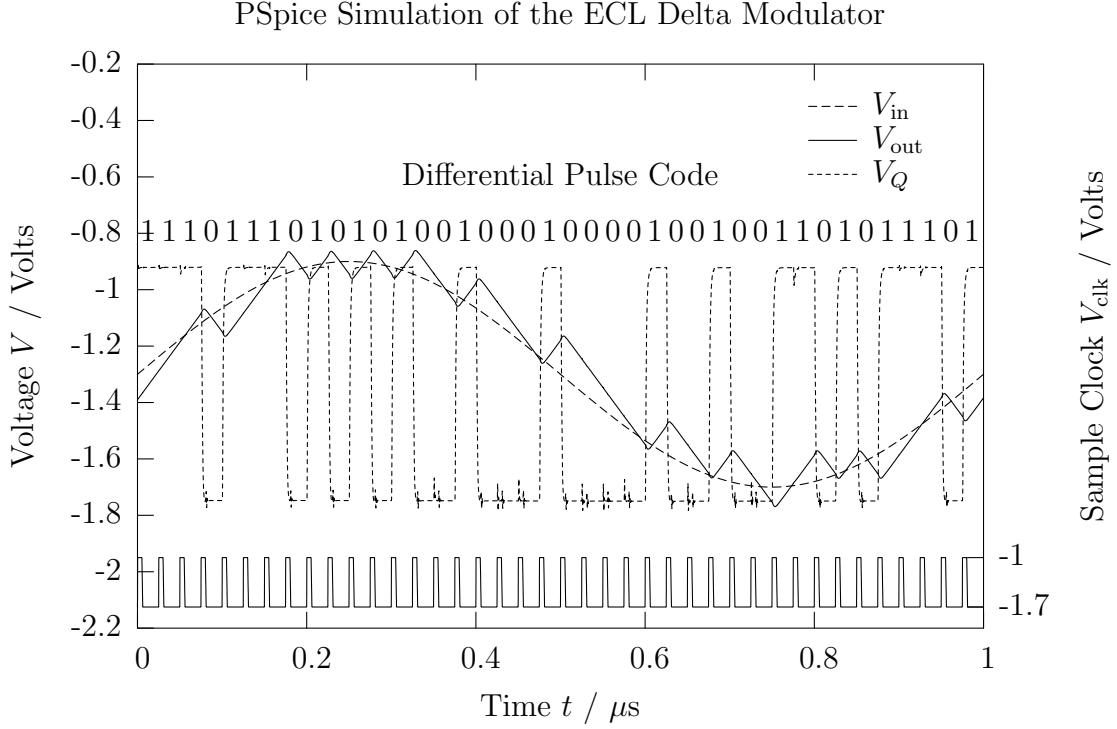
Figure 3.10.: Real-time sampling of a sinusoid by the ECL delta modulator. V_{in}: input sine-wave, $f_{\text{in}} = 1$ MHz; V_{out}: output of the integrator; V_Q: output of the D-FF; V_{clk}: sample clock, $f_{\text{clk}} = 40$ MHz. The sequence of the D-FF's logic states is the pulse coded signal (PSPICE simulation results).

If the frequency of the input signal increases, the integrator's time constant has to be decreased to fulfill the condition for non-overload (s. Fig. 3.11, B). Eq. 3.40 can also be interpreted as a condition for the maximum allowable amplitude A_{max} of an input signal with bandwidth f_0. This determines the theoretical upper value of the sampler's amplitude range. The lower value is the smallest amplitude of a sinusoid which still disturbs the idling pattern of the sampler. The idling pattern is a regular pattern of alternating rising and falling slopes, which occurs, when the input signal is a constant. The amplitude of the idling pattern is:

$$A_{\text{idle}} = \frac{\gamma}{2} = \frac{1}{2} \frac{|\Delta V_Q|}{t_c} \frac{1}{f_{\text{clk}}} \ . \tag{3.41}$$

The larger the input signal amplitude becomes with respect to Eq. 3.41, the better the tracking. According to Eqs. 3.40 and 3.41 the amplitude range covered by the delta modulator is:

$$R = \frac{A_{\text{max}}}{A_{\text{idle}}} = \frac{f_{\text{clk}}}{\pi f_0} \ . \tag{3.42}$$

This ratio is not really the dynamic range, since the minimum amplitude, which gives an acceptable decoded signal-to-noise ratio, is a subjective choice.
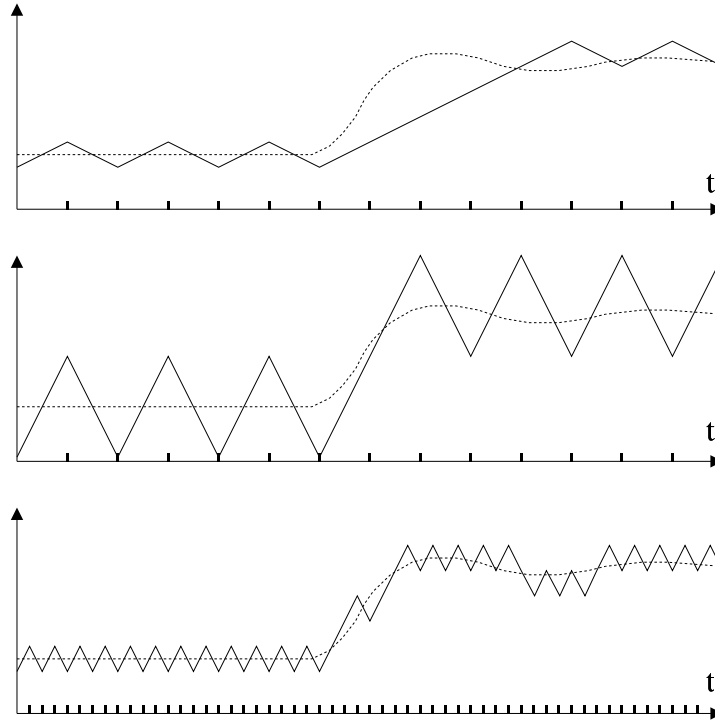
Figure 3.11.: Influence of the integrator's slew rate and sampling frequency on the accuracy of approximation in Delta Modulation. A: slope overload; B: faster ramp leads to increased quantization noise and loss of amplitude resolution; C: better approximation due to higher sampling frequency.

Each sampling process is accompanied by quantization noise which is due to quantized time and amplitude. The calculation of the quantization noise produced by delta modulators is not a trivial task. One of the simplest formula for quantization noise was derived by *de Jager* (1952):

$$N_q^2 = K_q \frac{f_c \gamma}{f_{\text{clk}}} \ . \tag{3.43}$$

The step size γ of integrator after one sampling period is given in Eq. 3.38. f_c is the bandwidth of the message band[8] of the codec, K_q is an arbitrary constant.
Hawksford and Darling (1990) calculated the Signal-to-Quantization-Noise Ratio (SQNR) for a sinusoidal input function under the simplified assumptions, that the system is not overloaded and the noise is random. They assume further, that the noise is band-limited with bandwidth f_b. Oversampling with $f_{\text{clk}} > f_b$ leads to a reduction of the noise level. To avoid slope overload Eq. 3.40 must hold. Thus the discrete voltage step size γ has to fulfill the following condition:

$$\gamma \leq 2\pi f_0 A_0 / f_{\text{clk}} \ . \tag{3.44}$$

The quantization noise power spans the range $\pm\gamma$ with a noise bandwidth of f_b.

---

[8]The range in the frequency spectrum used to code the signal.

3. OBSERVER: A Novel TDR Instrument Based on Delta Modulation

The total noise power is given as

$$N_q^2 = \int_0^{f_b/f_{\mathrm{clk}}} \gamma^2 df = \gamma^2 \frac{f_b}{f_{\mathrm{clk}}} \ . \tag{3.45}$$

Substituting Eq. 3.44 into Eq. 3.45 yields

$$N_q^2 = A_0^2 4\pi^2 \frac{f_0^2 f_b}{f_{\mathrm{clk}}^3} \ . \tag{3.46}$$

Since the mean square value of a sine is given by $S^2 = A_0^2/2$, the SQNR in dB is

$$\mathrm{SQNR(dB)} = 10\log_{10}\frac{S^2}{N_q^2} = 10\log_{10}\frac{A_0^2/2}{A_0^2 4\pi^2 f_0^2 f_b/f_{\mathrm{clk}}^3} = -19 + 10\log_{10}\left(\frac{f_{\mathrm{clk}}^3}{f_b f_0^2}\right) \ . \tag{3.47}$$

This expression does not take into account the noise due to slope overload. In case of OBSERVER it is sufficient, since its parameters are well chosen so that slope overload does not occur. A detailed analytical derivation of more general formulas describing quantization noise in delta modulators for Gaussian-type input signals and under slope-overload condition are given in *Steele* (1975) and a summary of this analysis in *Steele* (1980).

It will be shown later that the presented calculation of noise yields nothing but a theoretical lower bound often far exceeded in reality by other sources of noise. Crosstalk between different components on the printed circuit board, jitter of excitation and sample pulse, noise of the power supply, and noise inherent to the electronic parts are some examples leading to a larger signal degradation than expected from the above calculations.

3.4. Principles and Design of OBSERVER V2

OBSERVER differs significantly from conventional equivalent-time sampling instruments. The most important differences are: 1. the sampler is a delta modulator; 2. the programmable delay between excitation pulse and sampling clocks necessary to perform equivalent-time sampling is not realized by delay generators but by running excitation pulse and clock pulse trains at slightly different frequencies. Therefore the signal generators must be frequency programmable with very fine frequency resolution and phase stability. *Direct Digital Synthesis* (DDS) is the chosen method to realize programmable frequency generators because of its simple usage and robustness. An alternative would have been the principle of *Phase Locked Loop* (PLL). PLLs have been used by *Gerding et al.* (2003) in a pulse TDR for water level measurement.

OBSERVER comprises several functional blocks (Fig. 3.12) which are explained in more detail after the following general description. Two prototypes of the new TDR have been realized which are quite similar in function. They are referred to as version V1 and V2. The main difference between V1 and V2 is that latter uses a higher master clock speed (50 MHz instead of 25 MHz), is equipped with a local data storage (RAM), and has a second amplifier stage in the excitation pulse driver.
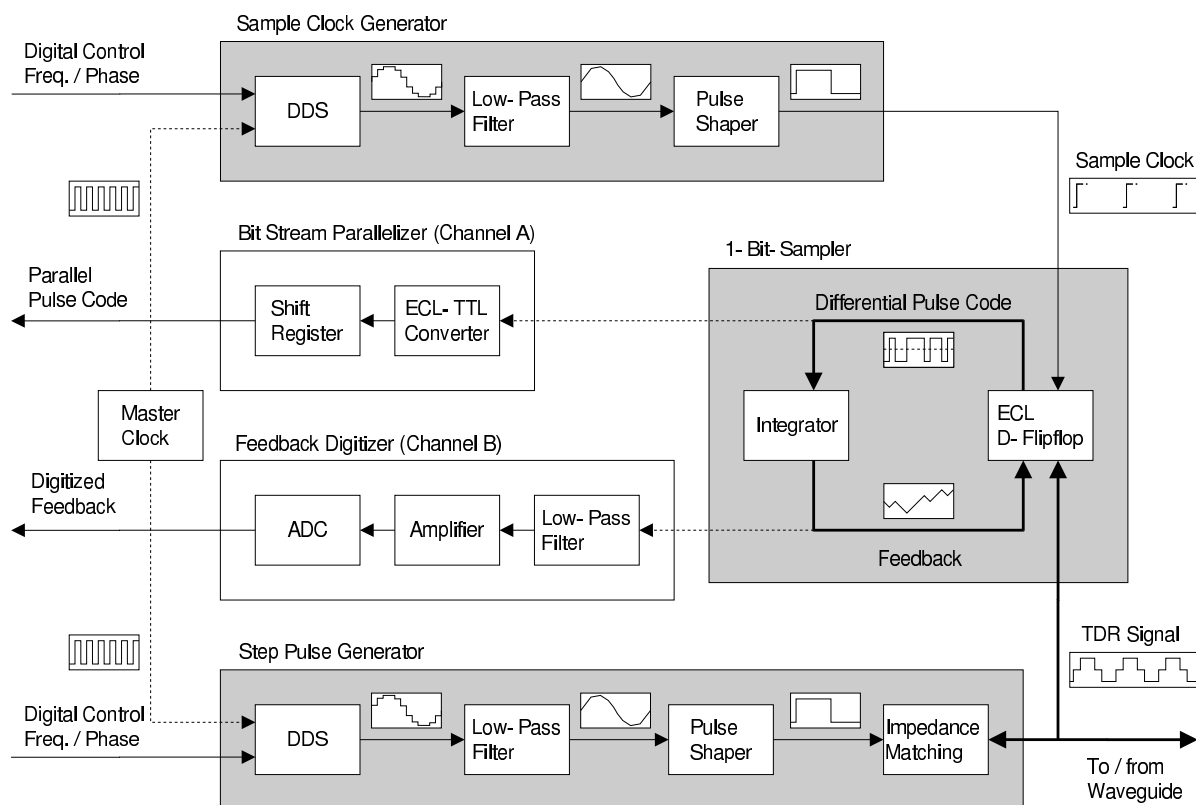

Figure 3.12.: Block diagram of OBSERVER V2.

The core of the new TDR is a *delta modulator* working in equivalent-time sampling mode. At each rising edge of the *sample clock* pulse train the sampler decides whether

the feedback has to rise or to fall in order to follow the *TDR signal*. Two channels have been realized to read out the information about the sampled waveform: either a direct link to the *quantizer's bit stream* (Channel A in Fig. 3.12), or a *digitization of the feedback* (Channel B in Fig. 3.12).

The *step pulse generator* producing the excitation pulse train sent along the connected waveguide consists of four stages. The first is the *direct digital synthesis (DDS)*, which generates a sine-wave of programmable frequency and phase. After having passed a *low-pass filter* stage the sinusoid is transformed into a square wave of same frequency. This is performed by a *pulse shaper* being the third stage. Each square pulse travels down the waveguide, generally causing reflections which travel back towards the step pulse generator. Since the square pulse is wider than the pulse's round-trip time forth and back the connected probe, the reflected wave superposes the incident (s. Fig. 2.2). The last stage in the pulse generating chain is an *impedance matching* circuit leading to a final absorption of the back propagating wave to avoid components traveling down the waveguide again. The sampler's high-frequency input is connected right after the last stage.

The *clock pulse generator* is similar to the step pulse generator except the lack of the final stage for impedance matching. The DDS of both signal generators are driven by the same *master clock* which guarantees high mutual phase stability.

To run the system in equivalent-time sampling mode it is necessary to realize a variable delay between excitation and clock pulse. This is achieved by running the two DDS at slightly different frequencies. The sample clock repetition rate f_{clk} is a bit smaller than the step pulse frequency f_{step}:

$$f_{clk} = f_{step} - f_{offset} \ . \tag{3.48}$$

The offset frequency f_{offset} is chosen to be 6 to 8 orders of magnitude less than f_{step} or f_{clk}, thus $f_{clk} \approx f_{step}$. During each TDR signal period one sample is taken leading to one additional bit in the continuous differential pulse code. OBSERVER V2 stores a segment of the stream in its local RAM of m bits size. The total measurement time t_{meas} needed to fill the RAM is

$$t_{meas} = m/f_{clk} \ . \tag{3.49}$$

Since the clock is a little slower than the step signal, the phase of the sample clock sweeps slowly across the TDR signal from sampling pulse to sampling pulse. After the time

$$T_{offset} = f_{offset}^{-1} \tag{3.50}$$

step and clock pulse are in phase again, indicating that one complete period of the TDR signal has been sampled. The result is a sampled approximation of the TDR signal on a much longer time scale (s. Fig. 3.7, B). The input signal period

$$T_{step} = f_{step}^{-1} \tag{3.51}$$

is dilated to the time scale T_{offset}. The dilation factor is

$$s = \frac{T_{offset}}{T_{step}} = \frac{f_{step}}{f_{offset}} \approx 10^6 \ldots 10^8 \ . \tag{3.52}$$

78

The range given for s is typical for the current application of soil moisture measurement. The sampling of one TDR pulse period takes T_{offset} seconds. During this time, $n_{\text{clk}} = T_{\text{offset}} \cdot f_{\text{clk}}$ sampling pulses occur. Thus one TDR signal of period T_{step} is sampled with n_{clk} points, yielding a theoretical temporal resolution of

$$T_s^{(r)} = \frac{T_{\text{step}}}{n_{\text{clk}}} = \frac{f_{\text{offset}}}{f_{\text{step}} \, f_{\text{clk}}} \approx \frac{f_{\text{offset}}}{f_{\text{step}}^2} = \frac{1}{s f_{\text{step}}} \ . \tag{3.53}$$

A typical order of magnitude is 1 MHz for f_{clk} and f_{step}, and $0.01 - 1$ Hz for f_{offset}, thus the theoretical sampling period yields

$$T_s^{(r)} \approx 10^{-14} \ldots 10^{-12} \text{ s} \ . \tag{3.54}$$

Of course, this range of extremely small sampling periods is purely academic. In reality the corresponding bandwidth cannot be reached, since it is limited by timing jitter, noise, and low pass effects of the electronics. However this small sampling period suffering from jitter indeed has a positive effect since it leads to an averaging over thousands of samples.

3.4.1. Parameter Settings

Different applications or probe configurations require different parameter settings for OBSERVER V2. The parameters to be chosen are

1. excitation pulse frequency f_{step},

2. frequency offset f_{offset},

3. and the integrator's time constant t_c.

The frequencies are programmable, whereas the time constant has to be realized in hardware.

The amplitude granularity γ (Eq. 3.38) should be as small as possible to track the signal with the least amplitude errors (the least SQNR). Therefore f_{clk} ($\approx f_{\text{step}}$) and t_c should be as large as possible. But this contradicts other objectives. The necessary trade-off will be illuminated by means of a practical application.

The laboratory experiment for monitoring transient soil moisture profiles with Spatial TDR serves as an example. The probes used are 0.6 m long connected to the TDR with a coaxial cable of approx. 15 m length. These outer conditions impose constraints on the parameter space.

Choice of Pulse Repetition Rate

To reduce noise the excitation pulse repetition rate f_{step} should be as large as possible but it is limited by the total length of connecting coaxial cable and probe. Fig. 3.13 is explaining why. It shows a typical TDR reflectogram on a large time scale. Rising and falling edge of the step pulse causes multiple reflection at the probe limits. This effect is called *ringing* (Fig. 3.13, 1).

```
HP54602B
```

```
CH1: -
CH2: TDR signal, vpos=-3V, 0.47m+T+2m+R1m+OE RG58, f=4.0001MHz
CH3: -
CH4: -
```
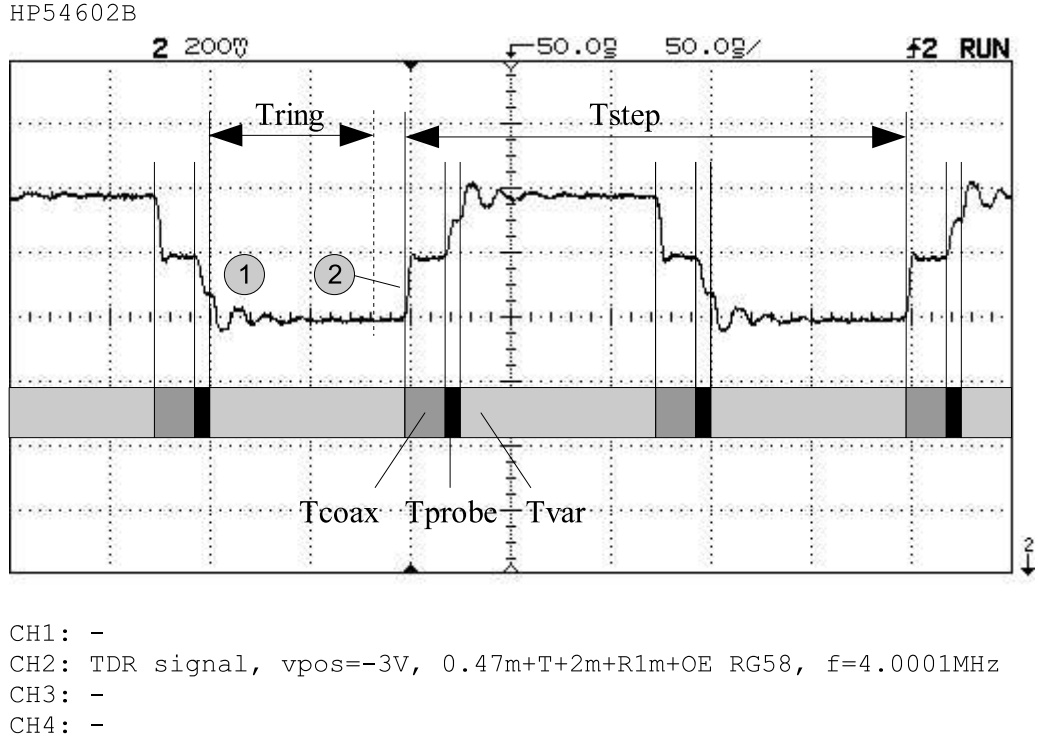
Figure 3.13.: Influence of excitation pulse repetition rate on the signal portion relevant to TDR. Pulse frequency $f_{\text{step}} \approx 4$ MHz, pulse period $T_{\text{step}} = 0.25$ μs, 50% duty cycle. 1: ringing caused by falling pulse edge; 2: rising edge of emitted pulse; T_{ring}: approximate duration of ringing; T_{coax}: travel-time in coaxial cable (2 m); T_{probe}: travel-time in probe, TDR is focused on (1 m ribbon cable in air); T_{var}: variable travel-time dependent on pulse period. An increase of the pulse repetition rate f_{step} leads to a decrease of T_{var} only.

.

The amplitude of these secondary reflections is decaying exponentially until it vanishes in noise. The approximate time span of ringing is denoted by T_{ring} in Fig. 3.13. It must be guaranteed that the ringing has died out, before the next pulse is emitted (Fig. 3.13, 2). Otherwise this unwanted oscillation would disturb the amplitude measurement and the moisture profile reconstruction.

The pulse travel-time T_{coax} in the connecting cable is fixed. On the large time scale the travel-time T_{probe} in the probe relevant for TDR varies only weakly. Thus these two time intervals can be assumed constant for now.

A variation of the pulse repetition rate f_{step} modifies the travel-time interval T_{var} only. A higher excitation pulse repetition rate f_{step} leads to a smaller pulse period T_{step}. Thus T_{var} becomes shorter and the ringing of the falling edge is shifted towards the next pulse, possibly reaching into the range of T_{probe}. The excitation pulse period T_{step} has to be chosen appropriately to avoid this disturbance:

$$T_{\text{step}} > 2(T_{\text{coax}} + T_{\text{probe}} + T_{\text{ring}}) \,. \tag{3.55}$$

The period of ringing is $2T_{\text{probe}}$, since it is caused by wave splitting occurring at both ends of the probe. The decay of ringing is a function of the signal attenuation within the probe embedded in the material under test. Therefore it is difficult to predict generally, after how many periods the ringing will have been vanished completely. In this respect the worst case is the least attenuating, in which the probe is surrounded by air like in the example of Fig. 3.13. In this case the ringing can be hardly distinguished from noise after 5 periods. The worst case duration of ringing is therefore: $T_{\text{ring}} \approx 10\, T_{\text{probe}}$. Substitution into Eq. 3.55 yields:

$$T_{\text{step}} > 2 \left(T_{\text{coax}} + 11\, T_{\text{probe}} \right) . \tag{3.56}$$

For the particular application in the lysimeter the travel-times are $T_{\text{coax}} \approx 150$ ns and $T_{\text{probe}} \approx 10$ ns. Thus

$$
\begin{aligned}
T_{\text{step}} &> 520 \text{ ns} \approx 500 \text{ ns} \\
\Rightarrow f_{\text{step}} &\leq f_{\text{step}}^{(\text{max})} = 2 \text{ MHz} .
\end{aligned}
\tag{3.57}
$$

The excitation pulse frequency in the lysimeter experiment should not exceed 2 MHz.

Choice of the Integrator's Time Constant

To reduce γ further with a given f_{step} it leaves to increase the time constant t_c, but this parameter is responsible for the agility of the OBSERVER's sampler. It has to be chosen appropriately to avoid slope overload. The fastest possible edge in the TDR signal of OBSERVER belongs to the emitted pulse since all other reflections have been low-pass filtered during their transition through cable and probe. The driver of the excitation pulse generator is a ECL line receiver MC100EP16 (*ON Semiconductor*, 2001a). According to its data sheet it reveals a pulse rise and fall time of $800\,\text{mV}/250\,\text{ps}$. As part of the OBSERVER's TDR step generator it drives 200 mV into 50 Ω probably in the same time.[9] Thus the maximum real-time slew rate to be sampled is

$$\left. \left| \frac{\partial V_{\text{in}}}{\partial t} \right|_{\text{max}}^{(r)} = \frac{0.2 \text{ V}}{250 \text{ ps}} = 0.8 \text{ V/ns} . \tag{3.58}$$

OBSERVER must be able to sample this fast transition in equivalent-time. The dilation factor s (Eq. 3.52) stretches the time axis. The transition from real-time to equivalent-time yields

$$\left. \left| \frac{\partial V_{\text{in}}}{\partial t} \right|_{\text{max}}^{(e)} = \frac{1}{s} \left| \frac{\partial V_{\text{in}}}{\partial t} \right|_{\text{max}}^{(r)} . \tag{3.59}$$

The slew rate of the delta modulator (Eq. 3.36) must exceed the maximum equivalent-time signal slew rate:

$$\frac{|\Delta V_{\text{Q}}|}{t_c} = \left| \frac{\partial V_{\text{out}}}{\partial t} \right| > \left. \left| \frac{\partial V_{\text{in}}}{\partial t} \right|_{\text{max}}^{(e)} \Leftrightarrow \frac{t_c}{s} < |\Delta V_{\text{Q}}| \left/ \left| \frac{\partial V_{\text{in}}}{\partial t} \right|_{\text{max}}^{(r)} \right. . \tag{3.60}$$

---

[9]An appropriate oscilloscope with a bandwidth ≥ 4 GHz to reliably measure the rise-time was not available.

3. OBSERVER: A Novel TDR Instrument Based on Delta Modulation

The ECL D-flip-flop used in the OBSERVER's DM is a MC100EP52 (*ON Semiconductor*, 2001b) with $\Delta|V_Q| = 0.8$ V differential output voltage swing. Substitution of this value and Eq. 3.58 into Eq. 3.60 yields:

$$\frac{t_c}{s} < 1\,\text{ns} . \tag{3.61}$$

This relationship has to be fulfilled to avoid slope overloading with the OBSERVER. It has been stated earlier that t_c should be as large as possible to reduce quantization noise. To avoid slope overload s has to be as large as possible, too. But now the next limitation for s comes into play (besides limited frequency resolution of the DDS): the OBSERVER's limited local memory of $m = 1$ Mbit size. With Eq. 3.53 the total length of the stored signal segment reads

$$T_{\text{RAM}} = m\,T_s^{(r)} \approx \frac{m}{s f_{\text{step}}} = \frac{m}{s} T_{\text{step}} . \tag{3.62}$$

The instrument must be capable of storing at least the Spatial TDR relevant signal portion describing the signal transition along the probe plus a bit of extra buffer preceding and following the most interesting time interval. In the current example of the lysimeter experiment the travel-time along the probe is roughly 10 ns. In this case the total sampling interval should be at least $T_{\text{RAM}} = 25$ ns. Since the TDR signal period is $1/f_{\text{step}} \geq 500$ ns (Eq. 3.59), Eq. 3.62 yields:

$$\frac{m}{s} \approx \frac{T_{\text{RAM}}}{T_{\text{step}}} \geq \frac{1}{20} . \tag{3.63}$$

Currently m is limited to approx. 10^6 bit. This constrains the dilation factor to

$$s \leq 2 \cdot 10^7 . \tag{3.64}$$

Substitution of this value together with $f_{\text{step}} \leq 2\,\text{MHz}$ into Eq. 3.52 yields:

$$f_{\text{offset}} \geq 0.1\,\text{Hz} . \tag{3.65}$$

According to Eq. 3.53 these parameters lead to a theoretical sampling interval on the real-time axis of

$$T_s^{(r)} = 2.5 \cdot 10^{-14}\,\text{s} = 250\,\text{fs} . \tag{3.66}$$

The remaining parameter is the integrator's time constant t_c. Its limit can be determined from Eq. 3.61:

$$t_c < 20\,\text{ms} . \tag{3.67}$$

The integrator of the DM is an operational amplifier with a R-C-feedback (s. Fig. B.1), whose time constant is $t_c = RC$. The values $R = 2 \cdot 47$ kΩ and $C = 100$ nF have been chosen yielding

$$t_c = RC = 9.4\,\text{ms} < 20\,\text{ms} . \tag{3.68}$$

Now all conditions are fulfilled.

Summary

The parameter values for OBSERVER V2 conforming to the requirements imposed by a 3-rod-probe of 0.6 m length and a coaxial cable (RG213) of 15 m are:

$$f_{\text{step}} = 2\,\text{MHz} \ , \ f_{\text{offset}} = 0.1\,\text{Hz} \ , \ t_c = 9.4\,\text{ms} \ . \tag{3.69}$$

3.4.2. Estimation of Quantization Noise

The amplitude granularity γ in Eq. 3.38 is a function of f_{clk}. Since in the particular equivalent-time sampling performed by OBSERVER V2 $f_{\text{clk}} \approx f_{\text{step}}$, the latter can be substituted into the equation yielding

$$\gamma = \frac{|\Delta V_Q|}{t_c} \frac{1}{f_{\text{step}}} \ . \tag{3.70}$$

Substitution of the values given in Eq. 3.69 yields

$$\gamma = \frac{0.8\,\text{V}}{9.4\,\text{ms} \cdot 2\,\text{MHz}} = 43\,\mu\text{V} \ . \tag{3.71}$$

Slope overload is avoided by the actual parameter values so that slope overload noise does not occur. The remaining part is granular noise due to quantization errors.

The TDR application is a special case since the input signal for the sampler is far from being random, in the contrary: it is almost totally deterministic and over longer time spans piecewise nearly constant. It is assumed that the sampling of the short signal edges does not contribute much to the total noise power. Therefore the input signal may be approximated by a square wave with piecewise constant voltage levels.

In this idealized case the idle pattern is prevailing. The sampler toggles at each sampling strobe generating a regular sequence of triangles. In this case the amplitude of the regular triangular wave $e(t)$ is $\gamma/2$. The quantization noise is the expected value of the noise power, the expected value of the squared noise amplitude:

$$N_q^2 = \left\langle e^2 \right\rangle = \lim_{t' \to \infty} \frac{1}{t'} \int_0^{t'} e^2(t)\, dt \ . \tag{3.72}$$

Since the idling pattern is regular, it suffices to regard one period T. The average of one triangle with squared amplitude yields:

$$N_q^2 = \frac{1}{T} \int_0^T e^2(t)\, dt = \frac{1}{T} \frac{(\gamma/2)^2 \cdot T}{2} = \gamma^2/8$$

$$\Rightarrow \quad N_q^2 \approx 2.3 \cdot 10^{-10}\,\text{V}^2 \ . \tag{3.73}$$

The signal power is approximately that of a square wave $x(t)$ with duty cycle of 50%. The amplitude of the emitted excitation pulse into $50\,\Omega$ is $A_0 = 200\,\text{mV}$, thus

$$S^2 = \left\langle x^2 \right\rangle = 1/2 \cdot A_0^2 + 1/2 \cdot 0 = A_0^2/2 \ \Rightarrow \ S^2 = 2.0 \cdot 10^{-2}\,\text{V}^2 \ . \tag{3.74}$$

The SQNR yields:

$$\text{SQNR} = \sqrt{S^2/N_q^2} \approx 10^4 = 80\,\text{dB} . \tag{3.75}$$

This is the SQNR expected for the chosen parameter values and under ideal conditions. It will be shown later by means of oscilloscope traces that the actual idling pattern is far from being ideal and that the real SQNR is much larger than expected.

Doubts are remaining concerning the suitability of the SQNR for the assessment of OBSERVER's performance. This parameter is a lump measure since it integrates the whole spectrum and is unable to consider local signal properties like edges which are so important for TDR application. The striking point with TDR is rather amplitude resolution than bulk noise power.

Furthermore most of the formulas for SQNR calculation assume random amplitude error presuming random input signals like speech and music but TDR reflectograms are deterministic. Another unsatisfying observation is that the SQNR could be easily modified by the duty cycle of the square wave.

Comparison to the Theoretical Noise Formula

As stated before *Hawksford and Darling* (1990) formulated a simple expression to estimate the SQNR in delta modulation (Eq. 3.47). Despite its simple form the formula is not easy to understand, especially its limitations. The following values are used to be fed into the SQNR-formula:

- TDR step pulse frequency $f_{\text{step}} = 2$ MHz (Eq. 3.69),

- sampling frequency $f_{\text{clk}} = 1/T_s^{(r)} = 4 \cdot 10^{14}$ Hz (Eq. 3.66),

- signal bandwidth $f_b = 1.4$ GHz (Eq. 3.83).

With these parameters the SQNR estimate based on Eq. 3.47 yields:

$$\text{SQNR} \approx 200 \text{ dB} . \tag{3.76}$$

This extremely high value is totally wrong. It completely overestimates the real SQNR. Especially the 3rd power of the sampling frequency blows up the result. *Hawksford and Darling* (1990) developed the formula for real-time sampling systems but in principle it should be applicable to equivalent-time sampling, too. It is not quite clear, where the deficiencies of the theoretical approach are in detail, but it can be stated, that the formula of *Hawksford and Darling* (1990) is not applicable to the OBSERVER.

3.5. Square Wave Generators

Both signal generators for excitation and clock pulse generation are very similar. The difference is that the former is equipped with an impedance matching circuit to adapt to the $50\,\Omega$ connecting probe cable (s. Fig. 3.12). The variable output frequency of such a square wave source is generated by Direct Digital Synthesis (DDS). Its output signal is filtered and transformed into a square wave by a kind of a comparator referred to as *pulse shaper*. The three components DDS, filter, and pulse shaper will be explained in more detail.

3.5.1. Direct Digital Synthesis

Direct Digital Synthesis (DDS) is a method to create sinusoidal voltage or current outputs with programmable frequency and phase (*Analog Devices*, 1999b). The first quarter of a digitized sine, i.e. phase angle $\phi \in [0, \pi/2)$, is stored in a read-only memory (ROM). The whole period can be generated from this information due to the symmetry of the sine. An address counter with programmable increment steps through the memory. The digital amplitude information is read from the memory cell the counter is pointing at, converted to an analog value, and given out. The address counter is clocked at a fixed rate but the programmable step size decides how many hops are necessary to complete one period of the sine-wave. This is how the output frequency is determined.

The reading of digitized values from a ROM is in effect nothing but sampling a sinusoid function. The DDS output is a staircase function and a more or less rough approximation of a continuous sinusoid. But the sampling theorem states that a sampled signal can be reconstructed completely if no frequency components of the signal are above the Nyquist frequency. The staircase function contains high frequency components which are necessary for the fast transitions between the piecewise constant signal levels. If the sinusoidal function is filtered arbitrarily, the fundamental sine-wave remains and is fully reconstructed, even at points, which were not sampled.
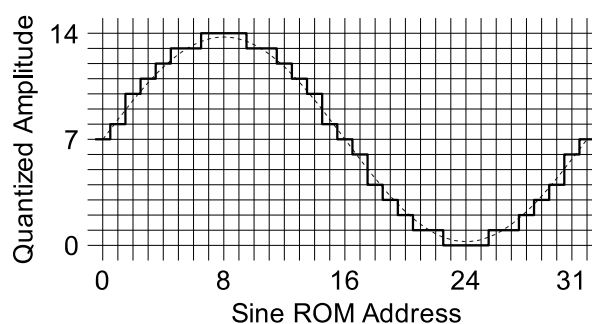

Figure 3.14.: Simplified example for a sine stored in DDS ROM. Memory size: $P = 5\,\mathrm{bit}$ ($2^P = 32$ storage cells), amplitude resolution: $Q = 4\,\mathrm{bit}$ ($2^Q = 16$ quantization levels, 15 used).

To better understand the principle of DDS it is helpful to imagine a whole period of a sinusoid with 2^P samples held in ROM. The resolution of the amplitude quantization is determined by the number Q of bits of a storage cell (Fig. 3.14). A so-called *phase accumulator* of N bit width generates the address a which points to a particular ROM cell. It is a flexible address counter, which is capable of holding a value a_i, to increment it by a programmable step size n_ϕ, and to store the result again. For now it is assumed that $N = P$. When the counter exceeds the maximum address $2^N - 1$, it rolls over. The carry is ignored, thus the address counter is cyclic modulo 2^N, i.e.

$$a_{i+1} = (a_i + n_\phi) \bmod 2^N \ . \tag{3.77}$$

This way the stored sine-wave is read from the beginning again. The staircase approximation of the sine at the output of the DDS comprises

$$n_{\mathrm{DDS}} = \frac{2^N}{n_\phi} \tag{3.78}$$

samples per period. The initial phase ϕ_0 is programmable, too. Before the accumulator starts incrementing it is initialized with a fixed value a_0 corresponding to the selected phase offset ϕ_0. The offset can be used to change the phase angle of the sine-wave relative to another DDS synchronized by the same master clock.

The phase accumulator is clocked by an external master clock of fixed frequency f_{mclk}. At each clock pulse the address a is incremented by n_ϕ and the stored digital sinusoid amplitude, the address currently points at, is transformed into an analog voltage by means of an internal digital-to-analog converter (DAC).
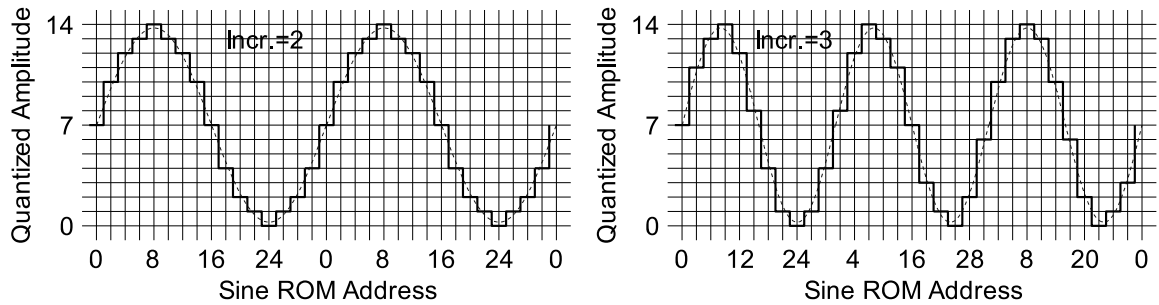
Figure 3.15.: Two examples of DDS sine approximations with different output frequencies due to different phase increments. Left: $n_\phi = 2$, right: $n_\phi = 3$. The staircase pattern varies from cycle to cycle for $n_\phi = 3$.

f_{mclk} determines the rate at which the ROM is read out and the address counter increment controls how many steps are necessary to loop through one complete period of the sinusoid: The larger the increment the faster the completion of a cycle and the higher the frequency of the sinusoid at the DDS output (s. Fig. 3.15). The output frequency is given by

$$f_{\mathrm{DDS}} = \frac{n_\phi}{2^N} \cdot f_{\mathrm{mclk}}, \ n_\phi \in [0, 1, \dots 2^N/2] \ . \tag{3.79}$$

The smallest step size $n_\phi = 0$ leads to a standing address counter yielding a constant output. The largest increment $n_\phi = 2^N/2$ leads to a sampled sine-wave of only two points, which corresponds to the Nyquist frequency. The accuracy is given by the finest frequency step of

$$\Delta f_{\text{DDS}} = \frac{f_{\text{mclk}}}{2^N} \ . \tag{3.80}$$

Phase Truncation

In real DDS chips the phase accumulator is wider than the DDS ROM, i.e. $N > P$. Only the P most significant bits of the phase accumulator are used to address the sine memory. The ROM size is limited due to its high price. The reason for using more bits in the phase accumulator than necessary lies in the improved frequency resolution (Eq. 3.80).

This so-called *phase truncation* leads to periodic errors in the DDS signal amplitude generating additional spurious frequencies in the spectrum of the synthesized sine-wave. These spurs are dependent on three factors: phase accumulator width (N bit), ROM size (P bit), and phase increment n_Φ. The first two are inherent to the DDS hardware, the last is varies with DDS output frequency. The spur pattern is not easy to predict. A detailed discussion about the effect of phase truncation and other sources of errors like DAC nonlinearity or reference clock timing jitter is found in the comprehensive DDS tutorial *Analog Devices* (1999b).

Integrated DDS Circuits Used in OBSERVER

OBSERVER needs two identical DDS chips to generate TDR excitation pulse and sampling pulse train. Both circuits are driven by a common master clock (s. Fig. 3.12). The DDS chip brands are AD9832 (*Analog Devices*, 1999a) and AD9835 (*Analog Devices*, 1998) for OBSERVER, version V1 and V2, respectively. In both cases the DDS are driven with their maximum master clock frequency. This is mostly due to phase truncation, which produces periodic errors in the DDS amplitude.

OBSERVER	V1	V2
DDS	AD9832	AD9835
f_{mclk}	25 MHz	50 MHz
$f_{\text{DDS}}^{\text{max}}$	12.5 MHz	25 MHz
Phase accum. width (N)	32 bit	32 bit
ROM address width (P)	12 bit	12 bit
DAC resolution	10 bit	10 bit
Δf_{DDS}	5.8 mHz	11.6 mHz

Table 3.1.: Important parameters of two DDS circuits used in OBSERVER V1 and V2, respectively.

Special phase registers can be used to determine the initial phase of the sine-wave, i.e. the initial value of the phase accumulator. The initial phase can be programmed with a resolution of $P=12$ bit.

Two examples of unfiltered DDS spectra (AD9832) with different fundamental frequencies are given in Fig. 3.16. The SFDR is not better than approx. 55 dB. The spur pattern is dependent on the output frequency.

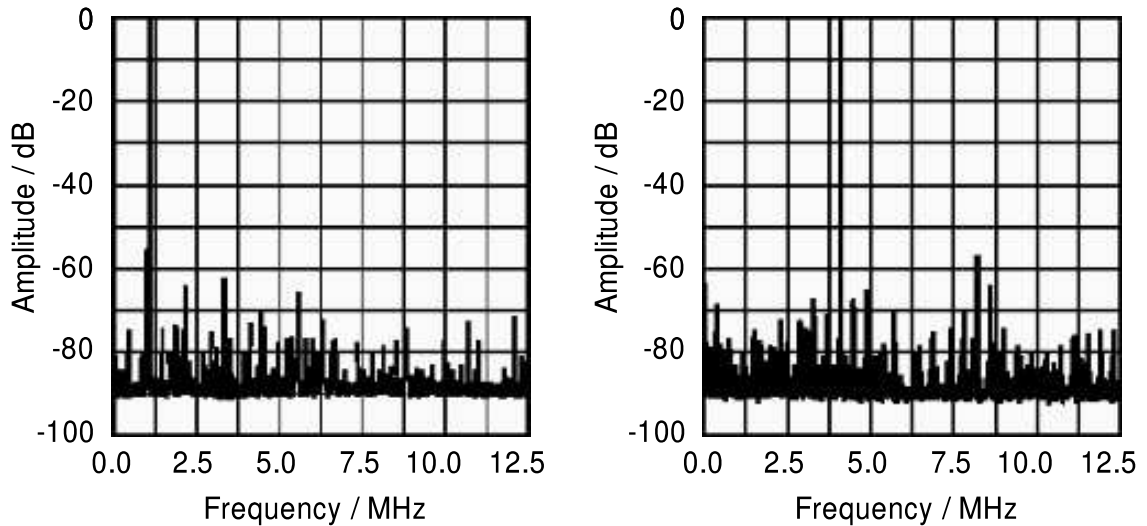Figure 3.16.: Unfiltered spectra of AD9832 DDS taken from the data sheet (*Analog Devices*, 1999a). Master clock frequency $f_{\mathrm{mclk}} = 25$ MHz, output frequency $f_{\mathrm{out}} = 1.1$ MHz (left) and $f_{\mathrm{out}} = 4.1$ MHz (right).

3.5.2. Low-Pass Filter

The generated sine-wave approximation of the DDS has to be filtered to suppress spurs and to yield the fundamental sinusoid as pure as possible. Therefore high frequency components have to be cut off. This is done by a low-pass filter. Its name indicates, that it lets pass spectral components with lower frequency, while higher frequencies are blocked. Since the filter can be regarded as a linear time invariant system, its effect on the input signal can be described either by a convolution of the input signal with the filter's pulse response function (PRF) in time-domain or by multiplying the spectrum of the input function with the filter's transfer function (TF) in frequency-domain. For the following investigation the spectral view has been chosen because it is better suited to display the filter characteristics and the interpretation of results is more lucid than in time-domain.

Generally a filter leads to an attenuation and a phase shift of a given frequency component of the input signal (Fig. 3.19). At lower frequencies a typical low-pass transfer function shows a flat plateau at the level of 1 up to a certain frequency (Fig. 3.19, dashed line). The corresponding frequency range is called *pass band*, because all frequency components of the input signal lying in the pass band are multiplied by 1, thus they leave the filter without attenuation. The frequency range at which the transfer function tends to 0 is referred to as *stop band*. A transition zone lies between pass and stop band, which is characteristic for the given filter.

An important parameter of such a filter is the cutoff frequency f_c. It is per definition the frequency at which the amplitude is attenuated by 3dB, i.e. the amplitude of the input signal's spectral component with frequency f_c is damped by a factor of $1/\sqrt{2} \approx 0.7$. Since the OBSERVER has been designed to run at frequencies up to 4 MHz, the filter cutoff frequency f_c was chosen to be 4.5 MHz.

For the sake of simplicity it was decided to use a passive filter consisting of passive electronic parts like capacitors and inductors. These filters are suitable for frequencies above 100 kHz. Many filter families of different characteristics exist. A 5th order Butterworth filter with a design cutoff frequency 4.5 MHz was chosen. The attenuation of an n-pole Butterworth filter is given by

$$\frac{A}{A_0} = \frac{1}{\sqrt{1 + \left(\frac{f}{f_c}\right)^{2n}}} \, , \tag{3.81}$$

with A the frequency dependent amplitude and A_0 an arbitrary reference amplitude. To check whether the real characteristics of the filter on the printed circuit board meets the design goal, measurements of signal amplitudes before and after the filter were taken by an oscilloscope for different frequencies.

Input and output signal of the low-pass filter for the frequency $f = 10\,\text{kHz}$ are given in Fig. 3.17. Input and output amplitude are the same and no phase shift occurs. The signal amplitude $A_0 \approx 1.02\,\text{V}$ is taken as reference for the following output amplitudes at different frequencies.
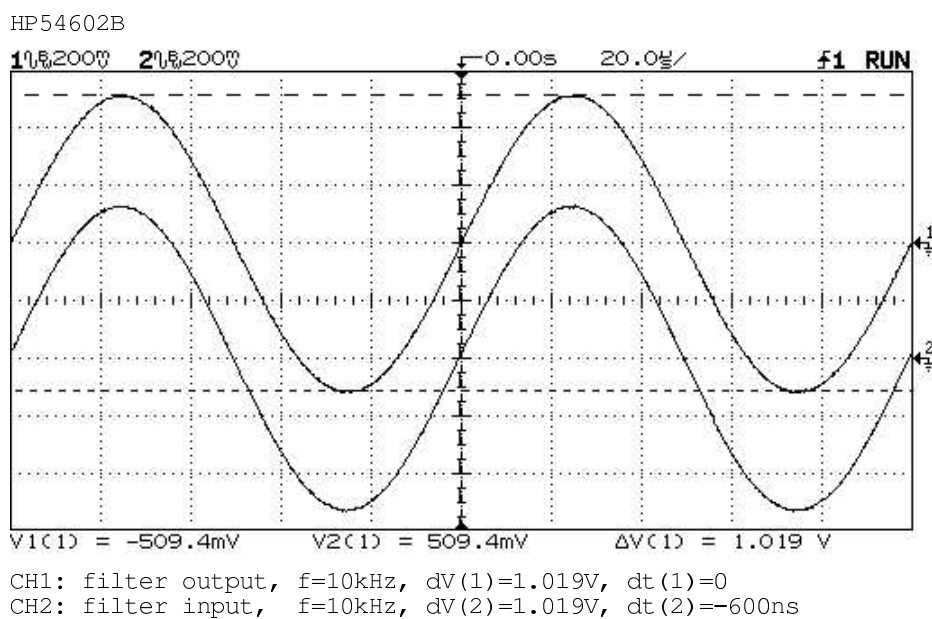
Figure 3.17.: Amplitude and phase of a sinusoid before and after the filter. Trace 1: filter output; trace 2: filter input; $f = 10\,\text{kHz}$.
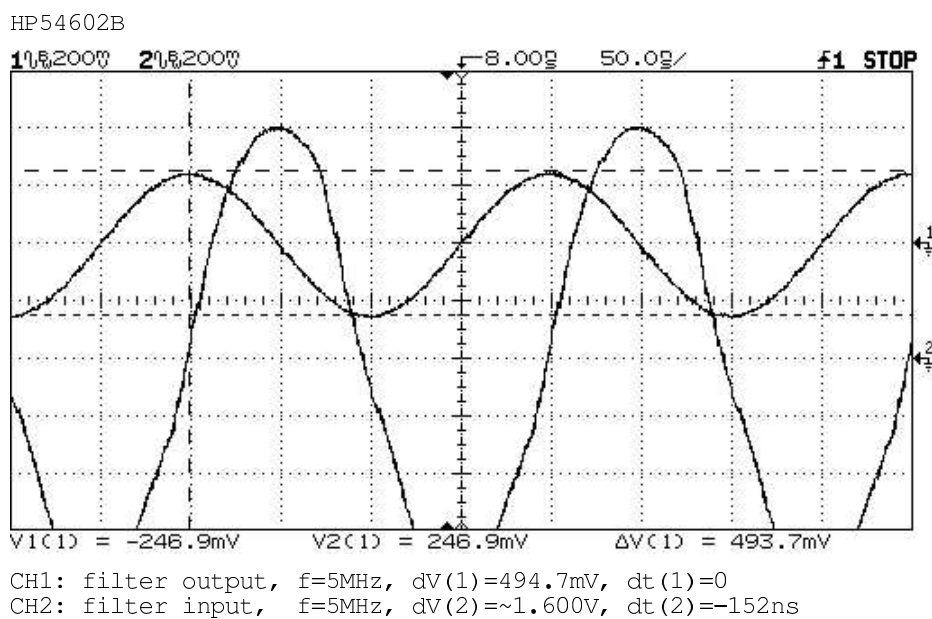
Figure 3.18.: Amplitude and phase of a sinusoid before and after the filter. Trace 1: filter output; trace 2: filter input; $f = 5\,\text{MHz}$.
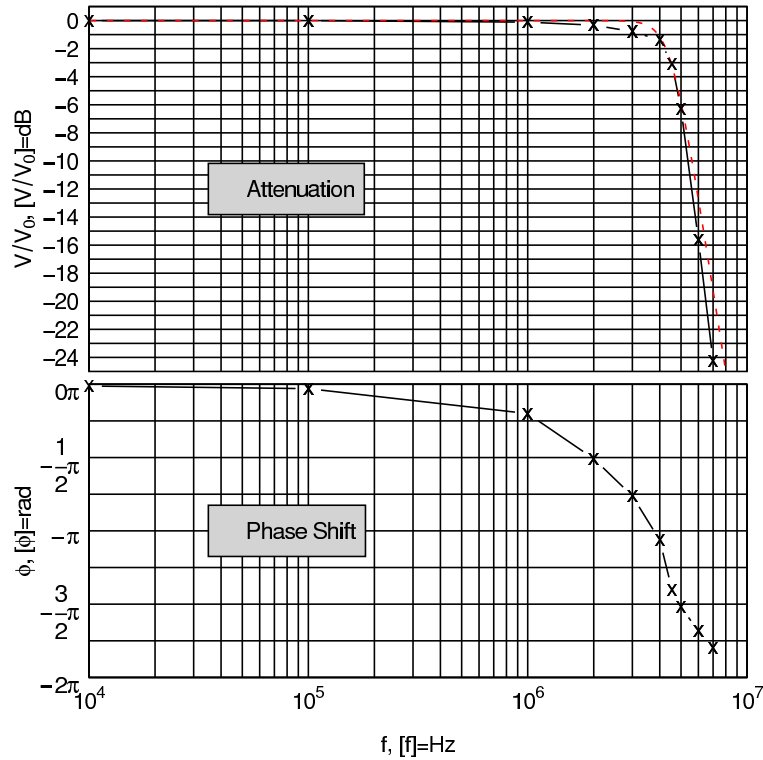
Figure 3.19.: Bode diagram of 5pole Butterworth low-pass filter, cutoff frequency $f_c = 4.5\text{MHz}$. Frequencies below 10kHz are omitted for clearance. Dashed line: theoretical attenuation, marks: measurements of attenuation and phase shift.

The attenuating effect of the filter at $f = 5\,\text{MHz}$ is displayed in Fig. 3.18. The output amplitude is obviously smaller than A_0 and a phase shift of approx. $1.5\,\pi$ is apparent. The amplitude of the input signal has been increased due to the effects of the filter. This type of measurement was repeated for a couple of different frequencies the results of which are plotted in Fig. 3.19 together with the expected attenuation (Eq. 3.81) from the filter design parameters. The real filter behavior meets the theoretical very well.

3.5.3. Comparator and Jitter

The comparator is necessary to generate a square wave from the programmable DDS output sinusoid. OBSERVER uses these square waves to emit the TDR excitation pulse and to generate the sampling strobes. Timing uncertainties between the two signal generators lead to a degradation of the sampling performance. The comparator is sensitive to a number of error sources which may lead to imprecise timing. Therefore the transformation of sine to square wave has to be looked at in more detail.

The sine-wave generated by DDS is filtered and fed into one input of the comparator. The second input is held at a constant reference voltage level which is the threshold for switching. If the sine exceeds the threshold voltage a logic 1 will occur at the

comparator's output. Otherwise the output will be in the logic state 0. A comparator is a zero cross detector for the input voltage difference. It maps the continuous input difference to two discrete output states. An arbitrary input signal is transformed into a sequence of 0 and 1 physically represented by two different voltage levels yielding a square wave.

The ECL line driver MC100EP16 is not a genuine comparator but due to the ECL's differential input stage it can be used as such. Its switching time is in the range of 250 ps, whereas the typical frequency of the sinusoidal input is around 1 MHz leading to a period of 1 μs. On the ECL time scale the 1000 times slower sinusoid looks almost like constant during the switching process. The comparator has to detect the exact instant when the two input voltages become equal while the reference input is constant and the other (the sine-wave) is approaching this threshold very slowly.

It is clear that small variations of the input can lead to large uncertainties in the exact timing of the output square wave, an effect called jitter. Jitter may be induced by random noise superposing the differential input signal (Fig. 3.20). Due to this amplitude disturbance the switching threshold may be crossed earlier or later than expected.
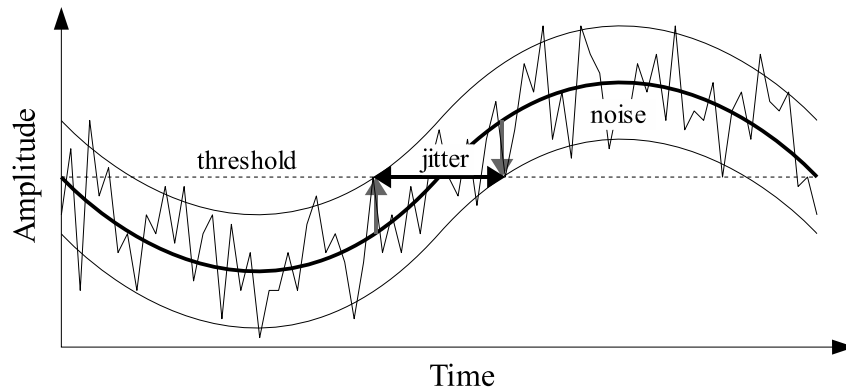
Figure 3.20.: Jitter due to random noise. Noise superposing the fundamental sinusoid (thick line) leads to a timing uncertainty for crossing of the voltage threshold.

Moreover with only one switching threshold the comparator may toggle multiple times when the difference between input signal and threshold becomes small. This toggling means an undefined state and would lead to unpredictable behavior in the electronics. Furthermore additional switching transients transfer unwanted energy into the circuit leading to increased signal disturbance due to capacitive or inductive coupling (crosstalk).

The toggling of the comparator can easily be avoided by introducing hysteresis, i.e. a second threshold (Fig. 3.21). When the rising input signal crosses the upper threshold, the output is switched to logic 1. At the same time switching threshold drops to a lower level instantaneously increasing the difference between input and threshold. Thus
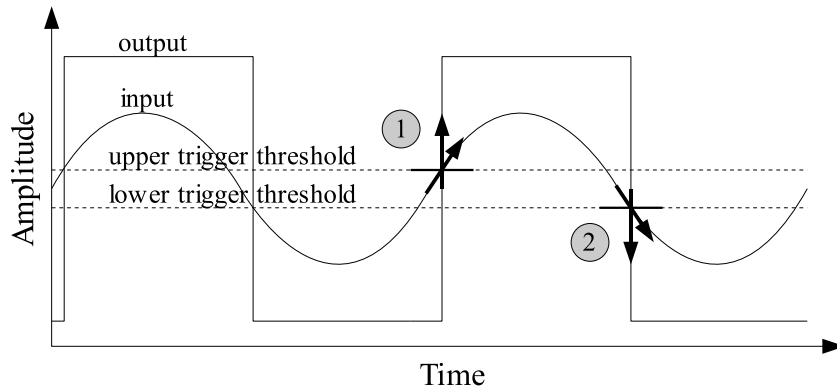
Figure 3.21.: Hysteresis. Output switching occurs when (1) rising input signal crosses the upper trigger threshold or (2) falling input signal crosses the lower trigger threshold.

additional noise on top of the input signal cannot lead to a second switching right after the first one. Now the falling branch of the input signal has to cross the lower threshold to provoke an output switching. When the output goes to logic 0 the threshold is raised again.
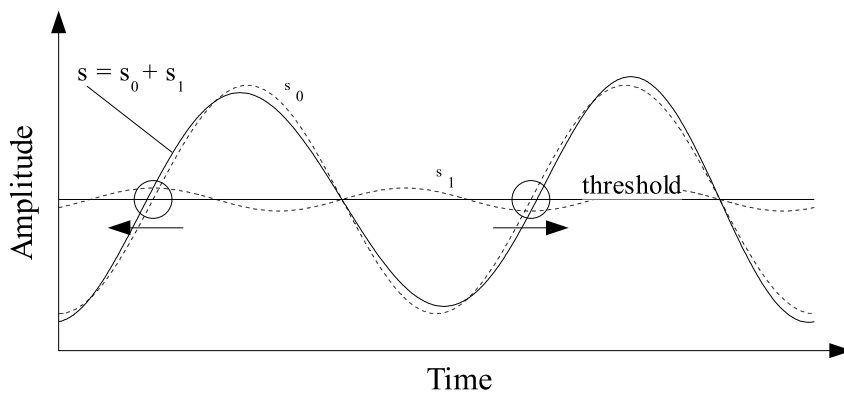
Figure 3.22.: Jitter due to spurious spectral components. s_0: fundamental oscillation; s_1: spurious component with small amplitude; $s_0 + s_1$: superposition of both oscillation leads to imprecise timing of threshold crossing.

Another source of jitter are spurious oscillations superposing the fundamental sine-wave (Fig. 3.22). These spurs manifest themselves as larger spectral lines reaching above the noise floor of the spectrum. The jitter originating from spurs is not purely random but reveals periodic behavior.

If the spurs were pure harmonics, i.e. their frequency were a multiple of the fundamental, the superposition would lead to a distorted sinusoid, but the time span between two adjacent switching instants would be constant. The measured amplitude spectra of the DDS used in OBSERVER V1 (s. Fig. 3.16) indeed show non-harmonic spurious components which may lead to jitter.

In the next section about performance measurements will be shown, that the jitter in OBSERVER's signal generators is a mixture of both, random and non-random components. The very nature of the latter is still not well understood. This so far unpredictable behavior of some jitter components is considered to be the major drawback of the current electronic circuit but newer DDS parts are available (e.g. AD9954) with much better performance and lower spurious frequency content. These parts would probably solve the problem.

3.6. Performance Measurements with OBSERVER V1

3.6.1. Excitation Pulse Rise-Time

The excitation pulse is driven by an ECL line receiver MC100EP16 (*ON Semiconductor*, 2001a). The data sheet states that its nominal rise-time may be faster than

$$t_r^{(d)} = 250 \, \text{ps} \, , \tag{3.82}$$

depending on the load connected to the output. The associated frequency bandwidth f_b of the pulse spectrum is estimated by means of the common rule[10]

$$t_r \cdot f_b = 0.35 \; \Rightarrow \; f_b = 1.4 \, \text{GHz} \, . \tag{3.83}$$

To reliably measure such a short pulse rise-time with a measurement error below 3% a digital storage oscilloscope of approx. 3 GHz analog bandwidth and a sampling frequency of 6 Gsamples/s would be required (*Agilent*, 2002). Such a high performance instrument was not available during the design phase of OBSERVER. The only oscilloscope is a HP54602B with 150 MHz analog bandwidth.

The best instrument with the highest bandwidth available is the OBSERVER itself. Thus this TDR prototype is used to give information about its own excitation pulse. Of course, an unknown pulse is tried to be measured with an instrument of unknown bandwidth. Therefore the determined pulse rise-time determined throughout this section is a lower bound. The real pulse rise-time is at least as fast as the measured one.

The following investigations have been done with OBSERVER V1. A RG58 coax cable of 0.47 m length was connected to the output of the instrument's excitation pulse generator, optionally plugged into the oscilloscope via a BNC T-connector. An oscilloscope probe was hooked to the delta modulator's feedback to measure V_{out}. The sampler of OBSERVER is used to stretch the time-base of the TDR signal so that it can be viewed with the low bandwidth oscilloscope.

---

[10]The factor of 0.35 in this rule is valid for oscilloscopes with Gaussian impulse response (*Agilent*, 2002).

HP54602B
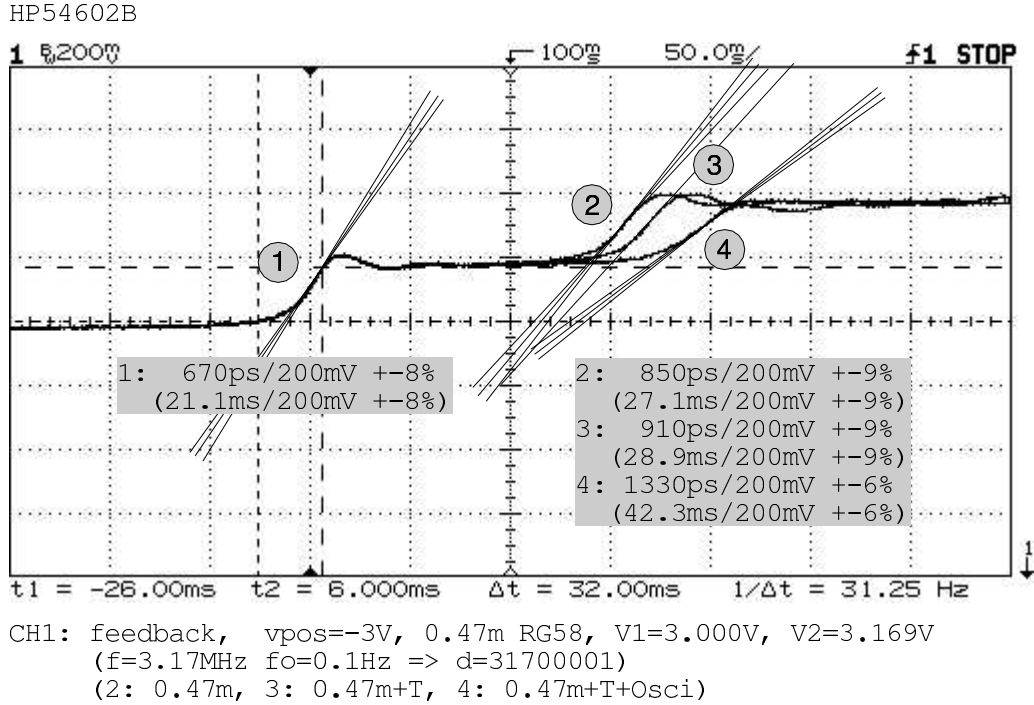
Figure 3.23.: TDR reflectogram of OBSERVER V1 to examine its excitation pulse. 1: emitted excitation pulse edge; 2: reflection after 0.47 m coax RG58; 3: T-connector hooked to the end of the coax; 4: T-connector plugged into the oscilloscope. $f_{\text{step}} = 3.17\,\text{MHz}$, $f_{\text{offset}} = 0.1\,\text{Hz}$.

Fig. 3.23 shows the oscilloscope traces of V_{out} for different experimental configurations in equivalent-time. The excitation pulse repetition rate is $f_{\text{step}} = 3.17\,\text{MHz}$ with an offset of $f_{\text{offset}} = 0.1\,\text{Hz}$ yielding a dilation factor of $s = 3.17 \cdot 10^7$ (Eq. 3.52). The oscilloscope's time-base of 50 ms/division has to be scaled by s to yield the real time-base of the pulse. Thus the new horizontal resolution is approx. 1.6 ns/div.

The first edge (1) is the emitted pulse. Its amplitude is 200 mV (in 50 Ω). On the displayed equivalent-time scale it reveals 21.1 ms rise-time. Translated to real-time, the measured rise-time for OBSERVER V1 yields

$$t_r^{(m)} = 670\,\text{ps} .\tag{3.84}$$

As stated before this is a lower bound. The real rise-time is equal or faster than $t_r^{(m)}$.

After approx. 5 ns (in real-time) the reflection at the open end of the coax occurs (2). After having passed 1 m coax (0.5 m forth and back) the remaining pulse rise-time is lowered to 850 ps. This is due to the low-pass characteristics of the cable. An additional T-connector at the end of the coax (3) prolongs the round-trip travel-time of the pulse slightly without a significant change of rise-time. But if the T-connector is plugged into the oscilloscope (4) the signal edge will be depressed due to the additional capacitive load of 13 pF at the oscilloscope input.

In the next experimental setup a moisture probe was connected to the OBSERVER to investigate the actual pulse form reaching the probe. The probe consisted of a 1 m long

HP54602B


```
1 ₿200ᵐ�室                     ⌐—100ᵐ�室    50.0ᵐ�室/      Sngl⨎1  STOP
```

V1(1) = 3.000 V   V2(1) = 3.169 V   ΔV(1) = 168.8mV

```
CH1: feedback,  vpos=(-2.8V,-3.2V,-3.6V),  0.47m RG58
     (f=4.0001MHz fo=0.1Hz => d=40001001)
```

HP54602B


```
1 ₿200ᵐ�室                     ⌐—1.20s    50.0ᵐ�室/      Sngl⨎1  STOP
```

V1(1) = 3.000 V   V2(1) = 3.169 V   ΔV(1) = 168.8mV

```
CH1: feedback,  vpos=(-2.8V,-3.2V,-3.6V),  0.47m RG58
     (f=4.0001MHz fo=0.1Hz => d=40001001)
```
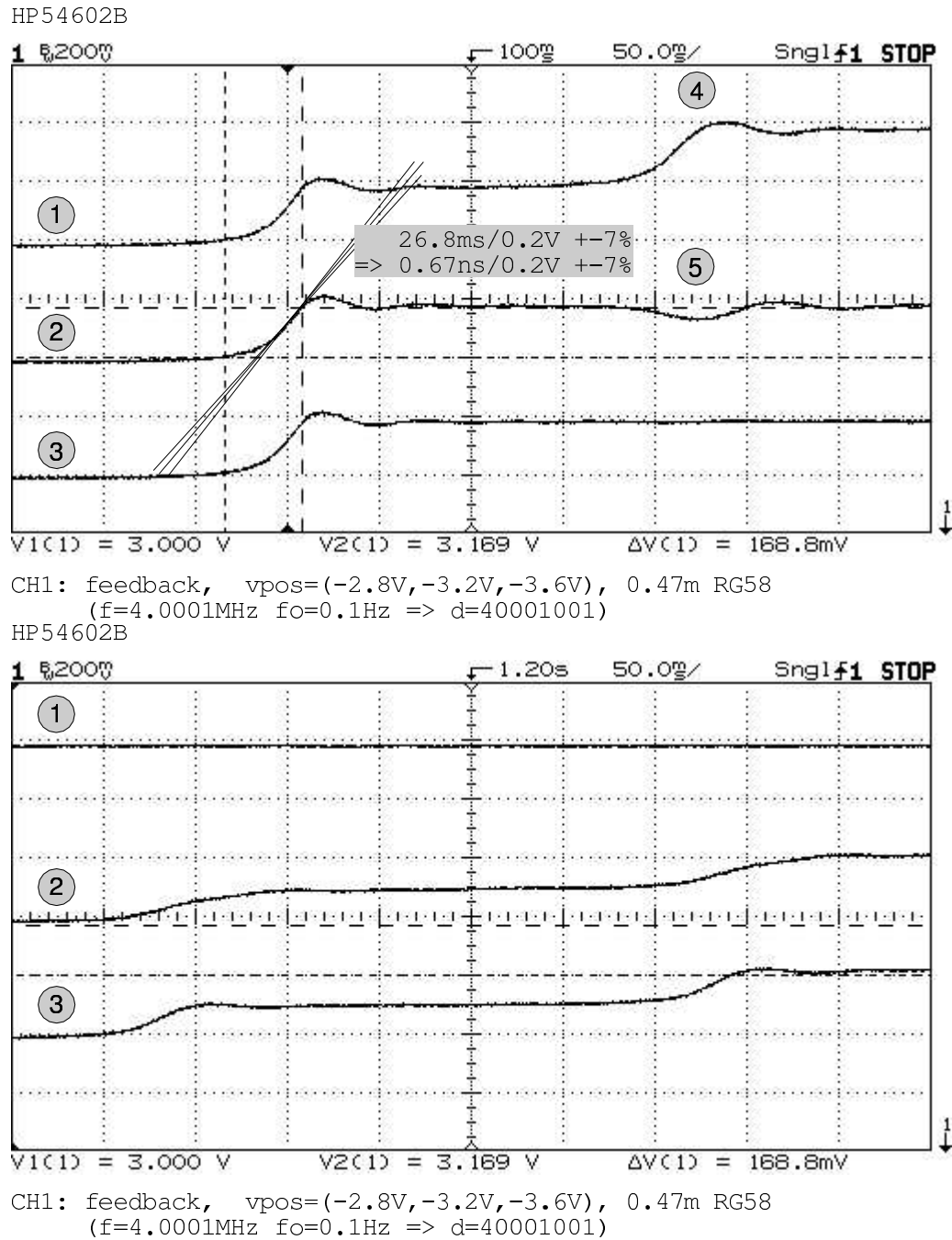
Figure 3.24.: Influence of moisture probe connected to OBSERVER V1 on the traces of V_{out}. Top: oscilloscope timing window around initial step. 1: 0.47 m RG58 soldered to OBSERVER, coax terminated with open T-connector. 2: connecting cable (2 m RG58) of moisture probe plugged to the T-connector and T-connector hooked to the oscilloscope. 3: same as 2 but T-connector un-plugged from oscilloscope; 4: reflection at open end; 5: disturbance due to oscilloscope connection. Bottom: oscilloscope timing window shifted to the moisture probe. 1,2,3: same experimental configurations as before. $f_{\text{step}} \approx 4\,\text{Mhz}$, $f_{\text{offset}} = 0.1\,\text{Hz}$.

3-wire ribbon cable (s. App. B.1) with a RG58 connecting cable of 2 m length. Including the piece of cable soldered to the OBSERVER the total coax cable length yielded 2.5 m or 5 m forth and back. The resulting traces are given in Fig. 3.24. Especially trace 3 impressively demonstrates that even a relatively short connecting cable (2.5 m) reduces the rise-time considerably before the pulse enters the moisture probe.

Summary

The measured pulse rise-time $t_r^{(m)} = 670$ ps with OBSERVER V1 is more than twice as large as expected from the data sheet. Strictly spoken the quality of this rise-time measurement cannot be unambiguously assessed because the bandwidth of the measuring instrument is not well known. But the rise-time has been improved much with OBSERVER V2 by adding an additional ECL line receiver in series to the first one. Since the sampler is capable of tracking even faster signal edges it is plausible that the measured rise-time $t_r^{(m)}$ is near the truth.

The above conducted detailed pulse rise-time measurement was not repeated for OB-SERVER V2 because of the remaining uncertainty due to the unknown sampler bandwidth. The pulse rise-time should be determined with a well-known high-speed oscilloscope.

Finally it has to be kept in mind that low-pass effects of coaxial cables will degrade every fast rising pulse edge to nanoseconds after only a few meter of signal propagation. This effect is unavoidable and so are long connecting cables in field application. Therefore the run for ever faster signal rise-time in such kind of application deems to reveal a lack of understanding how the system of TDR, cable, and probe is actually behaving in real field applications.

3.6.2. Jitter

Every sample has an uncertainty in timing because clock and TDR pulse occur at times which deviate from the ideal. Thus samples can be situated on the time axis only with a certain probability. This *timing jitter* is a stochastic process which can have more than one physical cause. The jitter generally differs from sampler to sampler. Even within one sampler different configurations or operation modes can cause different jitter patterns. These uncertainties cause systematic errors in sampling, which may be difficult or impossible to compensate depending on the jitter's nature.

The sampler of the OBSERVER suffers from jitter, too. The different jitter patterns have been investigated with an oscilloscope. Unfortunately the applied oscilloscope HP54602 is not capable of measuring the jitter directly, because its bandwidth is too limited. Furthermore in the relevant short time scale (max. horizontal resolution is 2 ns/div) it has to perform equivalent-time sampling collecting sampling points from a large number of signal realizations. But to reliably assess jitter it is necessary to compare different signal edges with each othesampled completely in real-time. Some modern sampling oscilloscopes (so-called digital phosphor oscilloscopes) are tracking fast transient signals

in real-time with an unprecedented repetition rate, store a number of them in a local memory, and are thus able to give information about the signal statistics.

With the oscilloscope available the jitter has to be measured indirectly with a trick. Therefore excitation pulse and sampling clock of OBSERVER are run at the same frequency ($f_{\text{step}} = f_{\text{clk}}$) so that a constant sampler output voltage V_{out} is expected with a level equal to the excitation pulse voltage at the sampling instant. The sampling instant in moved to the middle of the first fast rising edge of the TDR trace to transform a variation in sampling time to a variation in voltage level.

The rising edge of the TDR signal can be locally approximated around t_0 by a linear function, i.e. its Taylor series is cut after the first-order term. Then the time uncertainty Δt is transformed to a voltage uncertainty ΔV by

$$\Delta V \approx \left. \frac{\partial V}{\partial t} \right|_{t_0} \Delta t \ . \tag{3.85}$$

This relationship can be used to derive the timing jitter from the measured voltage uncertainty given the slew rate $\partial V / \partial t$. According to the last section the real pulse rise-time is unknown but the best estimate is the measurement performed by OBSERVER itself. The initial pulse step into $50\,\Omega$ is $V_r = 200\,\text{mV}$. Therefore is assumed that

$$\frac{\partial V}{\partial t} \approx \frac{V_r}{t_r} \approx \frac{V_r^{(m)}}{t_r^{(m)}} = \frac{200\,\text{mV}}{670\,\text{ps}} \ . \tag{3.86}$$

for OBSERVER V1. The probability distribution of the jitter turned out to be strongly dependent on the chosen output frequency. Different amplitudes and even changing multi-modal distributions occurred for different DDS settings.

In the first example of Fig. 3.25 both signal generators run exactly at $f_{\text{step}} = f_{\text{clk}} = 1.0\,\text{MHz}$, corresponding to a excitation pulse period $T_{\text{step}} = 1\,\mu s$. To shift the sampling instant into the first rising edge the phase offset of the clock DDS was set to $n_{\text{p}} = 11$, leading to a delay between excitation pulse and clock signal of

$$t_{\text{d}} = \frac{n_{\text{p}}}{2^{12}}\, T_{\text{step}} \approx 2.7\,\text{ns} \ . \tag{3.87}$$

The oscilloscope is triggered by the excitation pulse signal holding it at a fixed screen position. Neither the delay between the signals nor the jitter of the clock pulse can be seen due to the chosen time scale of 200 ns/division.

Ideally the output of the sampler should be a constant voltage leading to a thin horizontal signal trace on the oscilloscope screen. In reality the trace moves vertically leaving a broad band of possible voltages. Unfortunately the distribution of the trace's vertical position cannot be derived from the oscilloscope, but it is observed that a fast stochastic component was superposed by a much slower component with a large mean amplitude which reveals a complicated periodic nature leading to nearly discrete vertical jumps of the horizontal trace in the range of seconds. From Fig. 3.25 the total uncertainty in timing derived from the limits of the voltage band by means of Eqs. 3.85 and 3.86 yields:

$$\Delta t = \left(\frac{\partial V}{\partial t} \right)^{-1} \Delta V \approx \frac{670\,\text{ps}}{200\,\text{mV}} \cdot 125\,\text{mV} \approx 420\,\text{ps} \ . \tag{3.88}$$

HP54602B


```
CH1: feedback,    vpos=-3V, 0.47m RG58 no term
CH2: TDR signal,  vpos=-3V, 0.47m+T+15m+OE RG58, f=1.0MHz
CH3: sam. pulse,  vpos=-5V, TEK P6109, f=1.0MHz phc=11
CH4: -
```

Figure 3.25.: Sampler output uncertainty due to timing jitter between TDR signal (upper) and sample clock (lower) for $f_{step} = f_{clk} = 1\,\mathrm{MHz}$. The broad band ($\Delta V = 125\,\mathrm{mV}$) shows the area covered by the varying output level. The oscilloscope is not capable to resolve the multi-modal distribution within this uncertainty band.

To demonstrate the nontrivial dependency of the jitter on the DDS settings the frequencies were slightly modified to $f_{step} = f_{clk} = 1.0001\,\mathrm{MHz}$. Fig. 3.26 clearly shows that the voltage uncertainty and therefore the jitter was reduced dramatically. In this case the influence of a slow periodic component is not recognizable anymore. On the regarded time scale the process was deemed to be random. The measured width of the voltage band is $\Delta V = 37.5\,\mathrm{mV}$ yielding a timing uncertainty of

$$\Delta t \approx 125\,\mathrm{ps}\ . \tag{3.89}$$

Summary

A broad spectrum of jitter dynamics are realizable by changing the DDS frequencies. An extremely bad and an average case were demonstrated. It is difficult to describe the underlying stochastic processes and to identify their origins. For some DDS settings even apparently multi-modal distributions emerged showing the interference of at least two dynamic processes. Sometimes the total process could be split into a slow deterministic component of complicated dynamic and a fast random component.

```
HP54602B
```



```
CH1: feedback,    vpos=-3V, 0.47m RG58 no term
CH2: TDR signal,  vpos=-3V, 0.47m+T+15m+OE RG58, f=1.0001MHz
CH3: sam. pulse,  vpos=-5V, TEK P6109, f=1.0001MHz phc=11
CH4: -
```
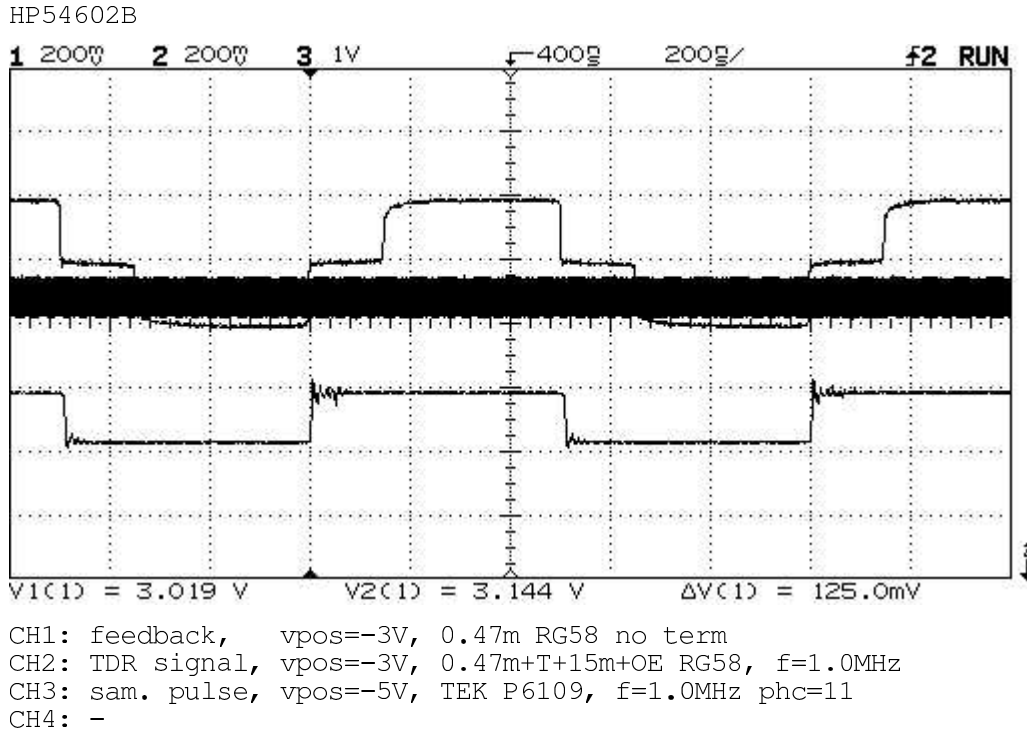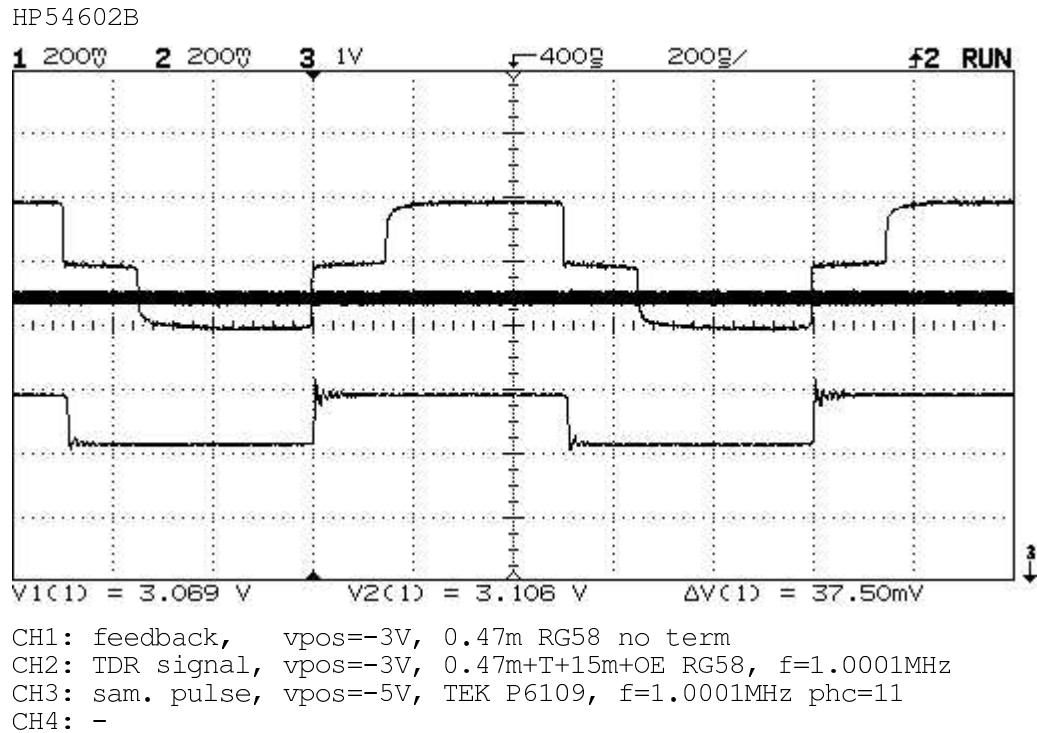
Figure 3.26.: Sampler output uncertainty due to timing jitter between TDR signal (upper) and sample clock (lower) for $f_{\text{step}} = f_{\text{clk}} = 1.0001\,\text{MHz}$. The voltage uncertainty band is $\Delta V \approx 37.5\,\text{mV}$) wide. The probability distribution of the voltage level is unimodal.

The origins of the jitter are difficult to identify, but the major contributions seem to come from the way the comparator generates a square pulse out of the filtered DDS output. Two hypotheses about the nature of the slower jitter components are made:

1. Due to inadequate suppression of high frequency components by the low-pass filter situated between DDS output and comparator small ripples of the sinusoidal staircase approximation remain and superpose the ideal sine-wave. This leads to an irritation of the switching time.

2. The switching thresholds of the Schmitt-trigger are drifting slowly due to saturation effects of the ECL line driver's input stage.

The first point could be reacted to by improved filtering and reduction of spurious frequency content of the DDS. The only effective way to increase the spurious-free dynamic range of a DDS is to increase the amplitude resolution of its internal digital-to-analog converter, i.e. by switching to improved DDS parts.

The second presumption lacks plausibility since saturation effects are expected to be frequency independent, at least a difference between $f_{\text{step}} = 1\,\text{MHz}$ and $f_{\text{step}} = 1.0001\,\text{MHz}$ should be unrecognizable for the circuit. This hypothesis is to be rejected.

But an unsatisfying fact remains: The jitter is largest for DDS settings which theoretically produce stationary staircase functions. The DDS are driven with $f_{\text{mclk}} = 25\,\text{MHz}$

and set to $f_{\text{step}} = f_{\text{clk}} = 1\,\text{MHz}$ output frequency. That means that each sine period is approximated by 25 points exactly. Therefore during each output signal period exactly the same 25 DDS ROM cells are read leading to the same 25 analog amplitude values. At least in theory this should be true for both signal generators. Even if harmonic ripples on top of the fundamental sine survived the low-pass filter, the error in comparator switching should be stationary, i.e. constant. So where does the very slow jitter component come from? The slowness of the process suggests an interference of two oscillations of similar frequency. But $f_{\text{step}} = f_{\text{clk}} = 1.0001\,\text{MHz}$ are similar, too, but in this case the slow process is imperceptible. This effect is not understood at all.

The jitter is the major drawback of the OBSERVER. The fast component has a low-pass effect but may be removed from the signal by deconvolution if it turns out to be random, i.e. has an identifiable probability density function. The slow component can lead to discrete jumps in the TDR reflectograms recorded with OBSERVER. It is probably impossible to remove them form the signal.

The jitter has to be studied in more detail for further design revisions. A relief is that a pragmatic workaround does exist: Discrete configurations of stable performance revealing low jitter may be figured out in laboratory and their exclusive selection could be guaranteed by appropriate control software.

3.6.3. Quantization Error and Other Noise Components

To examine the real quantization error of the delta modulator the sampler of OBSERVER V1 has been analyzed more closely. Version 2 of the instrument was not yet built when this investigation was conducted. The experimental amplitude granularity of OBSERVER V1 differs significantly from the optimized values calculated in Secs. 3.4.1 and 3.4.2. The suboptimal parameter choice for OBSERVER V1 is of no concern when theoretical and practical behavior of delta modulation are to be compared.

To investigate the idling pattern the delta modulator of OBSERVER V1 was set to stationary sampling ($f_{\text{step}} = f_{\text{clk}}$). The point in the TDR waveform to be sampled was selected in its baseline some nanoseconds before the first rising edge. The ideal idling pattern of the delta modulator is an alternating sequence of logic 1 and 0 (step up, step down), i.e. $101010\ldots$. In Reality the idling pattern deviates from the expected sequence as demonstrated in Fig. 3.27. The three traces of V_{out} were recorded for different sampling frequencies: f_{clk}=1, 2, and 4 MHz.

On trace 1 samples are taken every $1\,\mu\text{s}$. Ten of the sampling instants and the corresponding amplitude quantization are marked with points. The slew rate of the DM output is $|\partial V_{\text{out}}/\partial t| \approx 0.64\,\text{mV}/\mu\text{s}$. According to Eq. 3.38 actual sampling frequency and slew rate yield a amplitude granularity of $\gamma = 0.64\,\text{mV}$. The idling pattern shown in trace 1 deviates from the expected one, since it mainly comprises of an alternating sequence of double 1's and 0's, i.e. $11001100\ldots$. Furthermore V_{out} reveals a rising linear trend due to asymmetries between step up and down.

Surprisingly the overall shape of trace 2 and 3 are very similar to trace 1, although their sampling frequencies are twice and four times higher, respectively. Thus the decrease of γ has almost no effect on the granular noise. A certain voltage difference must be

reached to make the flip-flop toggle. It is stable, until the voltage difference exceeds a certain limit in the other direction. This is a strong evidence for hysteresis in the input stage of the D-flip-flop.
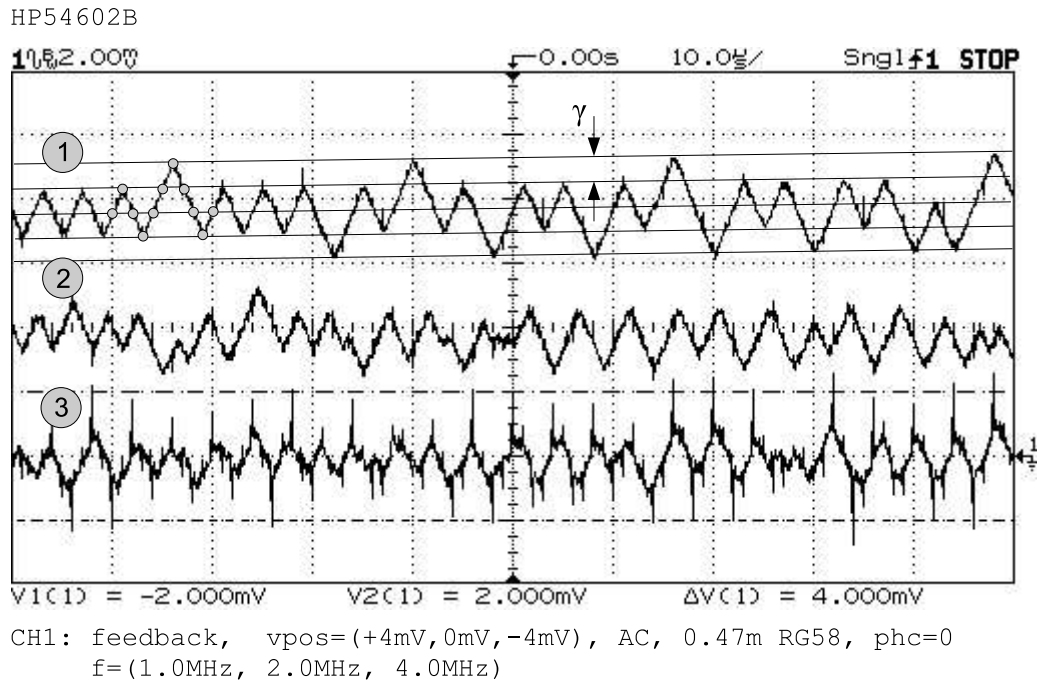
Figure 3.27.: Quantization error as function of frequency (measurement). All traces of V_{out} show actual idling pattern in real-time caused by stationary sampling ($f_{step} = f_{clk}$). 1: $f_{step} = 1$ Mhz, 10 Samples / 10 μs (indicated by points). The idling pattern deviates from ideal and reveals a rising trend. 2: $f_{step} = 2$ Mhz; 3: $f_{step} = 4$ Mhz. Nominal amplitude quantization $\gamma = 0.64$ mV.

The observations are interpreted by means of Fig. 3.28. This fictitious example encompasses both independent effects: hysteresis and asymmetry. The voltage hysteresis is indicated by a gray band. If a sample falls within this band, the voltage difference between the feedback V_{out} and the input V_{in} at the input of the D-flip-flop will not be large enough to provoke a reaction. V_{out} has to leave this band first to make the flip-flop toggle. This is also the reason why the real amplitude granularity does not decrease with rising sampling frequency.

The apparent rising trend of the amplitude levels is due to a slight asymmetry between the step size upward and downward. A step up is a bit larger than a step down. This effect is probably due to a very small bias current of the operational amplifier in the delta modulator. On average V_{out} tries to rise but must not deviate too far from the input signal. The DM forces V_{out} to follow V_{in}. The result are additional 0's for signal correction leading to a small imbalance between the average number of 0's and 1's. This

1 1 0 0 1 1 0 0 1 1 0 0 0 1 1 0 0 1 1 0 0 1 1 0 0 1 1 0 0 1 1 0 0 1 0 0 1 1 0 0

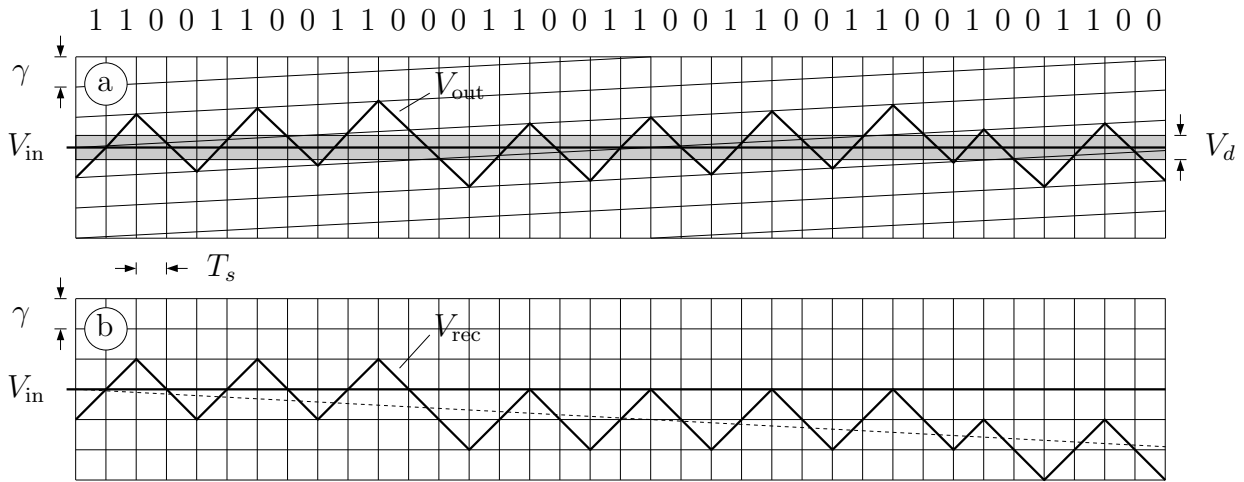Figure 3.28.: Effects of delta modulator asymmetry. Vertical lines: sampling instants; V_{in}: constant input voltage; V_{out}: output voltage (feedback) of the DM; V_{rec}: signal reconstructed from differential pulse code; T_s: sampling period; γ: DM step size; V_d: voltage hysteresis. The corresponding differential code is printed above the upper diagram.

has an important impact on the signal V_{rec} reconstructed from the differential pulse code. Since there are too many 0's the reconstructed signal is slowly falling. This effect is easy to compensate in software. In advance of every TDR signal recording the actual idling pattern is sampled. Afterwards this background is subtracted from the TDR trace with corrects for the trend.

Another eye-catching feature are the strong spikes in trace 3 of Fig. 3.27. Such observations are very difficult to interpret, since their existence or non-existence (c.t. trace 1 and 2) may be an artifact of the sampling oscilloscope. Its limited sampling frequency leads to aliasing and its limited bandwidth to signal distortion. Nevertheless these spikes have been looked at more carefully to learn more about noise in the OBSERVER.

Trace 1 in Fig. 3.29 is recorded with $f_{clk} = 4\,\mathrm{MHz}$ sampling frequency. Trace 2 in this figure shows an enlargement of a portion of trace 1 with a horizontal resolution of $500\,\mathrm{ns/div}$. The strong but short oscillations in trace 2 are switching transients generated by the D-flip-flop. In the middle of two of these major transients a smaller transient appears the origin of which is unclear.

The DDS master clock of OBSERVER V1 runs with $25\,\mathrm{MHz}$ producing 12.5 cycles in $500\,\mathrm{ns}$. The fine ripples on trace 2 have exactly the same frequency. Therefore this part of noise is assumed to be crosstalk from the master crystal oscillator. This close look to different features of the oscilloscope readings gives deeper insight into the quality of the circuit including the layout of the printed circuit board and helps to find ways of improving the instrument.

With respect to the TDR application the fine structures of noise play a minor role. The

```
HP54602B
```

CH1: feedback, vpos=(+4mV,0mV,−4mV), AC, 0.47m RG58, phc=0,
      f=4.0MHz, dt=(10us/div, 500ns/div)   (3.90)
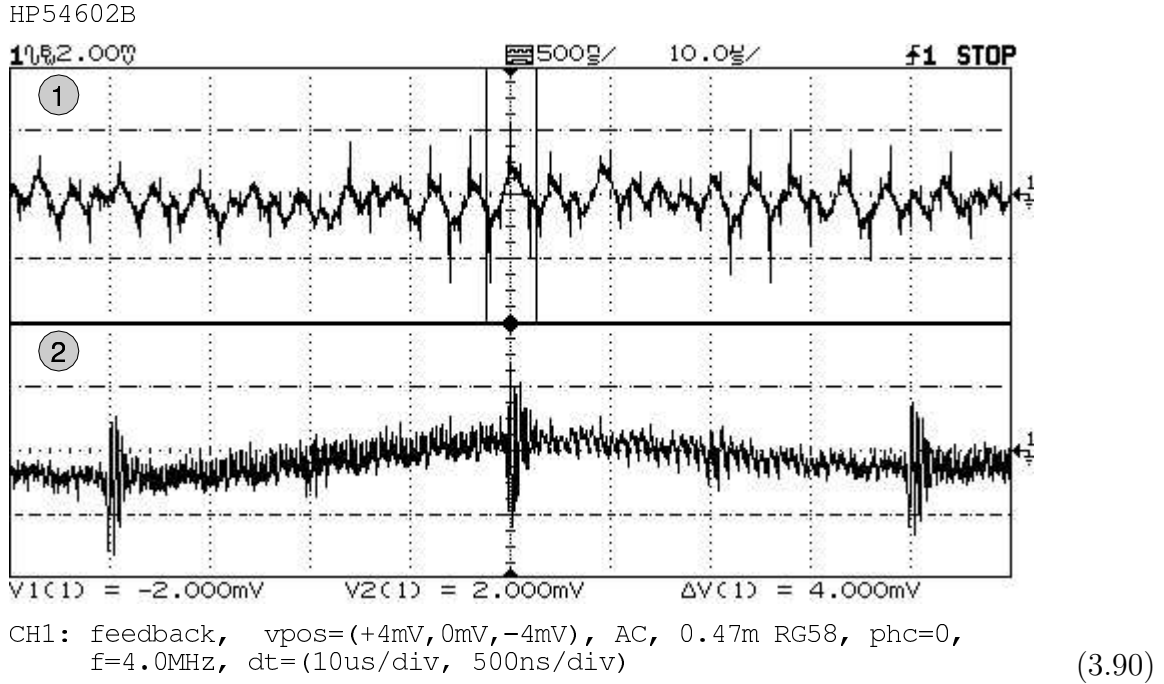
Figure 3.29.: Zoom into idling pattern. Sampling frequency $f_{\mathrm{clk}} = 4$ MHz, sampling period $T_{\mathrm{clk}} = 250$ ns, DDS master clock $f_{\mathrm{mclk}} = 25$ MHz. 1: hor. resolution $10\,\mu$s/div; 2: zoom of signal interval indicated by vertical lines in trace 1, hor. resolution 500 ns/div.

most important contribution to noise deems the coarse amplitude resolution leading to quantization errors. The SQNR is calculated under the simplifying assumptions of section 3.4.2. The minimum amplitude quantization step γ was determined from Fig. 3.27. The triangular waveform of V_{out} has a mean amplitude of at least 2γ. According to Eq. 3.73 with $\gamma = 2 \cdot 0.64$ mV the noise power yields

$$N_q^2 = 1/2\,(0.64\,\mathrm{mV})^2 = 2.07 \cdot 10^{-7}\,\mathrm{mV}^2 \; . \tag{3.91}$$

On the basis of the signal power given in Eq. 3.74 the SQNR yields

$$\mathrm{SQNR} = \sqrt{S^2/N_q^2} \approx 311 \approx 50\,\mathrm{dB} \; . \tag{3.92}$$

As stated before the SQNR is an unsatisfying performance measure because this lumped number does not tell much about the quality of signal tracking in TDR applications. The rms of the quantization error is deemed to be a better performance measure. In case of OBSERVER V1 with a sampling frequency of $f_{\mathrm{clk}} = 1$ MHz it yields

$$\sqrt{N_q^2} = 0.45\,\mathrm{mV} \; . \tag{3.93}$$

104

The slew rate of OBSERVER V2 has been set to $|\partial V_{\text{out}}/\partial t| \approx 170\,\mu\text{V}/\mu\text{s}$ which is nearly four times less. However it has not been checked yet if this modification really has an impact on the amplitude quantization error.

Summary

With OBSERVER V1 the nominal amplitude step is $\gamma = 0.64\,\text{mV}$ for a sampling frequency of $f_{\text{clk}} = 1\,\text{MHz}$ but the real granularity of V_{out} is twice as much. An increase of f_{clk} does not decrease the amplitude error, in contradiction to Eq. 3.38. This observation leads to the assumption of hysteresis in the input stage of the ECL D-flip-flop (MC100EP52). If the hypothesis turns out to be true the amplitude resolution will be limited by the minimum input voltage difference necessary to toggle the flip-flop. Therefore the amplitude granularity cannot be reduced below a certain threshold. The rms of the quantization error amplitude (Eq. 3.93) is 500 times smaller than the typical signal amplitude of 200 mV. The error can be further reduced by averaging. This performance should be sufficient for the application in Spatial TDR.

3.7. Signal and Data Processing of OBSERVER

This section focuses on the chain of data processing for OBSERVER V2. When the instrument performs a measurement, the delta modulator produces an un-interruptible continuous bit stream. The stream containing the pulse coded signal is cut into bytes and stored in OBSERVER's RAM. Fig. 3.30 demonstrates how the data is read from RAM, serialized, and integrated to reconstruct the sampled waveform.
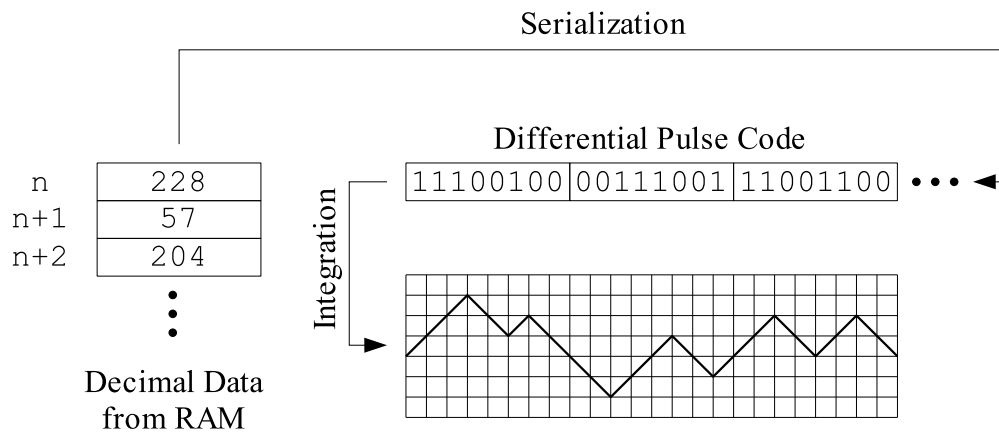

Figure 3.30.: Serialization of RAM data.

As explained before the slight asymmetry between the positive and negative voltage ramps of the delta modulator's integrator the reconstructed waveform shows a linear

trend (Fig. 3.28). This trend has to be removed by subtracting the idling pattern recorded right before the TDR signal sampling. Fig. 3.31 displays the results of the bit stream integration. The uncorrected TDR reflectogram S and the idling pattern B clearly show the falling trend. On this scale the idling pattern looks like a linearly falling line. This background is to be subtracted from the raw TDR reflectogram to yield the corrected TDR reflectogram: $R = S - B$.

Waveforms from Differential Pulse Code Integration
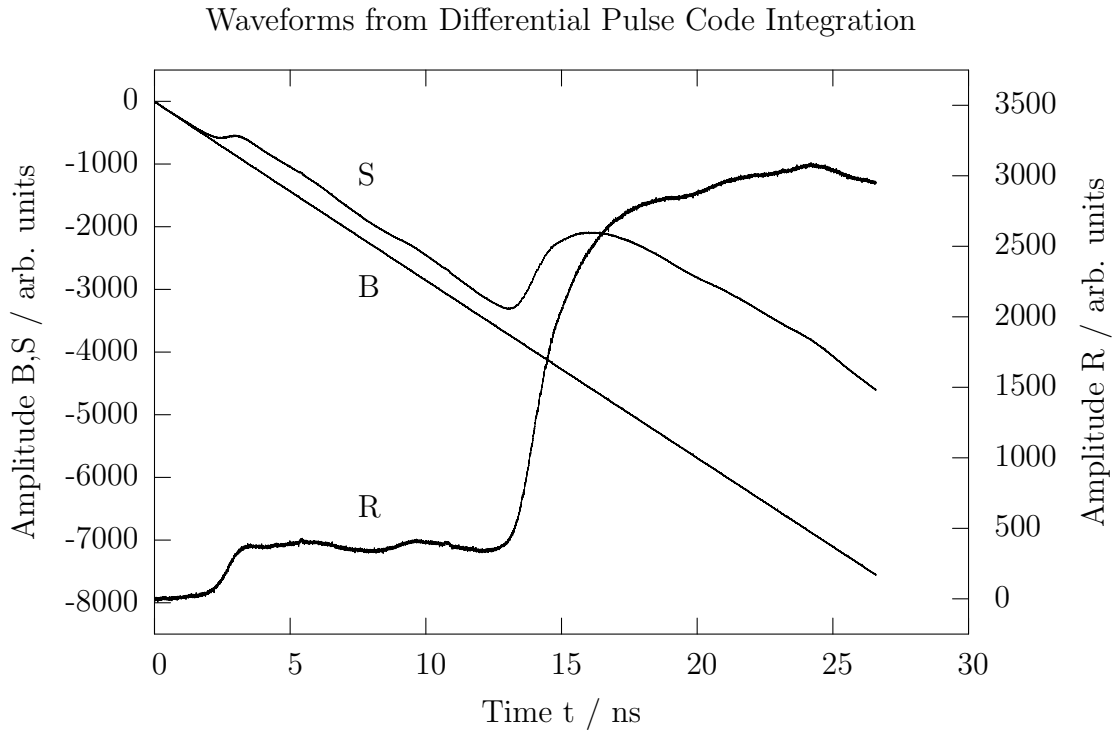
Figure 3.31.: Integrated bit streams and resulting TDR reflectogram. B: background, idling pattern; S: raw TDR signal; R: corrected reflectogram, $R = S - B$.

Each of the displayed OBSERVER traces consist of more than 10^6 points. According to trace B the difference between up and down are approx. 7500. An excess of 0's means that the upward step produced by the DM his larger than the opposite direction since it has to be compensated by a larger number of downward steps. A short calculation yields that a step up is roughly 1.5% larger than a step down.

The number of 10^6 samples per TDR trace is unnecessarily high and should to be reduced by averaging or re-sampling. This resulting waveform is still too noisy to be processed by the soil moisture reconstruction algorithm and must be smoothened by filtering. Fig. 3.32 shows two unfiltered reflectograms at different times during an infiltration experiment described in section 4.1. The trace R(t=0) represents the initial dry state of the soil. The other trace R(t=90) was recorded after 90 minutes of precipitation and infiltration. The curves differ strongly between 3.5 and 10.5 ns due to the dielectric effects of the infiltrating water. The corresponding amplitude reduction gives an impression of the

approximate dynamic range in the reflectograms under real field conditions. The noise amplitude has to be assessed in relation to this dynamic range covered in soil moisture measurements. The noise is much lower than the effect caused by soil moisture. These reflectograms are clearly distinguishable and carry information sharp enough to derive moisture profiles from them.
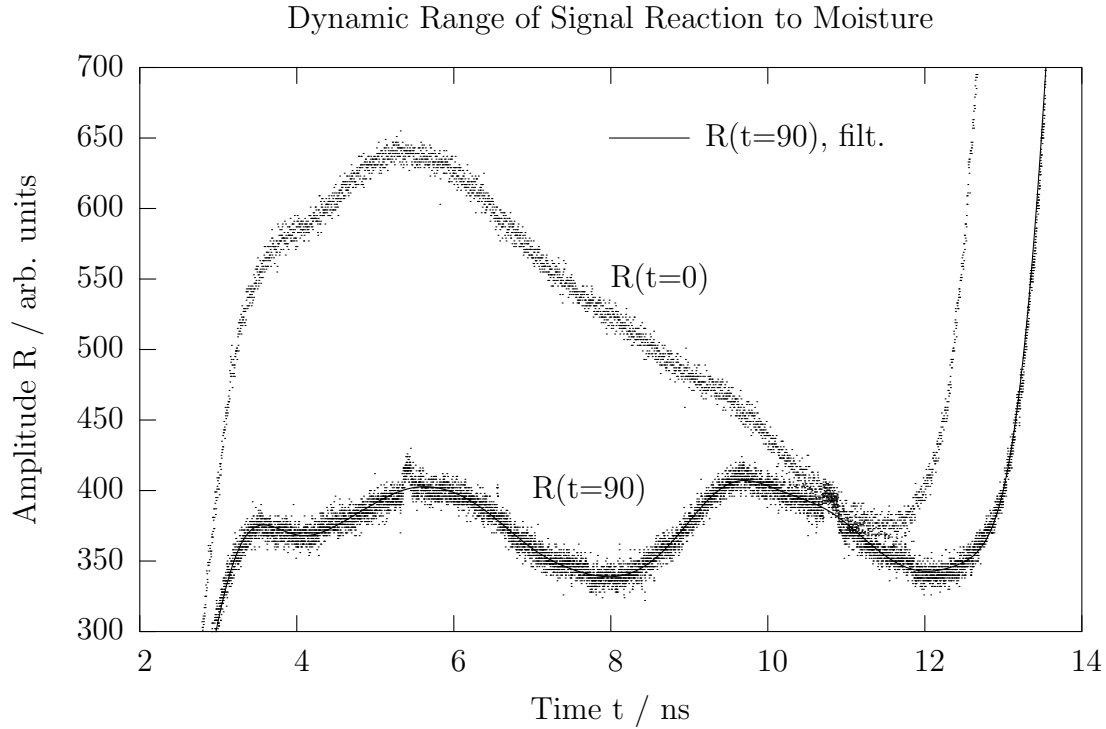
Figure 3.32.: Unfiltered reflectograms of OBSERVER, recorded during infiltration experiment at probe S2. R(t=0): reflectogram at initial dry state, data reduced, every 117th sample plotted; R(t=90): reflectogram after 90 min of irrigation, data reduced, every 43rd sample plotted; Solid line: low-pass filtered signal, 5th order Butterworth, 3 dB cutoff frequency $f_c = 800\,\mathrm{MHz}$. Horizontal stripes are due to amplitude quantization.

Fig. 3.32 clearly shows that the noise has a much higher frequency than the signal carrying information about soil moisture. It can be said that in the frequency spectrum the noise is not within the message band of the signal. Therefore it can be removed by filtering. However isolated disturbances obviously different in nature emerged in trace R(t=90) at approx. 5.5 and 10.8 ns. These bumps probably originate from non-random jitter components and are the biggest challenge for the next generation of OBSERVER. The moisture probe connected to the OBSERVER was a 3-rod-probe introduced before. The feeding coaxial cable was 14 m long leading to a low-pass filtering of the propagating EM waves. On basis of the reduced signal rise-time it is assumed that the signal bandwidth is below 800 MHz. This statement becomes plausible, when the noisy TDR

reflectogram is filtered by means of a Butterworth low-pass filter of 5th order with a 3dB-cutoff frequency of 800 MHz. The result is displayed in Fig. 3.32 as a smooth solid curve lying within the noisy band of R(t=90). The main shape of the reflectogram is reproduced by the filtered signal and the signal rise-time is conserved.

Dynamic Range of Signal Reaction to Moisture
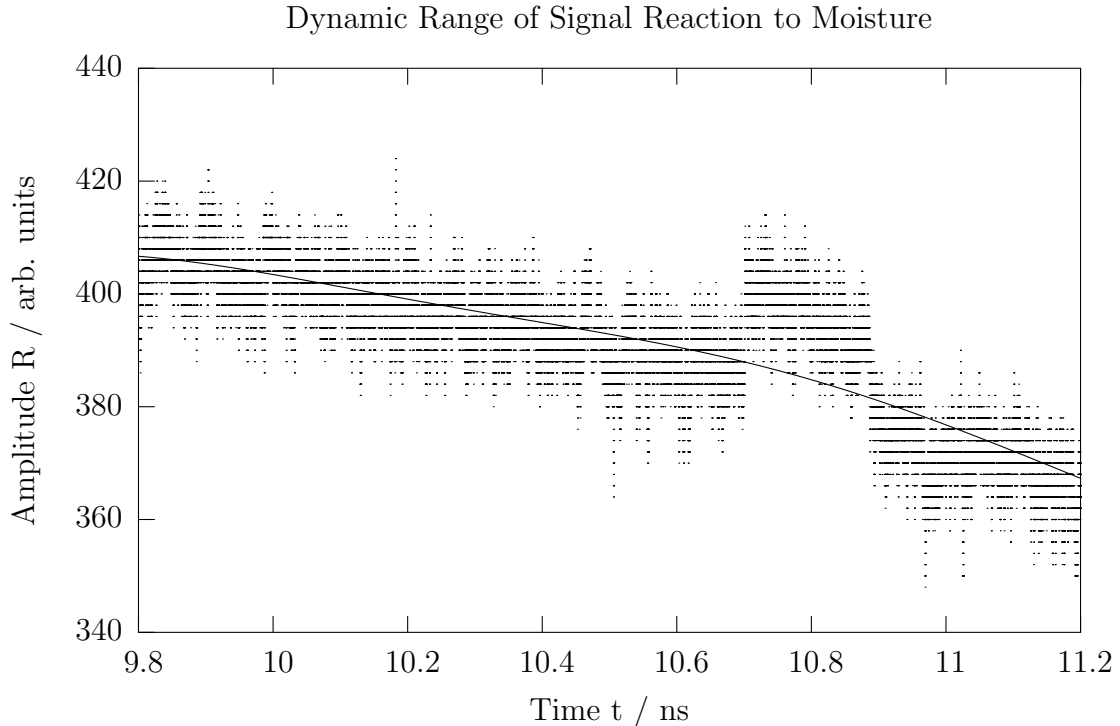
Figure 3.33.: Effect of low-pass filter. An enlarged portion of reflectogram R(t=90) shows a persistent discontinuity in the amplitude trace between 10.7 and 10.9 ns, which cannot removed completely by filtering. Horizontal stripes due to amplitude quantization.

However, the second major signal discontinuity around 10.8 ns is not removed completely by filtering but leads to a small local amplitude increase instead (Fig. 3.33). This will lead to an artifact in the soil moisture profile. The final filtered reflectogram is the best what we can get out of the current version OBSERVER. A detailed comparison between reflectograms produced by OBSERVER and a commercial Tektronix Metallic Cable Tester 1502B is given in Sec. 4.3.1, Figs. 4.29–4.32.

3.8. Discussion

Distinction to the Sampling Voltage Tracker

In the Internet news-group *sci.electronics.design* a discussion arose whether a delta modulator in the way used in OBSERVER is identical to the *Sampling Voltage Tracker* (SVT)

of the *American National Institute of Standards and Technology* (NIST) (*Souders et al.*, 1987; *Souders and Hetrick*, 1987; *McCabe*, 1975). The delta modulator always tries to minimize the input voltage difference as far as possible. In this respect it resembles the SVT but differs significantly from it in the way the signal under test is coded and sampled.

The main focus of the SVT is to determine voltage levels with very high precision. The SVT digitizes the analog feedback voltage with a high resolution analog-to-digital converter, e.g. 18 bits per sample, giving the absolute voltage level. In contrast the sampler of OBSERVER is optimized for TDR signal tracking for soil moisture determination. Simplicity, robustness, and cost effectiveness are important objective rather than extremely precise amplitude resolution. The sampler is a delta modulator, which produces a differential code of the waveform leading to an effective data compression due to the absence of redundancy. This code has to be integrated and filtered to reconstruct the signal. The consecutive application of differentiation and integration leads to a loss of the absolute signal level which in some applications could be a disadvantage.

Another difference is that the sampler of OBSERVER is continuously sweeping across the signal under test whereas the SVT is sampling the repetitive input signal at the same phase angle over many periods by setting a variable but fixed delay (or phase relation) between emitted excitation pulse and sample pulse. In case of SVT the amplitude is estimated from a high number of samples by calculating the median of the data, whereas the OBSERVER reflectograms are currently filtered to be improved.

Both instruments follow different objectives and do not share the same principles in coding and data processing. Thus OBSERVER and SVT are not the same.

State of Development and Future Improvements

The performance of the current prototype OBSERVER V2 is already so good, that its reflectograms are similar to those recorded by Tektronix Metallic Cable Tester 1502B, at least for probes with long connecting cables leading to a bandwidth reduction of the pulse reflections. A detailed comparison between the OBSERVER and Tektronix reflectograms is given in Sec. 4.3.1.

With respect to the first version the excitation pulse generator of OBSERVER V2 has been improved. The signal edges of the emitted voltage pulse are much steeper, but a further improvement is advisable, since the relatively slow onset of the excitation pulse (c.t. 4.29–4.32) leads to irritations in the determination of the exact temporal position of the reflections by means of the tangent method. One solution for this problem may be the exploitation of the focus on the falling signal edges instead of the rising ones. The transistors in the ECL output stage seem to be faster in the transition from conducting to non-conducting than vice versa. This may be the reason for the falling signal slopes being faster than the rising ones.

But the biggest problem and challenge is the jitter between excitation pulse and sampling strobe with its non-random contributions. These disturbances can probably be reduced by using better DDS parts now being available. They can be driven with much higher master clock frequency and have a tremendous SFDR due to enlarged amplitude resolution of their internal DAC.

The question of an appropriate interface to control the TDR instrument and to transfer the reflectograms to a computer has not been answered, yet. OBSERVER V2 has its own local RAM. The device is controlled and data is exchanged with a PC by means of a common PC parallel port (EPP). This method requires a lot of additional parts to interface the RAM like for example a synchronous address counter of 17 bits width. The printed circuit board becomes more stuffed, its price is higher, and the routing is more difficult. Therefore a USB interface might be an option. The data rate across this interface is much higher than with the ordinary parallel port so that the bit stream could be transmitted directly to the PC without the necessity of a local RAM. Furthermore the acceptance of the customers could be higher, because many modern laptop computers do not comprise a parallel port any longer.

4. Applications

4.1. Monitoring of Infiltration Fronts

The main objective of this thesis is to demonstrate the ability to track infiltration fronts along vertically installed rod probes with Spatial TDR. All the components introduced before, be them algorithms or other software, be them new electronic devices or other hardware like rod probes, have been developed for the particular application presented in this section. The following experiment is the very core of the whole work successfully demonstrating that the new framework is a solution to the problem of detailed soil moisture monitoring sufficient for many applications.

The experiment has been designed for three purposes: 1. Test of the reconstruction algorithm in conjunction with the new 3-rod-probe, 2. comparison between the TDR prototype OBSERVER and other commercial products, and 3. evidence of the small scale variability of soil hydraulic properties and its influence on infiltration even under laboratory conditions.

4.1.1. Experimental Setup

The experiment is carried out in a non-weighable lysimeter encompassing a cubic soil volume of 1 m^3 (Fig. 4.1). It is currently filled with a loamy sand (s. soil texture, App. A.1). The soil was poured in and compacted in layers of 0.1–0.2 m thickness.

Due to earlier experiments the saturated hydraulic conductivity of the soil was estimated to be $k_s^* \approx 10^{-5}$ m/s. It is equal to the Darcy flux density with unity hydraulic gradient (e.g. *Kutílek and Nielsen* (1994), pp. 88–89). To yield a rough estimate for the velocity v_p of a percolating infiltration front, it has to be divided by the soil porosity (e.g. *Roth* (1996), p. 25). Together with a soil porosity P of 30–40 % it leads to a pore velocity in the range of 0.1 m/h (s. App. A.1). Thus an infiltration front under nearly saturated conditions would reach the bottom of the lysimeter within hours which is a reasonable time span to conduct the infiltration experiment.

The bottom of the container is covered with a geotextile to drain infiltrated water towards the outlet situated in one corner. The amount of water leaving the lysimeter was not controlled during the experiment. The height of the soil column is 0.2–0.4 m larger than the lengths of the vertically installed probes. This additional distance is to minimize disturbances from below should capillary rise occur.

The lysimeter is instrumented with several probes (Fig. 4.2), the most important of which are the four 3-rod-probes installed vertically from the soil surface (S1–S4). The probes are positioned at the corners of a centered square with edges of 0.4 m parallel
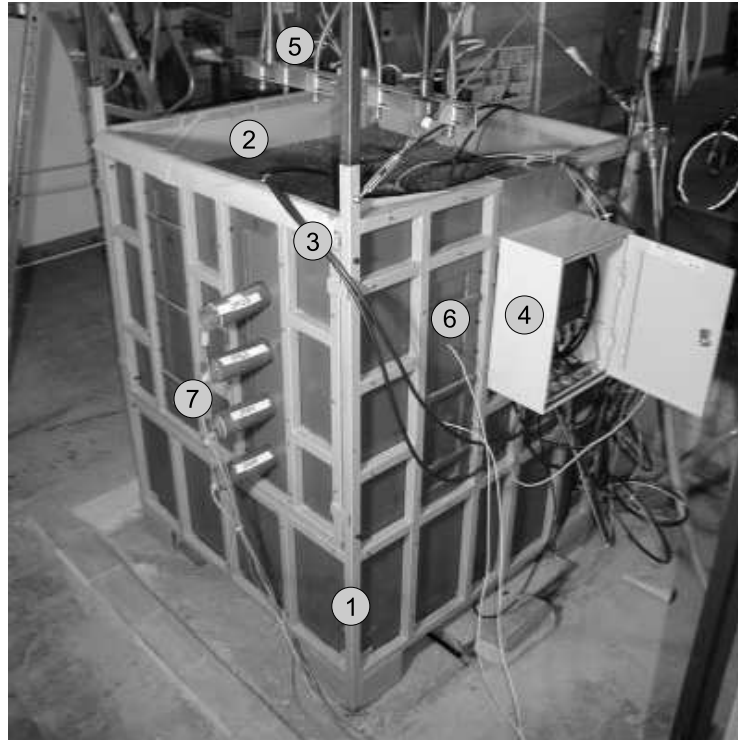
Figure 4.1.: Non-weighable lysimeter holding a 1 m³ soil body. 1: tubular steel frame; 2: soil; 3: probe connecting coaxial cables (RG213); 4: probe multiplexer (SNAPMUX); 5: spray nozzle bar; 6: position of two SISOMOPs; 7: IMKO Trime probes.

to the lysimeter walls. The soil surface is not perfectly horizontal but slightly tilted with a gradient pointing from S1 to S3. Thus if ponding occurs the water will flow towards the surface depression around S3 which lies approximately 5 cm deeper than S1 (s. Fig. 4.3). The length scale along each probe is related to the soil surface which defines the coordinate z = 0 m.

Each 3-rod-probe is connected to a multiplexer (mux) with a coaxial cable (coax) of 2 m length (Fig. 4.4). A coax of same length but without probe head connected to the mux is used to measure the input signal reaching the probes. This cable is referred to as S8. The coaxial cable used throughout the experiment is a *RG213* with 50 Ohms impedance but a much smaller attenuation than the common RG58. The connectors used are screwable N-type instead of BNC.

Additionally a 3-wire ribbon cable designed for moisture measurement (*Hübner* (1999)) of 0.8 m length has been buried vertically in soil right in the center of the 3-rod-probes. It has coax cables of 5 m length on both sides connecting it to the probe mux. At each side a relay is put between the coax and the ribbon cable which can be opened or closed externally. If the relay at the entrance to the ribbon cable is opened, the propagating pulse will see an open coax cable and an input signal measurement will be performed. If this switch is closed and the one at the end of the ribbon cable is opened, the signal
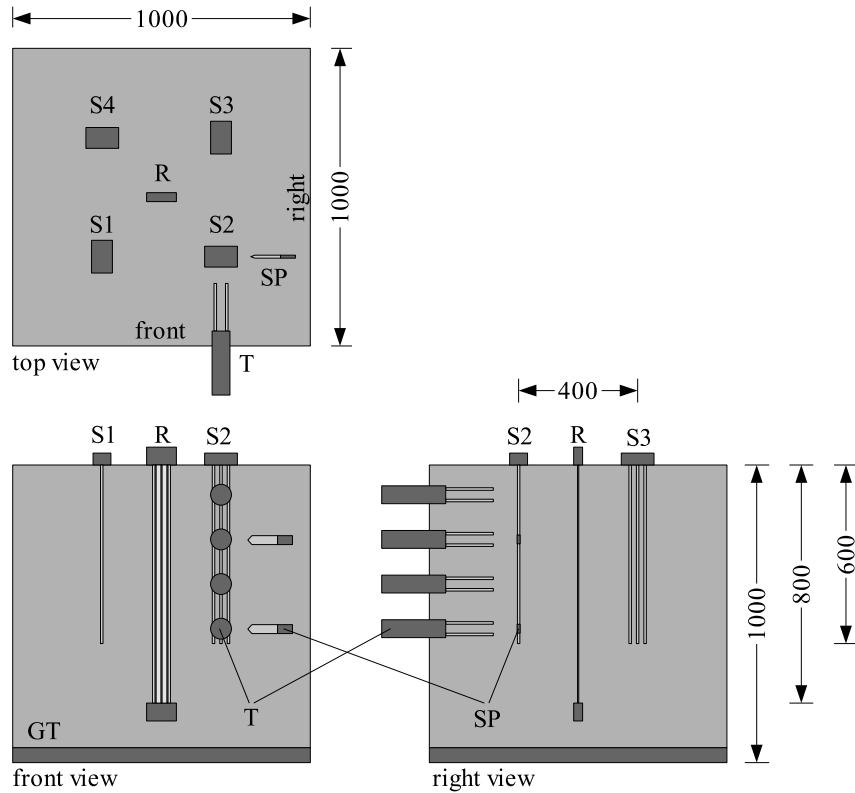
Figure 4.2.: Instrumentation of the lysimeter soil body. S1–S4: 3-rod-probes *SUSU03*; R: 3-wire ribbon cable *Taupe*; T: non-sampling TDR probes *IMKO Trime*; SP: Ring oscillator moisture sensor *SMG SISOMOP*; GT: geotextile. All lengths in mm.

and its energy will be totally reflected back into the system under test leading to the maximum possible signal power for the TDR trace.

The TDR measurement from the upper end of the vertical cable with first relay closed and second opened is named S5. The input signal measurement with full reflection at the first relay opened is called S5r. S5t denotes the measurement from top with second relay closed leading to a partial transmission of the signal into the coax at the lower end of the ribbon cable. The notation S6, S6r, and S6t, are the measurements from the lower end of the ribbon cable, respectively. Table 4.1 summarizes the naming of the probes and the configuration of the ribbon cable.

The multiplexer gathering the probes S1–S8 is named *probe multiplexer*. The probe mux is connected with a 11 m coax to a second reversely installed multiplexer (de-multiplexer, demux). All sampling TDR instruments under test are connected to this mux referred to as *device mux*. By means of this configuration each probe can be connected to each TDR.

Probe config.	Relay upper end	Relay lower end	Remark
S1	—	—	3-rod-probe
S2	—	—	3-rod-probe
S3	—	—	3-rod-probe
S4	—	—	3-rod-probe
S8	—	—	coax cable for 3-rod-probe input meas.
S5	1	0	ribbon cable from upper end, SUT
S5r	0	x	ribbon cable from upper end, input meas.
S5t	1	1	ribbon cable from upper end, lower end transm.
S6	0	1	ribbon cable from lower end, SUT
S6r	x	0	ribbon cable from lower end, input meas.
S6t	1	1	ribbon cable from lower end, upper end transm.

Table 4.1.: Notation of probe configuration. Relay state of the ribbon cable, 0: open; 1: closed; x: arbitrary.

Both multiplexers are of type *SNAPMUX* developed throughout this thesis, supported by the SMG (App. B.6).

Three sampling TDRs are used throughout the experiment: *Tektronix Metallic Cable Tester 1502B* (Tek1502B), *TDR100* by Campbell Scientific (identical to the HL1500 by Hyperlabs), and the *OBSERVER*, the new TDR prototype developed as part of this thesis.

Additionally, four non-sampling TDRs *IMKO Trime* and two novel moisture sensor prototypes *SISOMOP* with integrated temperature sensor have been installed horizontally. SISOMOP has also been developed in the scope of this thesis with support of the SMG (App. B.4). This cost-effective and reliable moisture sensor based on a ring oscillator is meant to be a simple alternative to TDR for applications where many stationary probes are needed and point-wise measurements are sufficient.

The devices are controlled by a Linux PC. An Embedded Linux version has been customized, running on low power industrial PCs to realize a scalable and flexible data logger for field applications. This system is named *ELEPHANT*: Embedded Linux Extensible Processor, Highly Applicable for Networking and Telemetry). An optional wireless modem allows to fetch the stored data and to control the system remotely for field applications. The software running on Linux to control the different TDRs (Tek1502B, TDR100, OBSERVER) and the multiplexers has been developed by the SMG.

A sprinkler is installed above the lysimeter for irrigation. It consists of spray nozzles mounted to a vertical bar which hangs below a carriage running on rails. The carriage periodically drives forth and back the rails to distribute the water homogeneously. A pressure tank is installed on top of the carriage partially filled with water. Water is

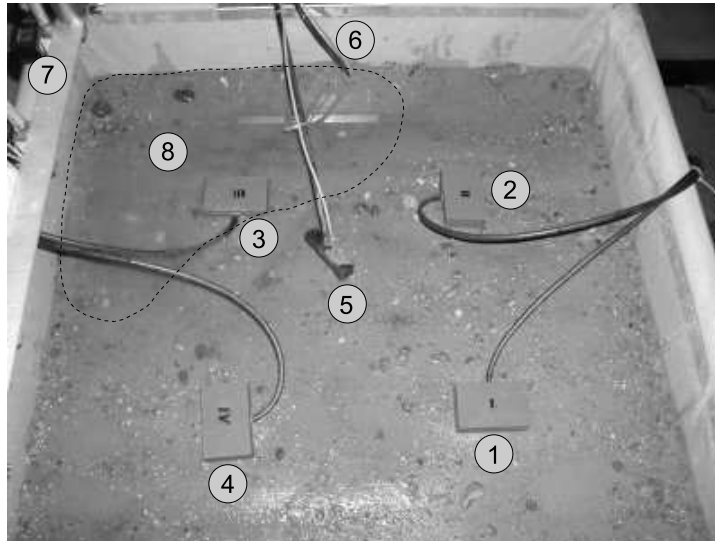Figure 4.3.: Soil surface with vertically installed probes after some time of irrigation. 1–4: four SUSU03 3-rod-probes; 5: upper end of moisture measuring ribbon cable (TAUBE); 6: coax cable to the lower end of ribbon cable; 7: spray nozzle bar; 8: ponded area indicated by dashed line.
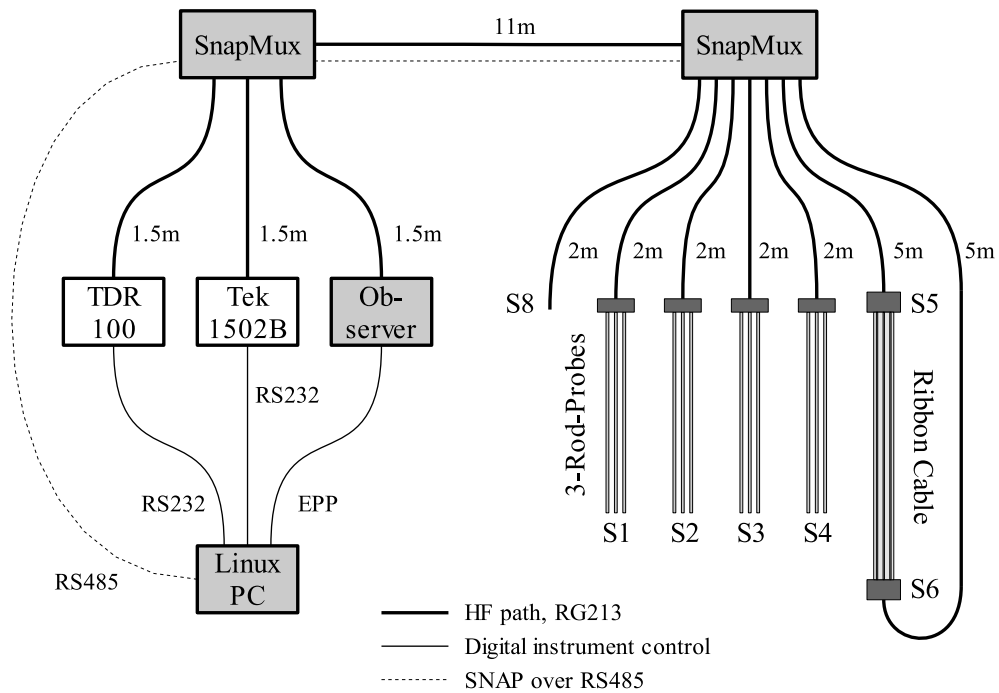

Figure 4.4.: Signal paths of the sampling TDRs. The instruments in light gray and the control software have been developed as part of this thesis.

pumped from a storage tank into the tank under constant pressure. The precipitation rate can be controlled by the switching ratio of the nozzle valves. The amount of cumulative precipitation is gauged by the filling of the storage tank.

4.1.2. Execution of the Experiment

Before the experiment was started the lysimeter stood for several weeks without distortion. The soil surface was extremely dry and very hard. Drops of water did not infiltrate but ran off on the surface. Therefore the upper layer of approximately 5–10 cm was ploughed with a garden tool.

The irrigation scheme, i.e. the precipitation rates and intervals (irrigation pulses), is displayed in Fig. 4.15. The beginning of the first irrigation defines the zero point of the time axis. The somewhat irregular precipitation pattern at the beginning of the experiment is due to the lack of experience with the infiltration characteristics of the particular soil. Its hydraulic conductivity was overestimated at first so that the precipitation rate had to be decreased to avoid extensive ponding. But ponding did occur after some 40 minutes. Very fine mobilized soil material sealed the surface around probe S1 so that surface runoff set in having flown towards S3 leading to ponding of some centimeters around S3 (Fig 4.3).

The end of the last precipitation pulse was at 335 minutes. Another 25 minutes later the soil water storage started to decrease, which can be seen from the corresponding storage curves S1–S4 in Fig. 4.15. The last measurement taken into account for the current analysis was taken at 480 minutes. Thus the total time of the experiment can be divided into two intervals, the wetting period, 0–360 minutes, and the drying period, 360–480 minutes.

Every ten minutes a measurement cycle was triggered consisting of two loops. The outer loop selected the three TDR instruments, the inner loop switched between the eleven probe configurations in the order of table 4.1. The sequence of the devices and the time needed for eleven measurements was 1. TDR100, 1:10 min, 2. OBSERVER, 1:40 min, 3. Tek1502B, 6:40 min, leading to a total cycle time of 9:30 min.

IMKO software was used to automatically read out the Trime probes every ten minutes. SISOMOP measurements were taken every ten minutes by manually reading from their control board display.

Each measurement is denoted by two times: the timestamp of the measurement cycle it belongs to and the real time when it was taken. Thus two measurements sharing the same timestamp could be more than nine minutes apart. The curves displayed in many of the following figures are labeled by their timestamp, not by their real time. This is particularly important for the comparison of measurements taken at one probe sharing the same timestamp but sampled with different instruments and thus at different real times.

116

4.1.3. Resulting Reflectograms

Particular emphasis is put on the analysis of the four 3-rod-probes, since they are going to be used in a flood warning project. The reflectograms taken by Tek1502B are chosen to be the reference due to the instrument's reliability and signal quality. Figs. 4.5–4.8 show the TDR signals of the irrigation experiment. The reflectograms of each probe are grouped in sets: one for the wetting (0–360 min) the other for the drying period (360–480 min). The curves are labeled by their timestamp. The horizontal time axes of the diagrams are restricted to 143–158 ns to zoom into the signal portion relevant to TDR. The unit of the vertical signal amplitude axis is arbitrary as long as it is linear and preserving relative differences. Here the raw counts of the Tek1502 ADC are given directly.

The features common to all measurements taken with Tek1502B at probes S1–S4 can be explained best by means of S2 because of the relative regular soil moisture dynamics observed at this probe. Fig. 4.6, top, shows the reflectograms taken at probe S2 during wetting. Two zero measurements have been performed: one at 0 minutes, one 30 minutes earlier. The TDR measurements earlier than timestamp +30 minutes are very noisy. The noise filter has been improved later by setting the so called *average factor* of the Tek1502B to 64.

The family of curves has two envelopes: the uppermost curve indicating the initial dry condition (timestamp 0) and the lowest curve taken in the most wet state of the soil column seen by S2 (timestamps 210 to 360). These limiting curves define the total dynamic range of the TDR curves. All other reflectograms must be located between these two extremes. After approximately 210 minutes the reflectograms of S2 do not change significantly any longer because the infiltration front has passed the probe end so that the control volume defined by the probe length of 0.6 m has been filled and stationary infiltration sets in.

The first reflection caused by the transition coax/probe is detected at approx. 144.25 ns. The second reflection coming from the probe end occurs somewhere between 154 and 155.5 ns: the wetter the soil the later the reflection. Due to the coated rod probe the total soil moisture dynamic from dry to wet leads to an increase of the pulse round trip travel-time of 1.5 ns only.

The advancing wetting front does not only shift the reflection at the probe end to larger times but also leads to a local amplitude depression of the reflectogram. The reflectogram at probe S2 at timestamp 30 is an illuminating example. In comparison to the zero state the signal amplitude is locally depressed right after the first reflection. A new signal slope emerges between 146 and 148 ns. This reflection is due to the transition between wet and dry soil. During precipitation this feature shifts to larger times as a consequence of the propagating infiltration front.

The wavy form of the upper and lower envelope is a sustaining feature evidently showing a systematic structure of the soil moisture along the probe persisting even under wetting. Probes S1 and S4 show this wave-like disturbance very clearly.

The figures showing the reflectograms during drying have been given another amplitude scale to resolve the much smaller effects. The evolution of the curves can best be

described as a small shifting towards higher signal amplitudes indicating decreasing moisture. The signals show that drying occurs surprisingly regular along the probe. Without being transformed into soil moisture the evolution of the raw reflectograms do already show very individual soil moisture dynamics at the four probe locations.

4.1.4. Reconstruction of Soil Moisture Profiles

The soil moisture profiles were reconstructed from the TDR reflectograms given in Figs. 4.5–4.8. The first step is to feed the reconstruction algorithm with the individual TDR reflectogram and the corresponding input signal. A probe inductance of $L' = 575$ nH/m has been taken for the algorithm (Tab. 2.1). To improve the quality of reconstruction the empirical relationship between capacitance C' and effective conductance G' given in Eq. 2.68 with parameter values of Tab. 2.3 has been used.

The reconstruction algorithm yields the capacitance profile along the 3-rod-probe. Three such capacitance profiles $C'(z)$ along probe S4 with timestamp 0, 90, 360 minutes are displayed in Fig. 4.9, top right. This graphic summarizes the procedure of soil moisture profile derivation from capacitance profiles yielded by the reconstruction algorithm.

The probe characteristic is needed to transform the capacitance of the nonuniform transmission line consisting of probe and material to the relative permittivity ϵ of the material only. This analytical function sometimes referred to as *capacitance model* is given in Eq. 2.26. Its experimentally derived parameters C'_1 and C'_2 are listed in Tab. 2.1. For the sake of simplicity the formula is repeated here:

$$C'(\epsilon_m) = \frac{\epsilon_m C'_1 \cdot C'_2}{\epsilon_m C'_1 + C'_2} = \frac{20.5\ \epsilon_m \cdot 356}{20.5\ \epsilon_m + 356}\ \text{pF/m} = \frac{7298\ \epsilon_m}{20.5\ \epsilon_m + 356}\ \text{pF/m}\ . \tag{4.1}$$

This *probe calibration function* is drawn in Fig. 4.9, bottom right.

While the last step in the derivation of soil moisture is governed by the probe the next transformation is ruled by the material properties. In the current case the material is soil, a mixture of rock, water, and air. Since no satisfying mixing rule has been found so far describing the dielectric properties of the mixture by those of its single constituents best results are yielded by an empirical relationship between the permittivity of the total mixture and the volumetric portion of the constituent water only. The empirical relationship between permittivity ϵ and volumetric water content θ has been derived experimentally in Sec. 2.7, Eq. 2.74. This function serves as a *material calibration*. For reasons of clarity the function is given here again:

$$\theta(\epsilon) = a + b \cdot \epsilon^c = (-41.1 + 30.1\ \epsilon^{0.31})\ \%\ . \tag{4.2}$$

The inverse of this relationship is displayed in figure 4.9, bottom left.

The last step is to relate the resulting volumetric moisture content to the location. The upper left quadrant of Fig. 4.9 shows the final results of soil moisture profiles $\theta(z)$.

It is a remarkable coincidence that the two particular calibration curves determined by the 3-rod-probe ($C'(\epsilon)$) and by the silty sand ($\epsilon(\theta)$), respectively, are very similar in shape for the given dynamic range, i.e. the range of occurring permittivities, whereas they are

Probe S1, 0 - 360 min

Probe S1, 360 - 480 min
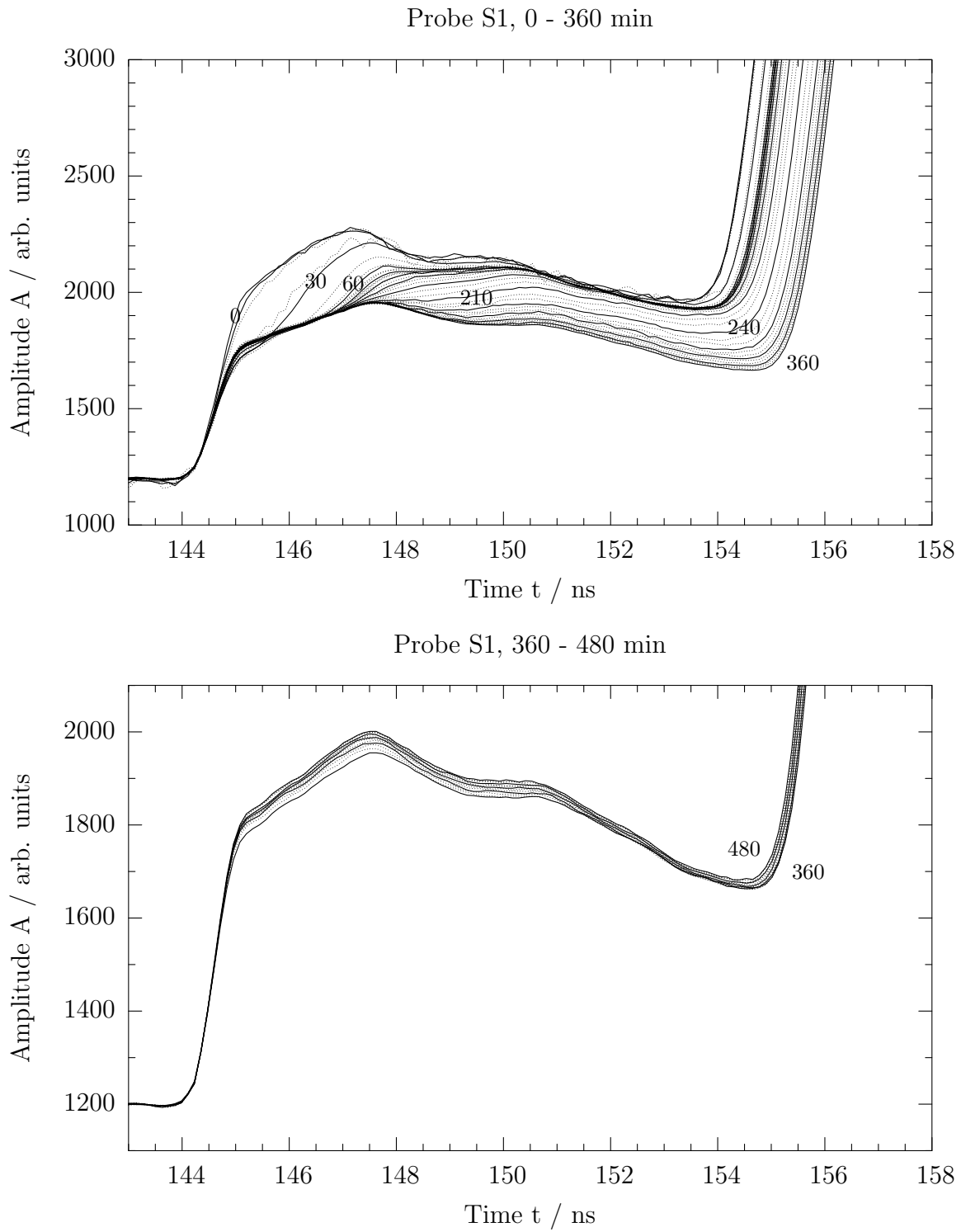
Figure 4.5.: Reflectograms at probe S1 during wetting (top) and drying (bottom). Curve labels: minutes since beginning of irrigation.
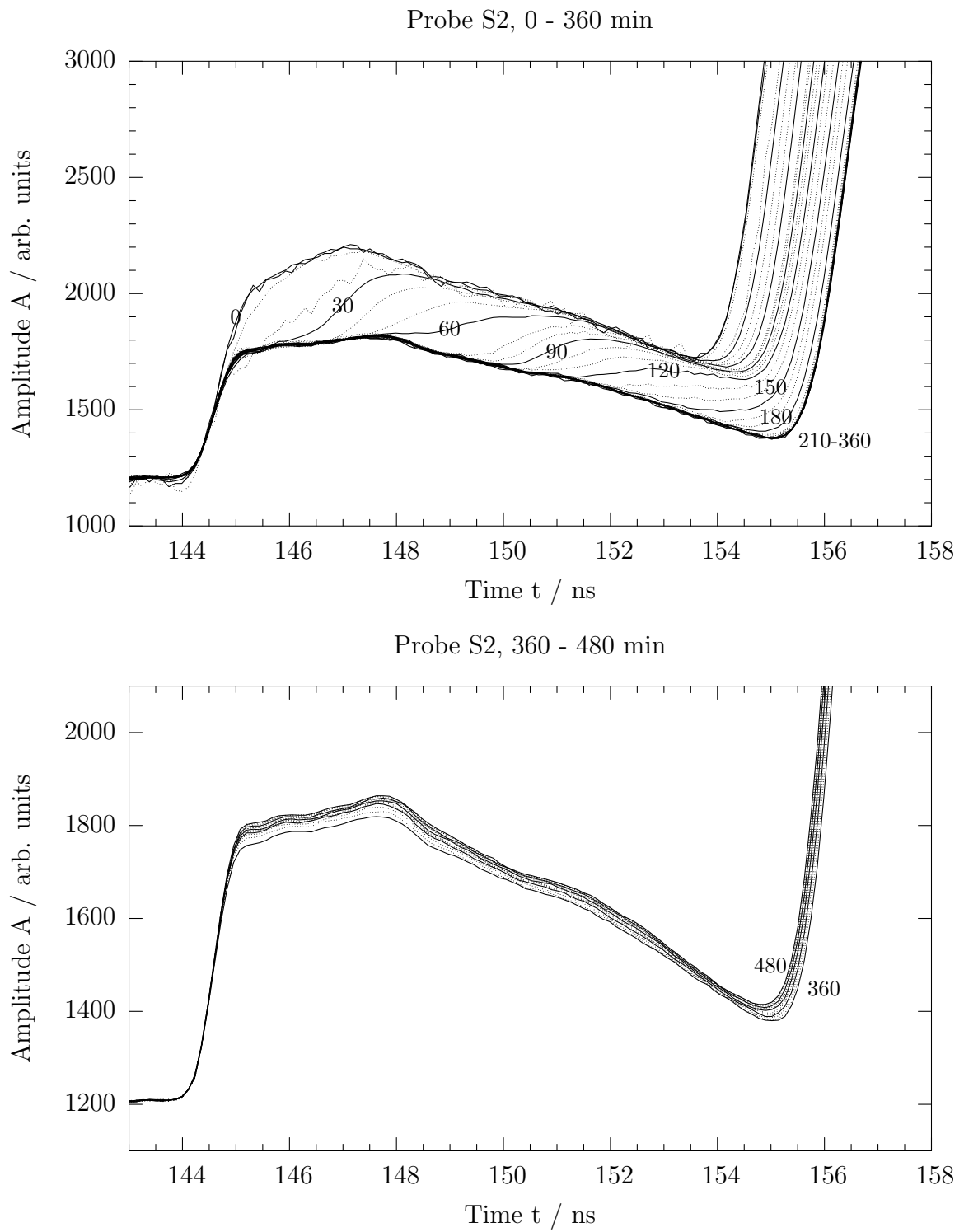
Figure 4.6.: Reflectograms at probe S2 during wetting (top) and drying (bottom). Curve labels: minutes since beginning of irrigation.

Probe S3, 0 - 360 min

Probe S3, 360 - 480 min
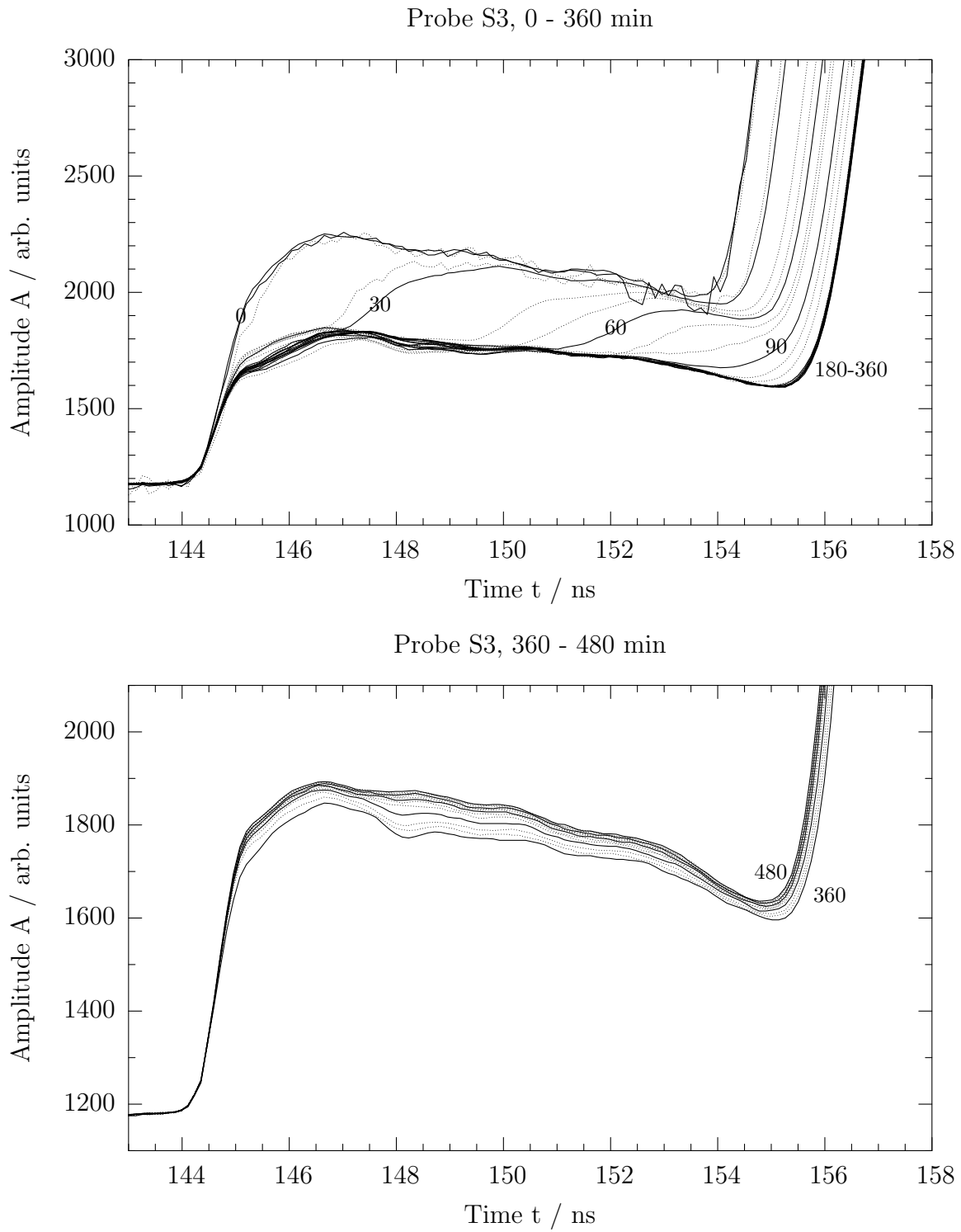
Figure 4.7.: Reflectograms at probe S3 during wetting (top) and drying (bottom). Curve labels: minutes since beginning of irrigation.

Probe S4, 0 - 360 min

Probe S4, 360 - 480 min
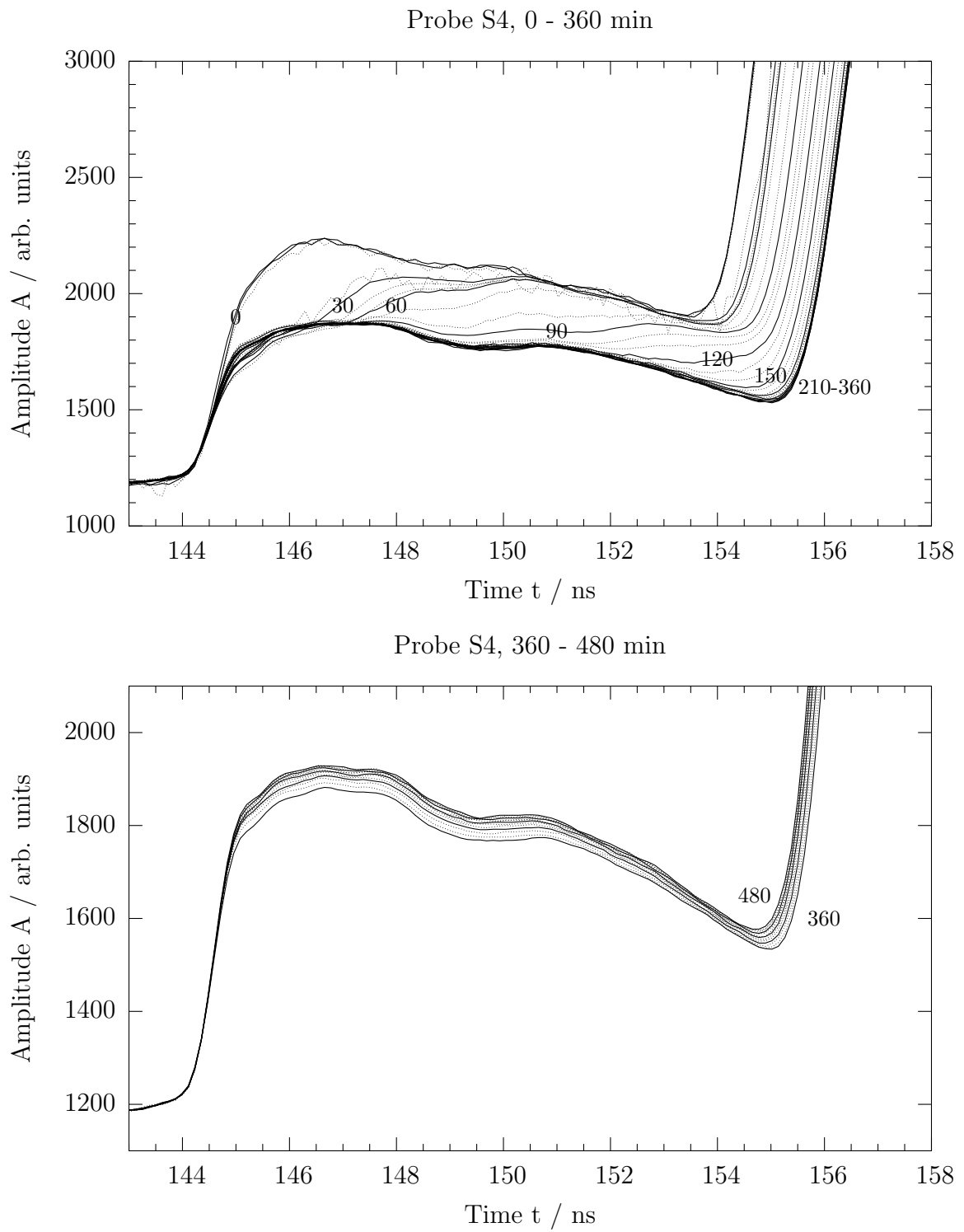
Figure 4.8.: Reflectograms at probe S4 during wetting (top) and drying (bottom). Curve labels: minutes since beginning of irrigation.
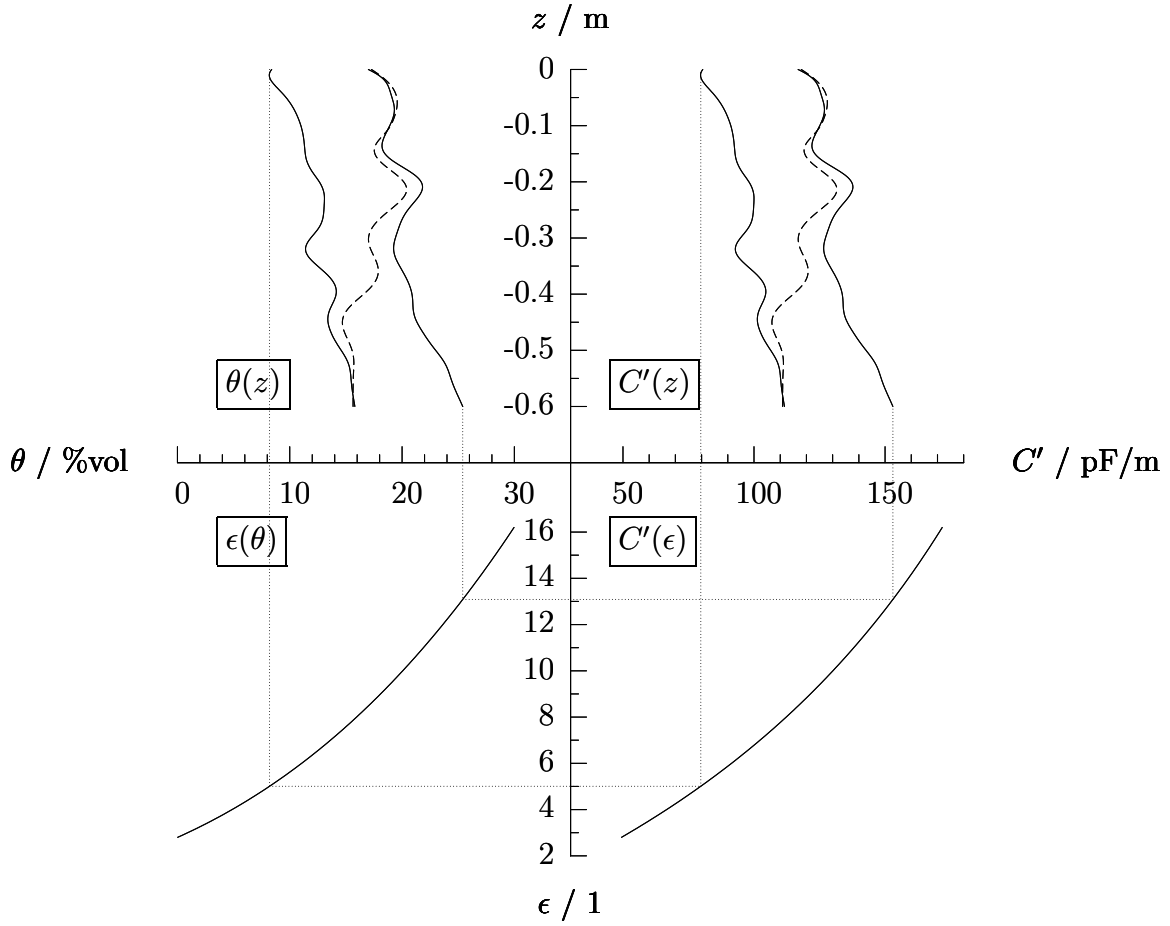
Figure 4.9.: Procedure of soil moisture determination: Transition from capacitance profile $C'(z)$ to water content profile $\theta(z)$ by means of two calibration functions. Examples given are results of probe S4 at 0, 90, and 360 minutes. Top right: capacitance profiles C' derived from the TDR reflectograms; bottom right: capacitance model for the 3-rod-probe; bottom left: empirical relationship between soil moisture θ and relative permittivity ϵ, top left: final soil moisture profiles. Thin lines show the approximate limits of the dynamic range observed for the particular soil and probe.

completely distinct in nature. This results in a nearly perfect linear relationship between capacitance and soil moisture within the given moisture range. This is why capacitance and moisture profiles look so similar.

Figures 4.10–4.13 show the reconstructed moisture profiles from the reflectograms given in figures 4.5–4.8. The moisture profiles $\theta(z)$ for each probe have been divided in two sets again, for the wetting (0–360 minutes) and the drying period (360–480 minutes). Additionally the in- or exfiltrated water $\Delta\theta$ only is displayed in units of volumetric water content (%vol). For that the evolving moisture profiles have been subtracted from a reference profile. In case of the wetting period the reference profile θ_0 is the zero state (timestamp 0), the moisture condition at the beginning of the experiment. In case of the drying period the reference has been chosen to be the profile θ_{360} at 360 minutes (timestamp 360), a state after the last precipitation pulse, when the effects of drainage just not have taken shape. Thus the moisture differences are defined as

$$\Delta_0\theta \;\; := \;\; \theta - \theta_0 \, , \tag{4.3}$$
$$\Delta_{360}\theta \;\; := \;\; \theta - \theta_{360} \, . \tag{4.4}$$

Figures 4.10–4.13 are organized as follows: Top row: wetting (infiltration under irrigation), bottom row: drying (exfiltration after irrigation), left column: absolute volumetric water content, right column: change in volumetric water content relative to the respective reference state.

It is obvious at first glance that the infiltration characteristic differs substantially from probe to probe. This is an expression of small scale variability of soil hydraulic properties in conjunction with locally different flow processes. A detailed discussion about the observations follows in Sec. 4.1.7.
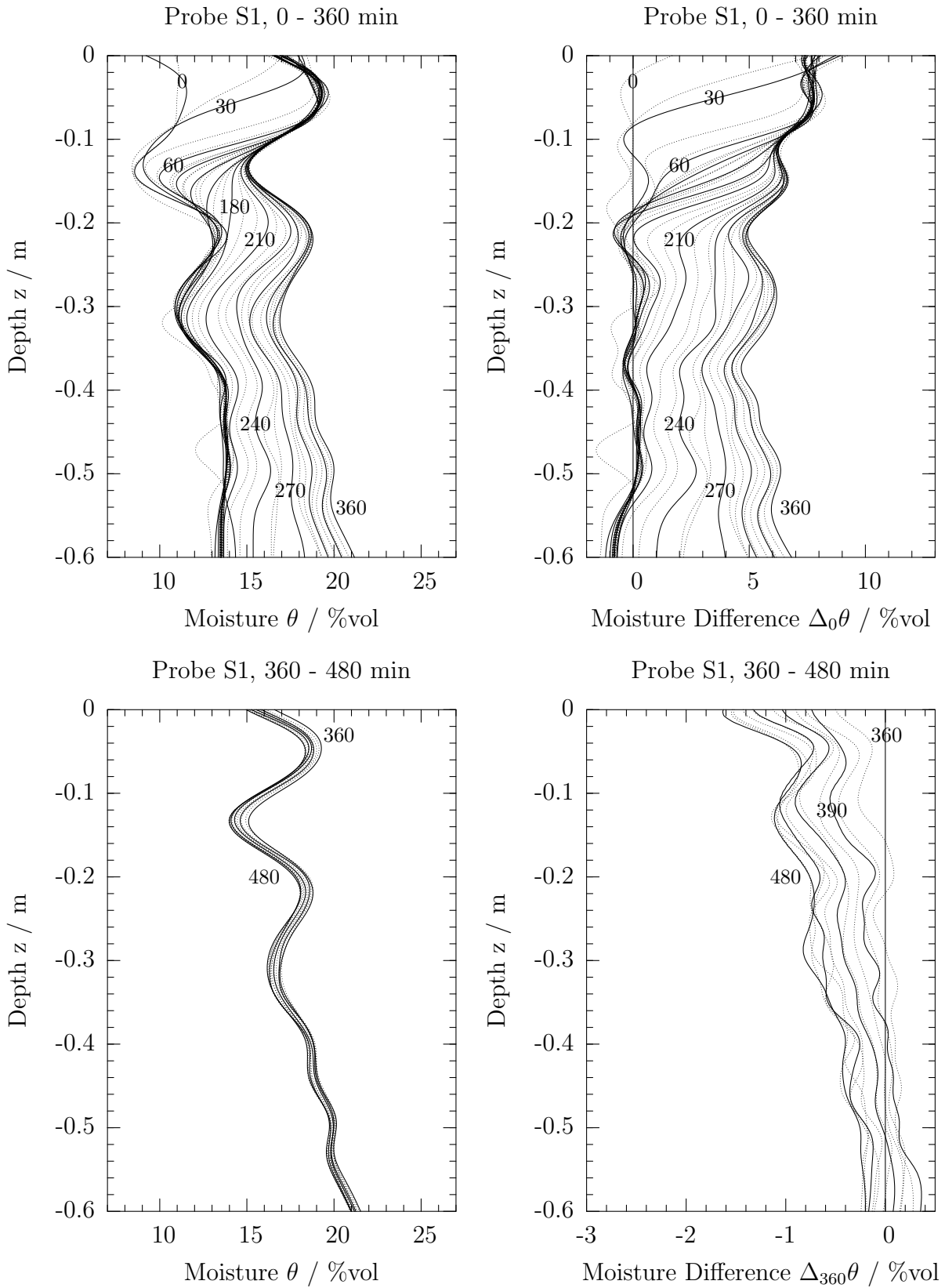
Figure 4.10.: Observed infiltration at probe S1. Upper row: wetting period, lower row: drying period, left column: absolute volumetric water content, right column: change in volumetric water content with respect to a reference state.
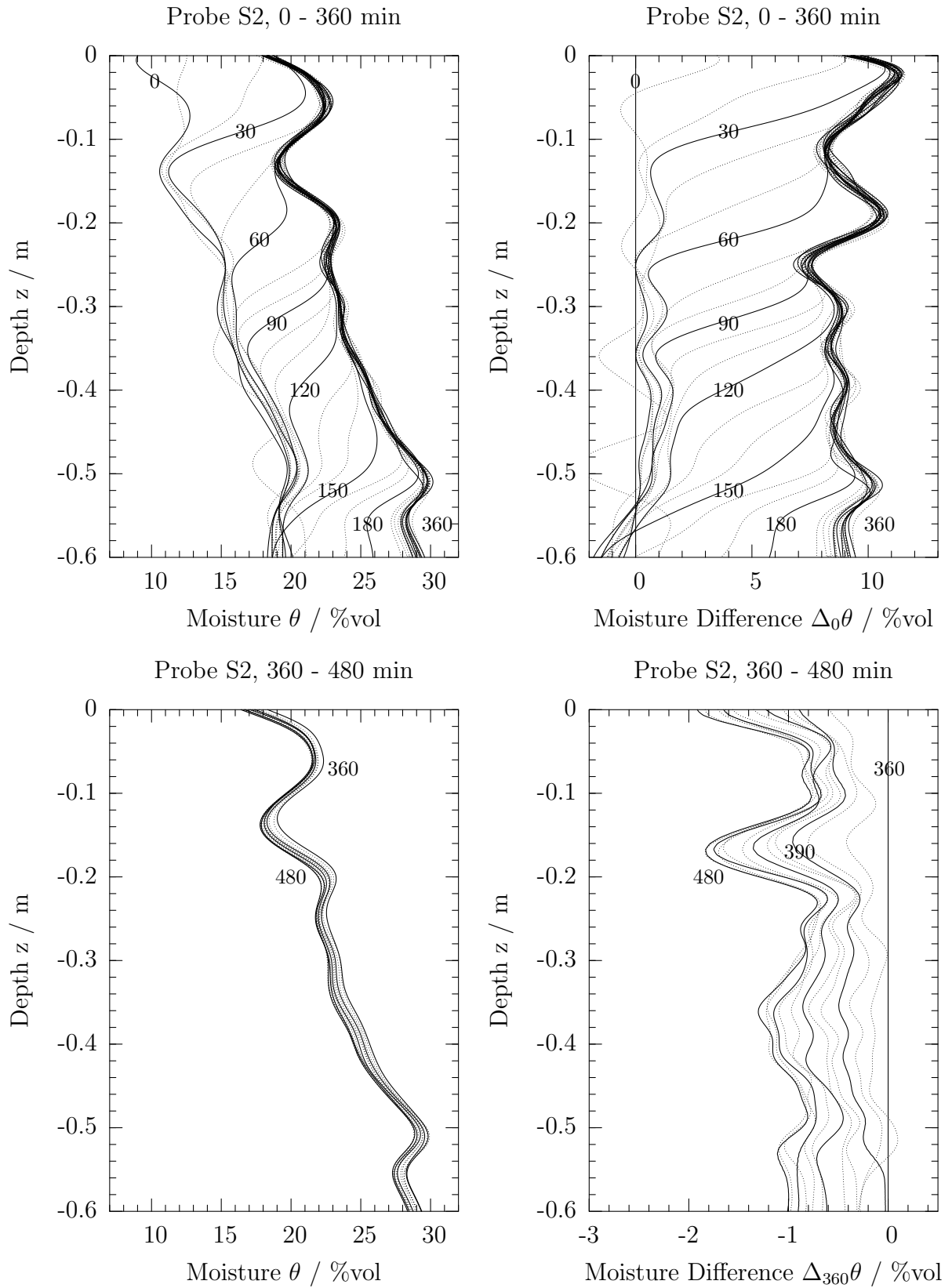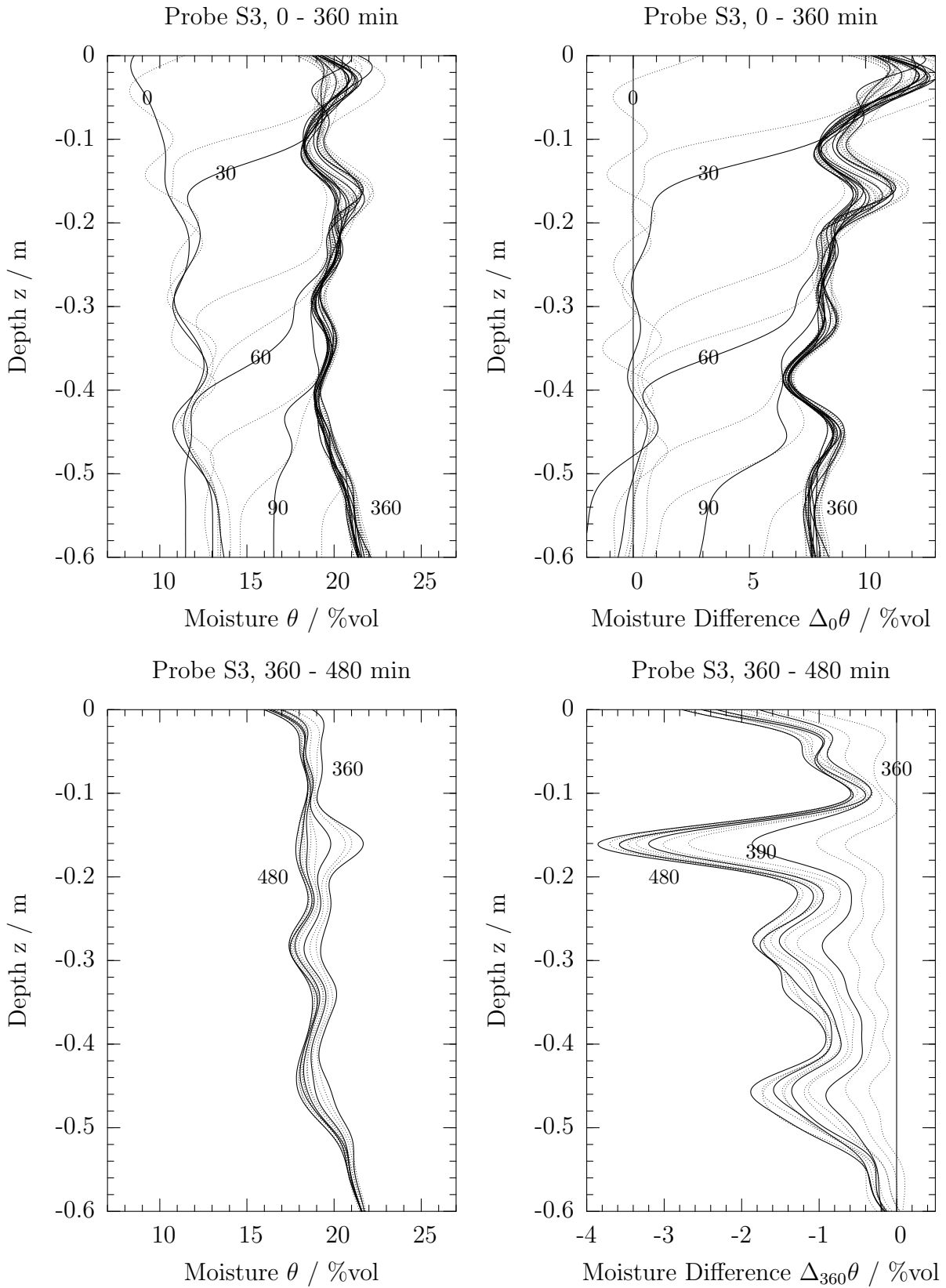
Figure 4.11.: Observed infiltration at probe S2.

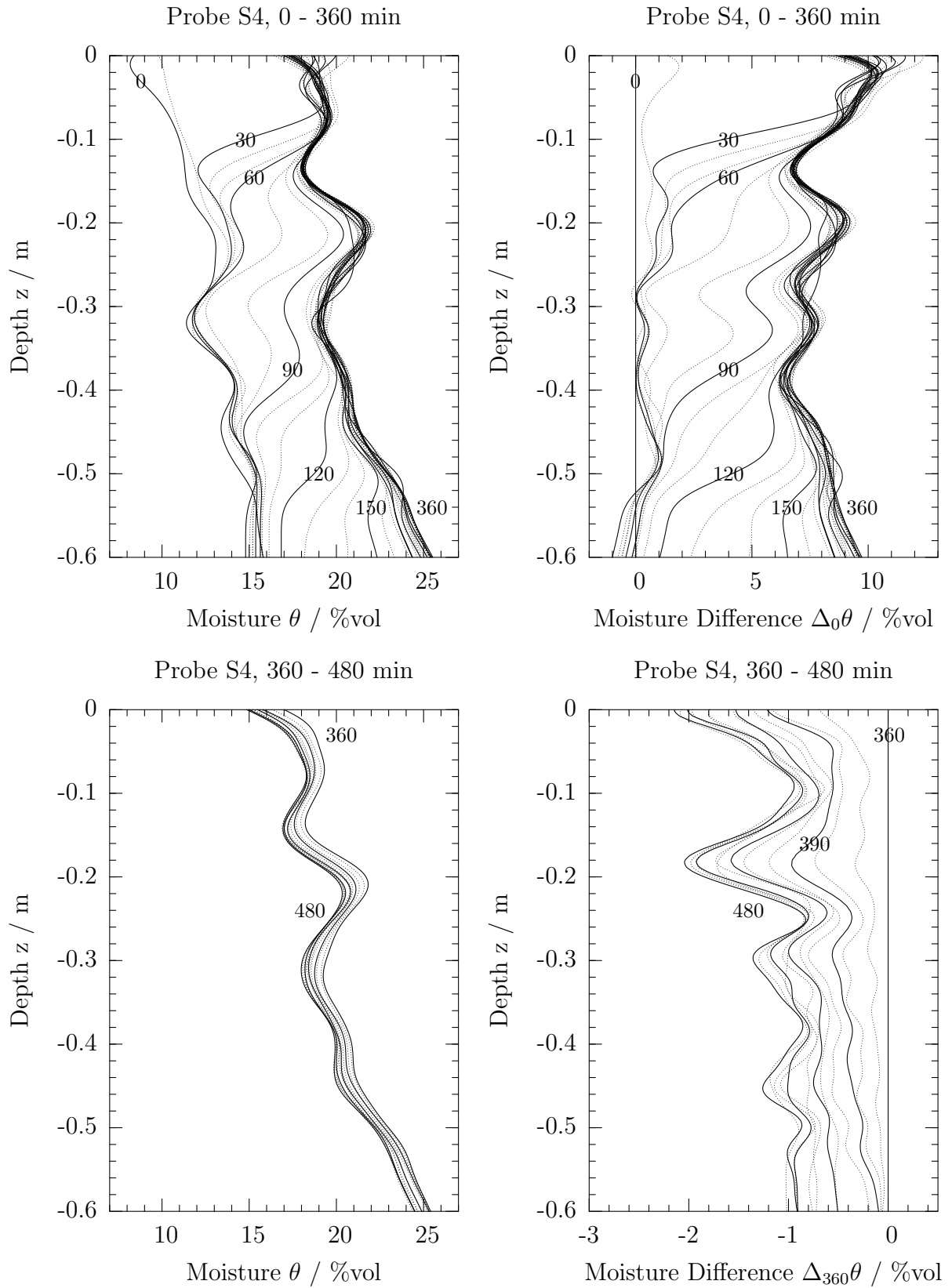Figure 4.12.: Observed infiltration at probe S3.

Figure 4.13.: Observed infiltration at probe S4.

4.1.5. Cumulative Water Content

To better assess the water content profiles and to compare them with common evaluation procedures of TDR measurements the mean water content along the probes is determined by averaging the profiles. For the subsequent analysis it is necessary to define some variables. The *cumulative volumetric water content* $\bar{\theta}$ within a soil column of length $|L|$ and base area A is defined to be the spatial average of soil moisture distribution in this volume. If the moisture is dependent on z only, the average can be expressed as

$$\bar{\theta}(t) = \frac{1}{|L|} \int_0^{-L} \theta(t, z) dz \; . \tag{4.5}$$

In this case the coordinate z has been chosen to be positive upwards making the co-ordinate L of the soil column bottom negative. The evolution of the cumulative water content derived from the moisture profiles for each probe is displayed in Fig. 4.14.

To determine how much of the precipitation water can be retrieved from the soil moisture measurements it is necessary to derive the amount of water stored in the observed volumes. The *water storage w* is the total amount of water within a given soil column. It can be expressed in units of volume, $[\text{L}^3]$, or in units of length, $[\text{L}]$. The latter would be the height of the water table within the column if the dry solid fraction were removed:

$$w[\text{L}^3] \quad = \quad \bar{\theta} \cdot V = \bar{\theta} \cdot |L| \cdot A \; , \tag{4.6}$$

$$w[\text{L}] \quad = \quad w[\text{L}^3]/A = \bar{\theta} \cdot |L| \; . \tag{4.7}$$

Water storage is dependent on the respective volume. Fig. 4.14 shows the water storage in mm determined for the soil columns observed by the 3-rod-probes. It is assumed that the water flux within the soil is purely vertical. As long as the infiltrating water has not reached the bottom of the control volume the rate of change of water storage equals the water flux j_w through the upper boundary:

$$j_w = \frac{dw}{dt} \; . \tag{4.8}$$

The flux may also be expressed as temporal change in volumetric water content:

$$j'_w = \frac{d\bar{\theta}}{dt} \; . \tag{4.9}$$

This simplified continuity equation and its implications is discussed in Sec. 4.4 in more detail. Under constant flux boundary condition, i.e. $j_w = $ const., the water storage (or the cumulative water content) w is rising linearly until no more water can be stored. During this first phase the increase of cumulative water content under constant flux infiltration can be described as:

$$g(t) := \bar{\theta}(t) = j'_w \cdot t + \bar{\theta}_i \; . \tag{4.10}$$

This equation is only valid until the first portions of infiltrating water are crossing the lower boundary of the control volume. Fig. 4.14 shows linear fits (g_{S2}–g_{S4}) to the first rising slopes of the cumulative water content curves where it makes sense. Corresponding

to Eq. 4.10 initial water content and flux have been derived from these linear approximations. The values are listed in Tab. 4.2.

When the volume of water entering the soil column through its upper boundary equals the volume leaving it through the lower boundary *steady state infiltration* is reached. Under this condition the soil moisture distribution and the total amount of water stored within the soil column theoretically are stationary, i.e. do not change with time. The steady state cumulative moisture is denoted by θ_{ss}. The steady state water content has been derived from the curves in Fig. 4.14 by fitting horizontal lines to appropriate curve segments. Tab. 4.2 summarizes these values.
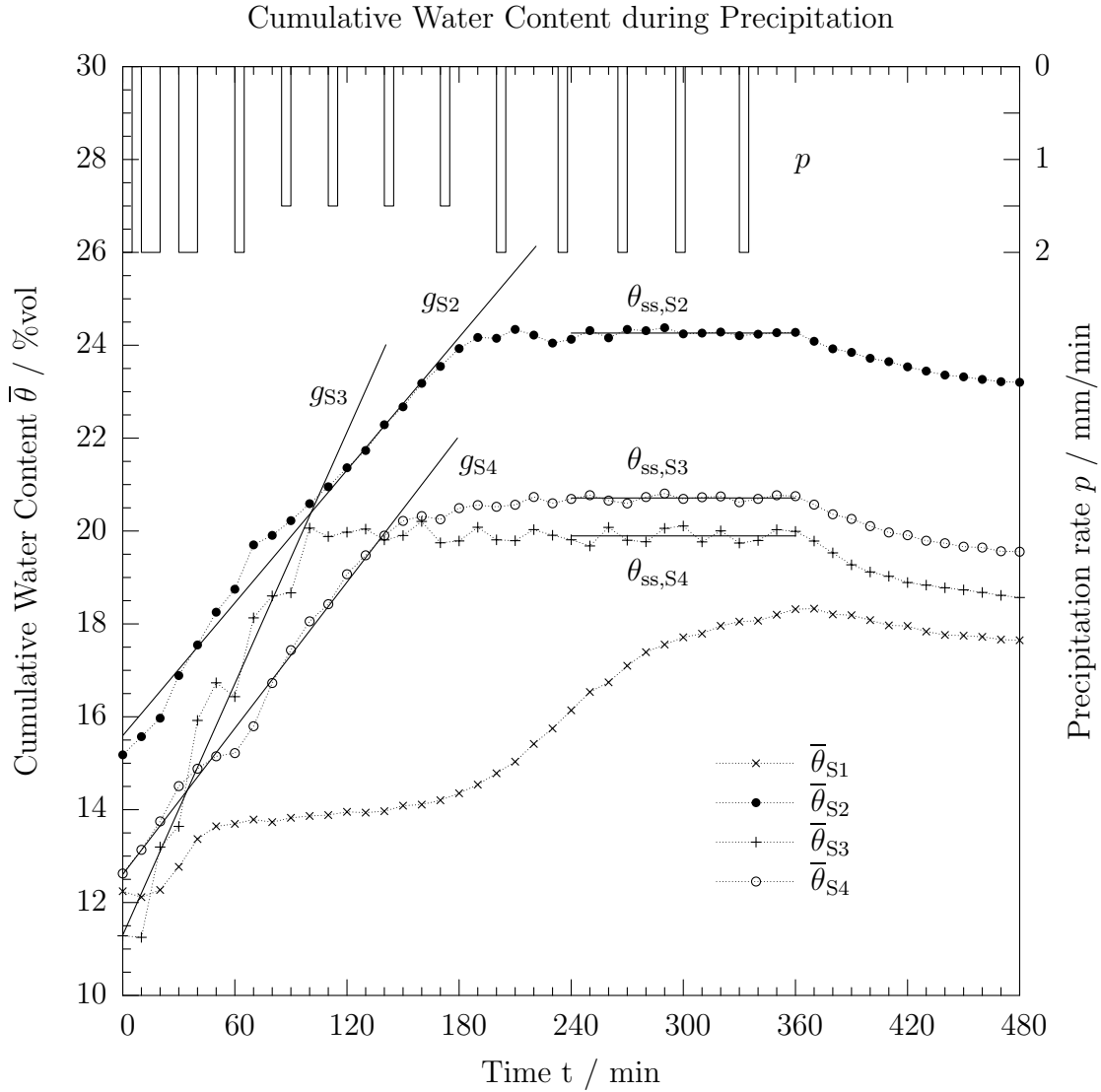

Figure 4.14.: Cumulative water content at probes S1–S4 from integration of water content profiles displayed in Figs. 4.10–4.13. θ_{ss}: steady state water content; g: linear fit to the curve segments during the filling phase.

Probe	$\overline{\theta}_i$	$\overline{\theta}_{ss}$	j_w'	j_w
	%vol	%vol	%vol/min	m/s
S1	12.3	not reached	not defined	not defined
S2	15.6	24.3	0.048	$4.8 \cdot 10^{-6}$
S3	11.3	19.9	0.090	$9.0 \cdot 10^{-6}$
S4	12.6	20.7	0.053	$5.3 \cdot 10^{-6}$

Table 4.2.: Initial and steady state cumulative water content, and flux density through upper soil surface corresponding to Fig. 4.14.

To test whether the water balance between cumulative precipitation and stored water could be closed during the first infiltration phase the water storage difference in units of $[L^3]$ was calculated:

$$\Delta w(t) = w(t) - w(0) = V \cdot \Delta\overline{\theta} = |L| \cdot A \cdot (\overline{\theta}(t) - \overline{\theta}_i) \; . \tag{4.11}$$

As long as no water leaves any of the four control volumes of depth $|L|$ across the lower boundary and no water is actually ponded, the total cumulative precipitation should be stored within the soil. Since no other information is available it is assumed that each of the monitored water storages has a base area of $A/4$ with A being the total area of the upper soil surface. Thus the total amount of observed storage content with equally weighted observations is:

$$\Delta\overline{w} = \sum_{i=1}^{4} |L| \, (A/4) \, \Delta\overline{\theta}_{Si} = \frac{1}{4} \sum_{i=1}^{4} V \, \Delta\overline{\theta}_{Si} = \frac{1}{4} \sum_{i=1}^{4} \Delta\overline{w}_{Si} \; . \tag{4.12}$$

Thus the total amount of measured storage content is the arithmetic mean of the individual storages defined by the soil columns around each probe. To yield the formula in units of $[L]$ both sides have to be divided by A. Fig. 4.15 shows the results of the individual water storage contents in comparison with the cumulative precipitation. Tab. 4.3 lists the maximum amount of stored water.

Probe	max. storage Δw_{max}	max. storage Δw_{max}	Time interval
	%	mm	for avg. / min
S1	6.8	40.7	[360]
S2	9.5	56.8	[100 . . . 360]
S3	9.3	55.8	[200 . . . 360]
S4	8.6	51.5	[250 . . . 360]

Table 4.3.: Maximum water storage of the soil columns observed by probes S1 to S4 in units %vol and mm corresponding to Fig. 4.15. Last column gives the time interval having been used for averaging.

At time $t = 80$ min none of the individual storages was filled. The cumulative precipitation up to this time was $P = 60$ mm but the total water storage was increased by $\Delta\overline{w} = 28$ mm only. With this procedure only half of the precipitation water is found in the soil. Three reasons may be identified for this discrepancy in water balance: 1. preferential flow occurred probably along the lysimeter wall and the vertical ribbon cable, 2. the soil columns the individual probes are representative for do not reveal the same base area $A/4$, i.e. the water storages have to be weighted differently, 3. more water than average was stored in unobserved regions in the lysimeter.
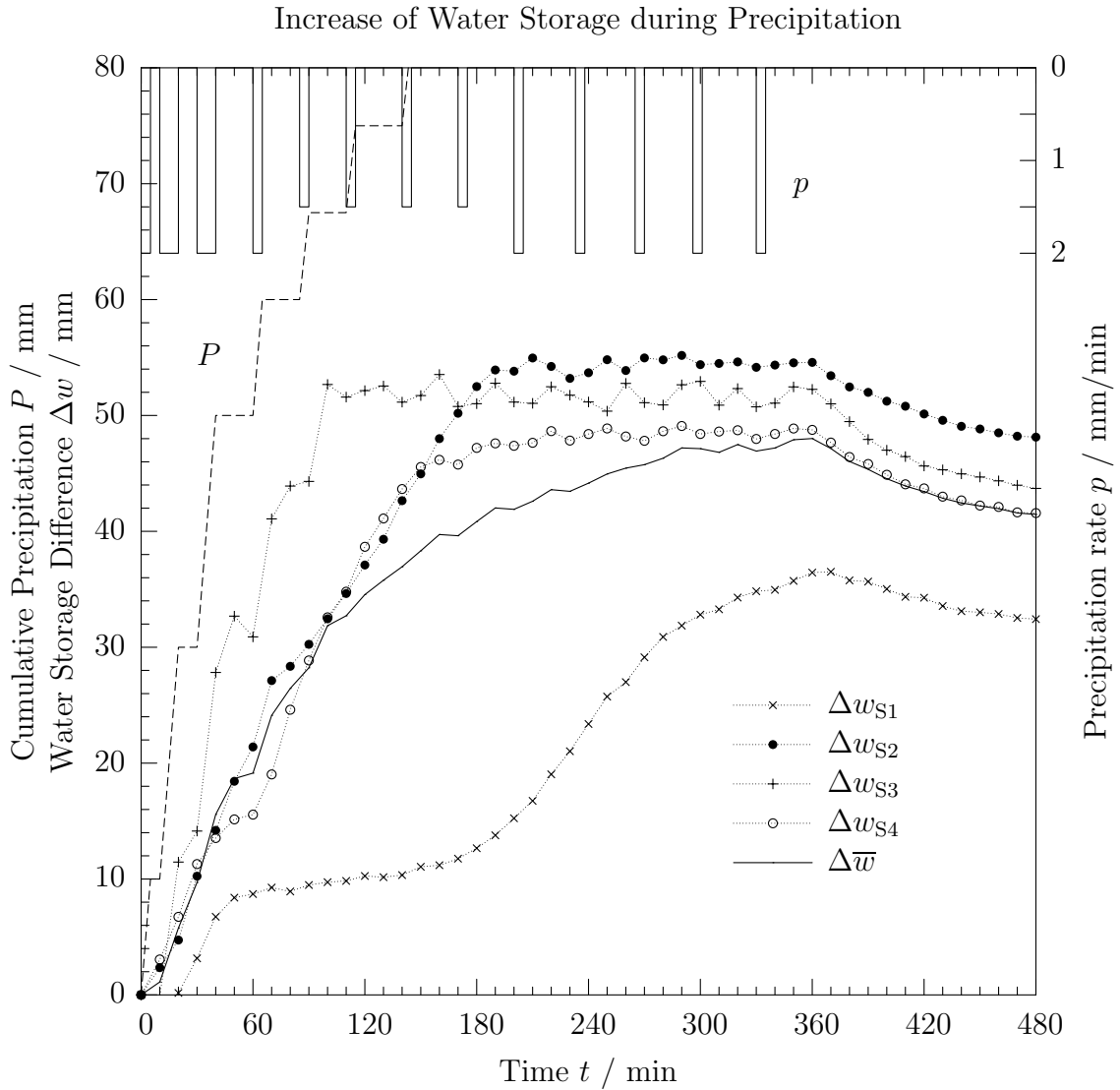

Figure 4.15.: Increase of water storage with respect to an initial state determined by TDR measurements under irrigation.

4.1.6. Uncertainties in Determination of Average Water Content

Ferré et al. (1996) showed in case the water content along a TDR-probe is nonuniform the average water content determined from TDR pulse travel-time will be correct only, if the travel-time is a linear function of the volumetric water content. This relationship is defined by electrical probe and dielectric soil characteristics. It is indeed often nonlinear, especially if coated probes are used.

If the travel-time is a nonlinear function of the water content the pulse travel-time will be influenced by the water content distribution along the probe even if the total water content is not changing. Expressed the other way round: different water content distributions with different average water content may lead to the same travel-time.

The measurement of the total pulse travel-time does not give any information about the distribution of water along the probe. If the average water content is determined by means of the total pulse travel-time t_0, it will be assumed implicitly to be constant, i.e. uniformly distributed. The average water content derived from travel-time only is referred to as $\theta(t_0)$. The influence of a nonuniform water distribution on the total amount of water for a given pulse travel-time can best be studied by means of the Taylor series of $\theta(t)$ around t_0:

$$\theta(t_0 + \Delta t) = \theta(t_0) + \left.\frac{\partial \theta}{\partial t}\right|_{t_0} \Delta t + \frac{1}{2} \left.\frac{\partial^2 \theta}{\partial t^2}\right|_{t_0} (\Delta t)^2 + R((\Delta t)^3). \tag{4.13}$$

The higher the moisture content the higher the travel-time, thus $\partial \theta/\partial t > 0$. All functions $\theta(t)$ found in literature are convex or linear (e.g. citetTopp:1980; *Roth et al.* (1990)), thus $\partial^2 \theta/\partial t^2 \geq 0$. Both relations are valid over the total co-domain of θ.

To investigate the influence of different water content distributions the path along the waveguide is cut into halves and the travel-time is increased by Δt for the first half and reduced by the same amount for the remaining half so that the total travel-time t_0 is held constant. It is assumed for now that the water content within each individual segment is constant. Then increase and decrease of travel-times are corresponding to water contents $\theta(t_0 + \Delta t)$ and $\theta(t_0 - \Delta t)$, respectively. According to the Taylor series the new average water content is

$$\begin{aligned}
\overline{\theta}_{t_0}(\Delta t) & := \frac{1}{2}[\theta(t_0 + \Delta t) + \theta(t_0 - \Delta t)] \\
& = \theta(t_0) + \frac{1}{2} \left.\frac{\partial^2 \theta}{\partial t^2}\right|_{t_0} (\Delta t)^2 + R((\Delta t)^4) \\
& \geq \theta(t_0).
\end{aligned} \tag{4.14}$$

Terms in Δt with odd exponent cancel mutually. The equality in the $\geq$ sign on the right hand side will generally hold if and only if $\theta(t)$ is a linear function of t. In this case a nonuniform distribution of water along the signal propagation will not influence the total pulse travel-time and the evaluation will lead to the correct average water content along the probe, in perfect accordance to *Ferré et al.* (1996).

Now the question arises: which are the maximum and minimum water contents for a given fixed travel-time t_0? If $\theta(t)$ is a convex function of t, then the function $\overline{\theta}_{t_0}(\Delta t)$

will be monotonically increasing with Δt. Thus the minimum average water content in accordance with the pulse travel-time t_0 is yielded if $\Delta t = 0$, which means that there is no water content difference between the two segments along the waveguide.

The distribution leading to the maximum water content for a given pulse travel-time t_0 can be derived from a thought experiment. Eq. 4.14 shows that the higher the difference Δt in travel-time along the two halves of the signal path the higher the average moisture content $\overline{\theta}_{t_0}(\Delta t)$. Thus to yield a total water content as large as possible it is necessary to shift as much water as possible from one segment to the other. Of course, the water content within the segments must be within reasonable limits.
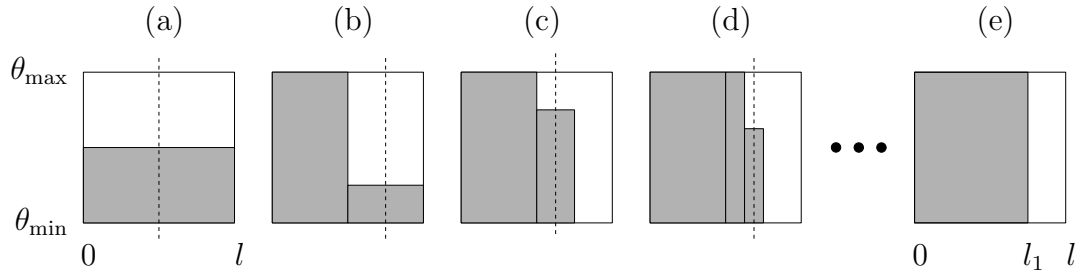

Figure 4.16.: Different moisture distributions leading to the same pulse travel-time t0. (a) minimum water content, uniform distribution; (b)–(d) intermediate states; (e) maximum water content, perfect layering. Abscissa: spatial coordinates along moisture probe; ordinate: volumetric water content with appropriate lower and upper bounds.

Fig. 4.16 shows that generally this procedure leaves one segment only partially filled. If this is divided further into halves, the same argument will apply again. The algorithm will end up with segments of maximum or minimum possible water content. A permutation of these segments does not influence the total travel-time. By gathering all dry segments on one side and all saturated segments on the other the distribution looks like one maximally filled layer of appropriate width followed by one minimally filled layer.

The average water content derived directly from travel-time θ_{time} compared to the mean water content determined from a soil moisture profile θ_{prof} is given Fig. 4.17. In principle the method of calculating θ_{prof} from a Spatial TDR moisture profile should give the correct average water content, since during the inverse modeling the total travel-time is held fixed, not the water content from travel-time analysis.

As predicted $\theta_{\text{time}} \leq \theta_{\text{prof}}$. The maximum water content would be yielded if the soil was separated into a totally dry (0 %vol) and totally wet (30 %vol) layer ($\theta_{\text{max}}^{(2)}$ in Fig. 4.17). Reasonable prior information may be used to better assess the uncertainty. If minimum and maximum water contents were limited to 8 %vol and 28 %vol for the two soil layers, the maximum possible total water content would decrease ($\theta_{\text{max}}^{(1)}$ in Fig. 4.17). In this case the uncertainty inherent to the water content derived from travel-time would be ± 0.5 %vol if θ_{prof} were the correct water content.

Cumulative Water Content during Precipitation
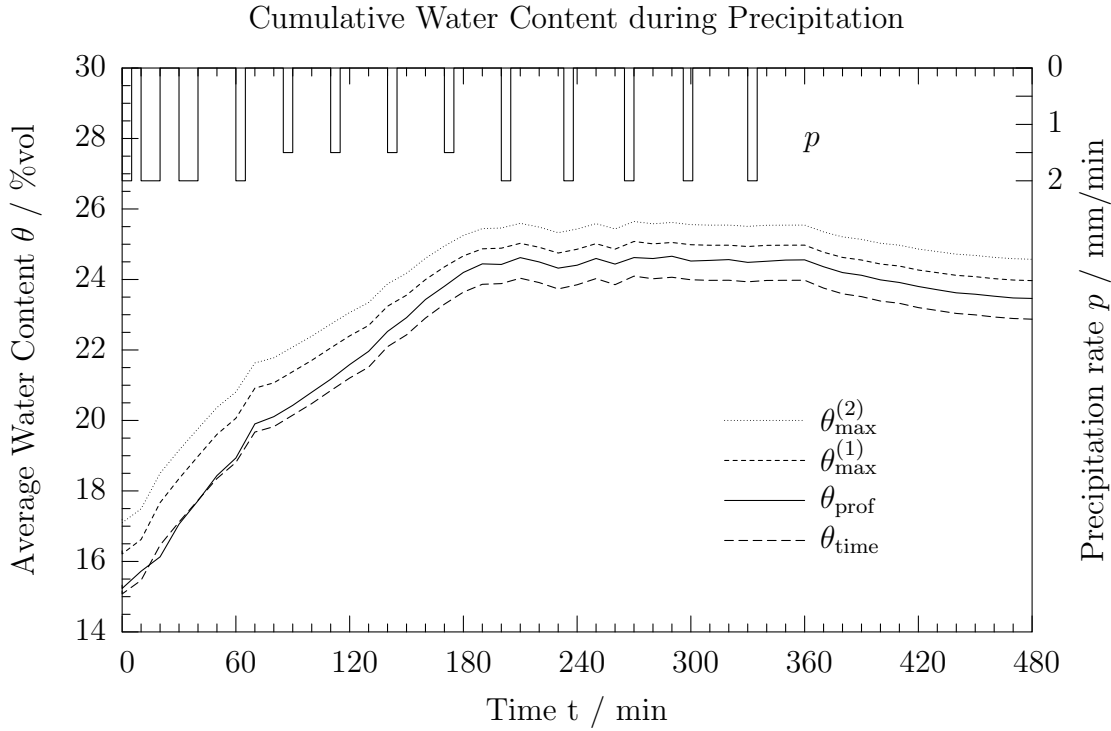
Figure 4.17.: Temporal evolution of average moisture content at probe S2 evaluated with different methods. θ_{time}: average water content resulting from TDR travel-time analysis; θ_{prof}: average water content from reconstructed soil moisture profiles, assumed to be the best estimate. In case of perfectly layered soil the error resulting from travel-time analysis can lead to $\theta_{\text{max}}^{(1)}$ (dry (8%vol) and wet (28%vol) layer) and $\theta_{\text{max}}^{(2)}$ (totally dry (0%vol) and totally wet (30%vol) layer).

4.1.7. Discussion

Generally the soil moisture dynamic differs vastly from probe to probe (Figs. 4.10–4.13). The dynamic range of possible moisture profiles along an individual probe during the irrigation phase (0–360 min) is limited by upper and lower bounds formed by initial and steady state water content profiles (Figs. 4.10–4.13). These envelopes reveal a linearly rising trend with depth. The average slope and average moisture of these bounds differ between the probes. The wavy structure of the envelopes is due to varying soil compaction. This shape is conserved, i.e. dryer layers remain dryer during infiltration. Differently compacted layers store a different amount of water, which e.g. can be seen clearly from the wavy upper envelope of S2's moisture difference profiles (Fig. 4.11, top right).

The dense sequence of infiltration fronts at probe S1 between approximately 60 and 180 minutes (Fig. 4.10, top right) shows an inhibition of vertical percolation. Two hypothesis may be formulated for this effect: 1. the flux from the soil surface is reduced or stopped;

2. a capillary barrier inhibits the vertical flow.

The first hypothesis is supported by the observation of mobilized fine soil particles which could have reduced the hydraulic conductivity by sealing the soil surface. An argument contradicting this assumption is that the water already in soil would have drained. This was not observed.

The second hypothesis is more likely but the question arises why no local increase of water content above the barrier was observed. The answer is lateral redistribution of infiltrating water on top of the barrier. Another seeming contradiction to the capillary barrier hypothesis is the continuing vertical movement of the infiltration front. The movement is very slow (5 cm in 3 hours) but it is obvious from the data. This might be explained by wall effects along the probe rods. Water could have percolated along these possible preferential flow paths. This local flow and corresponding wetting would mislead the interpretation of the moisture profiles because the sensitive area of the TDR probe is limited. It is very likely that the TDR did not 'see' a moving infiltration front but only local disturbances.

The moisture at S1 starts to increase below the inhibited infiltration front clearly after some 210 minutes. This behavior shows a strong evidence for horizontal flow components. The water is redistributing laterally within the soil body. The increase is relatively homogeneous between -0.2 and -0.6 m (Fig. 4.10, top right).

Probe S2 shows the most regular infiltration characteristic. No capillary barrier was observed and lateral flux is of minor importance.

Fastest infiltration was observed with probe S3. After approx. 2 hours the front had passed the lower boundary of the control volume. It is not clear why the infiltration of S3 is so much faster. Maybe this process is linked to the ponding which temporarily occurred around S3. The moisture profiles of S3 look somewhat noisy in the upper 0.2 m of the control volume. These local moisture variations also affect the cumulative water content curve of S3 (Fig. 4.15). These variations may be partly explained by the intermittent precipitation pulses.

A weaker inhibition of infiltration was observed at probe S4 between 30 and 60 minutes (Fig. 4.13, upper right). After 60 minutes a clear increase of water content below the slowly propagating infiltration front set in overlaying the regular vertical movement, also an evidence for lateral flow.

During the drying period (360–480 min) the probes show individual behavior, too. The most regular decrease of water content is with probe S1. The other probes — but especially S3 — show a layer in approx. 0.18 m depth which drained faster and more than the rest of the soil column. A faster drainage gives evidence for larger soil pores. It seems that this layer is less compact than the adjacent layer above. This condition may lead to a capillary barrier, an assumption in accordance with other observations stated above.

Some of the moisture difference profiles ($\delta_0\theta(z)$) of the irrigation phase (0–360 min) show negative values up to -2 %vol especially in the lowest 5 cm of the control volume. This local drying is an artifact probably due to an insufficiency of the reconstruction algorithm near the probe end (S. Schlaeger, personal communication). Negative moisture differences above -0.5 m depth are either caused by an insufficient reference (initial)

profile (e.g. Fig. 4.10, top right) or by disturbances in the reconstructed moisture profiles due to noisy TDR reflectograms (e.g. Fig. 4.11, top right, timestamps 10 and 20). Steady state infiltration was reached in soil column S2, S3, and S4. Column S1 had not reached constant steady state moisture distribution after 360 minutes (c.t. Fig. 4.14). The steady state cumulative water content for the different soil columns is listed in table 4.3. None of these values reached the theoretical maximum level which is equal to the soil porosity. The actual porosity in the lysimeter has not been determined directly but part of the same soil was analyzed separately (s. App. A.1). A porosity range of approx. 30–50% was realizable in another experiment (A. Scheuermann, personal communication). All steady state moisture contents were below even the smallest possible porosity. This is remarkable since ponding had occurred around probe S3. This was believed to be due to saturation excess but since the soil was far from being saturated ponding must have been due to infiltration excess. Transport and sedimentation of fine silt fraction could be the reason for the reduced hydraulic conductivity near the soil surface.

Despite the difficulties in accurate reconstruction and calibration the results of Spatial TDR are already promising. Soil moisture dynamic in the vadose zone can be monitored by this novel method with high spatial and temporal resolution. The lysimeter experiment impressively demonstrates how much information about small scale variability of soil is contained in the TDR reflectograms and their corresponding water content profiles. Capillary barriers and other blocking layers play an important role for local saturation in layered natural and agricultural soils. Local saturation as an effect of such barriers can be detected by Spatial TDR, which may lead to an improved assessment of the soil's storage capacity e.g. for flood warning. It has also been shown that in some cases even the existence of lateral flow components could be detected indirectly from the one-dimensional soil moisture dynamic.

4.2. Accuracy of Spatial TDR

Earlier experiments with probes connected from both sides and reconstruction of two parameter distributions have already shown a good agreement between reconstructed moisture profile and oven-drying-method for unsaturated conditions (*Schlaeger*, 2002). These findings give evidence for the feasibility of the measurement principle. Nevertheless the accuracy of water content profiles determined by Spatial TDR still has to be checked for the particular application of coated 3-rod-probes with TDR measurement from one side only.

4.2.1. Comparison to Oven Drying Method

To test the accuracy of Spatial TDR with the current set of calibration parameters a comparison with the oven drying method was performed. The latter is a well-accepted standard procedure and often serves as a reference measurement. With this procedures soil samples of known volume are taken, weighted, dried, and weighted again. The weight difference yields the gravimetric water content which can be transformed into volumetric

water content (s. Sec. 2.7). To compare reconstructed water content profiles resulting from Spatial TDR with oven drying method an experiment was conducted. A PVC box with three chambers holding a 3-rod-probe was built (Fig. 4.18). The chambers were filled with soil probes of different water content. With this setup a TDR measurement in a layered soil of piecewise constant water content was simulated. The chambers or 'soil layers' are referred to as 'L1', 'L2', and 'L3'.
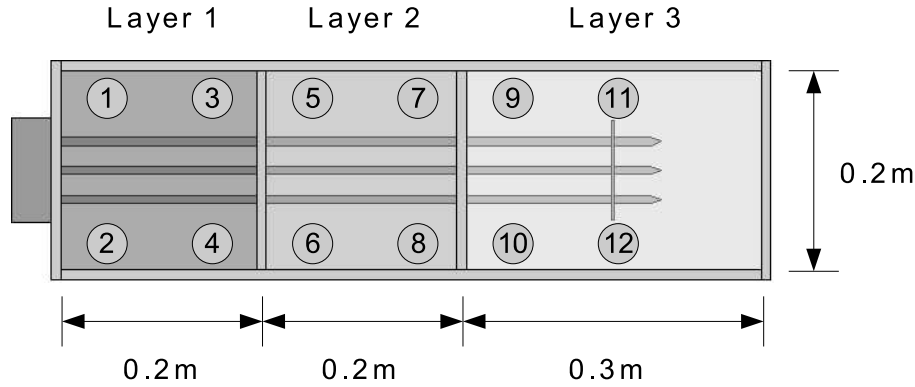

Figure 4.18.: PVC box with three chambers (layers) holding the 3-rod-probe horizontally. Circles indicate locations of soil samples for oven drying.

Three portions of the loamy sand (s. App. A.1) used in the infiltration experiment were mixed with different amount of water. For the sake of simplicity these mixtures are denoted by 'dry', 'moist', and 'wet', according to their moisture state. The soil preparation was similar to that of Sec. 2.6.

Four experiments were conducted with different fillings. From each chamber up to four soil samples were taken (Fig. 4.18) to determine the volumetric water content by the oven drying method. Tab. 4.4 summarizes the preparation of the experiments and the resulting soil moisture. For example in experiment number 2 (Exp. No.=2) the chambers L1, L2, and L3 were filled with dry, moist, and wet soil, respectively. Twelve soil probes were taken, four from each chamber.

The volume V_T of the soil samples is equal to the volume of the probe cylinder used. With this information the mass m_W of water lost by oven drying could be transformed into volumetric water content θ by means of Eq. 2.73. Average $\overline{\theta}$ and standard deviation $\sigma(\theta)$ of water content were calculated per layer.

It can be assumed that the stochastic variable θ follows a Gaussian probability density. The standard deviation σ of the experimental water content is a measure of uncertainty. The quotient $\sigma(\theta)/\overline{\theta}$ serves as a kind of relative error of the experimental outcome.

In each of the four experiments two TDR measurements were conducted, one with a short coaxial cable of 3.5 m between instrument and probe, the other with a long connection of approximately 14.5 m length (s. Fig. 4.4). The water content profile reconstruction was performed in the same way as in Sec. 4.1.4. Figs. 4.19–4.22 show the results. Each figure consists of two sub-diagrams: the top diagram shows the incident and reflected TDR signals and the signal approximation by Spatial TDR for short and long connecting

Exp. No.	Soil Sample	Layer	State	m_W / g	V_T / cm^3	θ / %vol	$\overline{\theta}$ / %vol	$\sigma(\theta)$ / %vol	$\sigma(\theta)/\overline{\theta}$ / 1
1	1	L1	dry	0.07	17.81	0.39			
1	2	L1	dry	0.07	17.81	0.39			
1	5	L2	dry	0.08	17.81	0.45			
1	6	L2	dry	0.07	17.81	0.39			
1	9	L3	dry	0.09	17.81	0.51			
1	10	L3	dry	0.08	17.81	0.45	0.43	0.05	0.11
2	1	L1	dry	0.08	17.81	0.45			
2	2	L1	dry	0.06	17.81	0.34			
2	3	L1	dry	0.08	17.81	0.51			
2	4	L1	dry	0.06	17.81	0.39	0.42	0.074	0.17
2	5	L2	moist	1.34	17.81	7.53			
2	6	L2	moist	1.45	17.81	8.14			
2	7	L2	moist	1.44	17.81	8.09			
2	8	L2	moist	1.38	17.81	7.75	7.88	0.29	0.04
2	9	L3	wet	2.33	17.81	13.08			
2	10	L3	wet	2.37	17.81	13.31			
2	11	L3	wet	2.47	17.81	13.87			
2	12	L3	wet	2.48	17.81	13.93	13.55	0.42	0.03
3	1	L1	dry	0.22	40.72	0.54			
3	2	L1	dry	0.25	40.72	0.6			
3	3	L1	dry	0.24	40.72	0.56			
3	4	L1	dry	0.23	40.72	0.56	0.57	0.03	0.04
3	5	L2	wet	5.49	40.72	13.48			
3	6	L2	wet	5.48	40.72	13.46			
3	7	L2	wet	5.55	40.72	13.63			
3	8	L2	wet	5.57	40.72	13.68	13.56	0.11	0.01
3	9	L3	moist	3.45	40.72	8.47			
3	10	L3	moist	3.38	40.72	8.3			
3	11	L3	moist	3.33	40.72	8.18			
3	12	L3	moist	3.33	40.72	8.19	8.29	0.13	0.02
4	1	L1	wet	5.35	40.72	13.13			
4	2	L1	wet	5.23	40.72	12.85			
4	3	L1	wet	5.25	40.72	12.89			
4	4	L1	wet	5.09	40.72	12.5	12.84	0.26	0.02
4	5	L2	moist	3.28	40.72	8.06			
4	6	L2	moist	3.25	40.72	7.99			
4	7	L2	moist	3.47	40.72	8.52			
4	8	L2	moist	3.49	40.72	8.56	8.28	0.30	0.04
4	9	L3	dry	0.21	40.72	0.52			
4	10	L3	dry	0.24	40.72	0.59			
4	11	L3	dry	0.22	40.72	0.53			
4	12	L3	dry	0.25	40.72	0.6	0.56	0.04	0.07

Table 4.4.: Preparation of the experiments and results from the oven drying method.

coax cable, the bottom diagram displays the corresponding water content distribution together with results from the oven drying method. The error bands of the reconstructed water content profiles indicate the influence of the calibration parameters C_1 and C_2 with their uncertainties.

Approximation of TDR Signal

Spatial TDR vs. Oven Drying

Figure 4.19.: Spatial TDR vs. oven drying. Sequence of material: dry/dry/dry. Top: reconstructed TDR reflectograms for short and long coax cable, bottom: moisture profiles from Spatial TDR (lines) and oven drying (points).

Approximation of TDR Signal

Spatial TDR vs. Oven Drying

Figure 4.20.: Spatial TDR vs. oven drying. Sequence of material: dry/moist/wet. Top: reconstructed TDR reflectograms for short and long coax cable, bottom: moisture profiles from Spatial TDR (lines) and oven drying (points).

Approximation of TDR Signal
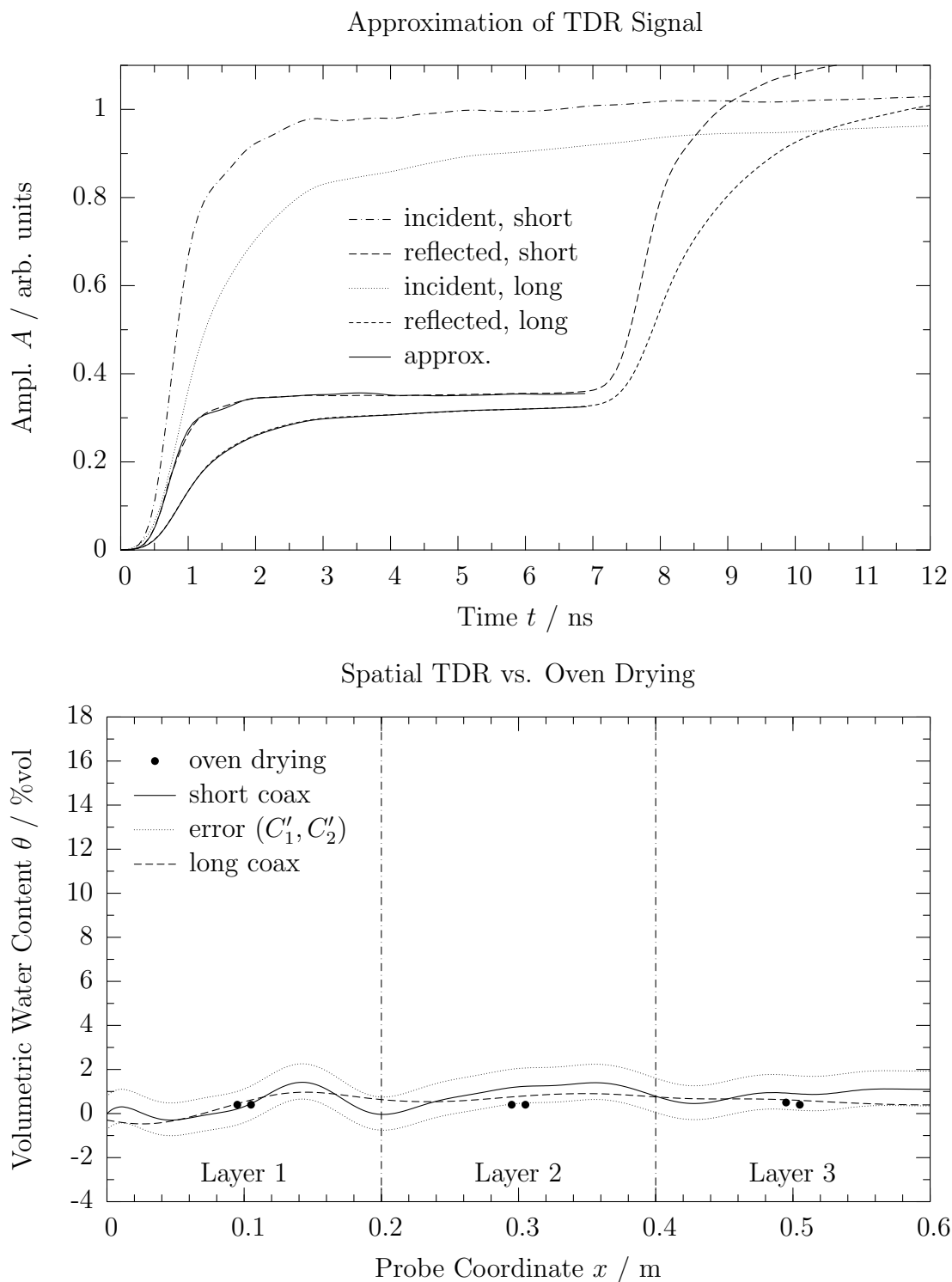

Spatial TDR vs. Oven Drying

Figure 4.21.: Spatial TDR vs. oven drying. Sequence of material: dry/wet/moist. Top: reconstructed TDR reflectograms for short and long coax cable, bottom: moisture profiles from Spatial TDR (lines) and oven drying (points).

Approximation of TDR Signal

Spatial TDR vs. Oven Drying

Figure 4.22.: Spatial TDR vs. oven drying. Sequence of material: wet/moist/dry. Top: reconstructed TDR reflectograms for short and long coax cable, bottom: moisture profiles from Spatial TDR (lines) and oven drying (points).
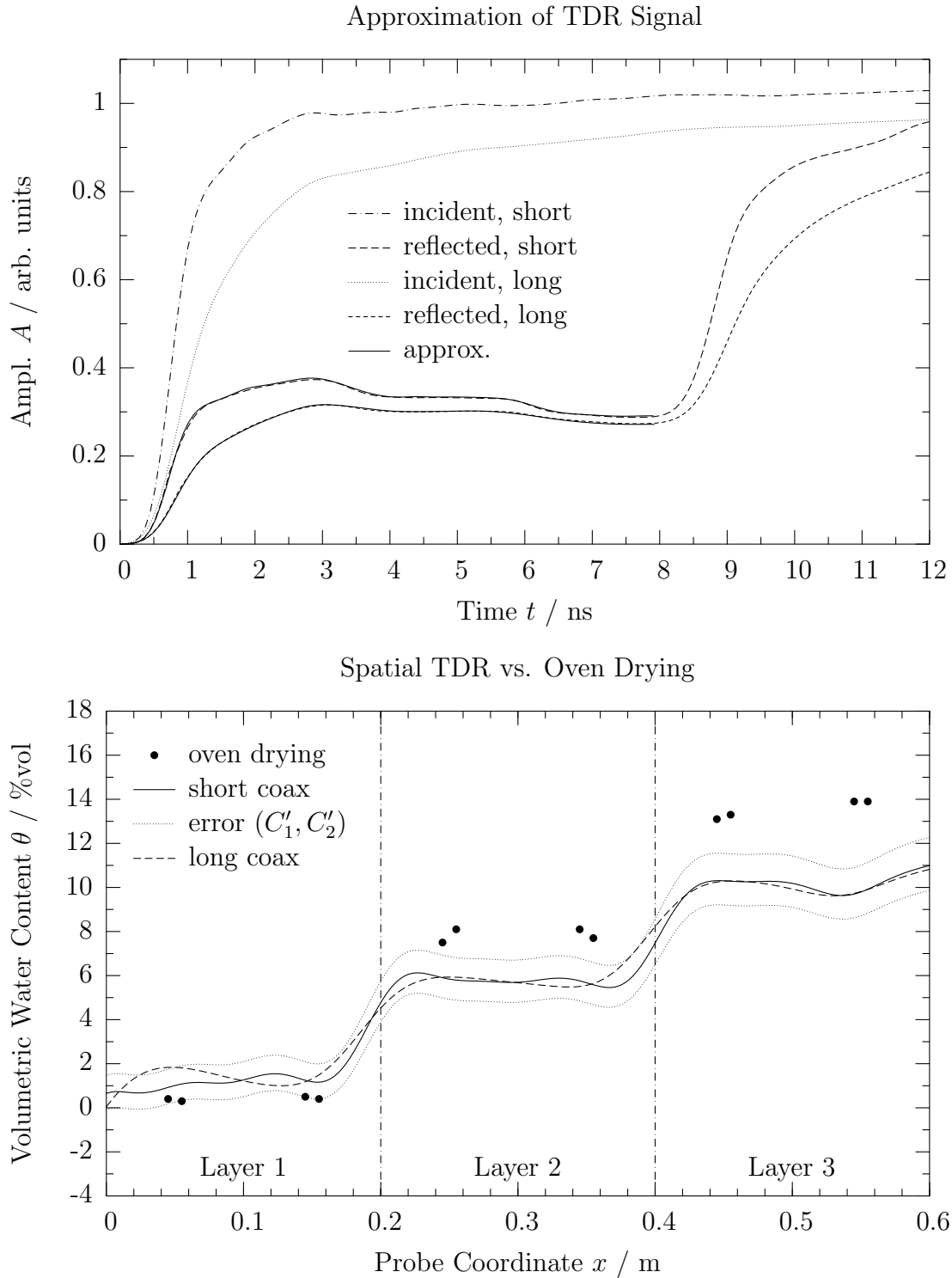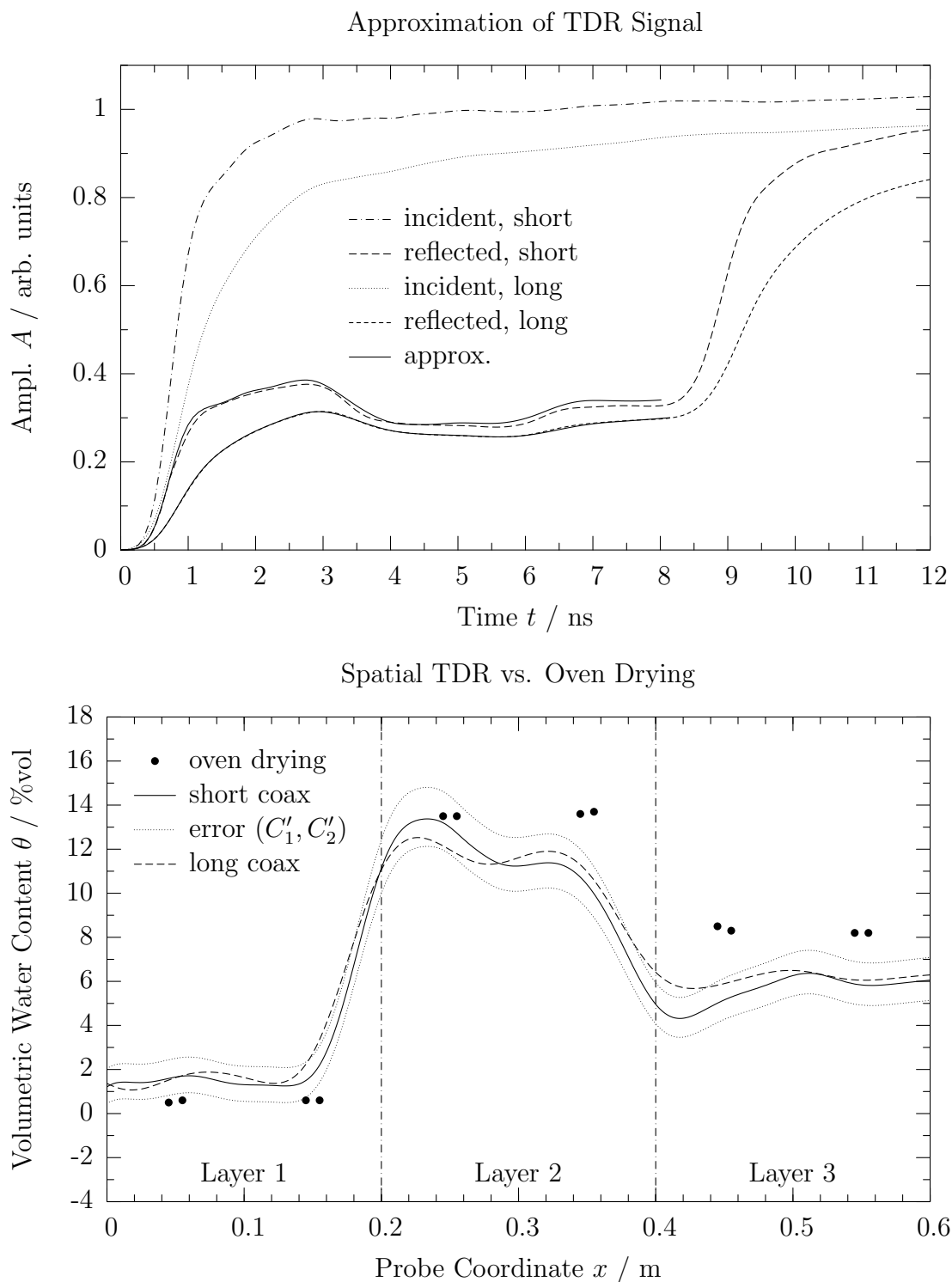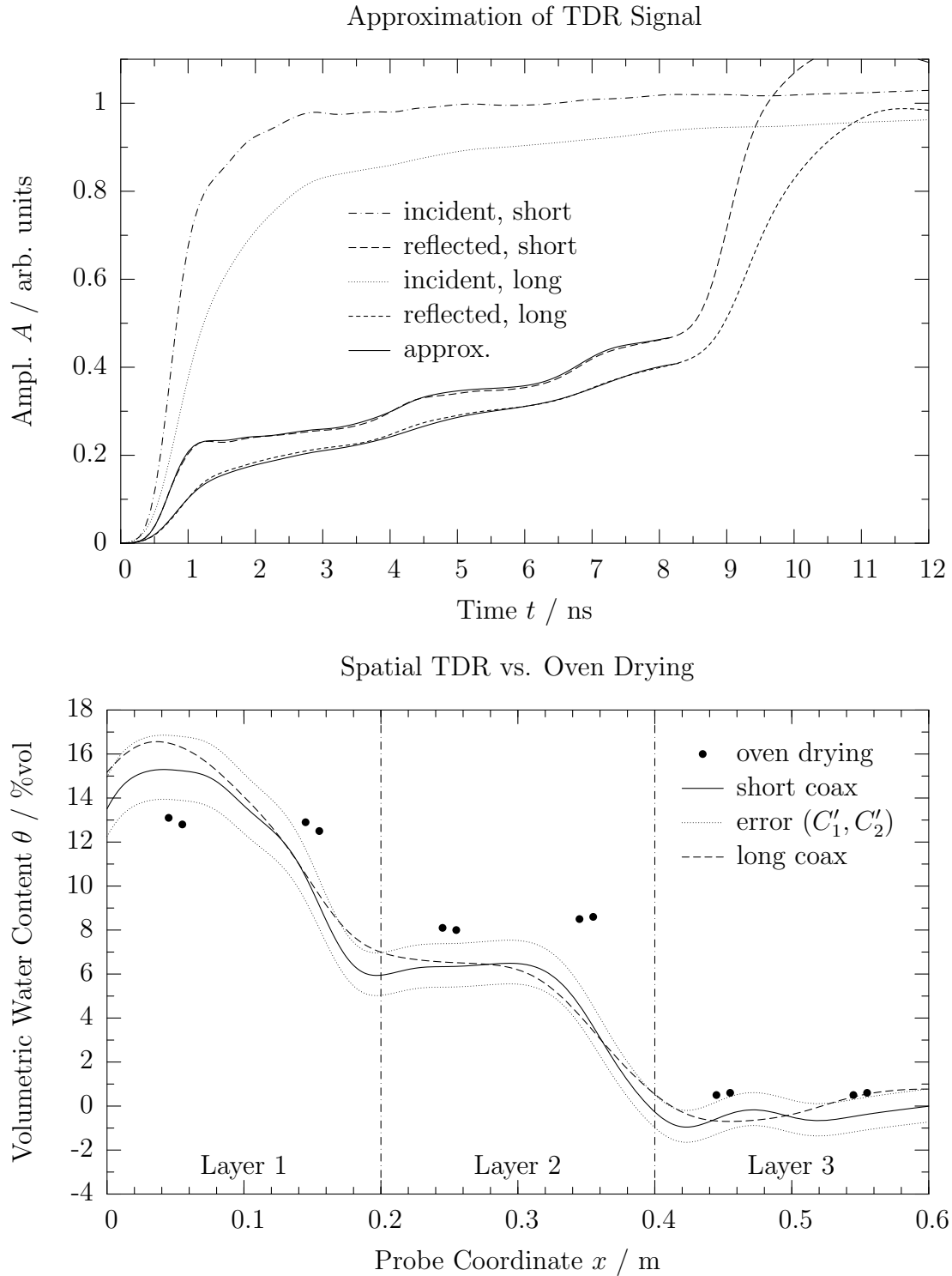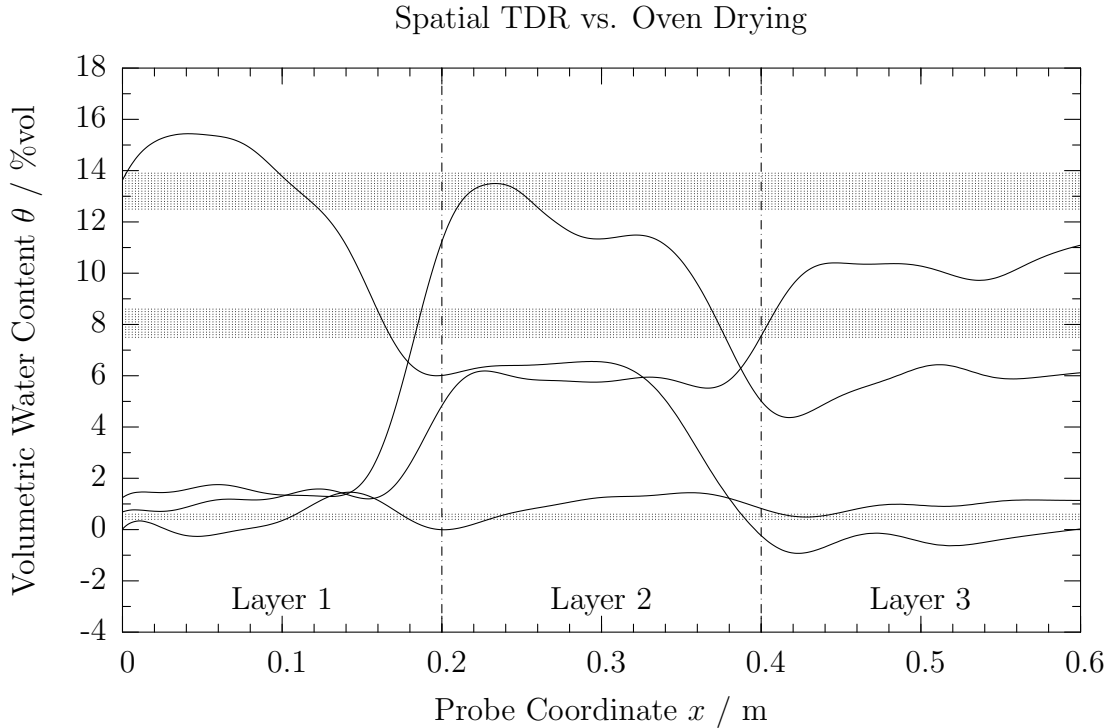
Spatial TDR vs. Oven Drying

Figure 4.23.: Comparison of all reconstructed profiles (short coax cable) with volumetric water content derived from oven drying. Gray horizontal bands indicate the range of water content from oven drying method.

Discussion

Fig. 4.23 summarizes the results. The piecewise constant water content distributions of the experiments are well reflected in the reconstructed moisture profiles. The average moisture levels from reconstruction for moist and wet layers are too dry in most cases by 2 %vol related to the corresponding oven drying results (e.g. layer 2 and 3 in Fig. 4.20, bottom). This systematic shift in moisture may be due to the fact that the moisture probe used in these experiments is not the one used for calibration. Production tolerances especially in the thickness of the rod coating could lead to such systematic errors.

A main deviation from expected behavior is found in layer 1 of the material sequence wet/moist/dry (Fig. 4.22, bottom). The first half of this layer is too wet, the second too dry. This is only partly reflected in the corresponding TDR signal reconstructions (Fig. 4.22, top). An explanation might be that the relatively strong impedance discontinuity between the non-ideal probe head and the adjacent wet soil layer leads to secondary effects which are not represented by the simple linear one-dimensional solution for the voltage pulse propagation in the reconstruction algorithm.

Layer 2 of material sequence dry/wet/moist (Fig. 4.21) shows a similar behavior but for different reason. A look at the corresponding TDR reflectogram and its reconstruction reveals an obvious difference caused by an insufficient convergence of the reconstruction

algorithm. The search algorithm did not find the global optimum but stuck in a local minimum of the error functional.

In the same cases (wet/moist/dry, dry/wet/moist) the positions of the chamber walls estimated from the edges in the reconstructed water content profiles are shifted to the left by 2–4 cm. It is not yet fully clear where this shift comes from but an attempt for explanation may be given for material sequence wet/moist/dry. It is obvious that the algorithm overestimates the moisture in the first half of layer 1. Since the higher the moisture the lower the TDR pulse velocity latter is underestimated. The edge in the TDR reflectogram linked to the water content discontinuity between layer 1 and 2 occurs at a fixed time. Simply spoken within this time the propagating pulse reaches the discontinuity in space. If the pulse is too slow, this will happen after distance too short, which means a shift to the left for the whole reconstructed profile.

Concerning the length of the probe cable no major differences in the resulting moisture profiles are observed. Generally is to be expected that because of the larger signal bandwidth a moisture probe with a short feeding cable yields a higher spatial resolution than a probe with long cable. This effect is not really observable in the current experiments due to the large spatial structures (i.e. the size of the chambers). Soil layers of smaller extent would reveal the difference.

In summary Spatial TDR is able to reflect the moisture profiles. The accuracy of the reconstructed profiles could have been increased easily by using some of them for calibration. Of course, the accuracy of the method is strongly dependent on the quality of the calibration and thus on production tolerances of the probes. Also the design especially of the probe head is crucial for the applicability of the reconstruction algorithm with its simplifying assumptions.

4.2.2. Electrodynamic Field Simulation

Due to the relatively small but significant discrepancies between reconstructed water content profiles and oven drying method the question arose whether the observed deviation is due to calibration or imperfect probe design or inherent to the reconstruction algorithm. To determine the accuracy of the reconstruction algorithm in principle under ideal conditions the laboratory experiment with the 3-rod-probe going through three different soil layers (Sec. 4.2.1) was reproduced with the numerical modeling system *Microwave Studio* (MWS, *Computer Simulation Technology* (2004)). This tool solves three dimensional electrodynamic wave equations in time domain and allows to simulate the TDR pulse propagation along a waveguide embedded in lossless or lossy material. Fig. 4.24 shows the setup of the virtual experiment which geometry similar to the laboratory experiment shown in Fig. 4.18. Rod diameter, coating thickness, and probe length are those of the real coated 3-rod-probe. One simplification has been made: The probe head is replaced by a connection between a $50\,\Omega$ coaxial cable directly joint to the steel rods.
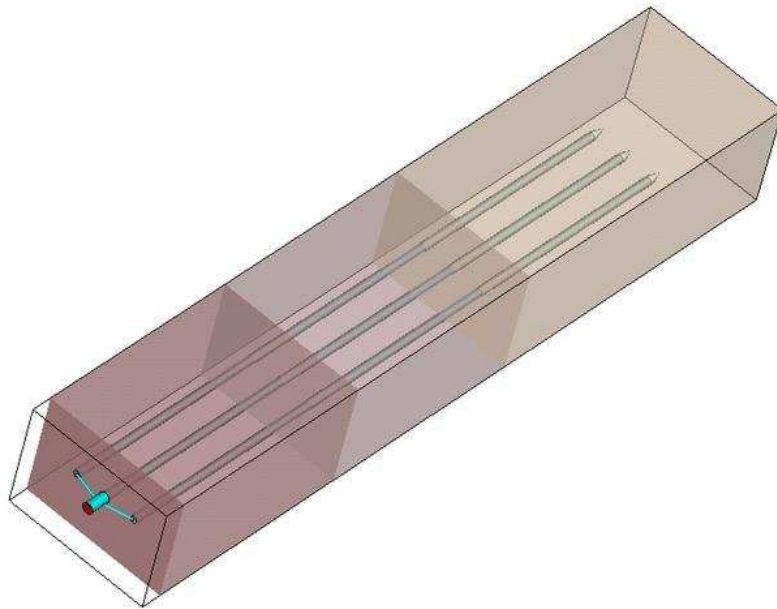
Figure 4.24.: Microwave Studio model of coated 3-rod-probe with simplified probe head in three lossy soil layers.

With this simulation environment it is possible to calculate TDR reflectograms under ideal conditions, i.e. with well-known dielectric permittivity and ionic conductance of the different material layers. These reflectograms generated from Maxwell equations (hereinafter referred to as *MWS reflectograms*) are fed into the Spatial TDR reconstruction algorithm based on the much simpler telegraph equation. Finally predefined and reconstructed material parameters are compared to assess the quality of the reconstruction algorithms and to investigate the influence of the simplifications inherent to the telegraph equation.

The necessary probe parameters L', C'_1, and C'_2 as well as the C'-G'-relationship are derived from the MWS reflectograms in the same manner as from the measured reflectograms (Secs. 2.5.1 and 2.6, respectively). The three chambers of the MWS model are filled with soil of different moisture. Not the water content is assigned to the virtual material in the model but the corresponding dielectric permittivity and ionic conductance. Moisture and these electrical parameters are related by the experimental findings presented in Sec. 2.7.

The three selected water contents used in the MWS model are those of the real soil/water-mixtures prepared in the experiment comparing Spatial TDR and oven drying (Tab. 4.4). Mean and standard deviation of moisture for each of the three mixtures was calculated by averaging all samples, which had been taken from this mixture in all experiments. The results are listed in Tab. 4.5.

state	Mean / %vol	Stddev / %vol	θ / %vol	ϵ / 1	σ / mS/m
'dry'	0.5	0.1	0.5	2.9	0
'moist'	8.2	0.3	8	4.9	14
'wet'	13.3	0.4	13	6.8	23

Table 4.5.: Mean and standard deviation of moisture for the soil samples shown in Tab. 4.4. θ: rounded water content; ϵ: dielectric permittivity according to θ (Fig. 2.22); σ: ionic conductance according to θ (Fig. 2.23). ϵ and σ used in MWS model.

The water content was rounded and the corresponding dielectric permittivity ϵ and ionic conductance σ determined (Tab. 4.5). These materials are filled into the MWS model in different sequences. For each sequence of materials two simulations are run: one without the other with consideration of ionic conductance ($\sigma = 0$ and $\sigma \neq 0$, respectively). The former is referred to as *lossless*, the latter as *lossy* case. The virtual system of probe and layered soil is excited with a voltage step pulse of 1 GHz bandwidth (rise-time approx. 500 ps) and 1 V amplitude. In summary the following steps have to be performed to estimate the accuracy of Spatial TDR by means of MWS:

1. Define a sequence out of dry, moist, and wet material for the MWS model,

2. derive the material properties *dielectric permittivity* and *ionic conductance* in the MWS model according to the selected material moisture,

3. simulate TDR signal propagation with MWS,

4. feed the resulting MWS reflectogram into the Spatial TDR algorithm,

5. transform the resulting capacitance profile into the dielectric permittivity profile,

6. apply the soil calibration function to get the volumetric moisture profile from the dielectric permittivity,

7. compare predefined and reconstructed moisture profiles.

Discussion

Figs. 4.25–4.28 show the results for the different material sequences. The following observations can be made: Reconstructed moisture profiles and presettings are generally in good agreement concerning position of layer interfaces and piecewise constant water content. In the lossless case the error in the reconstructed water content is less than 2%vol and mostly less than 1%vol.

The results for the lossy case are slightly worse. The lossy cases in Figs. 4.27 and 4.28 lead to unsatisfying moisture profile reconstructions. A glance at the corresponding TDR reflectograms reveals why: The converged solution for the reconstructed reflectograms are not optimal and deviate substantially from the predefined MWS reflectogram. The optimization process inherent to the Spatial TDR algorithm got stuck in a local optimum. The structures in the lossy TDR signals are less pronounced than in the lossless case. This may be the reason why the stronger deviations are mainly occurring with lossy materials.

The comparison between given MWS reflectogram (or real measurement) and the reconstructed signals gives information about the goodness of the converged solution, a valuable advantage of the method. When a result of Spatial TDR reconstruction is obviously suboptimal, the optimization process can be started again with better initial guess of the material parameters along the probe.

The MWS simulations show that an accuracy of 1%vol is theoretically achievable with Spatial TDR. This requires the rest of the system to be well-behaving, i.e. signal distortions generated by the probe head should be as small as possible to avoid higher order EM modes and radiation, and the probe must be calibrated very well. From these findings can be concluded that the systematic deviations between moisture reconstruction and oven drying investigated in Sec. 4.2.1 are mainly due to imperfect probe calibration.

Spatial TDR / MWStudio: Best TDR Signal from Inverse Modeling

Spatial TDR / MWStudio

Figure 4.25.: Material sequence: dry, moist, dry. Top: MWS reflectograms and Spatial TDR reflectogram reconstructions. Bottom: reconstructed moisture profiles. Horizontal lines: three moisture levels of predefined materials.

Spatial TDR / MWStudio: Best TDR Signal from Inverse Modeling

Figure 4.26.: Material sequence: dry, moist, wet. Top: MWS reflectograms and Spatial TDR reflectogram reconstructions. Bottom: reconstructed moisture profiles. Horizontal lines: three moisture levels of predefined materials.

Spatial TDR / MWStudio: Best TDR Signal from Inverse Modeling
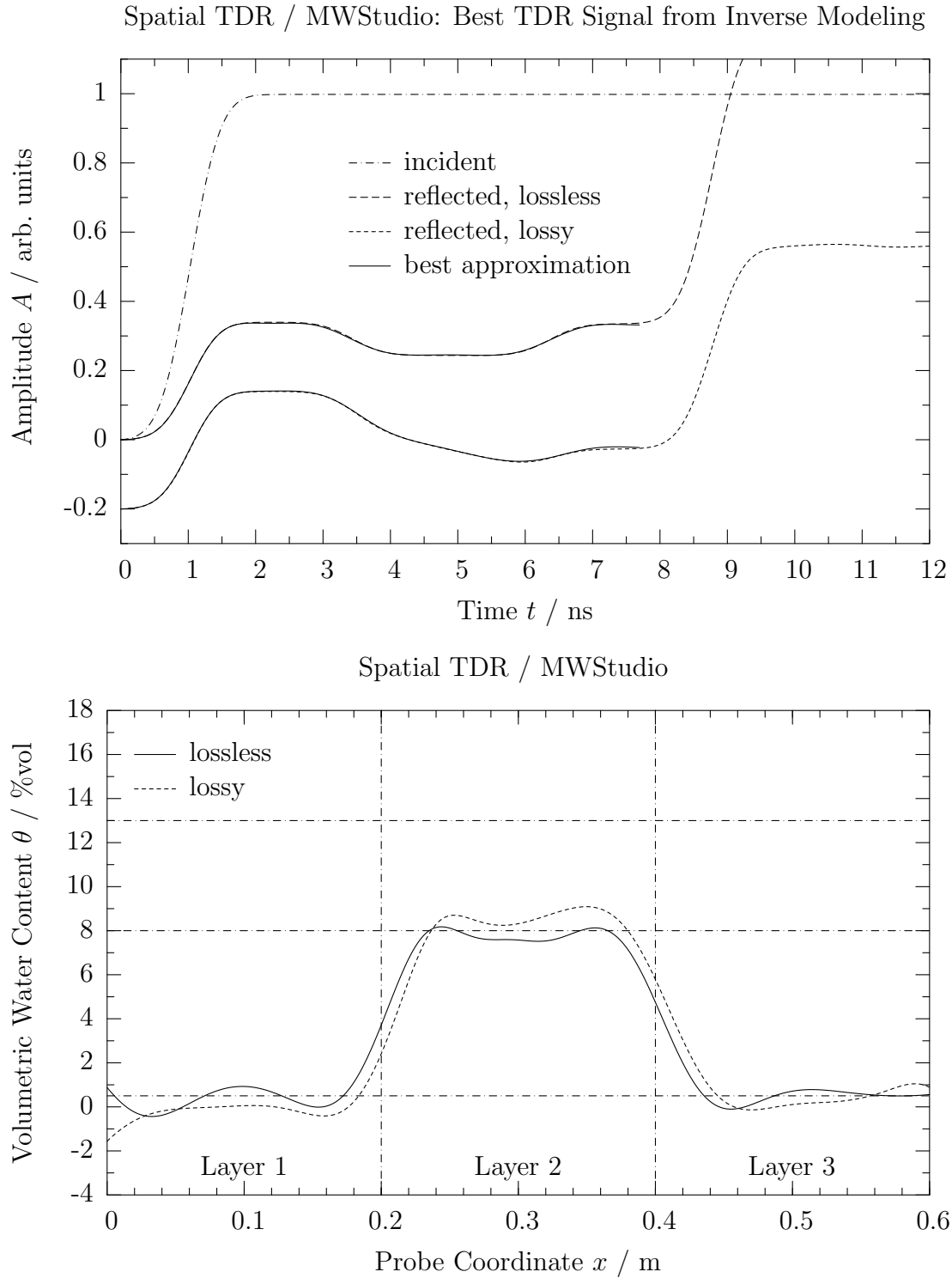

Spatial TDR / MWStudio

Figure 4.27.: Material sequence: wet, moist, dry. Top: MWS reflectograms and Spatial TDR reflectogram reconstructions. Bottom: reconstructed moisture profiles. Horizontal lines: three moisture levels of predefined materials.

Spatial TDR / MWStudio: Best TDR Signal from Inverse Modeling
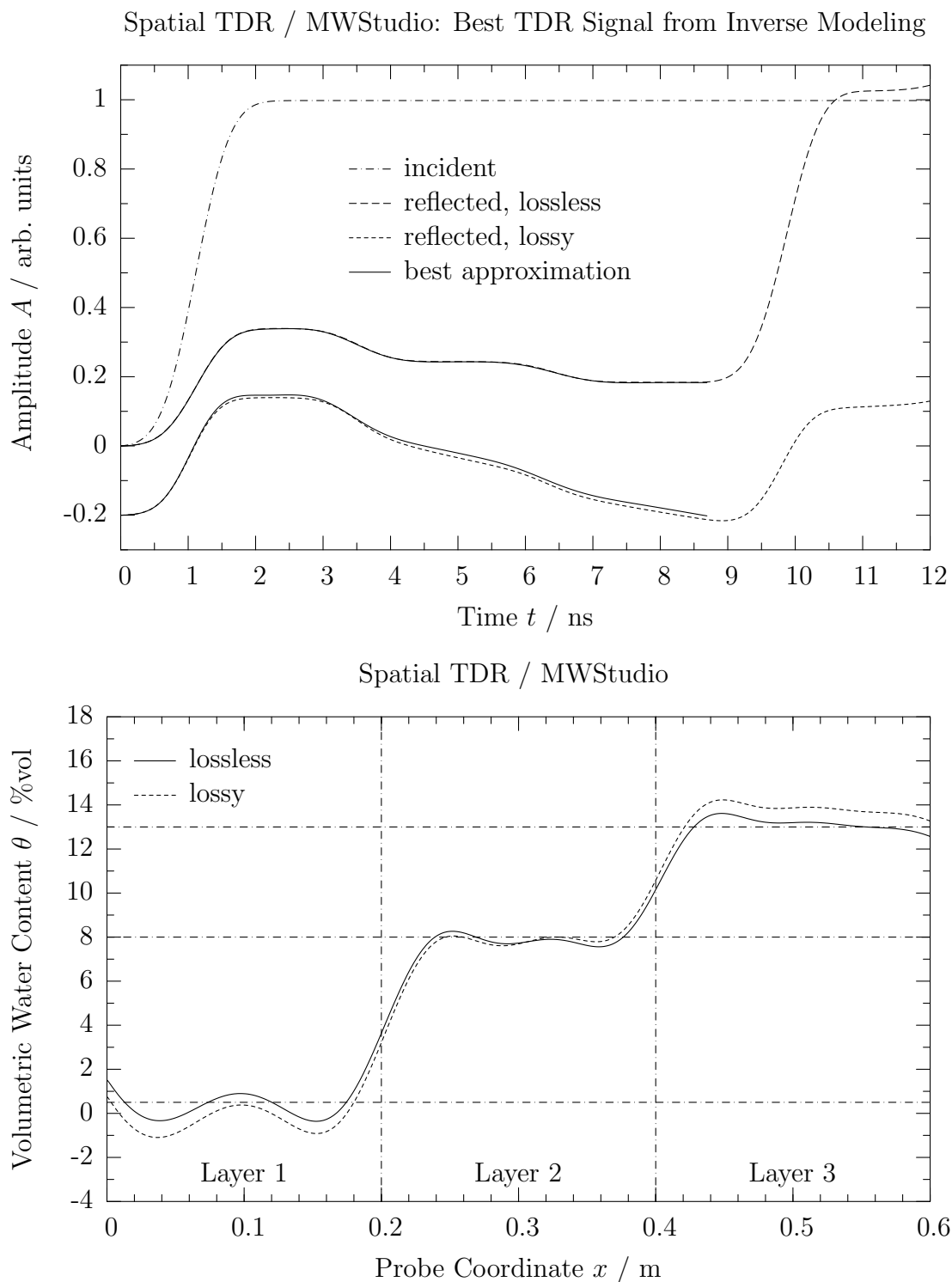

Spatial TDR / MWStudio

Figure 4.28.: Material sequence: moist, wet, dry. Top: MWS reflectograms and Spatial TDR reflectogram reconstructions. Bottom: reconstructed moisture profiles. Horizontal lines: three moisture levels of predefined materials.
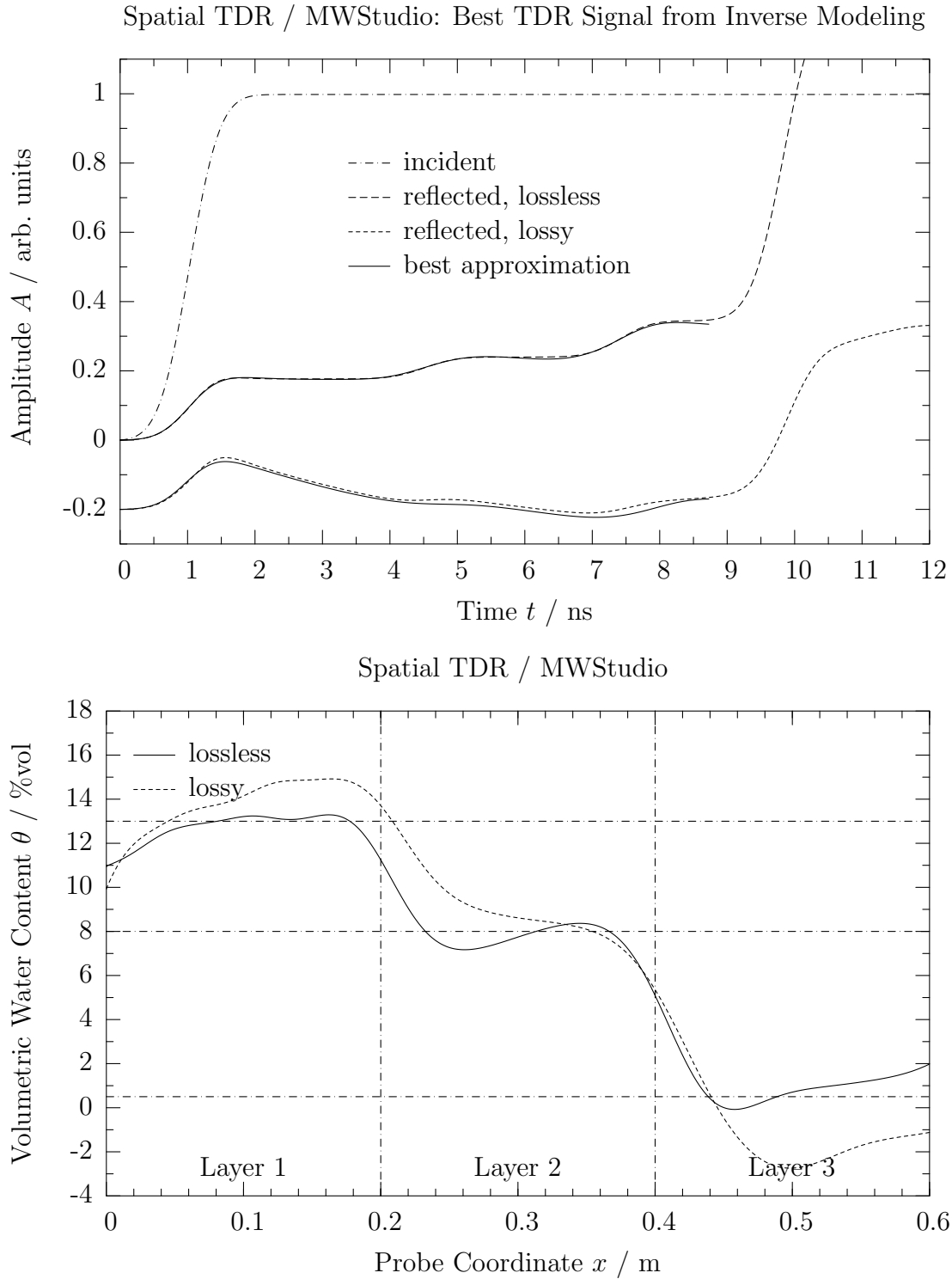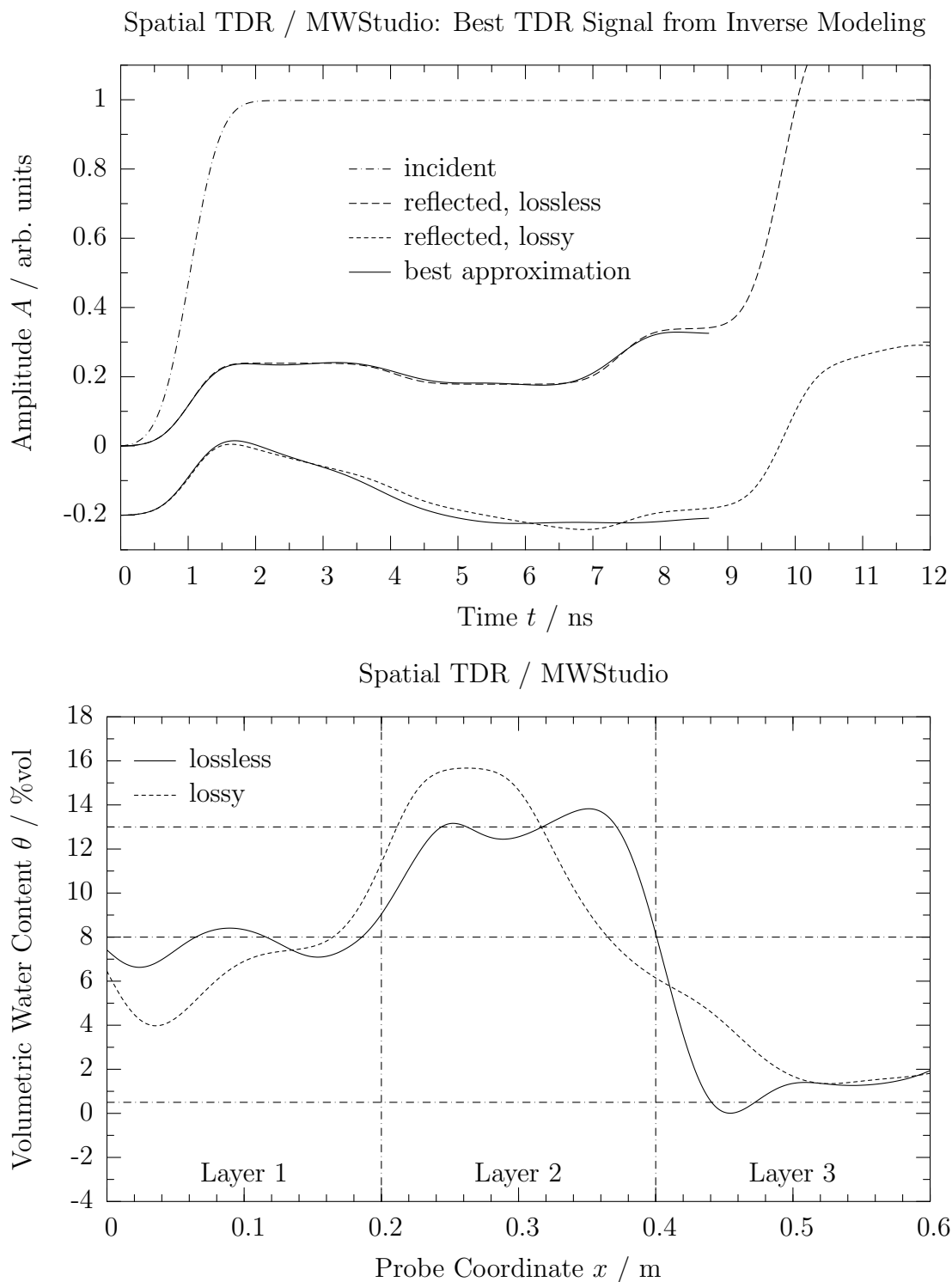
4.3. Soil Moisture Measurements with OBSERVER

4.3.1. Reflectograms

To test what finally has been achieved with the new TDR prototype, comparative measurements between the OBSERVER and Tektronix Cable Tester 1502B were performed. Some selected reflectograms of both instruments are shown in Figs. 4.29–4.32. The scales in the figures are those of OBSERVER. This instrument is not capable of an absolute time measurement but determines time differences to an arbitrary reference time. Since the OBSERVER's amplitude scale yielded by integration of the differential pulse code of the delta modulator the amplitude is also given relative to an arbitrary reference level (s. Chap. 3).

The Tektronix signals are a subset of the reflectograms given in Figs. 4.5–4.8. They have to be mapped to the OBSERVER's time and amplitude scale to be comparable. Therefore the Tektronix time scale is shifted until the first main reflections coincide with those of the OBSERVER. Multiplication of the time axis by a scaling factor is not allowed since it would spoil the pulse travel-time determination. Amplitude shifting and scaling are possible, because the amplitude ratio of incident and reflected wave portions are invariant under these transformations. In the following the major observations are commented.

General Impression

The general similarity between the reflectograms of OBSERVER and Tektronix 1502B is very promising. The OBSERVER prototype is capable of tracking the voltage trace in the sub-nanosecond region. The bandwidth of the instrument is more than sufficient to sample the TDR signal resulting from a 0.6 m waveguide connected with a 14 m coax cable. Of course, the signal bandwidth is lowered due to the relatively long connecting cable but this is rather usual for practical application. A diligent investigation of OBSERVER's reflectogram quality for short feeding cables has not been carried out, yet.

Failures

Some OBSERVER reflectograms failed completely, the reason of which has not yet been detected (e.g. Fig. 4.32, timestamp 120).

Slope

The maximum slope of first reflection sampled by OBSERVER is little less than the one recorded by Tektronix (e.g. Fig. 4.29, timestamp 0, $A = 350$), whereas the onset of the rising slope are differing significantly (e.g. Fig. 4.29, $t = 2.25$ ns). This difference is due to the shape of the emitted pulse. Since the slower onset is conserved during signal propagation, it manifests itself again at the second major reflection at the end of the probe (e.g. Fig. 4.31, timestamps 90–180, $t > 12.5$ ns).

Theoretically the shape of the excitation pulse does not play a role as long as it has the necessary bandwidth (high frequency components in the spectrum), since the system under test is assumed to be linear and time invariant. Practically the slow signal onset

with its round shape complicates the exact definition of the reflection instant by means of the tangent method (c.t. Sec. 2.2.1).

Noise

The OBSERVER reflectograms sometimes show a disturbing noise pattern which is not random but unpredictable, a phenomenon the very cause of which still is unclear (e.g. Fig. 4.30, timestamp 30 and 150). Is is deemed to originate from some effects in the instrument's electronic.

Temporal Shift of Reflectograms

With probe S3 (Fig. 4.31) the reflections at the propagating infiltration front reveal a temporal shift between Tektronix and OBSERVER, especially for timestamp 30 and 60. Only part of it may be explained by inaccuracies of the time scale transformation applied to the Tektronix reflectograms necessary to make the measurements comparable. The rest of the time shift is not a systematic error of the OBSERVER but can be explained by the water percolation continuing between the samples taken by the two instruments. This hypothesis can be tested with a rough estimate. The time elapsed between the measurements taken by OBSERVER and Tektronix is $\Delta t \approx 4$ min. The flux density at the upper boundary for probe S3 was estimated to be $j_w \approx 9 \cdot 10^{-6}$ m/s (Tab. 4.2). Together with an assumed porosity $P \approx 0.3$, the pore velocity yields: $v_P = j_w/P \approx 3 \cdot 10^{-5}$ m/s. Thus in the time Δt the infiltration front propagates the distance $\Delta s = v_P \cdot \Delta t = 7.2$ mm. This is 1.2% of the probe length $l = 0.6$ m.

The total pulse round trip time in the reflectograms with timestamp 30 (Fig. 4.31) is approximately $t_t \approx 10.25$ ns. Within the time Δt the reflection caused by the infiltration front has been shifted by $\Delta t_x \approx 0.25$ ns. This is 2.5% of the total round trip time. Since the variations are very small a linear relationship between spatial position of the infiltration front and the temporal occurrence of the corresponding reflection may be assumed. Thus a relative change of 1.2% in space should lead to a relative change of 1.2% in time. The actual change in time is 2.5% which is still very close to the expectation if the rough estimation procedure is considered. It is therefore possible and plausible, that the temporal shift between the reflections observed with the two TDR instruments is caused by the moving infiltration front rather than by a systematic error of the OBSERVER.

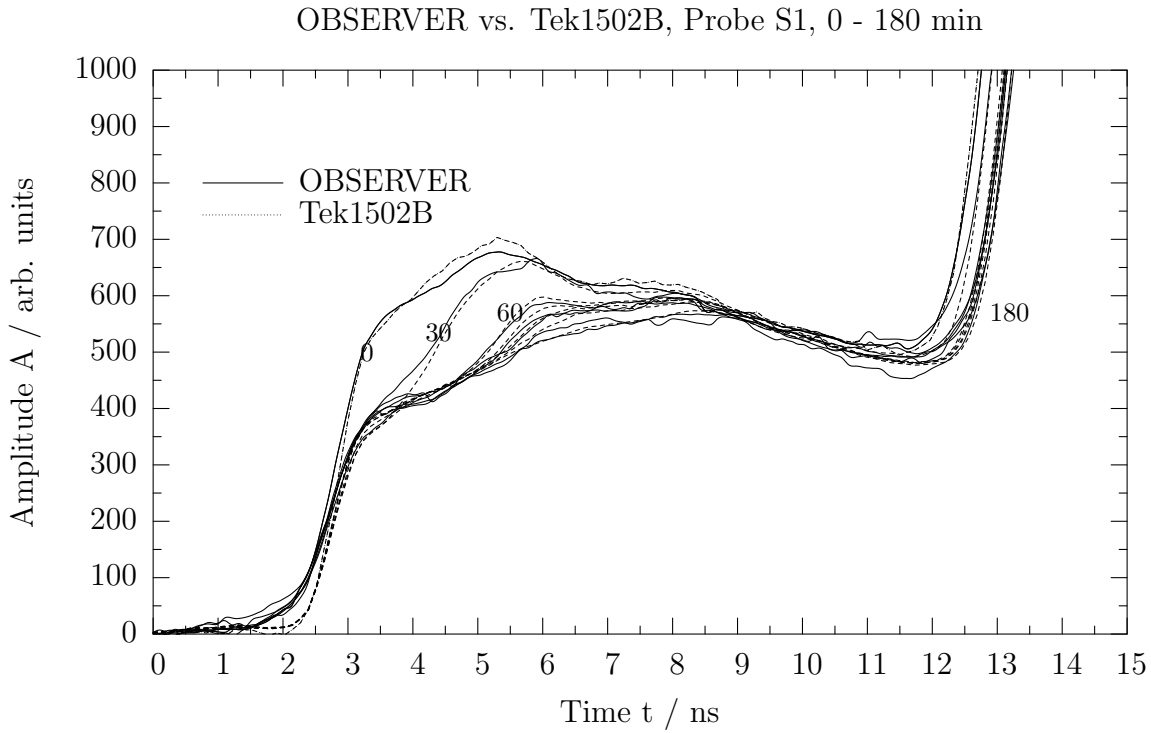Figure 4.29.: Reflectograms sampled by OBSERVER and Tektronix 1502B at probe S1.
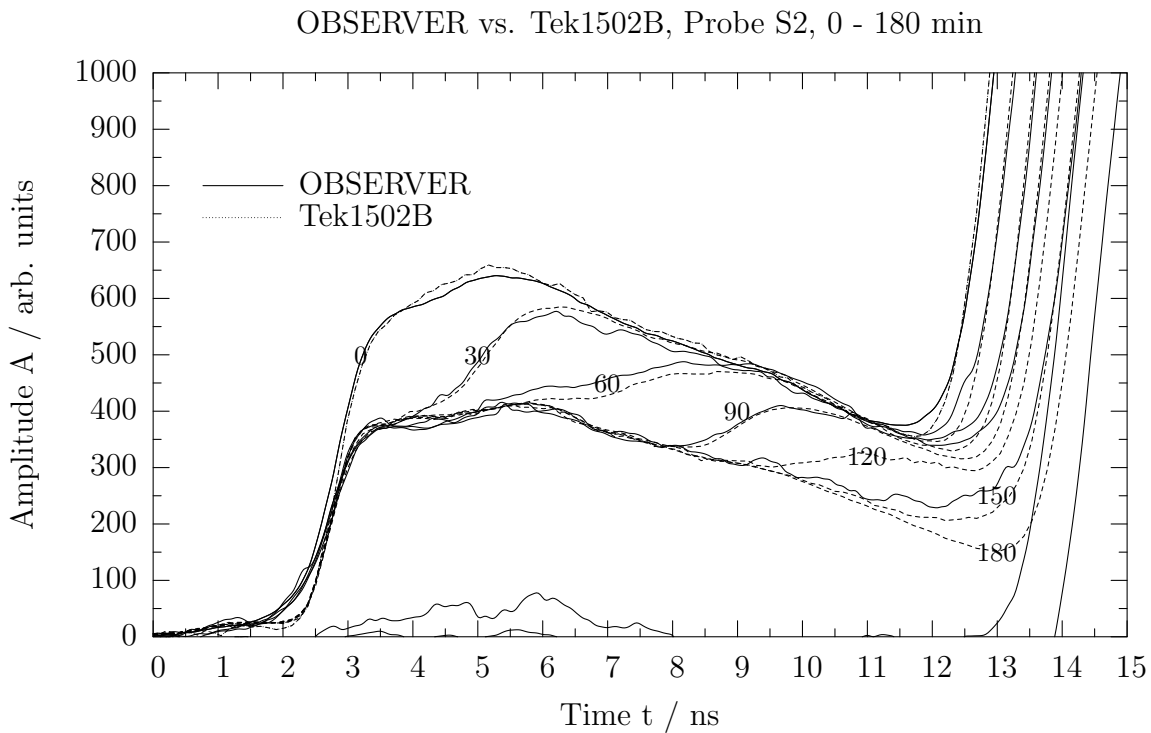
Figure 4.30.: Reflectograms sampled by OBSERVER and Tektronix 1502B at probe S2.

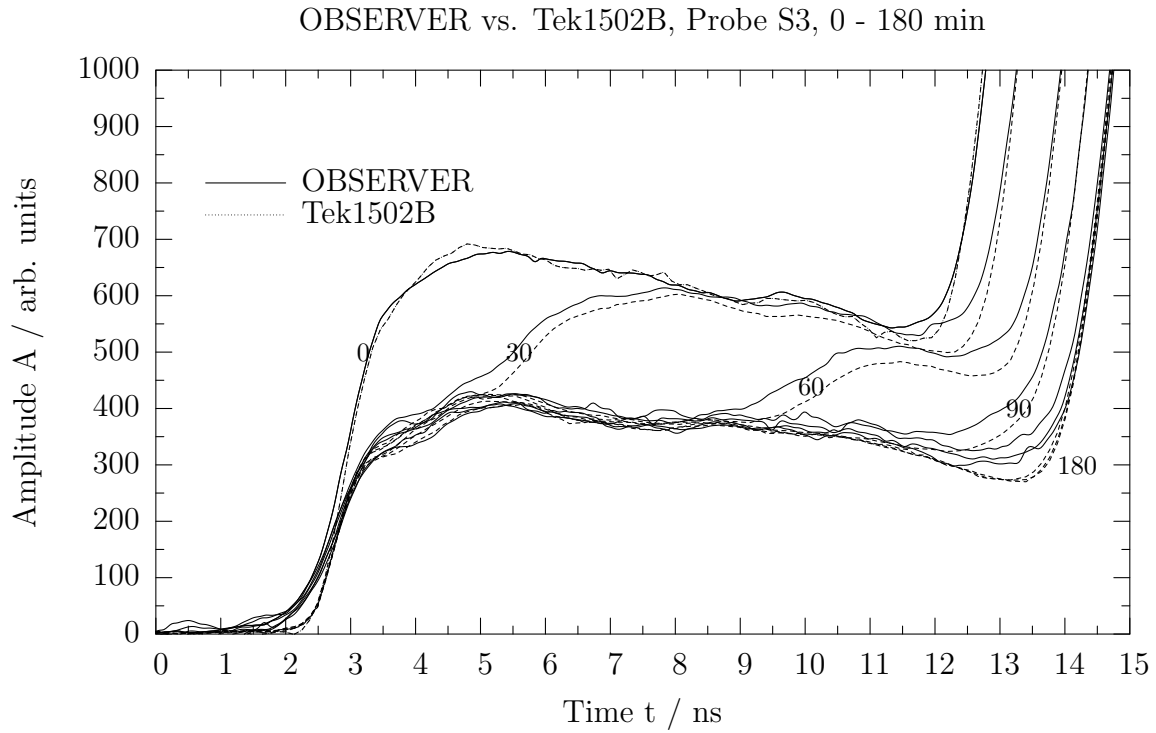OBSERVER vs. Tek1502B, Probe S3, 0 - 180 min

Figure 4.31.: Reflectograms sampled by OBSERVER and Tektronix 1502B at probe S3.

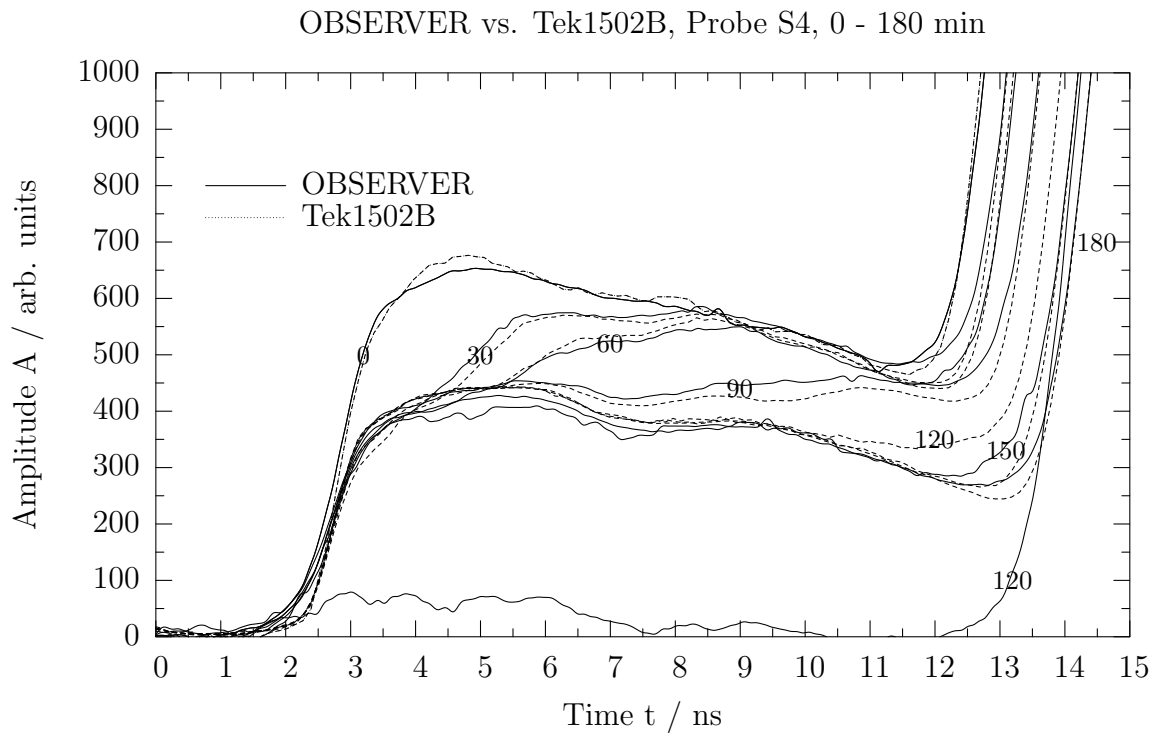OBSERVER vs. Tek1502B, Probe S4, 0 - 180 min

Figure 4.32.: Reflectograms sampled by OBSERVER and Tektronix 1502B at probe S4.

4.3.2. Reconstructed Soil Moisture Profiles

The reconstructed soil moisture profiles based on measurements with OBSERVER and Tektronix are displayed in Fig. 4.33. The timestamps range from 0 to 180 min with 30 min increment. Only those cases are shown in which a reconstruction was possible. Some OBSERVER reflectograms could not be processed by the current version of the reconstruction algorithm.

It is remarkable that some reconstructed OBSERVER profiles are drier than the corresponding reconstructions based on Tektronix data but simultaneously possess a trend which is very similar to the Tektronix profiles (e.g. Fig. 4.33, Probe S2, timestamp 60, 90, and 150; Probe S4, timestamp 150). This is an indication that the correct pulse travel-time determination is a major problem of the reconstruction algorithm, since the travel-time determines the average water content. Simply spoken the algorithm yields a total amount of water which is smaller than in reality. Nevertheless it distributes the remaining moisture along the probe such that the error functional of Eq. 2.21 becomes minimal under the given constraints. Therefore it drives the reconstructed profile toward the real profile and thus the profile derived from Tektronix reflectograms.

Some of the OBSERVER reflectograms make the reconstruction algorithm abort, e.g. 30, 60, and 90 for probe S3 in Fig. 4.31. The corresponding profiles are missing in Fig. 4.33. These reflectograms are not peculiar. They resemble the Tektronix reflectograms very well. The most obvious distinction is found at the onset of the second main reflection which may lead to an error in the travel-time which unrecoverable.

4.3.3. Discussion

The OBSERVER is capable of tracking TDR signals with sub-nanosecond resolution. The bandwidth of the instrument is wide enough to follow slopes of TDR pulse reflections after the pulse has passed a RG213 coaxial cable of 14 m length. Thus the prototype already meets one of the main performance requirements for a TDR in the targeted field application of distributed infiltration monitoring with probe clusters.

Improvements have to be made concerning the onset of the emitted TDR pulse to reduce uncertainties in the determination of pulse round trip time by means of the tangent method. This particular shape of the rising pulse edge is deemed to be inherent to the output stage of the pulse generating ECL device. The transistors of the output stage have to become conducting to produce a rising signal edge. This transition from blocking to conducting needs more time than the reverse operation. Therefore a simple solution of this problem might be the usage of the falling edge of the emitted pulse instead. From systems theory point of view the bandwidth of the emitted excitation pulse is important, not its shape. Therefore a steep negative signal transition is also feasible to excite the SUT.

Another important issue is the noise of the instrument. Unfortunately the noise is not purely random but has a non-vanishing autocorrelation and emerges in the message band. Thus without additional prior knowledge it is impossible to distinguish between error and true signal. These disturbances are not yet understood in detail.
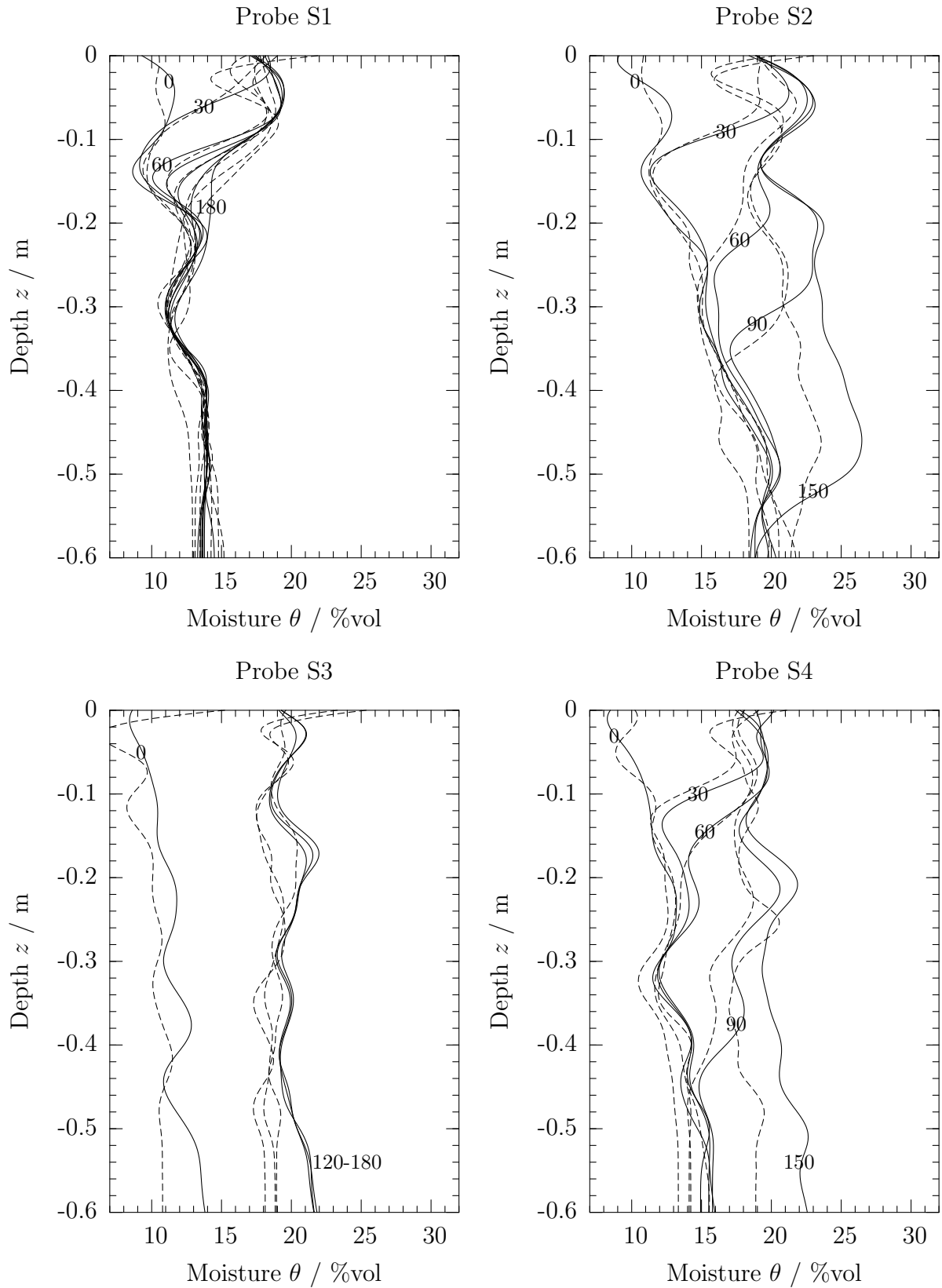
Figure 4.33.: Comparison of reconstructed moisture profiles based on measurements with OBSERVER (dashed line) and Tektronix (solid line).

4.4. Parameter Estimation of Hydraulic Properties through Constant Flux Infiltration

The aim of the following elaboration is to show, how TDR can be used to derive parameters describing important soil hydraulic properties. These quantities are crucial for investigations in the fields of irrigation, ground water renewal, and flood forecasting in small catchments.

In the past vertically installed TDR probes of several decimeters length measuring mean water content have been used to observe the temporal increase of cumulative soil water storage under constant flux precipitation produced by rainfall simulators (e.g. *Parkin et al.* (1995), *Si et al.* (1995)). Models have been used to describe the dynamics of the cumulative moisture content. If a model describes the water transport adequately, its parameter values will be deemed to be good estimates for the real soil properties. Some models use numerical solvers for the transport equation, others have analytical solutions, often restricted to special conditions.

Richards' equation is a widely used water transport model describing infiltration. This model has no general analytical solution. However, *Sander et al.* (1988a) and *Broadbridge and White* (1988) both have found analytical solutions of Richards' equation for the special case of constant flux boundary conditions and certain parametric forms of the model parameters, which are dependent on the water content. These solutions have been used several times for inverse modeling to derive soil hydraulic parameters from the dynamics of cumulative water content under constant rainfall simulators observed with TDR.

Moreover, the exact analytical solutions for special cases may be used to test numerical models concerning accuracy and stability. *Watson et al.* (1995) claimed to have found excellent agreement between these analytical solutions and other well-established numerical methods for solving Richards' equation.

However, cumulative water storage is an integral value of the vertical moisture distribution in a soil column. It does not say anything about local phenomena like saturation above less permeable soil layers or lateral flow components. If it were possible to measure the temporal evolution of the spatially resolved moisture profile, the assessment of the observed infiltration and the assumptions made for it would be improved. Therefore it is investigated, if Spatial TDR with its capability to observe moisture profiles could be used to better assess soil hydraulic parameters derived from traditional TDR application yielding bulk moisture content.

4.4.1. Base Equations

The entry of water into porous media like soil through its surface is called *infiltration*. The term *infiltration rate* denotes the flux density of water across a topographical soil surface. Many factors effect the infiltration rate, such as surface structure, vegetation cover, porosity and hydraulic conductivity of soil, and the initial state, i.e. the moisture

content. Steady-state infiltration is described by the *Darcy-Buckingham-Equation*

$$\vec{q} = -\underline{k}(\theta)\vec{\nabla}\Phi \, , \qquad (4.15)$$

with flux density $\vec{q}$, soil water potential Φ, and hydraulic conductivity $\underline{k}$, which in general is a tensor, reduced to a scalar k in case of homogeneous, isotropic soil properties. The negative sign at the right side expresses the flow runs downwards, opposite to the direction of the potential gradient. Like many other equations in physics (Ohm's law, law of Hagen-Poiseuille, and others) the Darcy-Buckingham equation simply expresses the fundamental principle, that a potential gradient causes a flux, regulated by a conductivity.

The potential Φ is a combination of the gravitational potential and the soil suction head Ψ, which is an expression of the soil pores' ability to physically bind water due to intermolecular forces. In hydrology energy is usually given in units of length. This implies, that the energy is given per unit weight force, $F = mg$. In these units the gravitational potential mgh is reduced to h or z, and the total potential is

$$\Phi = \Psi \pm z \, , \qquad (4.16)$$

with z increasing downwards (-) or upwards (+).

Eq. 4.15 may be used to describe unsaturated flow, if the flow is constant,

$$\frac{\partial \vec{q}}{\partial t} = 0 \, , \qquad (4.17)$$

and the outflow of water in the control volume equals the inflow,

$$\nabla \cdot \vec{q} = 0 \, , \qquad (4.18)$$

and the soil moisture within the control volume does not change,

$$\frac{\partial \theta}{\partial t} = 0 \, . \qquad (4.19)$$

The last two conditions also imply the absence of local sinks and sources in the control volume. If the soil moisture is changing within the control volume, i.e. $\partial\theta/\partial t \neq 0$, the Darcy-Buckingham equation has to be combined with the *continuity equation*,

$$\frac{\partial \theta}{\partial t} = -\nabla \cdot \vec{q} + S \, , \qquad (4.20)$$

which imposes a condition to the filling and emptying of soil pores. The continuity equation is a conservation law, which in case of soil water expresses, that a non-vanishing net flux of water through the boundaries of a control volume ($\nabla \cdot \vec{q} \neq 0$) either leads to a changing soil moisture ($\partial\theta/\partial t \neq 0$) or is caused by a source or sink (S) within the volume. In any case the total water balance has to be conserved.

For many investigations it is often sufficient to assume mainly vertical flux processes in soil, e.g., $\vec{q} = (0, 0, q_z)^T$. This implies, the soil water potential gradient is revealing only a

z-component. The flux divergence is reduced to a single partial derivative in z-direction. For the sake of simplicity this one-dimensional formulation is used throughout the text. The equations may be easily extended afterwards to two or three dimensions.

Substitution of flux density $\vec{q}$ in Eq. 4.20 by Eq. 4.15 without local sinks and sources and application of Eq. 4.16 yields

$$\frac{\partial \theta}{\partial t} = \frac{\partial}{\partial z}\left[k(\theta)\frac{\partial}{\partial z}(\Psi \pm z)\right] = \frac{\partial}{\partial z}\left[k(\theta)\frac{\partial \Psi}{\partial z} \pm k(\theta)\right] \ . \tag{4.21}$$

Equation 4.21 is called *Richards' equation*, which is widely used to describe the nonstationary, unsaturated single-phase flow. A positive or negative sign is yielded, if z is defined to be increasing upwards or downwards.

This complicated nonlinear partial differential equation (PDE) in θ has some unpleasant properties. First, it is coupled to a second variable, the suction head $\Psi(\theta)$. This function is highly nonlinear and exhibits marked hysteresis, which means two different suction head values can exist for the same moisture content, depending on whether the current moisture content θ was reached by draining or wetting. Second, the parameter $k(\theta)$ is a nonlinear function of θ. Third, the existence of a solution has not been proven, and no general analytic solution has been found. The first problem is addressed to by applying the following identity:

$$k(\theta)\frac{\partial \Psi}{\partial z} = k(\theta)\frac{d\Psi}{d\theta}\frac{\partial \theta}{\partial z} =: D(\theta)\frac{\partial \theta}{\partial z} \ . \tag{4.22}$$

The soil water *diffusivity* $D(\theta)$ summarizes the effects of hydraulic conductivity and gradient of suction head. Inserting equation 4.22 into 4.21 yields *Richards' equation in diffusivity form*:

$$\frac{\partial \theta}{\partial t} = \frac{\partial}{\partial z}\left[D(\theta)\frac{\partial \theta}{\partial z} \pm k(\theta)\right] \ . \tag{4.23}$$

This equation resembles that of molecular diffusion (Fokker-Planck or Fick's equation). Richards' equation is often used as the governing equation for unsaturated unstationary water flow (also multi-dimensional) in porous media (e.g. *Kutílek and Nielsen*, 1994) and many numerical models rely on this fundamental nonlinear PDE. Richards' equation has some limitations. Depending on the problem the PDE can be insufficient to describe saturated flow, if for example air is included in the flow. Many effects of such a multiphase flow cannot be covered by Richards' equation.

Since the main focus of the currently examined TDR application is on constant flux infiltration under unsaturated conditions, deficiencies in modeling a saturated flow regime are of minor concern. Another important point to mention is the monotonicity of the constant flux infiltration, which allows to neglect the previous mentioned hysteresis of the suction head.

4.4.2. Analytical Solution of Richards' Equation

It is convenient to apply a few linear transformations of soil moisture and hydraulic conductivity to yield dimensionless variables with normalized range. First the *reduced*

4. Applications

volumetric water content is introduced:

$$\Theta := \frac{\theta - \theta_i}{\Delta\theta} := \frac{\theta - \theta_i}{\theta_s - \theta_i} , \qquad (4.24)$$

with constants θ_i and θ_s being the initial and saturated volumetric water content, respectively. Thus $\Theta = 0 \Leftrightarrow \theta = \theta_i$ and $\Theta = 1 \Leftrightarrow \theta = \theta_s$. It is assumed, that initial and saturated water content are constant over depth, i.e.

$$\partial\theta_i/\partial z = 0, \text{ and } \partial\theta_s/\partial z = 0. \qquad (4.25)$$

Similarly the *reduced hydraulic conductivity* is defined as

$$K(\theta) := \frac{k(\theta) - k(\theta_i)}{\theta_s - \theta_i} . \qquad (4.26)$$

Richards' equation in diffusivity form (Eq. 4.23) is invariant under these transformations:

$$\frac{\partial\theta}{\partial t} = \frac{\partial}{\partial z}\left[D(\theta)\frac{\partial\theta}{\partial z} \pm k(\theta)\right] \Leftrightarrow \frac{\partial\Theta}{\partial t} = \frac{\partial}{\partial z}\left[D(\Theta)\frac{\partial\Theta}{\partial z} \pm K(\Theta)\right] . \qquad (4.27)$$

The partial derivative $\partial K/\partial z$ in Eq. 4.27 can be further evaluated. The resulting one-dimensional transport equation is a nonlinear convection-diffusion equation which describes single-phase flow in rigid, isothermal, homogeneous, isotropic, porous systems:

$$\frac{\partial\Theta}{\partial t} = \frac{\partial}{\partial z}\left[D(\Theta)\frac{\partial\Theta}{\partial z}\right] - \frac{dK(\Theta)}{d\Theta}\frac{\partial\Theta}{\partial z} \qquad (4.28)$$

Capital K and Θ term hydraulic conductivity and volumetric soil moisture content in their reduced form. The minus sign has been chosen to be directly comparable to most of the cited literature (z positive downwards). The following constant flux boundary and initial conditions are presumed for the problem:

$$\forall z \geq 0 \wedge t = 0 \quad : \quad \Theta = 0,$$
$$\forall t > 0 \wedge z = 0 \quad : \quad K(\Theta) - D(\Theta)\frac{\partial\Theta}{\partial z} = Q \equiv \text{const}, \qquad (4.29)$$

with

$$Q = q/(\theta_s - \theta_i) \qquad (4.30)$$

being the *reduced surface flux* constant over time. Eq. 4.28 can now be transformed into an analytically solvable form, if certain assumptions will be made about the parametric form of diffusivity D and conductivity K.

Choice of the Analytical Solution

Analytical solutions for the nonlinear transport equation 4.28 under constant flux boundary condition (Eq. 4.29) and appropriate parametric form for K and D have been presented independently by *Sander et al.* (1988a) (hereinafter referred to as SA) and

4.4. Parameter Estimation of Hydraulic Properties through Constant Flux Infiltration

Broadbridge and White (1988) (hereinafter referred to as BW). At a first glance the solutions seem to be different but in a second article *Sander et al.* (1988b) immediately commented on the paper of BW, where they showed the equivalence of both solutions. Another hint for the equality was given by *Watson et al.* (1995), who stated, that both have followed the general solution approach. This approach is detailed by *Rogers et al.* (1983), who originally intended to solve a two-phase oil and water infiltration problem. SA applied this solution to one-phase infiltration.

Despite the proof, that the final solutions of BW and SA only differ in the formulation of the parameters, which indeed can be transformed one into the other, a confusion has emerged in literature. *Parkin et al.* (1992) and *Parkin et al.* (1995) are examples, in which both solutions are claimed to be different and treated separately. The following comparison between SA and BW is meant to give some insight into the differences of their formulation.

As stated before appropriate parametric formulations for D and K have to be presumed in order to solve the transport equation under constant flux boundary condition analytically. Both SA and BW assume that the diffusivity D can be reasonably expressed by a function equivalent to the form proposed by *Fujita* (1952):

$$D(\Theta) = D_0(1 - \nu\Theta)^{-2} , \tag{4.31}$$

with initial diffusivity $D_0 = D(\Theta = 0)$, and a form parameter ν. In BW the parametric form for D looks different but is equivalent to equation 4.31. SA stated that according to *Rogers et al.* (1983) the most general K which allows for the linearization of equations 4.28, 4.29, and 4.31 is of the form

$$K_{\mathrm{SA}}(\Theta) = \frac{K_1 + K_2\Theta + K_3\Theta^2}{1 - \nu\Theta} , \tag{4.32}$$

with four parameters ν, K_1, K_2, and K_3. The parameter K_1 can be directly eliminated with the following condition, which simply expresses that initial water content leads to initial hydraulic conductivity (c.t. Eqs. 4.24 and 4.26):

$$K(\Theta = 0) = 0 \Rightarrow K_1 = 0 . \tag{4.33}$$

SA introduce the (reduced) saturated hydraulic conductivity K_s, because it is a commonly used parameter to describe soil hydraulic properties. This condition links K_2, K_s, and K_3:

$$K(\Theta = 1) = K_s \Rightarrow K_2 = K_s(1 - \nu) - K_3 . \tag{4.34}$$

Here SA stop to eliminate further parameters and discuss two cases of interest ($K_3 = 0$ and $K_2 = K_s$). They do not favor one particular parameter set. SA state: 'Of course the best function would be obtained by fitting the model [...] to measured data'.

BW have chosen another form for k with four parameters:

$$k_{\mathrm{BW}}(\theta) = \beta + \gamma(b - \theta) + \frac{\lambda/2}{(b - \theta)} . \tag{4.35}$$

4. Applications

It is a bit confusing, that their 'reduced' K is divided by $k(\theta_s) - k(\theta_i)$ instead of $\theta_s - \theta_i$ (BW, Eq. 11). Furthermore BW use one more condition (BW, Eq. 7) to decrease the number of free parameters:

$$\left.\frac{\partial k}{\partial \theta}\right|_{\theta=\theta_i} = 0 \ . \tag{4.36}$$

The only justification for this assumption given by BW is: 'In most practical applications, $k'(\theta_n)$ is negligible compared to $k'(\theta_s)$, so we may reasonably take $k'(\theta_n) = 0$.' In their notation θ_n means the initial water content and $k' = \partial k/\partial \theta$. Applied to the formulation of SA (Eq. 4.32) this translates to:

$$\left.\frac{\partial K}{\partial \Theta}\right|_{\Theta=0} = 0 \Rightarrow K_2 = 0 \ . \tag{4.37}$$

Together with Eq. 4.34 this leads to a relationship, which makes the apparently different formulations of BW and SA equal (*Sander et al.*, 1988b):

$$K_3 = (1 - \nu)K_s \ . \tag{4.38}$$

Sander et al. (1988b) showed, that with this last assumption also the hydraulic conductivities are identical, i.e. $K_{\mathrm{SA}} = K_{\mathrm{BW}}$. There is no principal difference between SA and BW so far.

According to *Parkin et al.* (1992) and also *Parkin et al.* (1995) the solutions of SA and BW differ slightly due to different parameterization for K. This is a contradiction to the identity stated by *Sander et al.* (1988b) before. As mentioned above, SA does not favor a certain parameter set and it is possible to choose a parameter set for K_{SA}, which perfectly matches that of BW.

Since there is no principal difference between the two solutions of BW and SA, the latter has been chosen for further investigations because of the somewhat clearer deduction and simpler notation.

Solution for Constant Flux Boundary Condition

Here the analytical solution $\Theta(t, z)$ of Richards' transport equation (Eq. 4.28) under constant flux boundary condition found by *Sander et al.* (1988a) will be presented and commented to some extent, since this is the chosen infiltration model to derive soil hydraulic properties from the infiltration experiments of Sec. 4.1. Furthermore the integration of $\Theta(z, t)$ along a soil column utilized by *Parkin et al.* (1992) will be unfolded to gain more insight into the implicit assumptions they made.

First of all dimensionless variables for space and time are introduced. If z and t are depth and time in SI units, their dimensionless counterparts are

$$x = \frac{Q}{D_0}z \ , \tag{4.39}$$

$$\tau = \frac{Q^2}{D_0}t \ . \tag{4.40}$$

4.4. Parameter Estimation of Hydraulic Properties through Constant Flux Infiltration

The solution is given in parametric form, i.e. reduced moisture content Θ and dimensionless spatial coordinate x are functions of a parameter ξ. Thus the moisture profile cannot be given directly as a function of depth x. For a given dimensionless time τ the dimensionless depth x is a function of ξ:

$$x(\xi, \tau) \;=\; -\frac{1}{\beta} \ln \left[\frac{\phi(\xi, \tau)}{\phi(0, \tau)} \right] . \tag{4.41}$$

For a fixed time τ the dimensionless depth x is mainly the logarithm of a function $\phi(\xi)$ (Eq. 4.44) divided by a constant $\phi(0)$. The volumetric soil water content Θ has the following parametric form:

$$\Theta(\xi, \tau) = \frac{1}{\nu} \left[1 + \beta \frac{\phi(\xi, \tau)}{\Phi(\xi, \tau)} \right] , \tag{4.42}$$

with $\Phi = \partial\phi/\partial\xi$ and β given below (Eq. 4.46). Thus

$$\Theta(\xi, \tau) = \frac{1}{\nu} \left[1 + \beta \left(\frac{\partial}{\partial\xi} \ln[\phi(\xi, \tau)] \right)^{-1} \right] . \tag{4.43}$$

To transform the coordinates to standard length units it is necessary to find the value of ξ, which corresponds to a particular x by inverse retrieval using Eq. 4.41. The task is: find the value of ξ, which leads to the chosen x. This value of ξ is then inserted in equation 4.42 to calculate moisture. The result is one coordinate pair (x, Θ) for a given instant of time.

The function ϕ is a sum of product terms which consist of exponential and cumulative error functions:

$$
\begin{aligned}
\phi(\xi, \tau) \;=\;& \frac{1}{2} \exp\left(a\xi - \frac{\delta\xi}{2} - \epsilon\tau \right) \operatorname{erfc}\left(\frac{\xi + 2a\tau}{2\tau^{1/2}} \right) \\
+\;& \frac{1}{2} \exp\left(-a\xi - \frac{\delta\xi}{2} - \epsilon\tau \right) \operatorname{erfc}\left(\frac{\xi - 2a\tau}{2\tau^{1/2}} \right) \\
-\;& \frac{1}{2} \exp(b\beta\tau - \beta\xi) \left[\operatorname{erfc}\left(\frac{\xi + c\tau}{2\tau^{1/2}} \right) - 2 \right] \\
-\;& \frac{1}{2} \exp(\beta b\tau + b\xi) \operatorname{erfc}\left(\frac{\xi - c\tau}{2\tau^{1/2}} \right) .
\end{aligned}
\tag{4.44}
$$

The cumulative error function serves basically as the form giving element for the infiltration front. The exponentials are responsible for the dispersion of the front. The partial derivative $\Phi = \partial\phi/\partial\xi$ needed to calculate the moisture reads:

$$
\begin{aligned}
\Phi(\xi, \tau) \;=\;& \frac{\partial\phi}{\partial\xi} \\
=\;& \left(\frac{a}{2} - \frac{\delta}{4} \right) \exp\left(a\xi - \frac{\delta\xi}{2} - \epsilon\tau \right) \operatorname{erfc}\left(\frac{\xi + 2a\tau}{2\tau^{1/2}} \right)
\end{aligned}
$$

$$
\begin{aligned}
- \quad & \left(\frac{a}{2} + \frac{\delta}{4}\right) \exp\left(-a\xi - \frac{\delta\xi}{2} - \epsilon\tau\right) \operatorname{erfc}\left(\frac{\xi - 2a\tau}{2\tau^{1/2}}\right) \\
+ \quad & \frac{\beta}{2} \exp(b\beta\tau - \beta\xi) \left[\operatorname{erfc}\left(\frac{\xi + c\tau}{2\tau^{1/2}}\right) - 2\right] \\
- \quad & \frac{\beta}{2} \exp(\beta b\tau + b\xi) \operatorname{erfc}\left(\frac{\xi - c\tau}{2\tau^{1/2}}\right) .
\end{aligned} \tag{4.45}
$$

The constants used above are defined as:

$$
\beta \;=\; \frac{K_2 + K_3/\nu}{Q} = (1 - \nu)\frac{K_s + K_3/\nu}{Q} , \tag{4.46}
$$

$$
\epsilon \;=\; \frac{\beta K_3}{\nu Q} , \tag{4.47}
$$

$$
\delta \;=\; \nu + \frac{K_2}{Q} + \frac{2K_3}{\nu Q} = \nu + \frac{(1 - \nu)K_s}{Q} + \frac{(2 - \nu)K_3}{\nu Q} , \tag{4.48}
$$

$$
a \;=\; \sqrt{\frac{\delta^2}{4} - \epsilon} , \tag{4.49}
$$

$$
b \;=\; \beta - \delta , \tag{4.50}
$$

$$
c \;=\; \delta - 2\beta . \tag{4.51}
$$

Cumulative Storage of Water Under Constant Flux Infiltration

TDR measurements under constant rain rate together with a model describing the infiltration under these conditions allow to estimate parameter values of soil hydraulic functions by inverse modeling. If the model matches the measurement well, its particularly parameterized soil hydraulic functions are deemed to be good representations for the real world properties.

Ordinary TDR methods without the capability of determining moisture profiles can still be used to measure cumulative water content in the soil column defined by the support of the TDR probe. The observed soil column is limited axially by the length L of the probe and laterally by the distribution of electromagnetic field energy penetrating the material. If the soil column under investigation is homogeneous and exposed to a constant precipitation rate, e.g. generated by a sprinkler, water transport in soil can be modeled by Richards' equation under constant flux boundary conditions yielding the parametric solution given in Eq. 4.42. The water content profile $\theta(z,t)$ in 'normal' units can be derived from this solution. $\theta(z,t)$ is to be integrated along the observed soil column of depth L to yield the cumulative water content $w(L,t)$ within this control volume for a given time:

$$
w(L,t) \;=\; \int_0^L \theta(z,t)dz , \tag{4.52}
$$

with z downwards increasing. If θ is the unreduced volumetric water content, w will be given in unit of length, i.e. millimeter or liter/square-meter. The cumulative water

content $w(L, t)$ along a probe can be measured with TDR directly without reconstruction of the moisture profile.

Parkin et al. (1992) integrated the analytical solutions of SA and BW for constant flux infiltration to calculate the cumulative water content in a certain soil layer. Since only the results of the integration are given in his article, the detailed way of integrating the solution of SA (Eq. 4.43) is presented here to see, if any hidden assumptions have been made.

The equation to be integrated is given in reduced variables. Thus the first step is the transition from unreduced (w) to reduced (W) form of the cumulative storage of water:

$$
\begin{aligned}
w(L, t) &= \int_0^L \theta(z, t) dz = \int_0^L \left[(\theta_s - \theta_i)\Theta(z, t) + \theta_i \right] dz \\
&= (\theta_s - \theta_i) \int_0^L \Theta(z, t) dz + \theta_i L \\
&= (\theta_s - \theta_i) W(L, t) + \theta_i L \ ,
\end{aligned}
\tag{4.53}
$$

with W being the reduced cumulative water content defined as:

$$
W(L, t) = \int_0^L \Theta(z, t) dz \ .
\tag{4.54}
$$

The solution for Θ given in Eq. 4.43 is neither given in z nor in t, but in ξ and τ. The time t can be directly substituted by τ with help of Eq. 4.40 without any change of the integral. Since z is the integration variable, the substitution rule for integrals has to be applied to perform the variable change to ξ. The existence of the integral and a well-behaving $z(\xi)$ presupposed, the change from z to ξ yields:

$$
\begin{aligned}
W(L, \tau) &= \int_0^L \Theta(z, \tau) dz \\
\Leftrightarrow W(L, \tau) &= \int_0^{\xi(L, \tau)} \Theta(\xi, \tau) \frac{\partial z}{\partial \xi} d\xi \ .
\end{aligned}
\tag{4.55}
$$

The upper integration limit

$$
\xi(L, \tau) =: \xi_L
\tag{4.56}
$$

cannot be expressed directly. Eqs. 4.39 and 4.41 have to be solved inversely for $z = L$ at each time τ with solution called ξ_L:

$$
L = -\frac{1}{\beta} \frac{D_0}{Q} \ln \left[\frac{\phi(\xi_L, \tau)}{\phi(0, \tau)} \right] \ .
\tag{4.57}
$$

The partial derivative of z over ξ is calculated from Eqs. 4.39 and 4.41:

$$
\frac{\partial z}{\partial \xi} = \frac{D_0}{Q} \frac{\partial x}{\partial \xi} = -\frac{D_0}{Q} \frac{1}{\beta} \frac{\partial}{\partial \xi} \ln[\phi(\xi, \tau)] \ .
\tag{4.58}
$$

4. Applications

Thus the complete integrand reads:

$$
\begin{aligned}
\Theta(\xi,\tau)\frac{\partial z}{\partial \xi} &= \frac{1}{\nu}\left[1+\beta\left(\frac{\partial}{\partial \xi}\ln[\phi(\xi,\tau)]\right)^{-1}\right]\left(-\frac{D_0}{Q}\frac{1}{\beta}\frac{\partial}{\partial \xi}\ln[\phi(\xi,\tau)]\right) \\
&= -\frac{1}{\nu}\frac{D_0}{Q}\left(\frac{1}{\beta}\frac{\partial}{\partial \xi}\ln[\phi(\xi,\tau)]+1\right) .
\end{aligned}
\tag{4.59}
$$

Now the integration turns out to be simple, since partial derivative and integration cancel. The result is:

$$
\begin{aligned}
W(L,\tau) &= -\frac{1}{\nu}\frac{D_0}{Q}\int_0^{\xi(L,\tau)}\left(\frac{1}{\beta}\frac{\partial}{\partial \xi}\ln[\phi(\xi,\tau)]+1\right)d\xi \\
\Leftrightarrow W(L,\tau) &= -\frac{1}{\nu}\frac{D_0}{Q}\frac{1}{\beta}\ln\left[\frac{\phi(\xi_L,\tau)}{\phi(0,\tau)}\right]-\frac{1}{\nu}\frac{D_0}{Q}\xi_L .
\end{aligned}
\tag{4.60}
$$

Equation 4.57 shows, that the logarithm in Eq. 4.60 is constant, which leads to a further simplification:

$$
W(L,\tau) = \frac{1}{\nu}L - \frac{1}{\nu}\frac{D_0}{Q}\xi_L .
\tag{4.61}
$$

Eq. 4.60 is the solution of the cumulative water storage dynamics under constant flux boundary condition in reduced formulation.
Now the transition to the unreduced form (Eq. 4.53) is performed:

$$
\begin{aligned}
w(L,\tau) &= (\theta_s-\theta_i)W(L,\tau)+\theta_i L \\
\Leftrightarrow w(L,\tau) &= \left[\frac{1}{\nu}(\theta_s-\theta_i)+\theta_i\right]L-\frac{1}{\nu}\frac{D_0}{q}\xi_L ,
\end{aligned}
\tag{4.62}
$$

with the reduced flux density being $Q = q/(\theta_s - \theta_i)$. Eq. 4.62 is the solution for the cumulative water storage in unreduced form.
To show the equivalence with the solution of *Parkin et al.* (1992), their particular choice of parameters is used, which is less general than the original formulation of SA. *Parkin et al.* (1992) assume, that the diffusivity constant D_0 (Eq. 4.31) can be expressed by other parameters:

$$
D_0 = \frac{(1-\nu)k_s}{\alpha(\theta_s-\theta_i)} = \frac{(1-\nu)K_s}{\alpha} ,
\tag{4.63}
$$

with an additional form parameter α. They assume further, that

$$
K_3 = 0 .
\tag{4.64}
$$

With $K_3 = 0$ the parameter β (Eq. 4.46) is simplified to:

$$
\beta = (1-\nu)\frac{K_s}{Q} = (1-\nu)\frac{k_s}{q} .
\tag{4.65}
$$

168

With this parameterization for β the expression for L (Eq. 4.57) becomes:

$$
\begin{aligned}
L &= -\frac{1}{\beta}\frac{D_0}{Q}\ln\left[\frac{\phi(\xi_L,\tau)}{\phi(0,\tau)}\right] \\
&= -\frac{1}{\alpha}\ln\left[\frac{\phi(\xi_L,\tau)}{\phi(0,\tau)}\right] .
\end{aligned}
\tag{4.66}
$$

Insertion of the chosen parameters (Eqs. 4.64–4.65) into Eq. 4.62 yields:

$$
w(L,\tau) = -\frac{1}{\alpha}\left[\frac{1}{\nu}(\theta_s - \theta_i) + \theta_i\right]\ln\left[\frac{\phi(\xi,\tau)}{\phi(0,\tau)}\right] - \frac{(1-\nu)k_s(\theta_s-\theta_i)}{\alpha\nu q}\xi_L .
\tag{4.67}
$$

By utilizing the special symmetry of the error function, $\mathrm{erfc}(x) + \mathrm{erfc}(-x) = 2$, it can be derived from equation 4.44, that

$$
\phi(0,\tau) = e^{-\epsilon\tau} ,
\tag{4.68}
$$

with ϵ from Eq. 4.47. Since *Parkin et al.* (1992) assume $K_3 = 0$ it follows, that $\epsilon = 0$ and therefore

$$
\phi(0,\tau) = 1 .
\tag{4.69}
$$

With this constant the solution 4.67 becomes identical to that of *Parkin et al.* (1992), Eq. 14. For further analysis the more flexible and handy solution of Eq.4.62 will be used.

4.4.3. Application to the Infiltration Experiment

The analytical solution (Eqs. 4.60 and 4.62) describing the filling of soil water storage under constant infiltration rate is applied to the measurements of cumulative water content during the lysimeter experiment (Fig. 4.14 and Tab. 4.2). The model parameters describing the infiltration best are also the best estimates for soil hydraulic properties. Still some parameter uncertainties will remain. Therefore it will be investigated, whether detailed water content profiles and their temporal evolution monitored with Spatial TDR are capable to reduce the parameter uncertainties for this particular infiltration model. But first the relationship between water storage change, surface flux, and unsaturated hydraulic conductivity is illuminated.

The continuity equation in differential form for fluids not changing their density (incompressible, isothermal) and without local sinks or sources reads

$$
\frac{\partial\theta}{\partial t} = \nabla \cdot \vec{q} .
\tag{4.70}
$$

Integration with respect to the control volume V with surface ∂V and application of the Gauss integral theorem leads to

$$
\int_V \frac{\partial\theta(\vec{x})}{\partial t}\,dV = \int_V \nabla \cdot \vec{q}\,dV = \int_{\partial V} \vec{q}\cdot d\vec{A} .
\tag{4.71}
$$

4. Applications

Since the control volume V is defined by the support of the TDR probe, it has a column-like shape with appropriate top and bottom area A and height L. Assuming θ is a function of z only and the flux is purely vertical, i.e. $\vec{q} = (0, 0, q_z)^T$, perpendicular to and constant across the upper $(\vec{A}_u)$ and lower boundary $(\vec{A}_l)$, the continuity equation is simplified to

$$A \frac{d}{dt} \int_0^L \theta(z) \, dz = \int_{\partial V} \vec{q} \, d\vec{A} = \vec{q_u} \cdot \vec{A}_u + \vec{q_l} \cdot \vec{A}_l = (q_u - q_l)A \ . \tag{4.72}$$

As long as the infiltrating water has not reached the lower boundary of the control volume, the flux across the bottom is zero, i.e. $q_l = 0$. In literature the flux q_u at the surface into the soil is sometimes called *Darcy flux* and denoted by j_w. Together with Eq. 4.52 the continuity equation becomes

$$j_w = \frac{d}{dt} \int_0^L \theta(z) \, dz = \frac{dw(L, t)}{dt} \ . \tag{4.73}$$

This equation, which has been used before (Eq. 4.8), simply expresses, that the temporal change of water storage within the control volume is equal to the flux through the upper boundary.

After the soil storage has been filled its water content does not change any more and steady state infiltration is reached. From Eq. 4.70 follows, that water is entering and leaving the control volume at the same rate. Under the assumption of homogeneous soil the moisture is constant within the soil column, i.e. $\partial\theta/\partial z = 0$ and $\partial k/\partial z = 0$ for $0 \leq z \leq L$. The soil suction head (or matrix potential) Ψ is a function of the water content and therefore also constant, i.e. $\partial\Psi/\partial z = 0$. Under these steady state conditions the Darcy equation (Eq. 4.15) yields:

$$q_{\text{ss}} = k(\theta_{\text{ss}}) = \text{const} = j_w \ . \tag{4.74}$$

The constant flux density j_w, with which the water infiltrates into soil body across its top surface, is equal to the unsaturated hydraulic conductivity $k(\theta_{\text{ss}})$ appearing with steady state infiltration. The cumulative infiltration model to be adjusted to the measurements is given in Eq. 4.62. For the sake of clearness it is repeated here again (after substitution of Eq. 4.56):

$$w(L, \tau) = \left[\frac{1}{\nu}(\theta_s - \theta_i) + \theta_i \right] L - \frac{1}{\nu} \frac{D_0}{q} \xi(L, \tau) \ . \tag{4.75}$$

The only time varying part is $\xi(L, \tau)$, which is yielded by inverse solution of Eq. 4.57 for given L and τ. Parameterization suggested by *Parkin et al.* (1992) is used to simplify the model (Eqs. 4.63 and 4.64). The model needs the following parameters:

q: constant flux density, equal to j_w, derived experimentally (Tab. 4.3).

θ_i: initial water content, derived experimentally (Tab. 4.3).

θ_s: saturated water content, could be derived from a separate experiment, currently used as parameter for model fitting.

k_s: saturated hydraulic conductivity, could be derived from a separate experiment, currently used as fitting parameter.

ν: form parameter of diffusivity, used as fitting parameter.

α: form parameter of diffusivity, used as fitting parameter.

L: depth of the control volume, probe length, $L = 0.6$ m.

To calculate the water content profile by means of Eq. 4.75 for a given parameter set the following steps have to be performed:

1. Choose a time t and transform it into dimensionless time τ by means of Eq. 4.40.

2. Search ξ_L which solves Eq. 4.57 for the fixed probe length L.

3. Insert ξ_L into Eq. 4.75 to yield the cumulative water content at time t along the probe of length L.

4. Goto step 1.

The following analysis is concentrated on probe S_2, because it shows the most regular infiltration characteristic. Fig. 4.34 displays the cumulative water content at this probe derived by integrating the soil moisture profiles determined by Spatial TDR (c.t. Fig. 4.15). The model parameters $q(= j_w)$ and θ_i have been taken from Tab. 4.2. The parameters ν, α, k_s, and θ_s were varied, until a good agreement between model and experiment was found, i.e. the model yielded the measured steady state water content θ_{ss} and the transition from linear rising to constant water storage fitted the shape of the experimental curve.

The slope of the linearly rising portion of the modeled cumulative storage curve is determined by q only. Diffusivity parameters α and ν are responsible for the shape of the transition between linear storage filling and steady state infiltration. k_s and θ_s together determine the amount of steady state water content θ_{ss}. However, there is no 1:1 relationship between these parameters and the particular curve features. A change of only one parameter has several effects.

Three different parameter sets yielding a reasonable similarity between model and experiment are listed in Tab. 4.6. The resulting water content curves are plotted in Fig. 4.34.

The propagating infiltration fronts yielded by the model for the three parameter sets are plotted in Fig. 4.35, left. All profiles have initial and steady state water contents constant over depth. They are very different from those determined by Spatial TDR. In order to compare the model with Spatial TDR the model results are mapped to the moisture difference profiles of S_2 plotted in Fig. 4.11, top right. The transformation of a simulated profile $\theta^{(s)}(z)$ to a profile $\Delta\theta^{(s)}(z)$ of water content difference reads

$$\Delta\theta^{(s)}(z) = \frac{\theta^{(s)}(z) - \theta_i}{\theta_{ss} - \theta_i} \, \Delta_0\theta_{360}(z) \, . \tag{4.76}$$
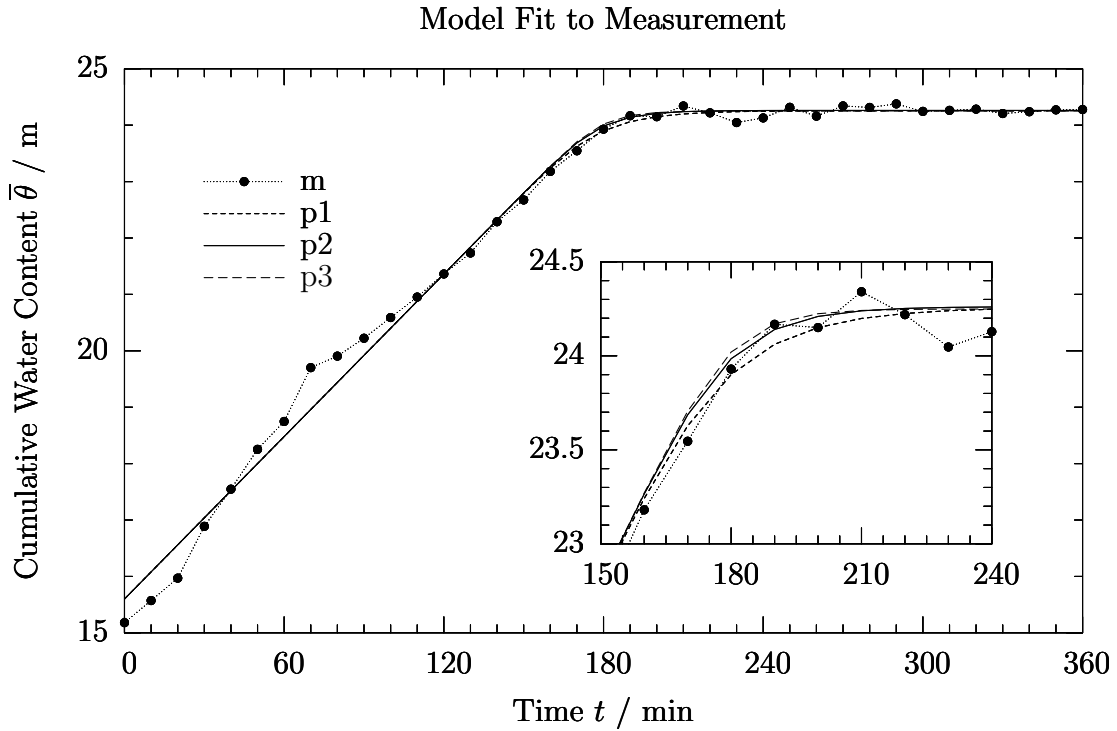
Figure 4.34.: Different parameter sets for constant flux infiltration model to fit experimental cumulative water content for probe S2, L=0.6 m.

Param. set	θ_i %vol	θ_{ss} %vol	q m/s	L m	k_s m/s	θ_s %vol	α 1/m	ν 1	K_3 1
p_1	15.6	24.3	$4.8 \cdot 10^{-6}$	0.6	$1.9 \cdot 10^{-5}$	28.1	30	0.85	0
p_2	15.6	24.3	$4.8 \cdot 10^{-6}$	0.6	$2.6 \cdot 10^{-5}$	30.0	50	0.85	0
p_3	15.6	24.3	$4.8 \cdot 10^{-6}$	0.6	$8.0 \cdot 10^{-5}$	37.8	100	0.9	0

Table 4.6.: A variety of parameter sets leading to acceptable fits of measured cumulative water content over time. Corresponding model results are plotted in Fig. 4.6. θ_i, θ_{ss}, and $q(= j_w)$ taken from Tab. 4.2.

$\Delta_0\theta_{360}(z)$ is the moisture difference profile at timestamp 360 min and nearly the upper envelope of all experimentally determined profiles of Fig. 4.11, top right (c.t. Eq. 4.3). Strictly spoken this transformation is physically incorrect. If the model were able to cope with initial or steady state soil moisture varying with depth, infiltration velocity would also vary locally corresponding to the changing hydraulic conductivity. But since the variance of the steady state water content with depth is small (relative to its mean value), it is assumed that the effects caused by these variations are also small and nearly linear functions of the deviation from the mean. In this case the effects should cancel in average. The resulting infiltration fronts are compared with experimental results in Fig. 4.35, right.
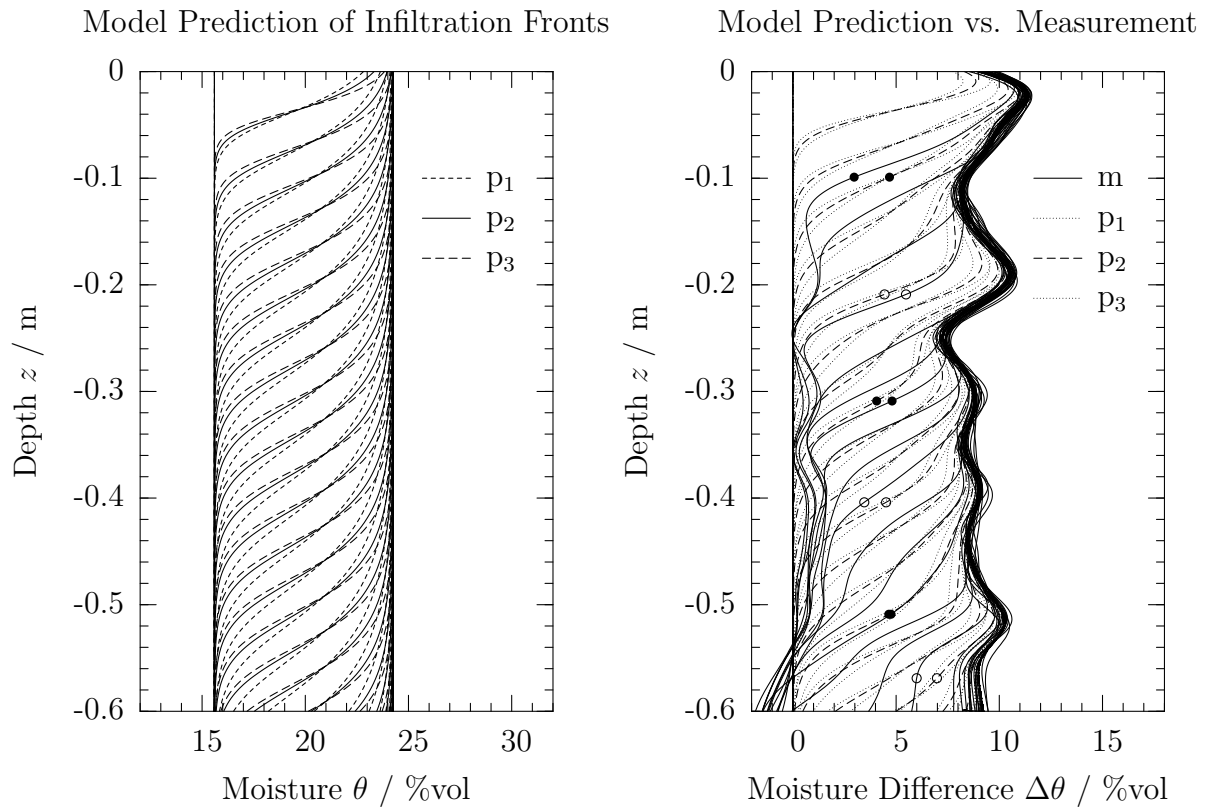

Figure 4.35.: Comparison between experimental water content profiles along probe S_2 and infiltration model results for the three model parameter sets p_1–p_3. Left: soil moisture profiles yielded by the infiltration model. Right: moisture difference profiles at probe S_2 measured with Spatial TDR (curve label m) versus model predictions. First timestamp of experimental profiles is 30 min. Some of the curves sharing the same timestamp are marked with equal symbols (open or closed circle). The upper envelope of profiles predicted by the model is matched to the upper envelope of the measured profiles by scaling to be graphically comparable 4.76.

4.4.4. **Discussion**

Prerequisites of the applied infiltration model are homogeneous soil, constant flux infiltration, purely vertical flow, and constant initial moisture. Probe S_2 was chosen for the analysis, because its infiltration characteristic was the most ideal of all probes.

The parameter sets listed in Tab. 4.6 lead to model results, which are very similar to the experimental outcome (Fig. 4.34). They are differing slightly in the transition form linearly increasing water storage to constant steady state moisture. The shape of this transition is determined by dispersion and velocity of the infiltration front. A considerable modification of soil hydraulic parameters (e.g. θ_s and k_s in set p_2 and p_3) may still lead to nearly the same model performance due to the large number of free parameters. The cumulative water content curves do not reveal which of these parameter sets is the best.

To gain more insight the sequence of modeled moisture profiles (Fig. 4.35, left) was transformed and compared to the moisture difference profiles determined experimentally by Spatial TDR (Fig. 4.35, right). Propagation velocity of the infiltration front and its slope are similar in experiment and simulation. However, additional information gained from a detailed look into the soil did not improve the assessment of model parameters (at least for the current case).

Thus depending on the specific application it may be necessary to reduce the number of unknowns (e.g. θ_s or k_s) by additional experiments based on different methods.

The infiltration dynamics observed with Spatial TDR reveals several effects, which are not covered by the selected infiltration model. A more sophisticated model with even more model parameters to cope with soil properties varying along the TDR probe will neither improve the estimation of soil hydraulic parameters, if no additional information is gained from other sources.

4.5. TDR Probe Cluster

The development of new hardware, software, and methods within the scope of this thesis is mainly targeting at field applications for monitoring infiltration dynamics on the spatial and temporal event scale. One essential outcome is the realization of an innovative TDR probe cluster as part of a comprehensive information system. *Heimovaara and Bouten* (1990) have connected several TDR probes by means of multiplexers to a central sampling TDR instrument. *Herkelrath et al.* (1991) have built a similar battery powered system equipped with a data logger and a tape recorder which allowed them to run the system for one week autonomously. These ideas were taken and extended by state of the art technologies.

A main objective for the new measuring system is flexibility. Spatial TDR is a young discipline and still under development. Methods, algorithms, and instruments like TDRs, multiplexers, and other supporting equipment together with the corresponding software are continuously improving. It is indispensable to have a system, which can be easily updated with new technologies and adapted to the experimenter's needs. This reduces time-to-application.

Flexibility, reliability, and sustainability of the system is guaranteed by choosing an industrial computer (IPC) as instrument controller and data logger. These commonly available computers designed for industrial automation are highly suitable for field applications. The device currently used is an Arcom Viper IPC (*Arcom*, 2004), which is based on a Intel XScale PXA255 CPU with ARM core. This CPU was specially developed for mobile devices like PDAs (personal data assistants). Despite its remarkable speed (400 MHz clock rate) it reveals a low power consumption which makes active cooling unnecessary. The current IPC together with its numerous interfaces needs 1.4 W only.

Linux has been chosen as operating system on the IPC because it is very stable and highly controllable. Such smart software distributions fitting on small devices are referred to as *Embedded Linux*. The Linux application software necessary to control the devices including the commercial instruments was developed within the scope of this thesis. The sampling TDR instrument of the measuring system is hooked on the Linux IPC with a standard RS232 serial interface (s. Fig. 4.36). Many moisture probes can be connected to the TDR by means of SNAPMUX multiplexers (s. App. B.6), which are controlled by the IPC over a RS485 field bus. The Linux IPC can switch the power for the external devices. This yields maximum power savings, so that the whole system can be powered by solar energy.

To exchange data with the measuring system the wireless network service *GPRS* (General Packet Radio Service) is used. UMTS would be much more powerful but is still not widely available. More information about wireless network standards is provided on the website *UMTSlink.at* (2004). A GPRS-modem is attached to the cluster controller. On system boot the IPC establishes a link to a GPRS service provider, who assigns a dynamic IP address to the system. The IPC becomes a full functional Internet node, which can be accessed under its IP address. The system is permanently online. It automatically transfers the connection parameters to the control host situated at the University of Karlsruhe. With this information it is possible to log in and establish an
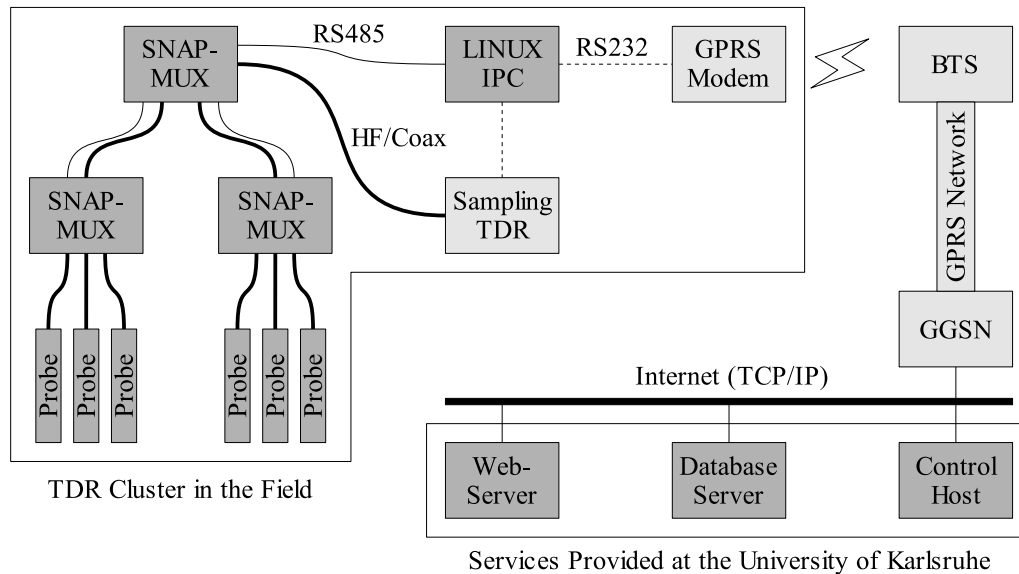
Figure 4.36.: Block diagram of the TDR cluster framework currently under construction. Components in darker gray are developed, programmed, or configured within the scope of this thesis with support by the SMG.

interactive session remotely or to transfer data to and from the system. This way the user has full control over the remote TDR cluster installed in the field. He may also change the system configuration or even install new software on the IPC remotely.

The measuring system takes TDR readings along the selected probes automatically. The IPC may be programmed to actively send the data to another computer (push), or an external host may look for new data on the IPC (pull). In the current design data is transferred actively to the control host at the university. The next step is to reconstruct the water content profiles from the TDR reflectograms. This demanding computation is performed on a Linux workstation cluster of the university's computer center.

It is planned to display the results in form of two-dimensional surface maps and vertical cross-sections through the vadose zone. The information will be provided by an Internet map server. The software used for this application is the open source UMN map server of the University of Michigan (*UMN Mapserver*, 2004). The realization of this information system is part of an ongoing research project. Fig. 4.37 shows a screen shot of a first test implementation (*Becker*, 2004).

4.5.1. Monitoring of Saturated Area Expansion

The new generation of the TDR probe cluster has not been tested yet, but its precursor successfully demonstrated the capability of the system. It was run continuously over three month to monitor the saturation of an area influenced by an ephemeral creek within the Goldersbach catchment next to the German city Tübingen. A research project of

Figure 4.37.: Test implementation of an application based on the UMN map server to provide information about the soil moisture state of a small catchment.

the Institut für Wasserbau (IWS), Universität Stuttgart, was aiming at an improved flood forecasting for this catchment based on assimilation of precipitation radar images (*Ehret*, 2003). The measurement infrastructure of this project and the collected data have been made available by the IWS. TDR readings were taken along 47 vertically installed 2-rod-probes every three hours. The data was stored locally and transfered to the data processing host once a week via a GSM modem.

Average soil moisture and water content profiles were reconstructed from the TDR reflectograms. Some problems were encountered during the reconstruction due to the applied unbalanced 2-rod-probes. These disturbances lead to imprecisions in the determination of absolute water content, especially within the first centimeters of the rods next to the probe head. Fig. 4.38 shows a two-dimensional map of the average moisture for a dry and a wet precondition. The growth of the zone of high average water content is obvious. An example of a vertical cross-section through the soil is given in Fig. 4.39. A wet zone in the deeper soil regions is clearly showing up.

The first generation of TDR cluster system used to obtain moisture distributions displayed in Fig. 4.39 had a number of disadvantages. Its IPC consumed too much energy
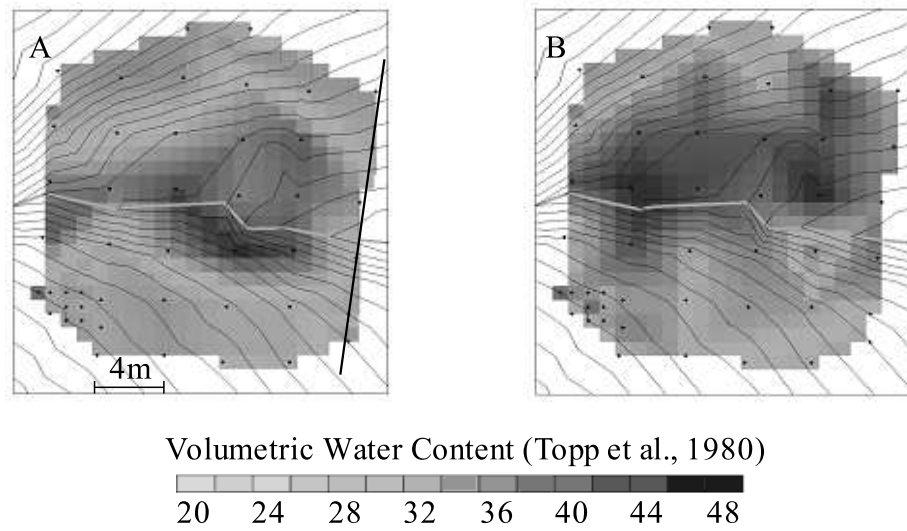
Figure 4.38.: Growing of a saturated area around an ephemeral creek monitored with a Spatial TDR cluster. The average moisture content was determined along 47 probes (black points). The creek is indicated by a bright, nearly horizontal line. A: dry condition; B: wet condition. The cross-section along the black line is shown in Fig. 4.39.
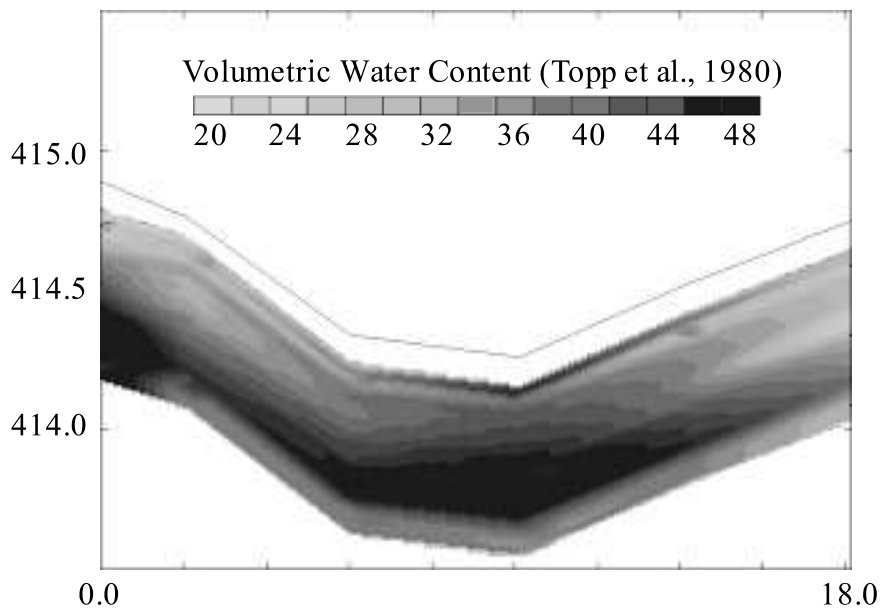

Figure 4.39.: Cross section through the vadose zone along the transect marked in Fig 4.38, A. Lengths in meters.

to be kept running. It had to be shut down instead. To wake up the system for a measurement cycle or for remote login an external microcontroller circuit was developed complicating the system design. The GSM modem was not as comfortable as a GPRS modem and the particular brand used tended to hang. The 47 channel multiplexer comprised by the system was not very reliable due to poor production quality. But the biggest disadvantage was due to the moisture probes. The predecessor of the currently applied 3-rod-probe SUSU03 was an unbalanced 2-rod-probe with a relatively large rod distance of approx. 5 cm. This probe produced a lot of disturbances at the junction of probe head and rods leading to higher electromagnetic wave modes. Thus right after the probe head the TDR pulse was not propagating in TEM mode making a reliable reconstruction of soil moisture in this upper region impossible.

Nevertheless the feasibility of Spatial TDR clusters for field applications has been successfully demonstrated by this system. With the current generation of measuring system most of the old drawbacks will be overcome. The new Spatial TDR cluster technology including improved data processing allows to derive soil water content profiles along many vertically installed 3-rod-probes in real-time.

5. Summary

The main objective of this thesis was to develop a measuring system for monitoring transient soil moisture profiles along several distributed moisture probes with high spatial and temporal resolution. The system is based on a method called *Spatial TDR*, which is an extension to common time-domain reflectometry (TDR). It is a combination of a sampling TDR instrument, a soil moisture profile reconstruction algorithm, and an appropriate waveguide as moisture sensor. The reconstruction algorithm is the key necessary to derive water content profiles from sampled TDR signals. It performs an inverse estimation of dielectric parameters along the waveguide, from which the water content profile can be calculated. The sophisticated algorithm of *Schlaeger* (2002) has been chosen to solve this inverse problem, because it is able to consider losses caused by ionic conductance and has no problem with multiple reflections during the TDR pulse propagation. Furthermore, its internal optimization approach is so fast, that it allows soil profile retrieval in real-time for the current use case with rod probes.

The soil moisture retrieval method was adapted for the application of coated 3-rod-probes. Therefore two steps had to been performed: First, the coated 3-rod-probe was calibrated diligently to determine the electrical parameters partly used in the reconstruction algorithm, and partly needed to parameterize the relationship between dielectric permittivity of the wet soil under investigation and the capacitance profile yielded by the reconstruction algorithm. For this purpose new calibration methods have been developed based on immersion experiments. This calibration procedure yields a robust estimate for the probe parameters, since a large number of measurements enters a regression model. A comprehensive sensitivity analysis was performed to illuminate the influence of probe parameter uncertainties on the final water content. The supposed parameter uncertainties were derived directly from measurements or from the application of Gauss' law of error propagation. An important result of this sensitivity analysis is, that even a small variation of the rod coating influences the water content measurement considerably. During the calibration experiments a 3 % time-base error was detected for one of the applied commercial TDR instruments (Tektronix Metallic Cable Tester 1502C) by means of an extensible hollow waveguide. The influence of the probe head on the measurements and the reconstructed water content profiles requires further investigations. The robustness of the 3-rod-probe has still to be proven in long-term field applications.

The second step needed to apply the reconstruction algorithm to rod probes was the determination of the empirical relationship between capacitance C' and effective conductance G' for the particular combination of probe and soil. This relationship was reduced to a simple parametric form and its parameter values were determined experimentally. The whole methodology of soil moisture profile retrieval was successfully tested in a

5. Summary

laboratory experiment. Four rod probes were installed vertically in a lysimeter filled with silty sand. They were connected to a Tektronix TDR instrument by means of self-made multiplexers. During a precipitation experiment TDR reflectograms were recorded every ten minutes at each probe. The high temporal and spatial resolution of the reconstructed soil moisture profiles opened a detailed view into the infiltration processes, which differed strongly from probe location to probe location. The differences are a reflection of the intended small scale variability of soil hydraulic properties due to the soil packing in the lysimeter. A local inhibition of infiltration could be observed, caused by a compacted soil layer, a capillary barrier, or by fine sediment reducing the hydraulic conductivity. Some profiles were wetted below the infiltration front giving evidence of lateral flow components. The information gain by Spatial TDR allows to assess infiltration features, which are difficult to interpret or are even not observable, when common moisture measuring technology is applied.

To assess the accuracy of Spatial TDR a further laboratory experiment was performed, in which the reconstructed moisture profiles were compared to the oven drying method. The moisture distribution was reproduced very well by Spatial TDR, whereas the absolute water content differed from the oven drying results in some cases up to 2%vol. This is supposed to be caused by remaining uncertainties in the probe calibration. Despite the diligent calibration procedure small parameter variations between probes of the same type caused by manufacturing tolerances had not been accounted for.

A electrodynamic simulation based on the full-wave solution of the Maxwell equations was used to test the limits of Spatial TDR under well-known conditions. These simulations show, that the optimal accuracy of Spatial TDR is around 1%vol up to now.

Another application was focused on inverse estimation of soil hydraulic properties from TDR measurements under irrigation. It was tested, whether Spatial TDR could improve the parameter estimation for an infiltration model based on the analytical solution of Richards' equation under constant flux boundary conditions. This model was applied to the lysimeter infiltration experiment to derive soil hydraulic parameters inversely. The model reproduced the cumulative water storage very well but with relatively high parameter uncertainty, i.e. different parameter sets led to the same model outcome. The detailed information provided by Spatial TDR about the spatial and temporal dynamic of soil moisture profiles did not lead to a reduction of parameter uncertainty because of the limited comparability of model and measurement. Observed features like initial water content not being constant over depth, local soil compaction, and lateral flow components could not be mapped by the model.

A main achievement of the thesis is the realization of a novel TDR prototype named OB-SERVER, which has been developed in collaboration with ADD Automation, Ontario, Canada. The sampler of this prototype is a delta modulator running in equivalent-time sampling mode. The necessary variable delay between TDR pulse emission and sampling strobe is realized by slightly detuned frequency programmable oscillators based on direct digital synthesis (DDS). For longer connecting probe cables as used in hydrological field applications the TDR reflectograms recorded by OBSERVER are already similar to the signal traces yielded by the commercial Tektronix Cable Tester 1502B. After having passed the connecting cable (approx. 14 m RG213) the emitted TDR signals of

OBSERVER and Tektronix 1502B reveal nearly the same edge steepness but the slower onset of the OBSERVER pulse may lead to a larger uncertainty in the determination of reflection instants by the tangent line method. The shape of the emitted pulse is not a fundamental problem and may be improved. A workaround could be to use the steeper falling pulse edges as excitation for TDR. A more complicated issue are non-random jitter components in the signal generators, the origin of which has not been fully identified, yet. New DDS integrated circuits, which had not been available during the design phase, have a much better performance and would probably solve the problem. Despite these issues OBSERVER has already proven to be an interesting alternative to conventional TDR instruments.

Parallel to the laboratory experiments an operational autonomous measuring system for monitoring transient soil moisture profiles was built and installed in the field. This TDR probe cluster consisted of nearly 50 coated 2-rod-probes connected to a Tektronix 1502B by means of self-made multiplexers. The probes were installed vertically on a fairly regular grid with 4 m spacing. The cluster was used to monitor the variable extent of a saturated area around an ephemeral creek. An industrial PC accessible over a wireless network was used to control the multiplexers and the TDR instrument. The whole system was solar powered. All software necessary to control the instruments and to automate the measurement process was developed in the scope of the thesis. The reconstructed soil moisture profiles were interpolated along transects to yield a two-dimensional picture of the soil moisture distribution for different cross-sections. Furthermore the average water content derived from TDR travel-time analysis was used to generate a map of lateral moisture distribution.

The reconstruction of water content profiles along the applied unbalanced 2-rod-probes led to erroneous results near the probe head. Higher order electromagnetic modes induced at the transition between probe head and rods may be an explanation for this finding. This disadvantage led to the development of the 3-rod-probe used in the laboratory, which showed a much better performance.

But even with wrong absolute moisture values along the reconstructed soil moisture profiles the main features of the subsurface water content distribution are still obvious. This field experiment impressively demonstrates the ability of the system to derive a quasi two- or three-dimensional view of subsurface soil moisture with high spatial and temporal resolution. The variable extent of the saturated area was clearly observable, both in average water content maps and vertical transects.

It has been demonstrated that Spatial TDR in combination with rod probes is capable of monitoring transient soil moisture profiles on a temporal and spatial scale, which match the scales of important hydrological processes on the field scale better than distributed point measurements with common TDR technology. This approach offers new possibilities to process hydrology.

The presented methodology is still under development. The first large field application will be realized in an ongoing research project, dedicated to improved flood warning in small catchments based on distributed online measurements of soil moisture profiles.

5. Summary

Recommendations for Future Research and Development Concerning Technology
A comprehensive review of available reconstruction algorithms should be made including comparative calculations based on standardized test cases for a variety of moisture probes and soils. These test cases could be based on TDR reference measurements or TDR reflectogram simulations generated by field theoretical simulation models. The latter alternative would be more flexible and reproducible.

Spatial TDR with its one-dimensional moisture profile could complement ground penetrating radar (GPR) to support multi-dimensional tomographic methods. The advantage of the former is the defined reflection at the end of the probe leading to relatively reliable moisture reconstructions, but Spatial TDR is stuck to the point. In contrast to that GPR has the ability to cover larger areas but the multi-dimensional water content estimation is intricate. As with Spatial TDR the reconstruction procedure for GPR requires a pronounced reflection in the ground, too, which can be difficult depending on the field situation. A combination of both methods could probably help to overcome some of the problems.

The sensitivity of the coated 3-rod-probe could be improved by reducing the capacitance of the rod coating. This could be achieved by isolating the middle rod only with a thin heat shrink (polyolefin resistive coating). This idea is inspired by *Nichol et al.* (2002). The lateral energy density distribution of the electromagnetic field of the coated 3-rod-probe may be used to estimate the sampling volume of the probe. This method was proposed by *Knight* (1992) and applied to 2-rod-probes.

The averaging of apparent dielectric permittivity derived by TDR in layered materials is subject of an ongoing discussion (*Schaap et al.*, 2003). Depending on the ratio of the minimum TDR signal wave length and the spacing of multi-layer material different average schemes have to be used. These schemes, which look like dielectric mixing rules, are called refractive index mixing method, ray theory, and effective medium theory, which is in fact the arithmetic mean. It can be assumed, that these findings are irrelevant for appropriate reconstruction algorithms based on the full wave solution of Maxwell's equations or the telegraph equation. Nevertheless this statement is to be proven.

The revolutionary next generation of wireless field scale communication networks will be mobile self-organizing ad hoc networks (e.g. *Hubaux et al.* (2001)). Spatially distributed wireless network nodes can identify their nearest neighbors and establish the network topology by themselves. Each node of such a network is receiver and transmitter, so that data can be transferred in a multi-hoc scheme. This allows for spanning larger distances in the field with relatively low transmission power. It is to be expected that self-organizing ad hoc networks will be established in a wide range of mobile applications with a large number of device nodes at low price. All these properties make such a network an ideal backbone for environmental monitoring. Such a system is going to be realized in a developing project in India (*Panchard*, 2003) aiming at the reduction of the *digital divide*. It would be interesting to apply this network technology to Spatial TDR, maybe in combination with simple soil moisture probes like SISOMOP.

Recommendations for Future Research and Development Concerning Application

The proposed Spatial TDR cluster has a large number of potential applications not only in field hydrology. Only a few examples will be given.

Geostatistical parameters (variogram estimate) of soil hydraulic properties like e.g. saturated hydraulic conductivity may be estimated from distributed moisture profile measurements with Spatial TDR. First promising results have been presented by *Zehe et al.* (2002).

A test of data assimilation schemes may be performed by comparing hydrological models updated with remote sensing data to measured profiles along several spatially distributed profile probes covering a larger area.

Spatial TDR will soon be used in conjunction with a novel probe design for dike monitoring to assess their stability in flood situations. A new research project, which has been started recently, is dealing with this topic.

Final Remark

For me is left to say, being involved in the development and application of a sophisticated technology like Spatial TDR is a lot of fun. I would like to thank all my friends and colleagues again, who have given me support. They are the main source of my enthusiasm.

A. Materials

A.1. Soil Characteristics in the Lysimeter

The lysimeter the infiltration experiments have been conducted in is filled with a loamy sand. The grain size distribution of the material is shown in Fig. A.1. The diagram expresses, that soil particles with a diameter d less than 0.1 mm comrpise 10% of the total soil mass and particles smaller than 0.5 mm sum up to 60% of the mass. These diameters defined by the sieve passing fraction are therefore termed $d10$ and $d60$, respectively. The uniformity coefficent is defined as $U = \text{d}60/\text{d}10$. This particular soil has a uniformity coefficient of $U = 0.5$.
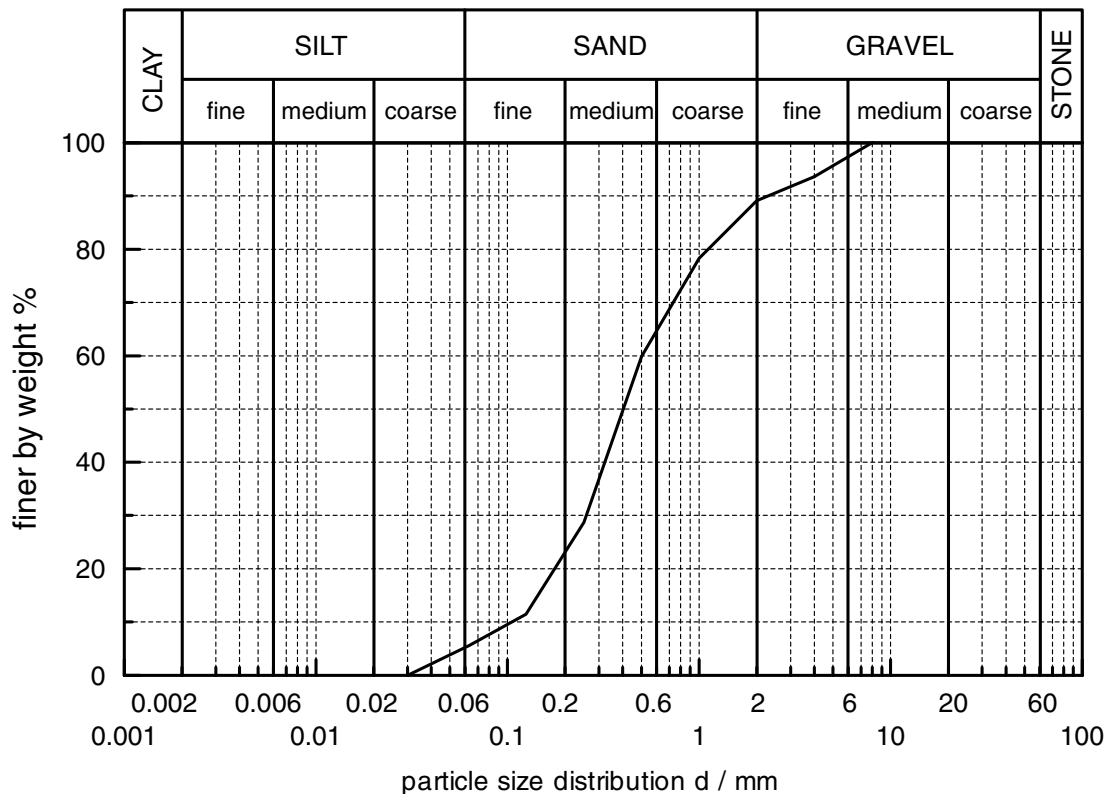
Figure A.1.: Grain size distribution of lysimeter material (loamy sand).

The soil water retention curve (e.g. *Kutílek and Nielsen* (1994)) describes the relationship between water content and the corresponding suction of the soil matrix: The drier the soil the stronger it sucks water. The soil water retention curve (Fig. A.2) was determined

by draining a soil sample by applying negative pressure head following the german specification *DIN 19683* (1973). The emperical parametrization of Mualem and van Genuchten (e.g. *Kutílek and Nielsen* (1994)) has been fitted to the experimental data. Parameters are listed in Fig. A.2.
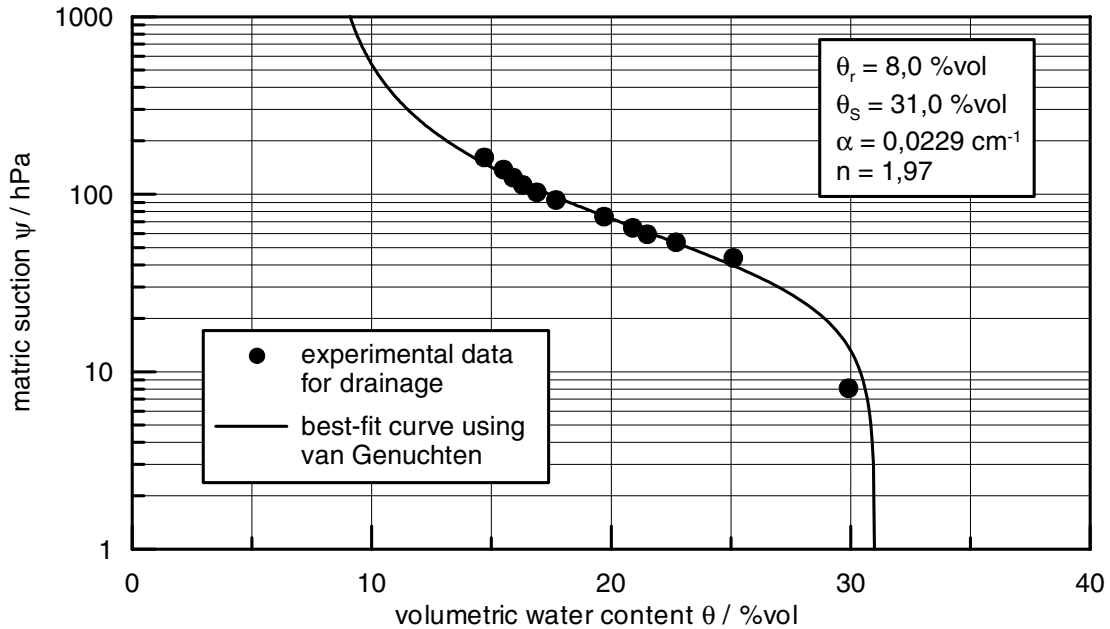
Figure A.2.: Soil water retention curve of lysimeter material. Curve determined from drainage with applied negative pressure head. Parametrization of Mualem / van Genuchten.

The saturated hydaulic conductivity k_s was estimated from the grain size distribution curve (Fig. A.1) by means of Bayer's empirical relationship (*Scheider*, 1992):

$$k_s = 0.01 \cdot C \cdot \mathrm{d}10^2 \, . \tag{A.1}$$

The parameter C is an emperical function of uniformity parameter U. The relationship is listed in *Scheider* (1992).

The Mualem / van Genuchten model in conjunction with the saturated hydraulic conductivity k_s leads the unsaturated hydaulic conductivity k. The estimated curve is displayed in Fig. A.3.
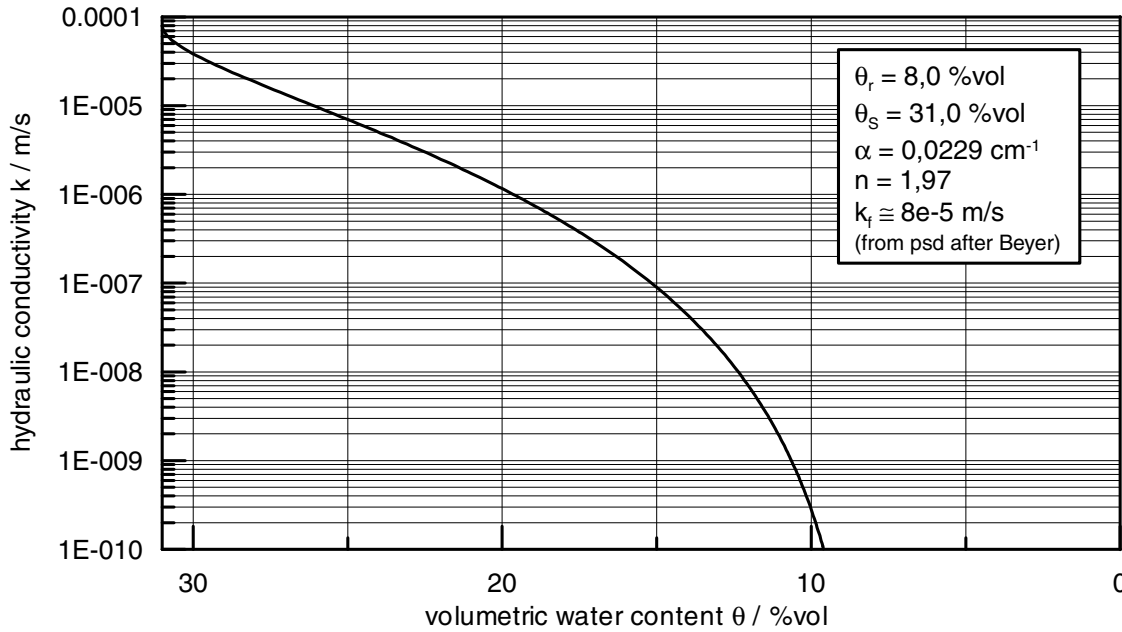
Figure A.3.: Unsaturated hydraulic conductivity k derived from saturated hydraulic conductivity k_s and the parameters of the Mualem / van Genuchten model.

A.2. Dielectric Permittivities of some Materials

Material	ϵ_s
air / vacuum	1
polyethylen (PE)	2.3
polyvenyl chloride (PVC)	$3.0\ldots3.2$
silica	$3.5\ldots4.5$
methanol	33.5
destilled water	81

Table A.1.: Typical static relative dielectric permittivities for several pure dielectrica. Values at room temperature (25°C). This table does not consider the permittivity's dependence on temperature, frequency, or ionic conductivity caused by dissolved ions in liquid dielectrica.

B. Measuring Instruments, Probes, and other Devices

B.1. Transmission-Line Parameters

Parameter	Symbol	Typical Unit	RG 58	Thin 3-Wire Ribbon Cable[a]	3-Rod-Probe SUSU03[b]
Resistance	R'	mΩ/m	0.01–0.1[c]	unknown	unknown
Inductance	L'	nH/m	250	726	575
Capacitance	C'	pF/m	100	70–175[d]	87–207[d]
Eff. Conductance	G'	mS/m	≈ 0	[e]	[e]
Cap. Model	C_1	pF/m	—	14.8	20.5
	C_2	pF/m	—	323	356
	C_3	pF/m	—	3.4	0

[a] According to *Hübner* (1999).
[b] Compare to Tab. 2.1.
[c] Skin effect, freq. 1 kHz – 1 GHz.
[d] Moisture 10–40 %Vol, θ-ϵ-relationship of *Topp et al.* (1980).
[e] Depending on soil salinity.

Table B.1.: Transmission-line parameters for frequently used cables and waveguides. Frequency dependence not considered.

The capacitance model for the probes, which are dependent on the material's permittivity, reads:

$$C'(\epsilon) = \frac{\epsilon C_1 \, C_2}{\epsilon C_1 + C_2} + C_3 \ . \tag{B.1}$$

B.2. Tektronix Metallic Cable Tester 1502B/C

The Tektronix TDR 1502B (or the similar 1502C) is a widespread instrument for soil moisture determination (e.g. *Topp et al.*, 1980). Since it was constructed as a cable

tester for coaxial 50 Ω computer networks it gives the signal on a length scale (meters or inch) instead of time. The sampling windows of this TDR equals its display. The part of the reflectogram shown on the display is the part, which is sampled. The sampling window is determined by three parameters: the position s_0 of its left border, its width Δs, and a velocity factor v_p, necessary to transform the length scale of the display back to the time axis, on which the sampling takes place.

The velocity factor v_p can be selected arbitrarily between 0.3 and 0.99 in steps of 0.01 by the operator. s_0 is manipulated by moving the instrument's cursor. Δs is defined by the knob setting for *distance per division* (dist/div). The display grid is divided horizontally into 10 divisions. Thus the total window width is given by $\Delta s = 10 \cdot (\text{dist/div})$. The transition from a spatial coordinate s to time t is done by the following rule:

$$t = \frac{2\,s}{v_p \cdot c_0}\;, \tag{B.2}$$

with c_0 the speed of light in vacuum. The factor of 2 is due to the pulse traveling a distance twice: forth and back. The above equation is used to translate part of the specifications listed in the Tektronix 1502B service manual into variables and units better suited to travel-time measurements (Tab. B.2).

excitation pulse

reflected rise-time	≤ 200 ps, into a precision short
pulse amplitude	300 mV nominal into 50 Ω load
pulse width	25 μs nominal
pulse repetition rate	200 μs (5 kHz)

time base

aberrations	±5% peak, for $t \leq 20$ ns
	±0.5% peak, for $t > 20$ ns
jitter	≤ 40 ps peak to peak, for $\Delta t = 2$ ns
	≤ 400 ps peak to peak, for $\Delta t = 20$ ns
samples per window	≤ 251

vertical scale

accuracy	within ±3% of full scale
displayed noise	≤ −46 dB peak, with no waveform averaging
	≤ −54 dB peak, with averaging of 128 wave-forms

output impedance   50 Ω ± 2%

Table B.2.: Part of the Tektronix 1502B specifications taken from the service manual. Units are modified.
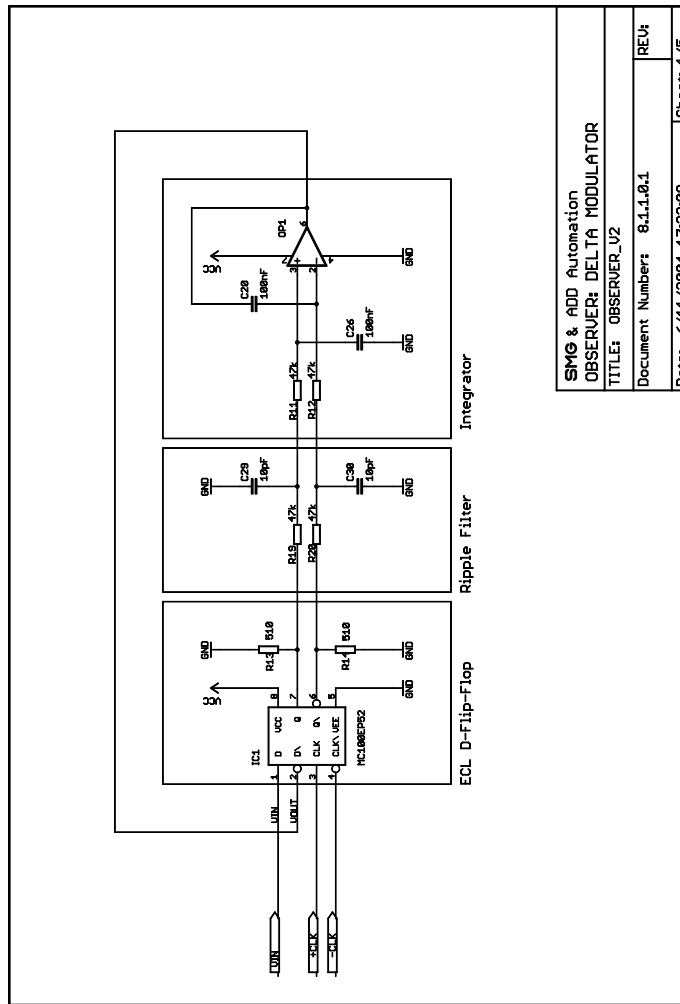
B.3. Selected OBSERVER Schematics

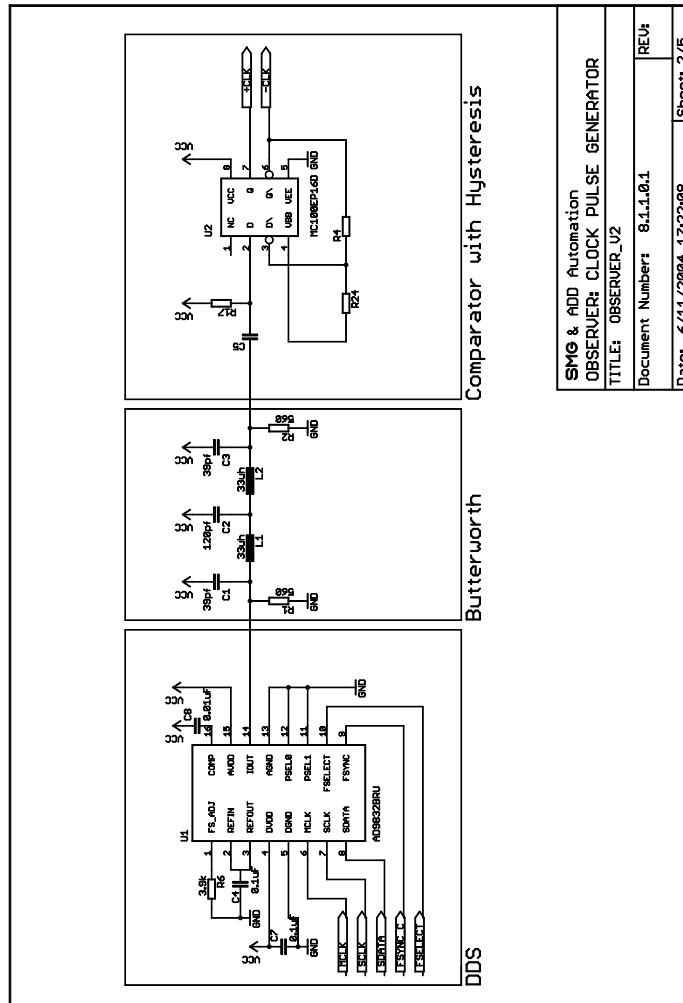Figure B.1.: Schematic of OBSERVER's delta modulator.

.

Figure B.2.: Schematic of OBSERVER's sampling clock pulse generator.

.

B.4. The Simple Soil Moisture and Temperature Probe SISOMOP

For many applications soil moisture measurement devices of the OBSERVER class or the like are still too expensive and offer more features than really needed. Therefore a prototype for a simple and economical soil moisture probe has been developed, which allows to measure the mean moisture in a small volume.

Another important state variable besides moisture is temperature. Temperature measurements are needed for many purposes: To detect if the soil is frozen, which would change its hydraulic properties drastically. To gain information important for energy budget investigations (soil heat flux). A coupled moisture and temperature sensor could help to get more insight into the problem of temperature as tracer.

Therefore a moisture and a temperature sensor have been combined in one device. The probe is named *Simple Soil Moisture Probe* (SISOMOP). Its temperature senor is common semiconductor bandgap temperature sensor. The soil moisture measuring part is based on an ring oscillator whose frequency is changing with water content.

Ring Oscillator

The core of the probe's moisture sensor is a ring oscillator based on a digital inverter, which acts like a line driver (s. Fig. B.3). This inverter drives a transmission line the end of which is fed into its input again. This makes the line driver oscillate. If a logic 1 state travels along the transmission line it will reach the input where it is inverted. The output of the line driver becomes logic 0 and this distortion propagates along the transmission line, until it reaches the input of the inverting line driver. It transformed into logic 1 and sent out again. The line driver toggles with a frequency determined by the propagation velocity of the positive and negative voltage pulses along the transmission-line.

If the transmission line is buried in soil, the pulse will interact with the surrounding medium, especially the stored water. The higher the moisture the higher the effective dielectric permittivity ϵ, leading to a lower wave propagation velocity v_p and a thus lower frequency of the ring oscillator.

The inverting line driver is realised in ECL logic. The transmission line consisting of two copper strips is etched on one side of a two-sided epoxy printed circuit board (PCB), which also carries the necessary electronic parts (Fig. B.4). This leads to a simple, robust, and cost-effective design. To seal the strip line and to protect it from scratches when pushed into soil, the transmission line is covered by a protective lacquer.

The lancet formed by the PCB is rigid and flexible at the same time due to the glass fiber substrate. The width of the PCB is 3 cm and the length of the part forming the ring line can vary between 10 and 20 cm depending on the user's need. The electronics occupy additional 5 cm.

The typical frequency range determined by the current ring line layout is around several hundred megahertz. This ring oscillator frequency is too high to be countable by a standard microcontroller. A frequency divider brings it down to a range which can be conveniently counted. To determine the frequency the microcontroller counts the signal transitions from logic 0 to 1 during a fixed predefined timing window. The resulting
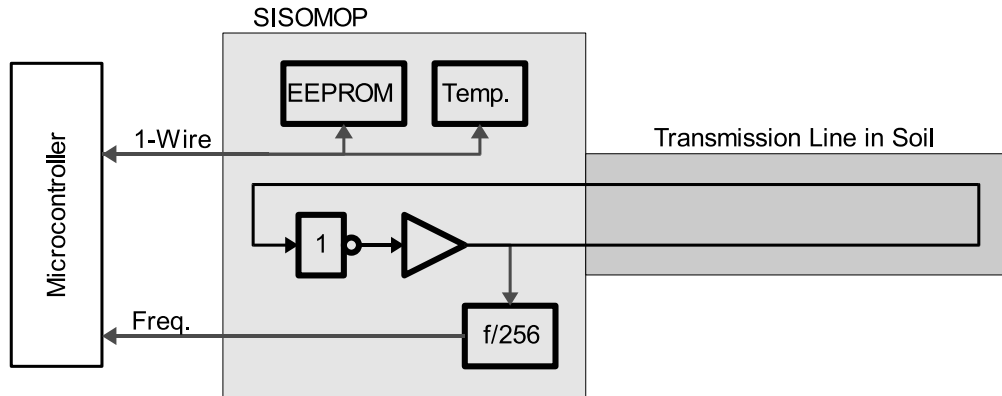
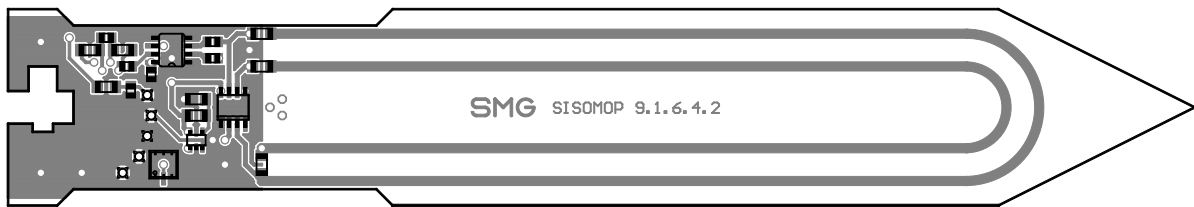Figure B.3.: Block diagram of the Simple Soil Moisture Probe + Temperature Sensor.

Figure B.4.: Printed circuit board of the Simple Soil Moisture Probe including surface
mounted parts (top layer only). Original size: 185 mm x 30 mm.

counts N_c are proportional to the oscillator frequency and thus for the propagation
velocity of the electromagnetic wave along the transmission line.

Integrated Temperature Sensor

The chosen temperature sensor DS18B20 (*Maxim*, 2002a) is a digital thermometer with
a so-called *1-Wire bus* interface. A microcontroller can communicate with the chip over
this interface, that only needs one date line and ground to transfer the digital data.[1]
The DS18B20 measures temperatures between $-55°$C and $125°$C with an accuracy of
$\pm 0.5°$C from $-10°$C to $85°$C without calibration or error correction. The maximum
resolution of 12 bits corresponds to temperature steps of $0.0625°$C.

A very useful feature of this integrated circuit is a unique 48 bit identifier stored in
its ROM. Thus the combined moisture and temperature sensor using this chip can be
identified uniquely. This information can be used to refer to sensor specific external
calibration data if needed.

---

[1]The application note *Maxim* (2002b) is an example for the communication between a microcontroller
and the DS18B20 using the 1-wire bus.

Bandgap Temperature Sensor

The DS18B20 is a so-called *bandgap based temperature sensor*. The bandgap is a typical property of semiconductors and refers to the gap between the energy range (band) of valence electrons responsible for the metal binding and the energy range of conducting electrons moving freely in the semiconductor lattice. In a semiconductor valence band and conduction band do not overlap but the energy gap E_0 between the bands is so small that the thermal energy of electrons under room temperature suffices to lift a few of them from the valence band to the conduction band. The probability for an electron having the energy $E > E_0$ follows a Boltzmann distribution:

$$P(E > E_0) = e^{-E_0/kT} \; , \tag{B.3}$$

with T being the absolute temperature in Kelvin, and the Boltzmann factor $k = 1.38$ Ws/K . This explains the effect of temperature on the number of charge carriers contributing the conduction.

The Boltzmann distribution is the deeper reason for the base-emitter junction in a transistor to reveal (approximately) an exponential dependency of collector current I_C on the base-emitter voltage U_{BE}:

$$I_C \approx I_0 \cdot e^{eU_{\mathrm{BE}}/kT} \tag{B.4}$$

If the base-emitter voltages U_{BE1} and U_{BE2} of two identical transistors are controlled such that the respective collector currents I_{C1} and I_{C2} are held constant, the difference in the base-emitter voltages is approximately proportional to the temperature (*Tuthill*, 1998):

$$\Delta U_{\mathrm{BE}} = U_{\mathrm{BE2}} - U_{\mathrm{BE1}} \approx \frac{kT}{e} \; \ln\left(\frac{I_{C2}}{I_{C1}}\right) \; . \tag{B.5}$$

The analog voltage ΔU_{BE} is then converted to a digital number with the help of an analog-to-digital converter. All these parts plus a sophisticated 1-wire interface are implemented in the DS18B20.

Calibration Function for Soil Moisture Determination

To determine a first (and still preliminary) calibratition function between volumetric moisture content *Theta* and corresponding SISOMOP counts N_c an experiment with dry sand was performed. Different moisture contents have been realized by mixing different ratios of water and sand. Two SISOMOP probes were stuck into the soil and the frequency counts read. The corresponding volumetric water content was detemined with a short TDR probe.

Summary

The first results are very promising. The probes are working. Differences between the two instruments are small. The sensitivity of the ring oscillator on moisture is very high. The SISOMOP is a simple, cheap, and robust instrument to measure soil water content with high precision. The temperature sensor is working, too, but still has to be tested carefully.
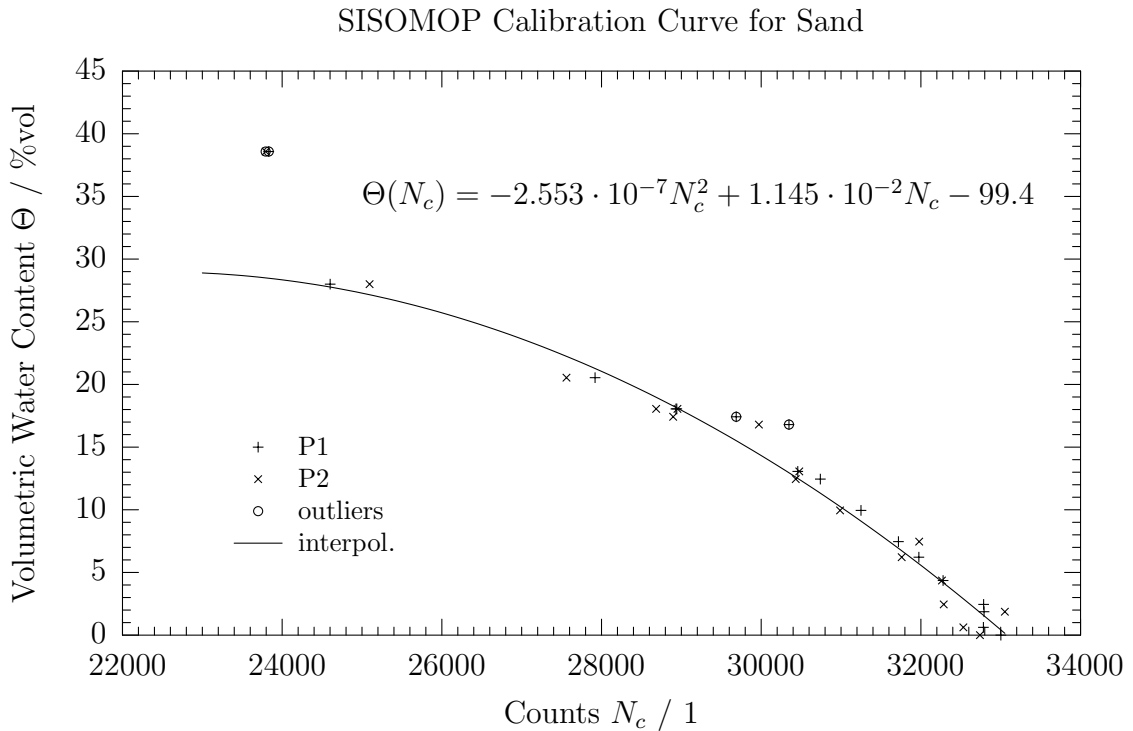
SISOMOP Calibration Curve for Sand

Figure B.5.: Empirical relationship between SISOMOP counts and volumetric water content. The measurements were performed with two probes P1 and P2. The fitting polynom equation is printed in the diagram.

B.5. Atmel AT90S8535 Multi-Functional Board

A microcontroller is needed to count the frequency of the SISOMOP moisture sensor output signal and to communicate with the temperature sensor. Since microcontrollers are needed at many places within the scope of this thesis, a new flexible circuit (Fig. B.8) has been designed to satisfy all the needs. The circuit is based on the Atmel microcontroller AVR AT90S8535. It is a reduced instruction set controller (RISC) with 8 kB flash ROM. It allows in-system-programming, i.e. no special external programmer is needed. Among other input/output devices it contains an 8-channel, 10-bit analog-to-digital converter and three counters/timers, one of which with 16 bit resolution. Each counter/timer has a programmable prescalar to occasionally run at a much lower frequencies than that of the connected crystal.

A powerful, easy to understand, and cost-effective BASIC compiler (BASCOM-AVR) is available for this controller, which stands for rapid prototyping.

The board (Fig. B.7) is equipped with illuminated LCD display (2x16 characters), serial interface configurable as RS232 or RS485, stabilized voltage reference for the internal analog-to-digital converter, some buttons and LEDs, real-time clock crystal, voltage regulator, and programming interface, which can be connected directly to the parallel

Figure B.6.: Photo of the multi-purpose microcontroller board.

port of a PC allowing for easy in-system-programming. The device is self-contained and can be used stand-alone without external circuitry except unregulated power supply. The board is highly configurable due to numerous jumpers.

Most of the signals are led to a 37 pin female header, so that the board can be conveniently mounted on top of a raster printed circuit board for rapid prototyping.

To determine the output frequency of the connected moisture probe TIMER0 is used to define a precise time interval during which COUNTER1 is counting the external rising edges of the probe pulses. After the time is over the counter is stopped and its value is proportional to the output frequency of the moisture probe.
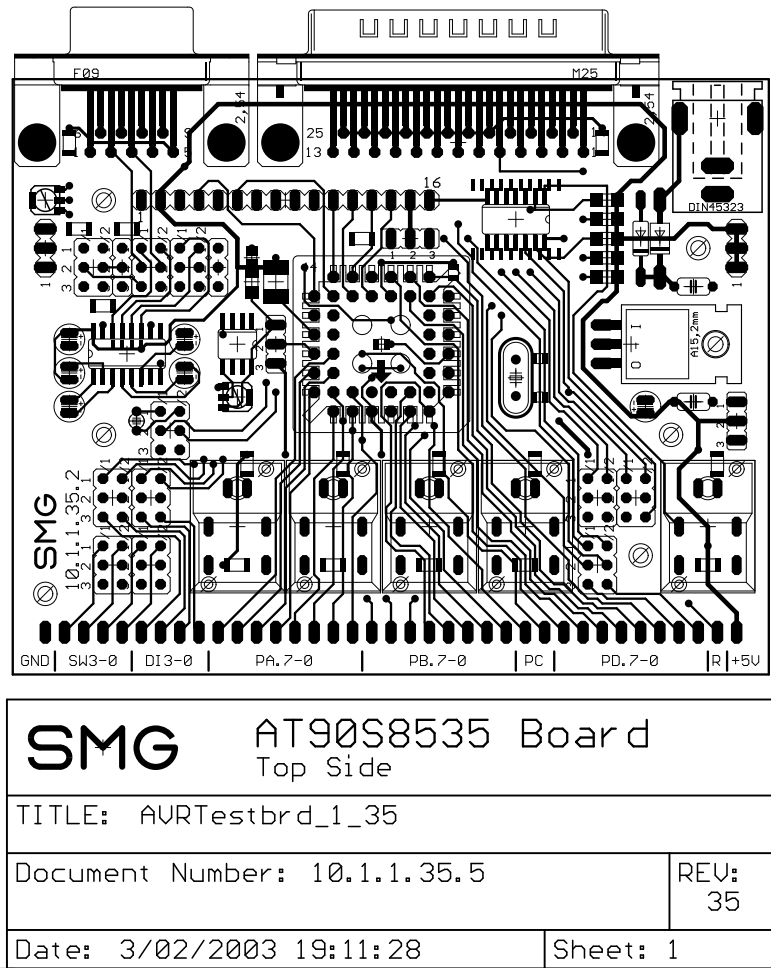
Figure B.7.: Top layer of the multi-purpose microcontroller board. LCD display not shown, CPU socket empty. Size without connectors: 10 cm x 8 cm.

Figure B.8.: Schematics of the multi-purpose board based on Atmel AVR AT90S8535 microcontroller. The LCD display is to be connected to connector SV1

B.6. 8-Channel Multiplexer SNAPMUX

SNAPMUX is a 8-channel-multiplexer with 50 Ω impedance developed by the SMG. It is controlled by the bidirectional scalable node address protocol (SNAP, *HTH* (2004)) over RS485 serial bus running at 9600 baud. The multiplexers can be cascaded to build a tree-like topology with distances of several hundred meters. The length of the high-frequency path is mainly limited by the attenuation of the coaxial cable connecting the components. The newest version of SNAPMUX has a built-in fault detection which physically checks whether a selected channel has been really switched to.
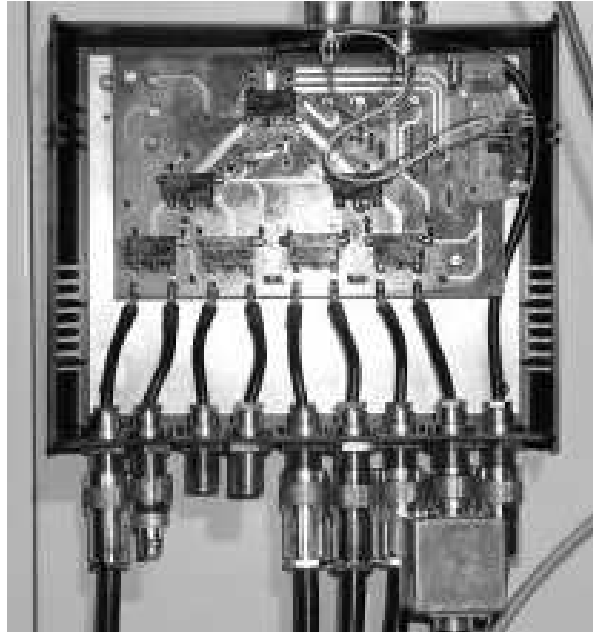
Figure B.9.: Photo of SNAPMUX, version 1.
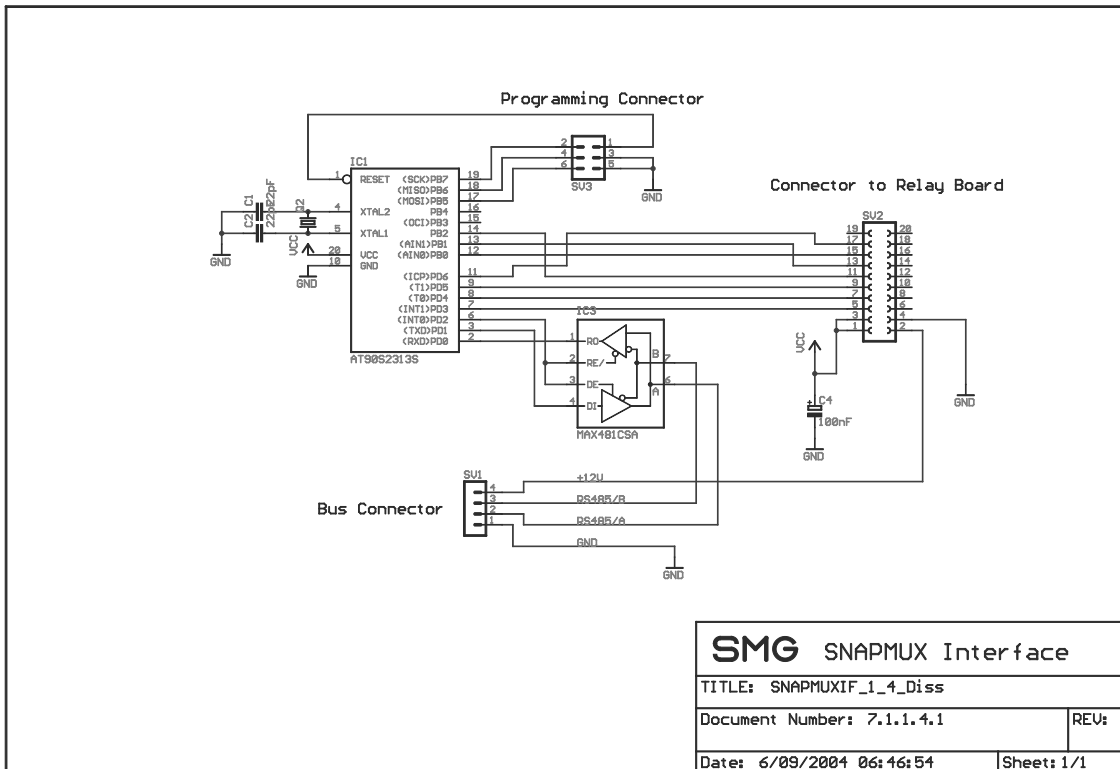
Figure B.10.: Schematic of SNAPMUX controller circuit.

C. Influence of Covariance on Interpolation by Kriging

C.1. Ordinary Kriging

This section does not claim completeness but is meant to give a rough idea of the basic principles of the Kriging method and what has to be regarded in order to avoid misuse of this interpolation scheme. Kriging is a family of different geosatistical methods, which is often applied for interpolating spatially distributed data (*Kitanidis*, 1997). The basic assumption is that the spatial distribution of a variable like for example soil moisture can be described by a random function or spatial stochastic process $Z(x)$. The objective is to estimate $Z(x)$ by means of a model and measurements.

A model often used is the intrinsic isotropic model, which claims that the mean of Z is constant, i.e. does not vary in space, and that the two-point covariance function depends only on the distance between the points:

$$\langle Z(x) \rangle \quad = \quad \langle Z(x_i) \rangle = m \; , \tag{C.1}$$

$$\mathrm{Cov}(x_i, x_j) \quad := \quad \langle (Z(x_i) - m)(Z(x_j) - m) \rangle = \mathrm{Cov}(|x_i - x_j|) = \mathrm{Cov}(h) \; , \tag{C.2}$$

with $h = |x_i - x_j|$ the distance of the separation vector. The angles $\langle \ldots \rangle$ denote the expected value. If a stochastic process Z fulfills these assumptions it is said to be stationary. The covariance at $h = 0$ is the variance of the random variable: $\mathrm{Cov}(0) = \mathrm{Var}(Z)$. It is also referred to as sill. The covariance function $\mathrm{Cov}(h)$ is an expression for the statistical dependence of two random variables being seperated by the distance h. The graphical representation of $\mathrm{Cov}(h)$ is also referred to as covariogram. In Kriging the so-called semivariogram $\gamma(h)$ is often used instead. It is defined as

$$\gamma(h) = \frac{1}{2}\mathrm{Var}(Z(x_i) - Z(x_j)) = \frac{1}{2}\left\langle (Z(x_i) - Z(x_j))^2 \right\rangle \; , \tag{C.3}$$

with $h = |x_i - x_j|$. In some practical cases the estimator of the semivariogram may be more robust than that of the covariance, since it does not require the estimation of the mean m. It can be shown that the following relationship between covariance and semivariogram holds:

$$\gamma(h) = \mathrm{Cov}(0) - \mathrm{Cov}(h) \; . \tag{C.4}$$

This equation shows that variogram and covariance contain the same information. When the stochastic process Z is stationary two important properties for the covariance function hold: the sill $\mathrm{Cov}(0)$ is finite and $\mathrm{Cov}(h)$ vanishes when h exceeds a value r called

range. Another important feature occuring in some empirical covariograms is the nugget effect N. It leads to a discontinuity in the covariance function at $h = 0$ (s. Fig. C.1). At $h = 0$ the point x_0 under investigation coincides precisely with one observed location x_i. Of cource, the best estimate for $Z(x_0)$ is $Z(x_i)$, since in this case both variables are perfectly correlated. But if the two points are not the same, i.e. are seperated only a bit, natural fluctuation of the observed process and measurement errors will reduce the correlation. The covariance drops immediately for $h > 0$ by the amount N yielding a singularity. The difference $Cov(0) - N$ is the amount of explained variance, N itself is uncertainty.

The selection of a semivariogram (or covariance function) narrows the variety of possible random functions Z. Up to now the measurements have only been used to erstimate a covariance function but not to further assess a particular random function Z. It might be compliant with the stationary (or intrinsic) model but not describing the measurements very well. This is where kriging comes into play. Oridinary kriging (OK) is a comparatively simple method which is well suited to explain the basic principles of kriging. In OK an unobserved variable at location x_0 is estimated by a linear combination of the observed random variables $Z(x_i)$ with different weights:

$$Z^*(x_0) = \sum_{i=1}^{n} \lambda_i Z(x_i) \tag{C.5}$$

The Kriging weights λ_i of this linear estimator are dependent on the distance between the observed locations x_i and the location x_0. The objective is to find the kriging weights for each particular location x_0 given the measurements. For the estimator to be unbiased the kriging weights have to fulfill a condition:

$$\langle Z(x_0) - Z^*(x_0) \rangle \overset{!}{=} 0 \quad \Rightarrow \quad \sum_{i=1}^{n} \lambda_i = 1 \tag{C.6}$$

A further constraint imposed on the estimator is that it must minimize the error variance:

$$\sigma_E^2 = \langle (Z(x_0) - Z^*(x_0))^2 \rangle \overset{!}{\to} \min . \tag{C.7}$$

This condition selects a unique solution from the ensemble of possible random functions. In this case the optimisation under side conditions can be best performed analytically by introducing a Euler-Lagrange multiplier μ. To yield the Lagrangian L of the problem the objective function σ_E^2 to be minimized is to be incremented appropriately with zero:

$$L(\lambda_1, \ldots, \lambda_n, \mu) = \sigma_E^2 + 2\mu \left(\sum_{i=1}^{n} \lambda_i - 1 \right) . \tag{C.8}$$

The extrema of L are found by setting the n first order partial derivatives $\partial L / \partial \lambda_i$ to zero. A linear equation system with $n+1$ unknowns is yielded represented best in matrix notation. The resulting kriging system reads:

$$\widehat{C}\vec{\lambda} + \vec{\mu} = \vec{c}_0 \quad \wedge \quad \sum_{i=1}^{n} \lambda_i = 1 . \tag{C.9}$$

The two-point covariance values $C(x_i, x_j) = C_{i,j}$ form the $n \times n$ covariance matrix $\hat{C}$:

$$
\widehat{C} = \begin{pmatrix}
C_{1,1} & C_{1,2} & \cdots & C_{1,n} \\
C_{2,1} & C_{2,2} & \cdots & C_{2,n} \\
\vdots & \vdots & \ddots & \vdots \\
C_{n,1} & C_{n,2} & \cdots & C_{n,n}
\end{pmatrix} . \tag{C.10}
$$

The matrix is symmetric and constant since according to the hypothesis of stationarity the two-point covariance function is dependent on the distance between the points only, which does not change. The diagonal elements are identical. The covariance vector c_0 depends on the particular location x_0 and comprises the covariances between $Z(x_0)$ and the remaining measurement locations:

$$
\vec{c}_0 = (C(x_0, x_1), \dots, C(x_0, x_n))^T = (C_{0,1}, \dots, C_{0,n})^T . \tag{C.11}
$$

The vector $\vec{\mu}$ consists of n identical coordinate values:

$$
\vec{\mu} = (\mu, \mu, \dots, \mu)^T . \tag{C.12}
$$

To solve the equation system it has to be reorganized. Both kriging conditions are merged in one matrix representation:

$$
\left(\begin{array}{cccc|c}
C_{1,1} & C_{1,2} & \cdots & C_{1,n} & 1 \\
C_{2,1} & C_{2,2} & \cdots & C_{2,n} & 1 \\
\vdots & \vdots & \ddots & \vdots & \vdots \\
C_{n,1} & C_{n,2} & \cdots & C_{n,n} & 1 \\
\hline
1 & 1 & \cdots & 1 & 0
\end{array}\right)
\begin{pmatrix}
\lambda_1 \\ \lambda_2 \\ \vdots \\ \lambda_n \\ \mu
\end{pmatrix}
=
\begin{pmatrix}
C_{0,1} \\ C_{0,2} \\ \vdots \\ C_{0,n} \\ 1
\end{pmatrix} \tag{C.13}
$$

Now the equation system is in the convenient form $\widehat{A} \cdot \vec{x} = \vec{b}$. The vector $\vec{x}$ comprises all unknowns. The symmetric matrix $\widehat{A}$ has full rank so that its inverse $\widehat{A}^{-1}$ does exist. To solve the equation system it has to be multiplied with the inverse from the left: $\vec{x} = \widehat{A}^{-1} \cdot \vec{b}$.

In practice many of the covariances $C_{0,i}$ are nearly zero due to the long distance between the respective locations. To accelerate the matrix inversion and to avoid numerical instabilities only the most important measurements leading to the highest covariance values are taken into account. Therefore the matrix elements have to be sorted and permuted, so that the elements with high influence are concentrated in a upper submatrix. Then only this submatrix is inverted and the corresponding kringing weights are used in the linear estimator.

Another important feature of the OK estimator is its exactitude property: $Z^*(x_i) = Z(x_i)$, for all i. The estimation at an observed location exactly reconstructs the measured value.

C.2. Influence of the Covariance Function

To illuminate the effects of the covariance function on the interpolation by ordinary kriging a simple piecewise linear model has been chosen:

$$\mathrm{Cov}(h) = \begin{cases} C_0 & : \quad h = 0 \\ (C_0 - N)(1 - h/r) & : \quad 0 < h < r \\ 0 & : \quad h > r \end{cases} \tag{C.14}$$

Usually the parameters C_O, N, and r of the theoretical covariogram are derived from the empirical covariance estimate based on measured data. For the current sensitivity analysis it is assumed that the covariance function is given. Range r and nugget effect N are varied and their influence on the kriging results are observed. The results are shown in Figs. C.1 and C.2.

If nothing were known about the spatial structure of the stochastic process the best estimate for $Z(x_0)$ would be the mean m. Ordinary kriging also yields this mean m as best estimate for a given loaction x_0, if influencing points with hard measured data are too far away, i.e. the distance is larger than the range defined by the covariogram. This is for example the case in Fig. C.1, 1b, at $x = 3$. The exactitude property of the kriging system reproduces the measured values correctly. Around these observations the estimations are quickly approaching the mean with increasing distance due to the short range. It looks as if the measurements generated islands in the ocean of mean.

If the nugget effect is increased the uncertainty increases. The information about the spatial structure decreases leading to more dull pictures. The islands tend to the mean but due to the exact reconstruction of the hard data by kriging the measured values begin to hover above the islands (e.g. Fig. C.1, 2b). If the nugget effect is increased further until it reaches the sill, information about the spatial structure drops to zero. The result is a global mean with singularities being the measurements (Fig. C.1, 3b). The same effect can be accomplished by setting the range to a very small value (Fig. C.1, 4b). This destroys any spatial structure.

It can be concluded that reasonable interpolation (which is not the trivial mean) is only yielded, if the range is much larger than the typical mutual distance between the observed locations. Only in this case the islands are merged leading to a relatively smooth surface (examples in Fig. C.2).
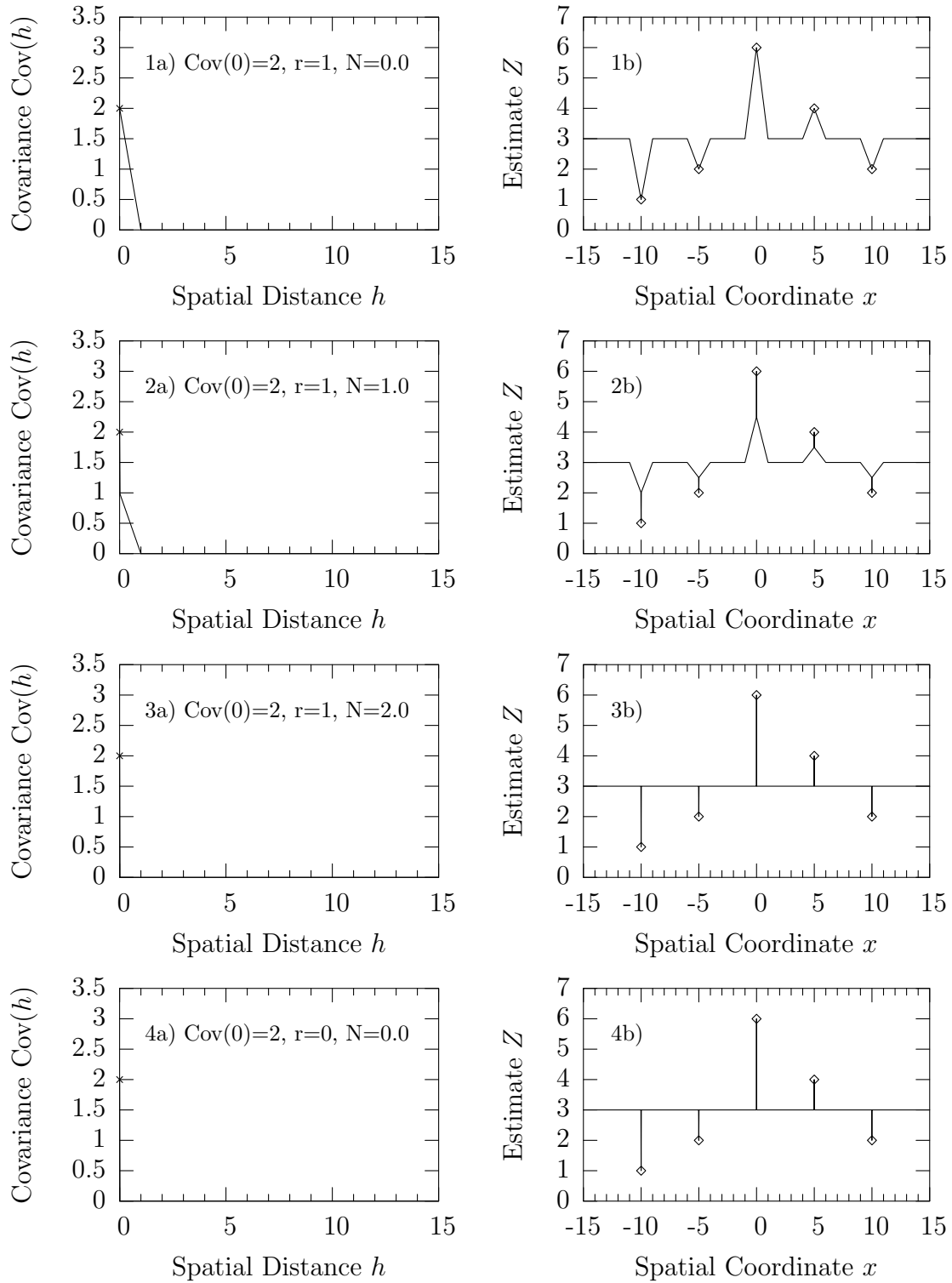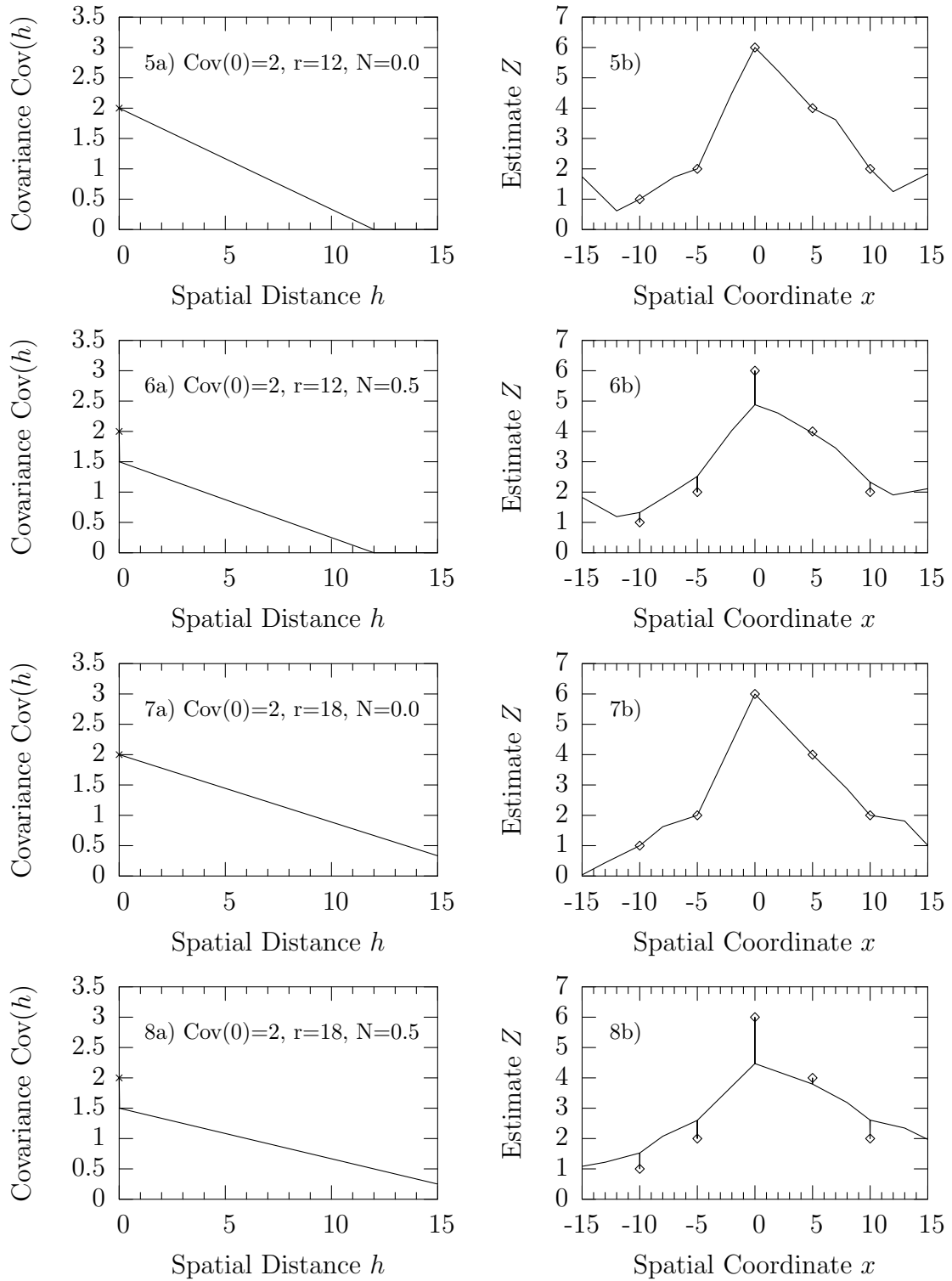
Figure C.1.: Different covariograms (left) and resulting interpolation by ordinary kriging (right). Cov(0): sill; r: range; N: nugget effect. Measured data indicated by open diamonds.

Figure C.2.: Different covariograms (left) and resulting interpolation by ordinary kriging (right). Cov(0): sill; r: range; N: nugget effect. Measured data indicated by open diamonds.

C.3. Influence on Kriging Systems with Prior Information

More sophisticated kriging schemes exist which allow to consider additional prior information in the estimation of the stochastic process. Among these are cokriging, external-drift-kriging (*Kitanidis*, 1997), and Markov-Bayes-updating (*Journel and Zhu*, 1990). The prior information or soft data must be available at both the sampled and unsampled locations. In Bayes-Markov-updating the soft data is classified. The class boundaries have to be chosen carefully so that enough observations lie in each class. On this basis a local prior cumulative distribution function (cdf) is determined for each class. Say the unobserved location x_0 lies within class A. Then the information about class A in form of its local prior cdf is used for a first guess of the random function Z at x_0. This map of prior estimation has to be corrected further by means of the measurements. The consideration of neighbouring information (similar to ordinary kriging) is called updating.

But soft data cannot compensate insufficient spatial connection due to too long distances between sampled locations with hard data. This is true for all kriging methods exploiting additional information. In such a case the updating by neighbouring information, — similar to the procedure in ordinary kriging —, is too weak to correct the prior estimation significantly and the prior information wins the battle. Therefore the estimation mainly will look like the soft information fed into the interpolation scheme if the observations are too sparse. This unsatisfying situation of the kriging results being heavily dependent on soft data rather than on hard measurements can only be overcome by a condensed sampling grid.

List of Symbols

Calligraphic Symbols

Symbol	Description	Unit	Equation
$\mathcal{F}$	Fourier transformation		3.4
$\mathcal{N}$	Gaussian distribution		

Latin Symbols

Symbol	Description	Unit	Equation
$A(t)$	Sine-wave		3.17
A_0	Amplitude of sine-wave		3.17
A_H	Amplitude of harmonic distortion (spur)		3.22
C'	Capacitance per unit length	F/m	2.19
C	Capacitance	F	3.68
C'_0	Parameter of C'-G'-relationship	F/m	2.68
C'_1, C'_2	Parameters of capacitance model	F/m	2.26
C'_d	Parameter of C'-G'-relationship	F/m	2.68
C_{os}	Noise reduction by oversampling	dB	3.19
D	Soil water diffusivity	m^2/s	4.22
D_0	Initial diffusivity	m^2/s	4.31
$\vec{E}$	electric field	V/m	2.1
$\vec{F}$	electrostatic force between two point charges	N	2.1
G'	Conductance per unit length	S/m	2.19
$G(\omega)$	Fourier transform of g		3.4
G'_{sat}	Maximum observed effective conductance	S/m	2.68
I	Current	A	
$I(x,t)$	Current wave	A	2.16
J	Error functional between measured and simulated voltage wave	V^2/s	2.21
K	Reduced hydraulic conductivity	m/s	4.26

K_1, K_2, K_3	Parameters of the hydraulic conductivity model used by SA	m/s	4.32
K_s	Reduced saturated hydraulic conductivity	m/s	4.34
L	Length of observed soil column	m	4.5
L'	Inductance per unit length	H/m	2.19
N	Width of DDS phase accumulator	bit	3.77
N_q^2	Noise power	V^2	3.73
P	Soil porosity	m^3/m^3	
$P(\omega)$	Power spectral density	dB	3.6
P_J	Phase noise power	dB	3.26
Q	Charge	C (= As)	2.1
Q	Reduced surface flux	m/s	4.29
R	Resistance	Ω	3.68
R	Taylor rest in Taylor series		4.13
R'	Resistance per unit length	Ω/m	2.15
S	Source or sink of water	%vol/s	4.20
S^2	Signal power	V^2	3.74
T_{clk}	Period of sampling clock	s	3.33
T_{coax}	Pulse travel-time along coax cable	s	3.55
T_{probe}	Pulse travel-time along probe	s	3.55
T_{ring}	Approximate duration of ringing	s	3.55
T_{offset}	Time needed in equivalent-time sampling to record a complete TDR signal period	s	3.50
T_s	Sampling interval	s	3.15
$T_s^{(r)}$	Theoretical real-time sampling interval	s	3.53
T_{RAM}	Signal length stored in OBSERVER's RAM	s	3.62
T_{step}	Period of TDR step pulse	s	2.10
V	Volume	m^3	
V	Voltage	V	
$V(x,t)$	Voltage wave	V	2.19
V_i^m	Incident voltage wave, measured	V	
V_{in}	Input voltage of delta modulator	V	3.32
V_r^m	Reflected voltage wave, measured	V	2.21
V_r^s	Reflected voltage wave, simulated	V	2.21
V_{rec}	Signal reconstructed from delta modulation code	V	
V_{out}	Output voltage of delta modulator	V	3.35
V_S	Volume of dry soil sample	m^3	
V_T	Total volume of wet soil sample	m^3	2.72
V_W	Volume of water in soil sample	m^3	2.72
w	Cumulative water content in reduced form	1	4.52

Z	Probe impedance	Ω/m	2.28
Z_0	Impedance of probe connecting cable	Ω/m	2.29
a	Spacing of outer rods of a rod probe	m	
a_i	DDS ROM address of the i-th step i		3.77
c_0	$= 2.997 \cdot 10^8$, speed of light	m/s	
d	Thickness of probe rod coating	m	
$e(t)$	Error of delta modulator prediction		3.29
$\vec{e_r}$	Unit vector colinear with $\vec{r}$	1	
f	Frequency	1/s	
f_0	Fundamental frequency of a periodic function	1/s	3.17
f_{DDS}	DDS output frequency	1/s	3.79
f_b	Signal bandwidth	1/s	3.45
f_c	Bandwidth of codec message band	1/s	3.43
f_{clk}	Sample clock frequency	1/s	3.33
f_{max}	Highest frequency of a band limited signal	1/s	2.20, 3.16
f_{offset}	Frequency offset between excitation and clock pulse generator	1/s	3.48
f_r	Relaxation frequency of water	1/s	
f_s	Sampling frequency	1/s	3.15
f_{step}	Repetition rate of step (excitation) pulse train	1/s	3.48
f_ν	Nyquist frequency	1/s	3.16
$g(t)$	Time-dependent function to be sampled		3.9
$g_1(t_n)$	Average of g around t_n		3.9
$g_2(t)$	Discrete sample of g_1		3.12
$h(t)$	Impulse response function		3.11
j_w	Water flux across soil surface	m/s, m^3/s	4.8
j_w'	Water flux across soil surface	%vol/s	4.9
k	Soil hydraulic conductivity	m/s	4.15
l	Physical rod length	m	
l'	Electric rod length	m	2.13
l_{coax}	length of coaxial connecting cable	m	2.11
m	Mass	kg	
m	RAM size	bit	3.62
m_{W}	Mass of water	kg	2.70
m_{S}	Mass of dry soil	kg	2.70
n_{DDS}	Number of samples per DDS output signal period	1	3.78
n_b	Number of bits for amplitude quantization	1	3.21

n_p	Number of sampled signal periods	1	3.21
n_p	Value of DDS phase register (phase offset)	1	3.87
n_s	Number of samples per signal period	1	
n_Φ	DDS ROM address increment		3.77
$p(t)$	Sample pulse train of delta modulation		3.29
q	Charge	C (= As)	2.1
$q(t)$	Differential pulse code		3.29
q_{ss}	Steady-state Darcy flux	m/s	4.74
$\vec{q}$	Darcy flux density	m/s	4.15
r	Distance between two point charges	m	2.1
s	Dilation factor in equivalent-time sampling		3.52
t	Time	s	
t_0	Instant of reflection at transition from coaxial cable to probe head	s	2.12
t_1	Instant of reflection at probe end	s	2.12
t_a	Two way pulse travel-time along the probe part in air	s	2.40
t_c	Integrator's time constant	s	3.35
t_d	Time (phase) shift between two DDS output sine waves of same frequency	s	3.87
t_h	Two way pulse travel-time in probe head	s	2.12
t_m	Two way pulse travel-time through material, w/o probe head	s	2.12
t_{meas}	Measurement time	s	3.49
t_n	Discrete sampling instant	s	3.13
t_r	Pulse rise-time	s	3.83
$t_r^{(d)}$	Pulse rise-time given in data sheet	s	3.82
$t_r^{(m)}$	Measured pulse rise-time	s	3.84
t_t	Total two way pulse travel-time	s	2.12
t_w	Two way pulse travel-time along the probe part in water	s	2.41
t_x	Instant of reflection at air/water interface	s	
v	Velocity	m/s	
v_a	Pulse propagation velocity along probe in air	m/s	2.31
v_{coax}	velocity in coaxial connecting cable	m/s	2.11
v_p	Pore velocity	m/s	
v_w	Pulse propagation velocity along probe in water	m/s	2.31
w	Gravimetric water content	kg/kg	2.70, 4.7
w	Cumulative water content within a soil column	m	4.52

x	Dimensionless space variable	1	4.39
$x(t)$	Input function of delta modulation		3.29
$y(t)$	Output function of delta modulation		3.29

Greek Symbols

Symbol	Description	Unit	Equation
Δx	Length increment (m)		
Δf	Error of f		
Δf_{DDS}	Frequency resolution of DDS	1/s	3.80
ΔV_D	Differential input voltage of D-FF		3.31
ΔV_{in}	Differential input voltage		3.32
ΔV_q	Output state of delta modulator		3.30
ΔV_Q	Differential output voltage of D-FF		3.34
$|\Delta V_Q|$	Constant differential ECL voltage		3.36
Θ	Reduced volumetric water content	1	4.24
Φ	Total soil water potential	m	4.16
Φ	Parametric function for the analytical solution of Richards' equation	1	4.45
Ψ	Soil suction head	m	4.16
α	Anisotropy factor	1	2.6
β	Parameter of the hydraulic conductivity model used by BW	1	4.35
γ	Granularity of amplitude quantization with Delta Modulators	V	3.38
δ	Angle between real and imaginary part of ϵ	1	2.5
$\delta(t)$	Dirac's delta distribution		3.12
ϵ	Relative dielectric permittivity	1	2.4
ϵ'	Real part of relative dielectric permittivity	1	2.4
ϵ''	Imaginary part of relative dielectric permittivity	1	2.4
ϵ_0	$= 8.854{\cdot}10^{12}$, absolute dielectric permittivity of vacuum	As/Vm	2.4
ϵ_a	Apparent dielectric permittivity from tangent line method	1	2.9
ϵ_a	$= 1$, relative dielectric permittivity of air	1	2.31
ϵ_{J}	Stochastic process describing jitter		3.25
ϵ_m	Relative dielectric permittivity of a material mixture	1	2.6

ϵ_w	Relative dielectric permittivity of water	1	2.31
θ	Volumetric water content	%vol $(=\text{m}^3/\text{m}^3)$	4.20
θ_i	Initial volumetric water content	%vol	4.24
θ_s	Saturated volumetric water content	%vol	4.24
$\overline{\theta}$	Spatial average of volumetric water content	%vol	4.5
$\overline{\theta}_i$	Initial average water content	%vol	4.10
$\overline{\theta}_{ss}$	Steady state average water content	%vol	
λ	Wave length	m	
$\lambda_{\min}$	Minimum wavelength of a band limited signal	m	2.20
μ	Relative magnetic susceptibility	1	2.23
μ_0	$= 4\pi \cdot 10^{-7}$, absolute magnetic susceptibility of vacuum	Vs/Am	2.23
ν	Parameter of the diffusivity model	1	4.31
ξ	Parameter of the analytical solution of Reichards' equation	1	4.41
ρ	reflection coefficient	1	2.29
ρ_{T}	bulk density of dry soil	kg/m^3	2.72
ρ_{W}	mass density of water	kg/m^3	2.72
σ	Ionic conductivity	S	2.4
σ_{J}	Standard deviation of process ϵ_{J}	$[\epsilon_{\text{J}}]$	3.26
τ	Dimensionless time variable	1	4.40
ϕ	Parametric function for the analytical solution of Richards' equation	1	4.44
ω	Angular frequency	rad/s	
ω_r	Relaxation frequency of water	rad/s	2.4
ω_s	Sampling frequency	rad/s	3.15

Abbreviations

rms	Root mean square
ADC	Analog-to-digital converter
D-FF	D-flip-flop
DAC	Digital-to-analog conerter
DM	Delta modulation, delta modulator
DDS	Direct Digital Synthesis
ECL	Emitter coupled logic
SFDR	Spurious-free dynamic range
SMG	Soil Moisture Group, a research group at the Univ. of Karlsruhe

SNR	Signal-to-noise ratio
SNQR	Signal-power-to-quantisation-noise ratio
THD	Total harmonic distortion
TDR	Time domain reflectometer, time domain reflectometry

Bibliography

Aeroflex/Metelics, Company website, http://www.metelics.com/, 2004.

Agilent, Understanding oscilloscope frequency response and its effect on rise-time accuracy, App. note 1420, http://www.agilent.com/, 2002.

Akers, N. P., and V. Vilar, RF sampling gates: a brief review, in *IEE Proc., part A*, vol. 133, pp. 45–49, 1986.

Analog Devices, AD9835 CMOS complete DDS, rev. 0, Data sheet, http://www.analog.com/UploadedFiles/Data_Sheets/7569011AD9835_0.pdf, 1998.

Analog Devices, AD9832 CMOS complete DDS, rev. A, Data sheet, http://www.analog.com/UploadedFiles/Data_Sheets/25499753AD9832_a.pdf, 1999a.

Analog Devices, A technical tutorial on digital signal synthesis, rev. 12, http://www.analog.com/UploadedFiles/Tutorials/450968421DDS_Tutorial_rev12-2-99.pdf, 1999b.

Analog Devices, Company website, http://www.analog.com/, 2004.

Arcom, Company website, http://www.arcom.com/, 2004.

Baker, J. M., and R. J. Lascano, The spatial sensitivity of time-domain reflectometry, *Soil Sci.*, *147*, 378–384, 1989.

Bárdossy, A., and W. Lehmann, Spatial distribution of soil moisture in a small catchment, part 1: Geostatistical analysis, *J. Hydrol.*, *206*, 1–15, 1998.

Bear, J., *Dynamics of fluids in porous media*, Elsevier, 1972.

Becker, R., Development of a flood warning method for small and middle sized catchments based on distributed online soil moisture measurements, internet map server, http://hydro.iwk.uni-karlsruhe.de/map-sulm/, 2004.

Becker, R., A. Brandelik, C. Hübner, W. Schädel, A. Scheumann, and S. Schlaeger, Soil and snow moisture measurement system with subsurface transmission lines for remote sensing and environmental applications: Results of the Soil Moisture Group of the University of Karlsruhe, in *Proceedings of the Open Symposium on Propagation and Remote Sensing*, URSI-Commission-F, 2002.

Bibliography

Beven, K. J., and M. J. Kirkby, A physically based, variable contributing area model for basin hydrology, *Hydrol. Sci. Bull.*, *24*, 43–69, 1979.

Blöschl, G., *Scale and scaling in hydrology*, vol. 132, Wiener Mitteilungen — Wasser, Abwasser, Gewässer ed., Institut für Hydraulik, Gewässerkunde und Wasserwirtschaft, Technische Universität Wien, 1996.

Bracewell, R. D., *The Fourier transform and its application*, 3rd ed., McGraw-Hill, 2000.

Broadbridge, P., and I. White, Constant rate rainfall infiltration: A versatile nonlinear model, 1, Analytic solution, *Water Resour. Res.*, *24*, 145–154, 1988.

Charlesworth, P., Soil water monitoring, *Irrigation Insights, 1*, Land & Water Australia, Canberra. http://www.lwa.gov.au/downloads/PR000236.pdf, 2000.

Computer Simulation Technology, Microwave Studio, http://www.cst.com/, 2004.

de Jager, F., Delta modulation: a new method of p.c.m. transmission using the 1 unit code, *Philips Research Report*, *8*, 442–446, 1952.

DIN 19683, Bestimmung der Saugspannung des Bodenwassers, in *Deutsche Normblätter*, Beuth-Vertrieb GmbH, Berlin und Köln, 1973.

Dooge, J. C. I., Looking for hydrologic laws, *Water Resour. Res.*, *22*, 46–58, 1986.

dos Santos, L. A., Développement d'une nouvelle méthode de détermination des profils de teneur en eau dans les sols par inversion d'un signal TDR, Ph.D. thesis, Laboratoire d'Etude des Transferts en Hydrologie et Environnement, Université Joseph Fourier - Grenoble I, France, 1997.

Ehret, U., Rainfall and flood nowcasting in small catchments using weather radar, Ph.D. thesis, Institut für Wasserbau, Universität Stuttgart, 2003.

Entekhabi, D., The hydrospere state mission: An overview, in *Geoscience and Remote Sensing Symposium, 2003. IGRASS '03*, vol. 3, IEEE International, 2003.

Entekhabi, D., et al., An agenda for land surface hydrology research and a call for the second international hydrological decade, *Bull. Amer. Meteor. Soc.*, *80*, 2043–2058, 1999.

Feng, W., C. P. Lin, R. J. Deschamps, and V. P. Drnevich, Theoretical model of a multisection time domain reflectometry measurement system, *Water Resour. Res.*, *35*, 2321–2331, 1999.

Ferré, P. A., D. L. Rudolph, and R. G. Kachanoski, Spatial average of water content by time domain reflectometry: Implications for twin rod probes with and without dielectric coatings, *Water Resour. Res.*, *32*, 271–279, 1996.

222

Fletcher, R., and C. M. Reeves, Function minimization by conjugate gradients, *The Computer Journal*, *7*, 149–154, 1964.

Fujita, H., The exact pattern of a concentration dependent diffusion in a semi-finite media, Part i, *Textile Res. J.*, *22*, 757–760, 1952.

Gans, W. L., The measurement and deconvolution of time jitter in equivalent-time waveform samplers, *IEEE Trans. Instr. Meas.*, *IM-32*, 126–133, 1983.

Gerding, M., T. Musch, and B. Schiek, Precision level measurement based on time-domain reflectometry (TDR) measurements, *Advances in Radio Science*, *1*, 27–31, 2003.

Gray, R. M., and D. L. Neuhoff, Quantization, *IEEE Trans. Inform. Theory*, *44*, 1–63, 1998.

Grayson, R. B., A. W. Western, F. H. S. Chiew, and G. Blöschl, Preferred states in spatial soil moisture patterns: local and non-local controls, *Water Resour. Res.*, *33*, 2897–2908, 1997.

Greffe, J. L., and C. Grosse, *Progress in electromagnetic research*, vol. 6, chap. 2: Dielectric properties of heterogeneous materials, pp. 44–100, Elsevier, New York, 1992.

Hakansson, G., Reconstruction of soil moisture profiles, Master's thesis, Royal Institute of Technology, Department of Electromagnetic Theory, Stockholm, Sweden, 1997.

Hasted, J. B., *Aqueous dielectrics*, Chapman and Hall, London, 1973.

Hawksford, M. O. J., and T. Darling, Oversampled analog-to-digital conversion for digital audio systems, *J. Audio Eng. Soc.*, *38*, 924–943, 1990.

He, S., V. G. Romanov, and S. Ström, Analysis of green's function approach to one-dimensional inverse problems. ii. simultaneous reconstruction of two parameters, *Journal of Mathematical Physics*, *35*, 2315–2335, 1994.

Heimovaara, T. J., Frequency domain analysis of time domain reflectometry waveforms: 1. measurement of the complex dielectric permittivity of soils, *Water Resour. Res.*, *30*, 189–199, 1994.

Heimovaara, T. J., and W. Bouten, A computer-controlled 36-channel time domain reflectometry system for monitoring soil water contents, *Water Resour. Res.*, *26*, 2311–2316, 1990.

Heimovaara, T. J., J. A. Huisman, J. A. Vrugt, and W. Bouten, Obtaining the spatial distribution of water content along a TDR probe using the SCEM-UA Bayesian inverse modeling scheme, *Vadose Zone J.*, *3*, 1128–1145, 2004.

Bibliography

Herkelrath, W. N., S. P. Hamburg, and F. Murphy, Automatic, real-time monitoring of soil moisture in a remote field area with time domain reflectometry, *Water Resour. Res.*, *27*, 857–864, 1991.

Hewlett-Packard, Pulse and waveform generation with step recovery diodes, HP Application Note 918, Hewlett-Packard, Palo Alto, CA, 1984.

Hilhorst, M. A., Dielectric characterisation of soil, Ph.D. thesis, Wageningen Agricultural University, Wageningen, The Netherlands, 1998.

Hook, W. R., N. J. L. Z. J. Sun, and P. B. Hook, Remote diode shorting improves measurement of soil water by time domain reflectometry, *Soil Sci. Soc. Am. J.*, *56*, 1384–1391, 1992.

HTH, Scaleable node address protocol, http://www.hth.com/snap/, 2004.

Hubaux, J. P., T. Gross, J. Y. L. Boudec, and M. Vetterli, Towards self-organized mobile ad hoc networks: the Terminodes project, *IEEE Communications Magazine*, *1*, 118–124, 2001.

Hübner, C., Entwicklung hochfrequenter Messverfahren zur Boden- und Schneefeuchtebestimmung, Wissenschaftliche Berichte, FZKA 6329, Forschungszentrum Karlsruhe, 1999.

Hübner, C., S. Schlaeger, R. Becker, A. Scheuermann, A. Brandelik, W. Schaedel, and R. Schuhmann, *Electromagnetic Aquametry*, chap. 14: Advanced measurement methods in time domain reflectometry for soil moisture determination, Springer, Berlin, Heidelberg, New York, 2004.

Huisman, J. A., S. S. Hubbard, J. D. Redman, and A. P. Annan, Measuring soil water content with ground penetrating radar: A review, *Vadose Zone J.*, *2*, 476–391, 2003a.

Huisman, J. A., J. J. J. C. Snepvangers, W. Bouten, and G. B. M. Heuvelink, Monitoring temporal development of spatial soil water content variation: comparison of ground penetrating radar and tiem domain reflectometry, *Vadose Zone J.*, *2*, 519–529, 2003b.

Jackson, J. D., *Classical Electrodynamics*, 2nd ed., Wiley, 1975.

Jackson, T. J., D. M. Le Vine, A. Y. Hsu, A. Oldak, P. J. Starks, C. T. Swift, J. D. Isham, and M. Haken, Soil moisture mapping at regional scales using microwave radiometry: The southern great plains hydrology experiment, *IEEE Transactions of Geoscience and Remote Sensing*, *37*, 2136–2151, 1999.

Jähne, B., *Digital image processing*, 5th ed., Springer, 2002.

Journel, A. G., and H. Zhu, *Integrating soft seismic data: Markov-Bayes updating, an alternative to cokriging and traditional regression*, Stanford Center for Reservoir Forecasting, 1990.

Kaatze, U., Microwave dielectric properties of water, in *Microwave Aquametry, Electromagnetic Wave Interaction with Water-Containing Materials*, edited by A. Kraszewski, TAB-IEEE Press Book Series, pp. 37–53, IEEE Press, New York, 1996.

Kirkby, D. R., A picosecond optoelectronics cross correlator using a gain modulated avalanche photodiode for measuring the impulse response of tissue, Ph.D. thesis, Department of Medical Physics and Bioengineering, University College London, 1999.

Kitanidis, P. K., *Introduction to Geostatistics : Applications in Hydrogeology*, Cambrigde University Press, 1997.

Knight, J. H., Sensitivity of time domain reflectometry measurements to lateral variations in soil water content, *Water Resour. Res.*, *28*, 2345–2352, 1992.

Kobayashi, H., M. Morimura, K. Kobayashi, and Y. Onaya, Aperture jitter effects in wideband ADC systems, in *13th Annual Conference of the Society of Instrument and Control Engineers on Japan (SICE)*, pp. 1089–1094, IEEE Press, 1999.

Kutílek, M., and D. R. Nielsen, *Soil Hydrology*, Geoecology textbook, Catena Verlag, Cremlingen-Destedt, 1994.

Laug, O. B., T. M. Souders, and D. R. Flach, A custom integrated circuit comparator for high-performance sampling applications, *IEEE Trans. Instr. Meas.*, *41*, 850–855, 1992.

Le Vine, D. M., A. J. Griffis, C. T. Swift, and T. J. Jackson, Estar a synthetic aperture microwave radiometer for remote sensing applications, *Proceedings of the IEEE*, *82*, 1787–1801, 1994.

Lehmann, W., Anwendung geostatistischer Verfahren auf die Bodenfeuchte in ländlichen Einzugsgebieten, Ph.D. thesis, Institute of Hydrology and Water Resources Management, University of Karlsruhe, Germany, 1995.

Leviatan, L., and A. T. Adams, The response of a two-wire transmission-line to incident field and voltage excitation, including the effects of higher order modes, *IEEE Trans. Antennas and Prop.*, *AP-30*, 998–1003, 1982.

Lundstedt, J., Inverse problems to nonuniform transmission-lines, Ph.D. thesis, Royal Institute of Technology, Department of Electromagnetic Theory, Stockholm, Sweden, 1995.

Malicki, M. A., and W. W. Skierucha, A manually controlled tdr soil moisture meter operating with 300 ps rise-time needle pulse, *Irrigation Science*, *10*, 153–163, 1989.

Maxim, Application note 729: Dynamic testing of high-speed ADCs, part 2, http://www.maxim-ic.com/appnotes.cfm/appnote_number/729, 2001.

Bibliography

Maxim, DS18B20 programmable resolution 1-wire digital thermometer, data sheet, http://pdfserv.maxim-ic.com/en/ds/DS18B20.pdf, 2002a.

Maxim, Application note 162: Interfacing the DS18x20/DS1822 1-wire temperature sensor in a microcontroller environment, http://pdfserv.maxim-ic.com/en/an/app162.pdf, 2002b.

McCabe, S. P., A sampling voltage tracker for analyzing high speed waveforms, Master's thesis, Univ. of California, Los Angeles, 1975.

McGlynn, B. L., J. J. McDonnel, and D. D. Brammer, A review of the evolving perceptual models of hillslope flowpaths at the Maimai catchment, new zealand, *J. Hydrol.*, *257*, 1–25, 2002.

Merz, B., and E. Plate, An analysis of the effects of spatial variability of soil and soil moisture on runoff, *Water Resour. Res.*, *33*, 2909–2921, 1997.

Microirrigation Forum, Soil moisture sensors, http://www.microirrigationforum.com/new/sensors/, 2004.

Monett, M., ADD Automation, company website, http://www3.sympatico.ca/add.automation/, 2004.

Mulvey, J., Sampling oscilloscope circuits, *Tech. rep.*, Tektronix, Beaverton, 1970.

NASA, HYDROS science objectives, http://hydros.gsfc.nasa.gov/sci.php, 2004.

Nichol, C., R. Beckie, and L. Smith, Evaluation of uncoated and coated time domain reflectometry probes for high electrical conductivity systems, *Soil Sci. Soc. Am. J.*, *66*, 1454–1465, 2002.

Nissen, H. H., P. A. Ferré, and P. Moldrup, Time domain reflectometry developments in soil science: I. unbalanced two-rod probe spatial sensitivity and sampling volume, *Soil Sci.*, *168*, 77–83, 2003.

ON Semiconductor, MECL system design handbook (HB205/D), http://www.onsemi.com/pub/Collateral/HB205-D.PDF, 1988.

ON Semiconductor, MC10EP16, MC100EP16 3.3V/5V ECL differential receiver/driver, data sheet, rev. 3, http://www.onsemi.com/pub/Collateral/MC10EP16-D.PDF, 2001a.

ON Semiconductor, MC10EP52, MC100EP52 3.3V/5V ECL differential data and clock flip-flop, data sheet, rev. 2, http://www.onsemi.com/pub/Collateral/MC10EP52-D.PDF, 2001b.

Oswald, B., Full wave solution of inverse electromagnetic problems, Ph.D. thesis, Swiss Federal Institute of Technology, Zürich, Switzerland, 2000.

Panchard, J., COMMON-Sense net: water management for agriculture in semi-arid areas by means of wireless sensor networks, project proposal, http://www.icawww.epfl.ch/panchard/, 2003.

Parkin, G. W., D. E. Elrick, and R. G. Kachanoski, Cumulative storage of water under constant flux infiltration: Analytical solution, *Water Resour. Res.*, *28*, 2811–2818, 1992.

Parkin, G. W., R. G. Kachanoski, and D. E. Elrick, Unsaturated hydraulic conductivity measured by time domain reflectometry under a rainfall simulator, *Water Resour. Res.*, *31*, 447–454, 1995.

Peschke, G., C. Etzenberg, and G. Müller, Experimental analysis of different runoff generation mechanisms, in *Proc. of the ERB-Conf. on Catchment Hydrol. and Biochem. Processes in Changing Environment*, edited by J. Bucek, pp. 109–112, Liblice, 1998.

Pohlmann, K. C., *Principles of digital audio*, 4 ed., McGraw-Hill, New York, 2000.

Robinson, D. A., S. B. Jones, J. M. Wraith, D. Or, and S. P. Friedman, A review od advances in dielectric and electrical conductivity measurement in sois using time domain reflectometry, *Vadose Zone J.*, *2*, 444–475, 2003a.

Robinson, D. A., M. Schaap, S. B. Jones, S. P. Friedman, and C. M. K. Gardner, Considerations for improving the accuracy of permittivity measurements using time domain reflectometry; air-water calibration, effect of cable length, *Soil Sci. Soc. Am. J.*, *67*, 62–70, 2003b.

Rogers, C., M. P. Stallybrass, and D. L. Clements, On two phase filtration under gravity and with boundary infiltration: Application of a Bäcklund transformation, *Nonlinear Anal. Theory Methods Appl.*, *7*, 785–799, 1983.

Roth, K., Lecture notes in soil physics, version 3.2, http://www.iup.uni-heidelberg.de/institut/forschung/groups/ts/students /lecture_notes/sp3.html, 1996.

Roth, K., R. Schulin, H. Flühler, and W. Attinger, Calibration of time domain reflectometry for water content measurement using a composite dielectric approach, *wrr*, *26*, 2267–2273, 1990.

Sander, G. C., J.-Y. Parlange, V. Kühnel, W. L. Hogarth, D. Lockington, and J. P. J. O'Kane, Exact nonlinear solution for constant flux infiltration, *J. Hydrol.*, *97*, 341–346, 1988a.

Sander, G. C., J.-Y. Parlange, V. Kühnel, W. L. Hogarth, and J. P. J. O'Kane, Comment on "Constant rate rainfall infiltration: A versatile nonlinear model, 1, Analytic solution" by P. Broadbridge and I. White, *Water Resour. Res.*, *24*, 2107–2108, 1988b.

Bibliography

Schaap, M. G., D. A. Robinson, S. P. Friedman, and A. Lazar, Measurement and modeling of tdr signal propagation through layered dielectric media, *Soil Sci. Soc. Am. J.*, *67*, 1113–1121, 2003.

Schädel, W., Grundlagen zur Erstellung eines Hochwasserwarnsystems auf Basis von verteilten Online-Bodenfeuchtemessungen, Ph.D. thesis, Institute of Water Resources Management, Hydraulic and Rural Engineering, University of Karlsruhe, Germany (in progress), 2005.

Scheider, K. J., *Bautabellen*, 10 ed., Werner-Verlag, 1992.

Scheuermann, A., S. Schlaeger, C. Hübner, A. Brandelik, and J. Brauns, Monitoring of the spatial soil water distribution on a full-scale dike model, in *Proceeding of the Fourth International Conference on Electromagnetic Wave Interaction with Water and Moist Substances*, edited by K. Kupfer, pp. 343–350, Weimar, 2001.

Scheuermann, A., S. Schlaeger, J. Brauns, C. Huebner, and A. Brandelik, Bestimmung von Feuchteprofilen mittels TDR während eines Einstauversuches an einem naturgemässen Deichmodell, *Technisches Messen*, *69*, 37–42, 2002.

Schlaeger, S., Inversion von TDR-Messungen zur Rekonstruktion räumlich verteilter bodenphysikalischer Parameter, Ph.D. thesis, Institut für Bodenmechanik und Felsmechanik, Universität Karlsruhe, 2002.

Schlaeger, S., A fast TDR-inversion technique for the reconstruction of spatial soil moisture content, *Hydrol. Earth Sys. Sci. Discuss.*, *2*, 971–1009, 2005.

Schmugge, T. J., T. J. Jackson, and H. L. McKim, Survey of methods for soil moisture determination, *Water Resour. Res.*, *16*, 961–979, 1980.

Schuhmann, R., Kontrolle von Barrieren: Bestimmung der hydraulischen Leitfähigkeit anhand des Bodenwassergehalts, Ph.D. thesis, Institute of Water Resources Management, Hydraulic and Rural Engineering, University of Karlsruhe, Germany, 2002.

Si, B., R. G. Kachanoski, F. Zhang, G. W. Parkin, and D. E. Elrick, Measurement of hydraulic properties during constant flux infiltration: Field average, *Soil Sci. Soc. Am. J.*, *63*, 793–799, 1995.

Soil Moisture Group, Website, http://www.smg.uni-karlsruhe.de/, 2004.

Souders, T. M., and P. S. Hetrick, Accurate rf voltage measurements using a sampling voltage tracker, *IEEE Trans. Instr. Meas.*, *38*, 451–456, 1989.

Souders, T. M., K. Schoenwetter, and P. S. Hetrick, Caracterization of a sampling voltage tracker for measuring fast, repetitive signals, *IEEE Trans. Instr. Meas.*, *IM-36*, 956–960, 1987.

228

Souders, T. M., D. R. Flach, C. Hagwood, and G. L. Yang, The effects of timing jitter in sampling systems, *IEEE Trans. Instr. Meas.*, *39*, 80–85, 1990.

SOWACS, Soil water content sensor email discussion group, http://www.sowacs.com/, 2004.

Stacheder, M., C. Hübner, S. Schlaeger, and A. Brandelik, *Electromagnetic Aquametry*, chap. 16: Combined TDR and low frequency permittivity measurements for continuous snow wetness and snow density determination, Springer, Berlin, Heidelberg, New York, 2004.

Steele, R., *Delta Modulation Systems*, Pentech Press, London, 1975.

Steele, R., SNR formula for linear delta modulation with band-limited flat and rc-shaped gaussian signals, *IEEE Trans. Comm.*, *28*, 977–1984, 1980.

Tektronix, *1502C service manual, part no. 071067800 (online available at http://www.tektronix.com/)*, Tektronix Inc., 1999.

Tektronix, Real-time versus equivalent-time sampling, http://www.tek.com/Measurement/App_Notes/RtvET/ap-RtvET.html, 2003.

Todoroff, P., and J. Luk, Calculation of in situ soil water content profiles from tdr signal traces, *Measurement Science & Technology*, *12*, 27–36, 2001.

Topp, G. C., State of the art of measuring soil water content, *Hydrological Processes*, *17*, 2993–2996, 2003.

Topp, G. C., and P. A. Ferre, *Methods of soil analyis, part 4*, vol. 5, chap. Physical methods, pp. 417–545, sssa book series ed., Soil Science Society of America, Madison, WI, 2002.

Topp, G. C., J. L. Davis, and A. P. Annan, Electrodynamic determination of soil water content: measurements in coaxial transmission lines, *Water Resour. Res.*, *16*, 574–582, 1980.

Topp, G. C., J. L. Davis, and A. P. Annan, Electromagnetic determination of soil water content using tdr: I. applications to wetting fronts and steep gradients, *Soil Sci. Soc. Am. J.*, *46*, 672–678, 1982.

Topp, G. C., M. Yanuka, W. D. Zebchuk, and S. J. Zegelin, The determination of electrical conductivity using TDR: Soil and water experiments in coaxial lines, *Water Resour. Res.*, *24*, 945–952, 1988.

Topp, G. C., S. Zegelin, and I. White, Impacts of the real and imaginary components of relative permittivity on time domain reflectometry measurements in soils, *Soil Sci. Soc. Am. J.*, *64*, 1244–1252, 2000.

Bibliography

Tuthill, M., A switched current, switched-capacitor temperature sensor in $0.6 - \mu$m CMOS, *IEEE Journal of Solid-State Cicuits*, *33*, 1117–1122, 1998.

Ulaby, R. K., R. K. Moore, and A. K. Funk, *From theory to applications*, vol. 3 of *Microwave remote sensing*, Artech House, Norwood, MA, 1986.

UMN Mapserver, Homepage of the UMN internet map server, http://mapserver.gis.umn.edu, 2004.

UMTSlink.at, Introduction to UMTS, http://umtslink.at/UMTS-Start.htm, 2004.

Verspecht, J., Compensation of timing jitter-induced distortion of sampled waveforms, *IEEE Trans. Instr. Meas.*, *43*, 726–732, 1994.

Walker, J. P., G. R. Willgoose, and J. D. Kalma, One-dimensional soil moisture profile rertieval by assimilation of near-surface observations: a comparison of algorithms, *Advances in Water Resources*, *24*, 631–650, 2001.

Walker, J. P., J. P. Houser, and G. R. Willgoose, Active microwave remote sensing for soil moisture measurement: a field evaluation using ers-2, *Hydrol. Process., in print*, *18*, 2004.

Watson, K. K., V. A. Sardana, and G. C. Sander, Comparison of analytical and numerical results for constant flux infiltration, *J. Hydrol.*, *165*, 101–112, 1995.

Western, A. W., G. Blöschl, and R. B. Grayson, Towards capturing hydrological significant connectivity in spatial patterns, *Water Resour. Res.*, *37*, 83–97, 2001.

White, I., and S. J. Zeglin, *Handbook of Vadose Zone Characterization and Monitoring*, chap. Electric and dielectric methods for monitoring soil-water content, pp. 343–385, Lewis, Ann Arbor, 1995.

Zegelin, S. J., I. White, and D. R. Jenkins, Improved field probes for soil water content and electrical conductivity measurements using time domain reflectometry, *Water Resour. Res.*, *25*, 2367–2376, 1989.

Zehe, E., and H. Flühler, Slope scale distribution of flow patterns in soil profiles, *J. Hydrol.*, *247*, 116–132, 2001.

Zehe, E., R. Becker, and W. Schädel, May we identify the spatial variability of soil hydraulic properties based on measurements with Spatial TDR? a) model study, in *Geophysical Research Abstracts Vol. 4*, European Geophysical Society XXVII General Assemby, 2002.

Bisher erschienene Mitteilungen aus dem
Institut für Wasserwirtschaft und Kulturtechnik

Bisher erschienene Mitteilungen aus dem Institut für Wasserwirtschaft und Kulturtechnik

Heft 154/1968
Ein Beitrag zur Erforschung von örtlichen Auskolkungen hinter geneigten Befestigungsstrecken in Abhängigkeit der Zeit; E. Mosonyi, B.Schoppmann
Institutsberichte über die Modellversuche seit 1962
Institutsberichte über die Exkursionen des Lehrstuhls für Wasserbau und Wasserwirtschaft seit 1965; E. Mosonyi, B. Schoppmann

Heft 155/1969
Kolkbildung in feinen oder leichten Sohlmaterialien bei strömendem Abfluß; J.W. Dietz

Heft 156/1969
Widerstandskräfte und Energiedissipation bei Verteilerklötzen im Wechselsprung; R. Muser
Schwebstofführung feinsandiger Wasserläufe; St. Bruk

Heft 157/1969 °
Widerstand schräg angeströmter Rechengitter; J. Zimmermann
Untersuchungen zur Durchströmung des Kraghammer Sattels an der Biggetalsperre nach neuentwickelten Methoden der Felshydraulik; W.Wittke, Cl. Louis

Heft 158/1970 °
Hydrodynamik der nichtstationären Dränung; G. Karadi, J. Gyuk, R.A.Williams
An Experimental Study of Thin-Sheet Flow over Inclined Surfaces; O.N Wakhlu
Schiffsträgheitskräfte als Indikator für die Güte von Schleusenfüllsystemen; E. Mosonyi, R. Muser
Schwall- und Sunkerscheinungen aus Schleusenbetrieb in Schiffahrtskanälen; Maßnahmen zur Sicherung des Schiffahrtsbetriebes; R. Muser, G. Meder
Beitrag zur Berechnung von Schleusenfüllungen; H.H. Bernhart
Spitzenmaßstab und L-O-Integrator, ein Gerät zur genauen Messung des Wasserspiegels in Modellversuchen; W. Götz, K. Schwedes
Turbulenzmessungen in Wasser mit Heißfilmanemometer; B. Schoppmann
Messung von Größe und Richtung der mittleren Geschwindigkeit in einem zweidimensionalen Strömungsfeld; K. Schwedes
Parameterfreie statistische Methoden zur Analyse von Datenreihen; H. Eggers
Dreidimensionale, anisotrope Kluftwasserströmung; W. Wittke

Heft 159/1972 °
Ein Verfahren zur Richtungs- und Betragsbestimmung von Vektoren mittlerer Strömungsgeschwindigkeit einer turbulenten Strömung; K.Schwedes, H. Weiher
Hydraulische Stabilität bei Wasserkraftanlagen; H. Berge
Land Reclamation Projects as Essential Elements of Economic Development Programmes; G.E. Papadopoulos
Institutsberichte über Modellversuche u. Forschungsarbeiten seit 1969
Institutsberichte über die Exkursionen des Lehrstuhls für Wasserbau und Wasserwirtschaft seit 1969

Heft 170/1984   *Druckerhöhungenh durch instationäre Vorgänge in Schiffsschleusen mit großen Stufenhöhen; P.M. Schmelzle*

Heft 171/1984   *Beitrag zur Hydromechanik von Schwall- und Sunkwellen; N. Göbel*

Heft 172/1985   *Abschiedskolloquium zu Ehren von Herrn Prof. Dr.-Ing. Dr.rer.techn., Dr.sc.h.c., Dr.-Ing. E.h., Dr.sc.h.c., Dr.sc.h.c. E. Mosonyi*

Heft 173/1986 °   *Vor- und Nachteile des naturnahen Gewässerlaufes im Vergleich zu kanalisierten Fließgewässern; H. Willy*

Heft 174/1986   *Naturnahe Umgestaltung ausgebauter Fließgewässer. Beiträge zum Wasserbaulichen Kolloquium am 14.02.1986 in Karlsruhe*

Heft 175/1986 °   *Naturnahe Umgestaltung ausgebauter Fließgewässer Projektstudie; K. Kern, I. Nadolny*

Heft 176/1987 °   *Der Einfluß von Querströmungen auf ein Schiff bei beschränkten Fahrwassertiefen; F. Bakowies*

Heft 177/1988   *Zur Bemessung von Geschiebeabzügen; G.M. Kley*

Heft 178/1988   *Hydraulik der kontinuierlichen und intermittierenden Furchenbewässerung: ein hydrodynamisches Modell; M. Awwad*

Heft 179/1990   *Sturzwasserbewässerung. Bewässerung mit Niederschlagswasser ohne Zwischenspeicherung im Sahel; W. Klemm*

Heft 180/1991   *Beiträge zur naturnahen Umgestaltung von Fließgewässern*

Heft 181/1991 °   *Naturgemäße Bauweisen von Sohlenbauwerken und Fischaufstiegen zur Vernetzung der Fließgewässer; R.-J. Gebler*

Heft 182/1991   *Untersuchungen zum Stabilitätsverhalten von Gerinnesohlen; A.Dittrich, M. Rosport, O. Badde*

Heft 183/1993   *Der Einfluß der Belüftung auf die Kavitationserosion; N. Eisenhauer*

Heft 184/1993   *nur als Buch erhältlich bei Springer Verlag: Grundlagen naturnaher Gewässergestaltung. Geomorphol. Entwicklung von Fließgewässern; K. Kern*

Heft 185/1993   *Ausbauoptimierung dezentraler Wasserkraftsysteme; H. Hildebrand*

Heft 186/1994   *Turbulente, abgelöste Zweischichtenströmung über Sohlschwellen in einem offenen Rechteckgerinne; U. Kertzscher*

Heft 187/1994   *Untersuchung des Niederschlags- und Abflußgeschehens im westafrikanischen Sahel. Abschätzung des Wasserdargebots aus kleinen Einzugsgebieten mittels stochastischer Methoden unter Verwendung von Satellitenbilddaten; W. Tauer*

Heft 219/2002   *Kontrolle von Barrieren: Bestimmung der hydraulischen Leitfähigkeit an Hand des Bodenwassergehaltes; R. Schuhmann (auch elektronisch unter: http://www.ubka.uni-karlsruhe.de/eva/index.html)*

Heft 220/2003   *Langfristige, hydrologische Betrachtung der Grundwasserdynamik am Beispiel der Mittleren Elbe; P.-A. Burek (auch elektronisch unter: http://www.ubka.uni-karlsruhe.de/eva/index.html)*

Heft 221/2003   *Wassermengenbewirtschaftung im Einzugsgebiet der Ruhr: Simulation und Echtzeitbetrieb; T. Brudy-Zippelius (auch elektronisch unter: http://www.ubka.uni-karlsruhe.de/eva/index.html)*

Heft 222/2004   *Russisch-Deutsches Wörterbuch für Wasserwirtschaft; R. Krohmer, I.S.Rumjanzev*

Heft 223/2004   *Mobilisierung und Immobilisierung von mineralischen Feinstkorn-aggregaten an Gewässersohlen; J.-W. Kim (nur elektronisch unter: http://www.ubka.uni-karlsruhe.de/eva/index.html)*

Heft 224/2004   *Strömungsstruktur und Impulsaustausch in gegliederten Gerinnen mit Vorlandvegetation; I. Schnauder (nur elektronisch unter: http://www.ubka.uni-karlsruhe.de/eva/index.html)*

Heft 225/2004   *Towards Decision Support Models for Un-gauged Catchment in India, The Case of Anas Catchment; A. K. Singh (nur elektronisch unter: http://www.ubka.uni-karlsruhe.de/eva/index.html)*

Heft 226/2004   *Integrales Hochwasser-SimulationssystemNeckar – Verfahren, Werk-zeuge, Anwendungen und Übertragungen; P. Oberle (auch elektronisch unter: http://www.ubka.uni-karlsruhe.de/eva/index.html), noch nicht erschienen, Mai 2005*

Heft 227/2004   *Small Hydropower Plants Based Power Systems for Remote Regions; R. K. Maskey (nur elektronisch unter: http://www.ubka.uni-karlsruhe.de/eva/index.html) noch nicht erschienen, Mai 2005*

Heft 228/2004   *Spatial Time Domain Reflectometry for Monitoring Transient Soil Moisture Profile; R. Becker (nur elektronisch unter: http://www.ubka.uni-karlsruhe.de/eva/index.html)*

Heft 229/2005   *River Flood Prediction Systems: Towards Complementary Hydrodynamic, Hydrological and Data Driven Models with Uncertainty Analysis; R. Shrestha (auch elektronisch unter: http://www.ubka.uni-karlsruhe.de/eva/index.html) noch nicht erschienen Mai 2005*

Heft 230/2005   *Empfehlungen zur naturnahen Gewässerentwicklung im urbanen Raum –unter Berücksichtigung der Hochwassersicherheit-; B. Lehmann (auch elektronisch unter: http://www.ubka.uni-karlsruhe.de/eva/index.html)*

Heft 231/2005   *Einfluß der Oberflächenströmung auf die permeable Gewässersohle; S. Vollmer (auch elektronisch unter: http://www.ubka.uni-karlsruhe.de/eva/index.html)*

Heft 232/2005   *Optimization of Internal Hydraulics and of System Design for PUMPS AS TURBINES with Field Implementation and Evaluation; P. Singh (auch elektronisch unter: http://www.ubka.uni-karlsruhe.de/eva/index.html)*

Bestellungen an: *Institut für Wasserwirtschaft und Kulturtechnik*
Bibliothek
Universität Karlsruhe
Kaiserstr. 12
D-76128 Karlsruhe
Tel.: (0721) 608 6389
Fax: (0721) 60 60 46
e-mail: raskob@iwk.uka.de

_____

° vergriffen

LEBENSLAUF

Rolf Becker
Diplom-Physiker
geboren am 04.03.1967 in Wesel
verheiratet, zwei Kinder

BERUFSERFAHRUNG / PROJEKTE

03/2005 – heute	Entwicklungsingenieur, IMKO Micromodultechnik GmbH, Ettlingen
06/1995 – heute	Wissenschaftlicher Mitarbeiter, Institut für Wasser und Gewässerentwicklung, Universität Karlsruhe (TH)
07/2002 – heute	Projekt „Hochwasserfrühwarnsystem": Entwicklungsleitung, gefördert durch das Land Baden-Württemberg
01/1999 – 12/2004	Projekt „Hochwasserregionalisierung": Software-Entwicklung, gefördert durch die Landesanstalt für Umweltschutz, Baden-Württemberg
01/1997 – 06/2001	Projekt „Morphodynamik der Elbe": Geodaten-Management, gefördert durch das Bundesministerium für Bildung und Forschung

STUDIUM / SCHULBILDUNG / ZIVILDIENST

10/1995 – 6/1997	Fernuniversität Hagen, verschiedene Kurse zur Weiterbildung in Informatik und Wirtschaft
07/1995 – 12/1996	Mitglied des Graduierten-Kollegs „Ökologische Wasserwirtschaft", gefördert durch die Deutsche Forschungsgemeinschaft
10/1988 – 02/1995	Studium der Physik an der Universität Bonn Schwerpunkte: Atmosphärenphysik, Teilchenphysik, Chemie, Physiologie
10/1986 – 05 /1988	Zivildienst in Krankenpflege (München) und Naturschutz (Wesel)
08/1973 – 05/1986	Grundschule und Gymnasium in Wesel

AUSLANDSERFAHRUNG

07/1994 – 08/1994	Wissenschaftler bei der internationalen Forschungskampagne „Echo-94", Andøya-Rocket-Range, Norwegen
04/1995 – 05/1995	Gastwissenschaftler am Meteorologischen Institut der Universität Stockholm, Schweden

Karlsruhe, den 11.07.2005